SEISMIC PERFORMANCE QUANTIFICATION OF CONCRETE BLOCK MASONRY STRUCTURAL WALLS WITH CONFINED BOUNDARY ELEMENTS AND DEVELOPMENT OF THE NORMAL STRAIN-ADJUSTED SHEAR STRENGTH EXPRESSION (NSSSE)

SEISMIC PERFORMANCE QUANTIFICATION OF CONCRETE BLOCK MASONRY STRUCTURAL WALLS WITH CONFINED BOUNDARY ELEMENTS AND DEVELOPMENT OF THE NORMAL STRAIN-ADJUSTED SHEAR STRENGTH EXPRESSION (NSSSE)

By
BENNETT RALPH BANTING
B.Eng & Society (McMaster University)

A Thesis Submitted to the School of Graduate Studies

in Partial Fulfilment of the Requirements for the Degree of

Doctor of Philosophy

McMaster University

DOCTOR OF PHILOSOPHY (2013) McMaster University

(CIVIL ENGINEERING) Hamilton, Ontario

Title: Seismic Performance Quantification of Concrete Block Masonry Structural Walls with Confined Boundary Elements and Development of the Normal Strain-adjusted Shear Strength Expression (NSSSE)

Author: Bennett Banting, B.Eng & Society (McMaster University)

Advisor: Dr. W. El-Dakhakhni

Number of Pages: xii, 199

ABSTRACT

The masonry construction industry represents a historically significant and substantial portion of both existing and new residential, commercial and institutional low- to medium-rise structures across Canada. Although commonly chosen for its aesthetic qualities by architects, structural masonry walls constructed with concrete block units are also an effective lateral force (wind or seismic) resisting system. The purpose of this dissertation is to address what are perceived to be overly conservative and outdated practices within masonry construction and design by adopting analysis and design practices which have had success with similar reinforced concrete wall systems. The results from a test program reporting on the behavior of nine fully-grouted reinforced masonry (RM) structural walls containing confined boundary elements are analyzed and presented according to force-, displacement- and performance-based seismic design considerations. The boundary element containing four vertical bars with lateral confinement stirrups selected represents a readily codified and practically achievable means of achieving seismic performance enhancement. The design and detailing of the specimens represented a range of parameters that would be anticipated to vary within low- to medium-rise RM buildings. In addition, an analytical study is carried out to derive, from first principles of stress equilibrium and strain compatibility, the necessary constitutive material and mechanics-based equations needed to solve for the state of shear stress and strain in an idealized cracked masonry macro-element. The algorithm proposed is validated by comparing the proposed model to existing test data and is further developed towards predicting the design shear strength of RM structural walls. The results from these experimental and analytical research programs are subsequently used to provide a set of proposed code clauses at the end of the thesis. Prescriptive design requirements are proposed for a new category of *Special Ductile Masonry Shear Wall* containing boundary elements including integration of a new shear strength expression. These clauses have been written with the intention of adoption within the CSA S304.1 and the MSJC North American masonry designs standards.

ACKNOWLEDGEMENTS

"What can be asserted without proof can be dismissed without proof."
-Christopher Hitchens

The financial support on behalf of the McMaster University Centre for Effective Design of Structures (CEDS) funded through the Ontario Research and Development Challenge Fund (ORDCF) as well as the Natural Sciences and Engineering Research Council (NSERC) of Canada is greatly appreciated. Provision of mason time by Ontario Masonry Contractors Association (OMCA) and Canada Masonry Design Centre is also appreciated. The supply of half-scale blocks by the Canadian Concrete Masonry Producers Association (CCMPA) is gratefully acknowledged.

I would like to thank my advisor, Dr. El-Dakhakhni for all his input, mentoring, long discussions, constructive criticism and friendship. I would also like to thank the other members of my committee, Dr. Wilson, Dr. Tait, Dr. McDermid and Dr. Abrams for their valuable advice and suggestions throughout this process.

Of course my experimental work would never had happened without the help of my friends and colleagues Kevin Simonds, Mark Hayman, Omar El-Azizy, Mustafa Siyam, Paul Heerema, Kevin Hughes, Joe Wierzbicki, Ahmed Mostafa and of course, Marwan Shedid for teaching me everything he knows about masonry structural walls and the ways of the ADL. Finally, a special thanks has to go to Mr. Kent Wheeler, without whom I would probably still be in the ADL toiling away in futility.

I would like to thank Mr. David Stubbs of the Canada Masonry Design Centre for his supervision of my Industrial NSERC Scholarships as well as instructors Tim, Scott, Mario and Clay of the Ontario Masonry Training Centre for all their help in constructing and transporting my wall specimens.

Finally, I would like to thank my family for their support over these years with a very special thanks to my wife (Professor) Jennifer Drake, without whom I would have surely dropped out or gone mad a long time ago.

TABLE OF CONTENTS

LIST OF FIGURES

LIST OF TABLES

DECLARATION OF ACADEMIC ACHIEVEMENT

This research presents experimental and analytical work carried out solely by Bennett Banting, herein referred to as "the author" with advice and guidance provided by the academic supervisor Dr. Wael El-Dakhakhni. Information that is presented from outside sources which has been used towards analysis or discussion, has been cited when appropriate, all other materials are the sole work of the author.

CHAPTER 1: INTRODUCTION

1.1 Motivation for Research

The masonry construction industry represents a historically significant and substantial portion of both existing and new residential, commercial and institutional low- to medium-rise structures across Canada. Although commonly chosen for its aesthetic qualities by architects, masonry *structural wall*s comprised of concrete block units are also an effective lateral force (wind or seismic) resisting system. The design of masonry structural walls in low-rise structures tends to be driven by seismic load requirements because of the typically high stiffness and large mass of masonry buildings. As a result, the current edition of the National Building Code of Canada (NBCC) (2010) places severe limits on the use of masonry in regions of moderate seismic risk. However, with increased conservatism in the latest seismic hazard maps as well as new limitations on structures considered to have a "high importance," satisfying seismic design requirements in an efficient and economical way remains challenging for masonry designers. The limits imposed on masonry structures are derived from historical observations of past building performance, expert opinion and experimental data when available (Mitchell et al. 2003). Unfortunately, there is a substantive lack of experimental data related to seismic behavior of masonry structural wall buildings. Furthermore, much of the historical observations made related to masonry seismic performance are based on unreinforced and un-engineered masonry, which typically suffer a brittle and catastrophic failure. In addition, only recently, there has been a shift for masonry from an empirical, or *rule of thumb,* designed material to an engineered one. As a result, there are only a few engineering schools in Canada that incorporate comprehensive engineered masonry design courses, which may result in the expert opinions from practicing engineers to be skewed. A remedy for the current state of affairs with regards to masonry design code interpretation is to increase the amount of high quality experimental research and analytical studies. This is needed to the extent that future building code decisions need not have to rely so heavily on qualitative assertions and historical inference. Without continued advancement of masonry as a structural material, there will always be a justified hesitation on behalf of those charged with setting building and design codes to adopt an excessively conservative disposition.

In conclusion, it is the view of this author, as well the motivation for this dissertation, that there is already an inherent conservatism within the masonry structures design standard produced by the Canadian Standards Association (CSA) S304.1 (CSA 2004a), as well within the seismic design portion of the NBCC (2010), that is not an accurate reflection of the behavior engineered masonry structural wall buildings are capable of. The approach taken by this author will be through a thorough analytical and experimental program based on adapting accepted, and much less conservative, design practices used with reinforced concrete (RC) to reinforced masonry (RM) structural wall design. Whereby, RM refers to masonry walls constructed with hollow concrete block units that contain vertical and horizontal reinforcement and a high slump concrete material, referred to as *grout*, used to fill voids and bond with reinforcement.

1.2 Theme and Objectives of Dissertation

The dissertation has been assembled into a *sandwich thesis* format comprised of four journal articles. These articles represent the independent work of the author of this dissertation, Bennett Banting, henceforth referred to as "the author" and are all co-authored with the thesis supervisor, Dr. El-Dakhakhni. With each of these articles, the author acted as the principal investigator and writer. In every instance Dr. El-Dakhakhni acted in a technical advisory and editorial role and provided feedback and suggestions during document assembly. The four articles contained within this body of work were written with the objective of testing and codifying the flexural behavior of an enhanced masonry shear wall configuration containing boundary elements. In addition, a more accurate method of predicting the shear strength of current masonry shear wall construction is also presented. The objective of this research is to improve upon the actual seismic performance of masonry shear walls as well as the ability of a designer to predict such performance with goal of improving masonry structures. The results from this experimental and analytical research program are subsequently used to provide a set of proposed code clauses at the end of the dissertation. Prescriptive design requirements are proposed for a new category of *Special Ductile Masonry Shear Wall* containing boundary elements including integration of a new shear strength expression. These clauses have been written with the intention of adoption within the CSA S304.1 and the MSJC North American masonry designs standards. Research objectives specific to each paper are described for each article below:

The second and third chapters of this dissertation describe the experimental program and the experimental results, respectively, for the testing of half-scale shear walls with confined boundary elements. These two chapters contain the combined works from two journal articles, which have been integrated together to provide better flow of the dissertation:

Banting, B. R. and El-Dakhakhni, W. W. (2012). "Force- and Displacement-Based Seismic Performance Parameters for Reinforced Masonry Structural Walls with Boundary Elements." *ASCE Journal of Structural Engineering* Vol. 138(12), 1477-1491.

Banting, B. R. and El-Dakhakhni, W. W. (2013a). "Seismic Performance Quantification of Reinforced Masonry Structural Walls with Boundary Elements." Submitted to *ASCE Journal of Structural Engineering,* Accepted with Revisions for 2nd Round of Review on Feb. 11, 2013.

These chapters provide experimental results and analysis related to the experimental testing of 9 RM structural walls detailed with confined boundary elements. The objectives of these articles are to disseminate valuable experimental evidence needed to establish the seismic performance characteristics for a new RM structural wall category to resist seismic loads. These articles also aim to illustrate the effects of changes in total applied axial load as well as changes in wall detailing as they relate to the seismic behavior masonry walls. In addition, comparison between the behavior between walls constructed with different geometric properties, such as their height, length and height-to-length ratio is also presented. Experimental observations have been made regarding different seismic design methodologies, such as the currently adopted force-based design as well as next-generation displacement- and performance-based design methodologies. This includes observations made regarding wall stiffness, damping, curvature, ductility, flexural, shear and sliding deformations contribution to total top displacement and the occurrence of different forms of damage in the walls.

The fourth chapter of the dissertation presents analysis of the experimental data as well as information that was presented in the previous two articles relating to analysis, but is largely comprised from the work in the following article:

Banting, B. R. and El-Dakhakhni, W. W. (2013b). "Seismic Design Parameters for Special Masonry Structural Walls Detailed with Confined Boundary Elements." Submitted to *ASCE Journal of Structural Engineering* on Dec. 12, 2012.

The principal objectives of the research program presented in this article are related to the analysis of the experimental data needed towards the development and ultimately adoption of a new category of RM structural wall for seismic design. A theoretical methodology is derived and validated for use to estimate the parameters necessary within a force-based design, such as: strength, displacement, plastic hinge length, elastic stiffness and ductility. A methodology is proposed to estimate the ultimate compressive strain in the confined boundary element. In addition, a new approach to estimate an effective plastic hinge is developed that integrates varying angles of shear crack inclination. Finally, within the objectives of this article is establishing digital image correlation as a potential analysis tool for use on RM structural wall tests. A methodology is proposed to estimate crack damage in walls and drift-based fragility functions are presented to be used towards next-generation performance-based seismic design codes.

The fifth chapter of the dissertation presents the derivation of a new shear strength expression for fully-grouted masonry shear walls and is derived from the work in the following article:

Banting, B. R. and El-Dakhakhni, W. W. (2013c). "Normal Strain-Adjusted Shear Strength Expression for Reinforced Masonry Structural Walls." Submitted to *ASCE Journal of Structural Engineering* and Accepted with Revisions for Revise for Editor Only on Dec. 14, 2012.

The principal objectives of this portion of the overall dissertation are related to enhancing the current understanding of the diagonal tension shear failure mechanism of fully-grouted reinforced concrete block structural walls. An analytical study is carried out to derive, from first principles of force equilibrium and strain compatibility, the necessary constitutive material and mechanics-based equations needed to solve for the state of shear stress and strain in an idealized cracked masonry macro-element. The proposed algorithm is validated by comparing the proposed model to existing macro-element (small panel) test data. The second part of this article is related to the assumptions and derivations

necessary to apply this approach to predict the design strength of RM structural walls. The proposed expression was found to be significantly more accurate than existing shear strength expressions and is further simplified in a code-ready format. The work presented in this article also served as a basis towards the analysis of walls tested as part of the experimental portion of the research program. The derived expressions facilitate quantifying the effects that shear crack propagation have on other aspects of the seismic design such as: wall stiffness, occurrence of predefined damage states, shear spread of flexural plasticity and the potential for degradation to lateral strength as a function of increased ductility.

The articles in the dissertation follow a cohesive theme aimed at expanding and improving upon the current knowledge-base as well prescriptive design requirements related to the seismic design of RM structural walls containing confined boundary elements. The published works contained in this dissertation invariably contain some overlap with regards to their coverage of relevant literature as well some aspects related to the methodology of the test program. To address this overlap the materials presented in these papers have been reorganized into three separate chapters dealing with: the experimental program, experimental results and analysis. At instances where experimental data or analysis conducted in one of the articles is used in another, it is explicitly cited, otherwise it is original work unique to the article. In addition, the raw experimental data from previous testing by Shedid (2009) and Shedid et al (2010a) was integrated into some analysis aspects for comparison purposes, and at such instances proper citation is provided. In the next section a comprehensive literature review is presented covering, in greater detail, the topics related to this dissertation.

Finally, in the sixth chapter of this dissertation a series of preliminary code clauses are presented. Based on the design requirements for similar reinforced concrete walls, a step-by-step procedure to design a *Special Ductile Masonry Shear Wall* is given. In addition to this, code clauses are also proposed with a new shear strength expression developed in Chapter 5. These clauses have been written in a similar format to the language and pre-existing requirements of the CSA S304.1 masonry design standard. This is done to facilitate the integration of these or similar requirements into current CSA S304.1 and MSJC masonry design standards in North America in the near future.

1.3 Literature Review

Due to the limitations in presenting detailed literature reviews within scholarly journal articles the following section is intended to serve as a detailed overview and critical review of relevant topics covered by this dissertation. The topics covered by this literature review begin with an overview of the current seismic code climate in North America as it relates to masonry design, next the behavior of reinforced masonry (RM) structural walls is discussed in a generalized sense. The definition and history of development of plastic hinge expressions are summarized, followed by a review of experimental tests on RM structural walls failing in flexure. Subsequently, an overview of the importance of wall curvature as it relates to wall behavior is presented and a review of test data related to improving the seismic behavior of RM with confinement is given. Finally, experimental testing of RM structural walls that fail in shear is presented.

1.3.1 Overview of Force-Based Seismic Design Codes

Initially, structures were designed for seismic forces by assuming elastic material behavior, which for masonry is very hard to preserve due to its weak tensile strength and tendency for cracking. However after the Long Beach (1933) and El Centro (1940) earthquakes, structures that would have exceeded their theoretical strength were observed to remain standing (Riddle 2008). It was Housner (1956) and Tabinashi (1956) who suggested that structures could survive strong earthquakes if they could safely deform beyond their elastic strength limit. This was made possible theoretically if the energy imposed on the structure, had it remained elastic, could be dissipated by the inelastic response, thus leading to the *equal energy* assumption. The difficulty with this assumption was that a structure would require a substantially higher displacement capacity to ensure that adequate energy is dissipated. Veletsos and Newmark (1960) noted that using elastic-perfectly plastic single-degree-of-freedom (SDOF) systems subject to ground motion records did not produce the higher displacements expected from an equal energy approach, but rather elastic and inelastic systems tended to share an *equal displacement*. The equal displacement assumption would be further refined as it applied to low frequency-high period structures by Veletsos and Newmark (1964) and eventually lead towards the adoption of force-based, “R” reduction factors that could account for the reduced force demands imposed on an inelastic system relative to an equivalent elastic system. This modification factor is typically related by the ratio of the inelastic displacement to the elastic displacement of a

structure, further referred to as its *ductility*. Therefore a higher ductility would theoretically result in reduced seismic force demands.

It was proposed by Shibata and Sozen (1974) that structures which contain multiple degrees-of-freedom under dynamic excitation could represented by a SDOF *substitute structure* possessing similar stiffness, strength and displacement capacity properties to the more complex structure. Furthermore, because only the stiffest elements within a structure are anticipated to resist seismic loads, the structure can be represented solely by its seismic force resisting system (SFRS), which for masonry structures is the structural wall system. Therefore, proper detailing must be provided in the structural walls to permit the required ductility-based reduction of seismic force. Ensuring a flexural failure mechanism governs structural wall behavior rather than a more brittle shear failure is one means of providing the necessary ductility, and is the foundation of the *capacity design* philosophy described by Park and Paulay (1975). Currently, the NBCC (2010) adopts both the equal displacement assumption and capacity design philosophy for seismic design.

In order to take advantage of the ability of structures to deform beyond their elastic limit in a ductile manner facilitated through the cracking of masonry or concrete, and the yielding of steel, a designer may select from 30 recognized SFRS (NBCC 2010). The NBCC assigns two seismic force "R" modification factors by which the elastic seismic force can be reduced by: the first is related to the ductility of the SFRS, R_d, and the second is based on the ratio of the anticipated overstrength (assumed versus actual strength) of the SFRS, R_o, as depicted in Fig. 1.1. The requirements for detailing that must be assured within the design of a SFRS are set-out by the relevant materials' design standard, which are for example the CSA S304.1 for masonry structures (CSA 2004a) and the CSA A23.3 for concrete and prestressed structures (CSA 2004b). Higher levels of R_d typically correspond with more restrictions on detailing and more complex design. The elastic force-based method employing the equal displacement assumption is employed in Canada as well as in the U.S.A. by the American Society of Civil Engineers (ASCE) building code ASCE 7-10 (2010). The dynamic force and displacement generated for an elastic responding structure of stiffness (natural period) equal to the SFRS can be considered as an equivalent static force of V as shown in Fig. 1.1a. Whereby, the SFRS can be designed for a reduced force of V/R_dR_o if proper assurance is provided through meeting prescriptive design requirements for the SFRS as indicated in Fig. 1.1a. The

reality is, however, that a masonry SFRS is actually constructed with several structural walls acting together, as indicated in Fig. 1.1b. Therefore, it would be imperative from a design perspective to ensure that each of the individual walls possesses sufficient ductility and/or drift capacity to ensure the desired behavior of the SFRS.

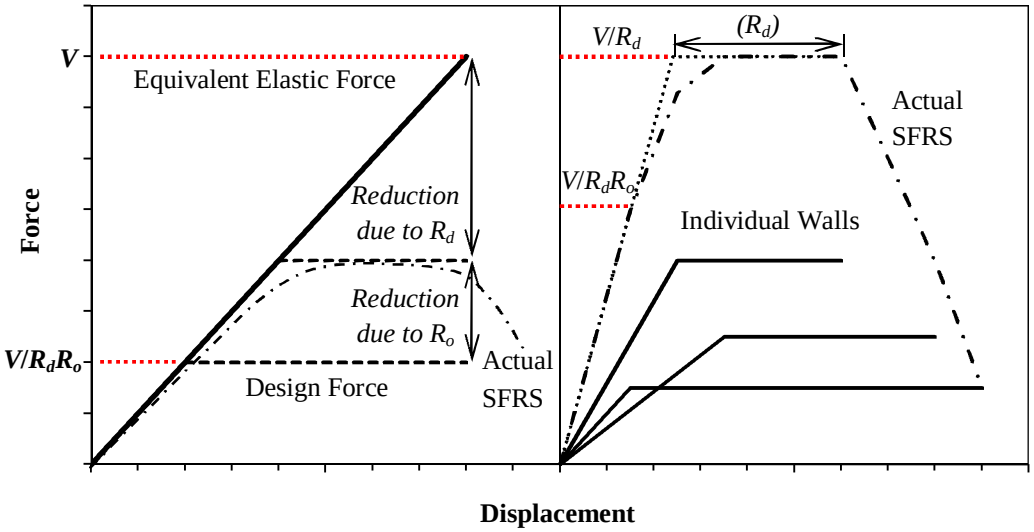

Figure 1.1 - Seismic Forces Generated by the Equal Displacement Assumption: a) Definition of R_d, R_o and b) Illustrating how a Structure is influenced by Individual Walls

It is clear from Fig. 1.1a, that the elastic design forces derived for a particular SFRS can be significantly reduced with increased values of R_dR_o. However, it is also evident from Fig. 1.1b that careful consideration of individual wall behavior must be taken to preserve the assumed minimum ductility capacity possessed by the entire SFRS used to determine R_d.

New RM structural wall construction in seismically active areas of Canada as well as the U.S.A. generally requires concrete block units, fully-grouted and detailed with horizontal and vertical steel reinforcement. This is very similar to RC structural wall construction with regards to material behavior and analysis of strength and displacement. In Canada, designers may currently choose from three values of R_d for masonry structural wall SFRS, R_d = 1.0, 1.5 and 2.0. In regions with moderate seismic risk the two options of interest in new construction are masonry structures detailed to possess *limited ductility* (R_d = 1.5) or *moderate*

ductility (R_d = 2.0). By contrast, designers considering RC may select from an additional structural wall SFRS called *ductile walls*. The CSA A23.3 (CSA 2004b) allows for ductile RC walls to possess an R_d of 3.5, which is 75% greater than the maximum allowed for new RM construction. The value of R_d is increased when stringent prescriptive design requirements are met, including but not limited to: a double curtain of reinforcement at the wall ends and special detailing of lateral stirrups within a specially designated zone of *concentrated vertical reinforcement* (CSA 2004b) capable of carrying high compressive strain and resisting buckling of vertical reinforcement. In American design, both the *special reinforced masonry* structural wall category defined by the Masonry Standards Joint Committee (MSJC 2011) and *special reinforced concrete* structural wall category defined by the American Concrete Institute (ACI) 318-11 (2011) include special provisions to ensure that adequate confinement in the compression toes of the walls is provided, with both materials permitted the same force reduction factor, *R* value of 5.0 (ASCE 2010), which is a combination of overstrength and ductility. Furthermore, in a recent study by the National Institute of Standards and Technology (NIST) GRC 10-91-8 (2010), it was noted that both special RC and RM wall categories equally satisfied collapse prevention criteria following non-linear dynamic analysis. In conclusion, the level of inelastic deformation capacity of masonry structures is recognized in the U.S.A. as being capable of an equal performance with RC, when similar restrictive prescriptive requirements are followed. Therefore, it is reasoned that RM and RC structural wall systems should each be assigned more or less the same levels on R_dR_o imposed by the NBCC, pursuant to the fact that a sufficiently conservative and thorough set of prescriptive requirements, that includes for example confinement of the masonry, are satisfied.

1.3.2 Overview of Performance- and Displacement-Based Seismic Design Codes

With plans to adopt more categorizations of SFRS for the next edition of the NBCC to be published in 2015, there is still a persisting belief among many in the design community that a SFRS comprised of masonry materials is inherently less ductile than its RC counterpart. However, since the advent of the Structural Engineers Association of California (SEAOC) Vision 2000 document (SEAOC 1995), a growing emphasis is being placed on system-level, rather than material-based or component-level, structural performance. Eventually this will lead to a shift away from using the current qualitatively assessed force-based response modification factors towards performance-driven designs based on several factors

that may include more relevant critical aspects such as life safety, extent of damage and rehabilitation costs to name but a few.

It has been suggested that the current elastic force-based design methodology employing the equal displacement assumption and using fixed material-based seismic force modification factors will produce widely variable results between otherwise identical SFRS when aspects such as repair costs and drift-based damage are considered (Nasser and Krawinkler 1991, Priestley 2000). Priestley et al. (2007) also describes a number of inconsistencies associated with using an elastic approach to design, such as: period elongation from reduced wall stiffness with increased top drifts, increased damping exhibited by walls which have cracked or reinforcement that has yielded and system level effects on component behavior, which tend to be overly simplified or completely neglected. For instance, two structures designed to withstand the same level of force which possess the same categorization of SFRS may actually experience different levels of damage. Quantifying the level of damage sustained by a structure can be conveniently, and accurately, related back to peak displacement (drift) demands. For instance, Park et al. (1985) and Park and Ang (1985) expressed the damage of RC elements based on historical observations in terms of a damage index. It was observed that the extent of damage sustained in RC elements after seismic events could be related to both the level of peak drift as well as hysteretic energy absorbed by the system. It has been observed in studies by Li and Weigel (2006), Ahmed et al. (2010) and Murcio-Delco and Shing (2011) that experimentally tested RM walls sharing the same failure mechanisms could be related by their damage performance via peak lateral drift sustained during loading cycles. Therefore, drift and damage, rather than force, would be a better measure of earthquake resistance and performance.

Within this dissertation, these *next-generation* seismic design codes are classified as performance-based or displacement-based design. Whereby, performance-based design is a general term for a seismic design approach that considers the occurrence of specific damage states as they are related to the functionality or remediation costs associated with different design levels of seismic events. Whereas displacement-based design aims to achieve the same goals as performance-based design, but is done through solely using the inelastic properties of a SFRS, and peak spectral ground displacements, rather than accelerations. Currently, the Federal Emergency Management Agency (FEMA) document 237 that was later superseded by FEMA document P695 (ATC 2009),

set-out the need for experimental and analytical work towards the quantification of performance-based design levels of all different SFRS. Initial studies into FEMA P695 suggest a need for further experimental and analytical work on all types of masonry SFRS (NIST 2010). Presently, FEMA 306 (ATC 1998) provides quantitative and qualitative guidelines for a variety of different levels of damage for different SFRS, including RM. A total of five different damage states are described for RM, corresponding to different levels of remediation and reductions in capacity and stiffness are based crack width, crack pattern and the occurrence of crushing or spalling of masonry or buckling of vertical reinforcement. Currently being developed by the ATC-58-1 document (ATC 2011) is a set of guidelines towards the development of drift-based fragility functions. Fragility functions are statistical curves comprised of a smoothed probability distribution function derived from experimental and/or analytical results that relate the occurrence of a predefined damage state to a demand parameter such as peak drift. The application of fragility functions within a rational design process of a SFRS is incumbent upon the quantification of the latter's characteristic load-displacement response and seismic performance parameters.

In conclusion, there is an immediate need to establish prescriptive detailing methods to assure that RM structural wall SFRS can develop the strength and ductility required within force-based design but also to assess their seismic behavior with respect to the occurrence of damage-based performance levels as well as their non-linear displacement-based properties. The following sections will provide a critical review of the current knowledge-base related to the seismic performance of RM as a SFRS.

1.3.3 Behavior of RM Structural walls

The behavior of RM structural walls can be described in terms of three principal mechanisms with reference to Fig. 1.2. Each mechanism may be acting alone or in any combination with the others:

1. Flexural bending of the wall characterized by the formation of horizontal bed joint cracks and yielding of vertical reinforcement. Flexural bending of a wall beyond its elastic limit will form a plastic hinge region where inelastic rotations will be concentrated and significant seismic energy dissipation takes place concentrated in the lower portion of the wall. Failure is characterized by the

crushing of masonry and grout under compression, buckling of vertical reinforcement under compression and/or fracture of reinforcement under tension.

2. Shear deformation of the wall characterized by the formation of large diagonal cracks that may form over the entire height of the wall. Reinforcement that spans the crack openings will offer resistance against a diagonal tension failure of the wall, which may lead to failure characterized by the crushing of a diagonal strut. Walls undergoing significant flexural deformations will have reduced shear strength an areas where flexural rotations are concentrated.

3. Base and bed joint sliding of the wall that can be resisted by sufficient vertical reinforcement along the base acting as dowels.

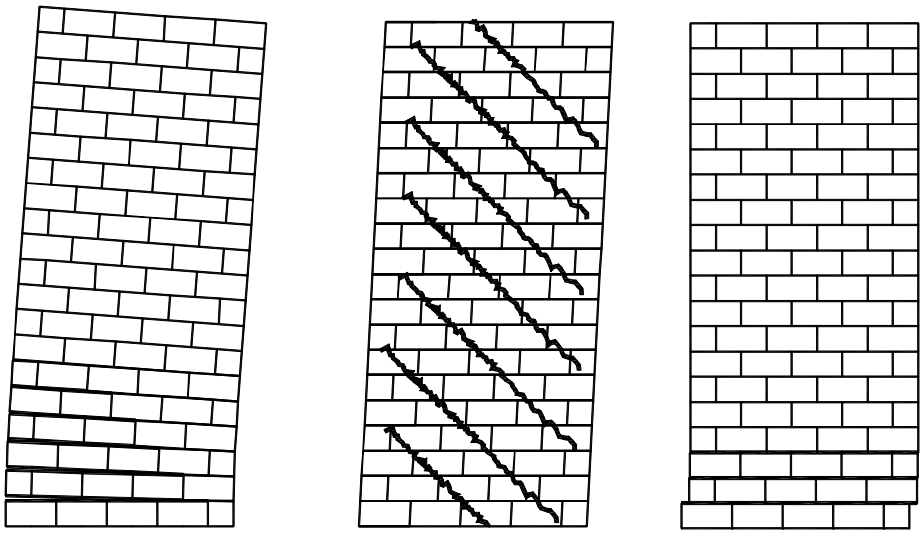

Flexure **Diagonal Tension Shear** **Base and Bed Joint Sliding**

Figure 1.2 – Behavior of RM Structural walls

Priestley et al. (2007) proposed that the seismic drift demand of a structural wall can be estimated from analysis derived from a non-linear push-over analysis such as that proposed by the ASCE 41 document (2006) based on flexural theory. However, the potential to develop a simple theoretical model to estimate these seismic performance parameters for shear-critical RM walls is complicated because of the non-linear interaction between masonry units, grout, mortar, and vertical and horizontal steel reinforcement under shear (Tomaževič 1999). As a result, extensive experimental verification is required to move forward from

empirical expressions to determine shear strength (V_n) or otherwise arbitrary limits on the displacement ductility (μ_Δ) capacity of shear governed walls. The large size of RM structures normally precludes testing of large scale buildings and because the behavior of a masonry structure is determined from the behavior of the individual walls, RM structural walls are typically tested in isolation. In addition, due to the dependency of wall behavior to a particular ground motion, testing of isolated walls is normally done in a quasi-static fashion with fully-reversed cycles of increasing lateral displacement applied. The results from quasi-static tests can be used as a conservative measure of the response of a structural element during dynamic excitation as described by the testing protocols described by Krawinkler at al. (2002) and adopted by FEMA document 461 (ATC 2007). As such, with respect to determining the properties of RM structural walls with regards to design code development only quasi-static tests are considered with fully-grouted and reinforced concrete block structural walls.

1.3.4 Plastic Hinging of RM Structural walls

In ductile masonry structural walls governed by flexural failure, a plastic hinge mechanism will form whereby inelastic rotations are concentrated toward the base of the wall. The plastic hinge zone would represent the area over which a constant level of inelastic rotation is maintained such as to act as an effective hinge for which the wall can be idealized to rotate about. Within the capacity design philosophy, the plastic hinge region represents a load-path dependent energy dissipating mechanism requiring special detailing to ensure the high strains and inelastic curvatures can be maintained. Estimates of the plastic hinge region as it applies toward RM structural wall design have been typically derived from analysis of RC members. Mattock (1967) used the results of RC beams and proposed a plastic hinge length (shown in terms of wall parameters), which was modified by Paulay and Uzumeri (1975), who recommended two specific equations for application with RC walls, based on the height (h_w) and length (ℓ_w) of the wall shown in Table 1.1, ℓ_w is wall length and h_w is wall height taken equal to the shear span for cantilever walls. Paulay and Priestley (1992) suggest a range of values based on reinforcement and Further equations proposed for RM walls by Priestley and Kowalsky (1998) and Priestley et al. (2007) shown in Table 1 relate the plastic hinge with the wall dimensions and reinforcing bar properties such as its diameter (d_b), yield strength (f_y) and ultimate strength (f_u). Finally, Bohl and Adebar (2011) most recently proposed a lower bound estimate for isolated structural walls based on the level of axial stress (P/f'_cA_g).

Table 1.1 – Suggested Plastic Hinge Lengths of Structural walls

Idealized Plastic Hinge (ℓ_p)	Source
$0.5\ \ell_w + 0.05\ h_w$	Mattock (1967)
$0.4\ \ell_w + 0.05\ h_w$	Paulay and Uzumeri (1975)
$0.2\ \ell_w + 0.075\ h_w$	
$0.08\ \ell_w + 0.022\ d_b\ f_y \approx \ell_w/2$ and $0.3 < \ell_p / \ell_w < 0.8$	Paulay and Priestley (1992)
$0.2\ \ell_w + 0.022\ h_w$	Priestley and Kowalsky (1998)
$0.2\ (f_u/f_y - 1) \times h_w + 0.1\ \ell_w + 0.022\ d_b\ f_y$	Priestley et al. (2007)
$(0.2\ell_w + 0.05h_w)(1.0 - 1.5P/f'_cA_g) \leq 0.8\ell_w$	Bohl and Adebar (2011)

For RM structural walls to develop significant displacement ductility, damping and overall energy dissipation required to resist strong ground motions, the plastic hinge zone must be capable of withstanding relatively high plastic curvatures. Plasticity of RM structural walls is generally characterized by cracking of masonry and yielding of vertical reinforcement. Once all tension vertical reinforcement within the wall cross-section develop its yield strength, it can be shown that the moment capacity (M) of the wall remains nearly constant as indicated in Fig. 1.3. As strains in the reinforcement are increased, wall curvature will also increase, which can be determined from strain compatibility assuming plane section analysis as depicted in Fig. 1.3. Whereby, first yielding of the vertical reinforcement is characterized by a depth of compression zone c_1 and a resulting wall curvature of ϕ_1, where $\phi_1 = \varepsilon_m/c_1$, and ε_m is the strain in masonry required for equilibrium with the tensions forces in the reinforcement and any axial load.

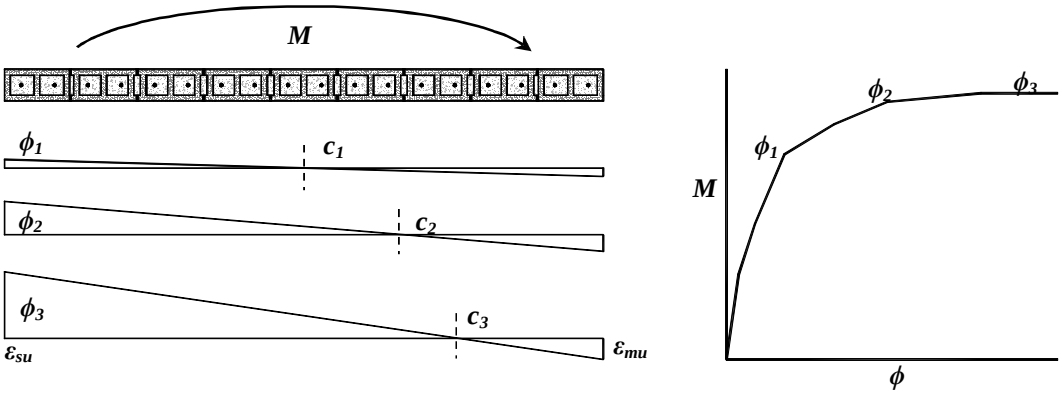

Figure 1.3 – Curvature in Wall Cross-Section

Subsequently, as the moment is increased to the maximum capacity of the wall the neutral axis will shift (c_2) and based on force equilibrium much higher strains in the reinforcement will be achieved resulting in an increased curvature (ϕ_2). Past this point, there will be nominal changes to the moment capacity M, as well as depth of neutral axis (c_3), but increased curvatures (ϕ_3) until a limiting strain in the reinforcement (ε_{su}) or masonry (ε_{mu}) is reached. As yield strains begin to form in the vertical reinforcement, it will gradually spread over the plastic hinge region of the walls as indicated in Fig. 1.4.

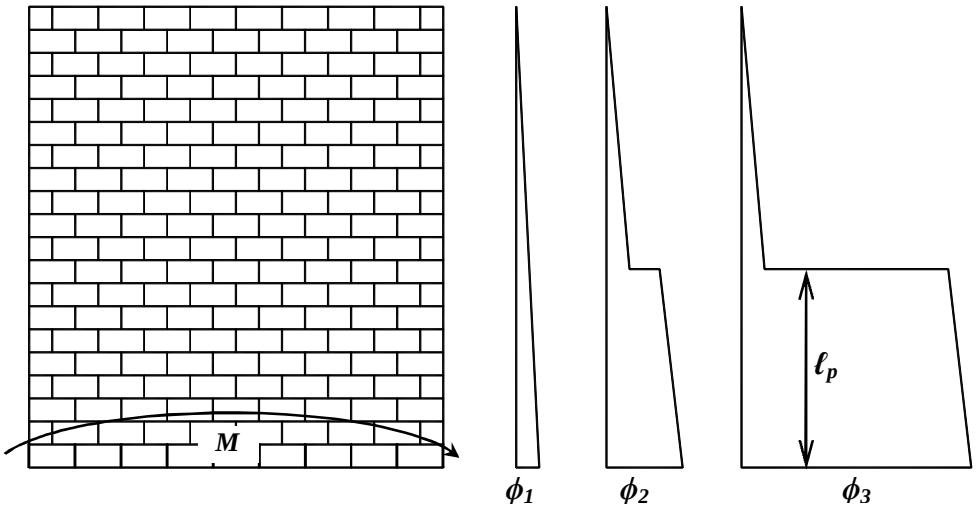

Figure 1.4 – Inelastic Curvature Spreading over Plastic Hinge

Whereby, the top displacement of the wall corresponding to the yield curvature is defined as Δ_y and can be determined from double integration of yield curvature profile as given in Eq. 1.1. The ultimate top displacement, Δ_u, can be determined by adding the total plastic displacement, Δ_p determined in Eq. 1.2, with Δ_y, such that displacement ductility can be determined as $\mu_\Delta = (\Delta_p + \Delta_y) / \Delta_y$.

$$\Delta_y = \frac{\phi_1 h_w^{\,2}}{3} \tag{1.1}$$

$$\Delta_p = (\phi_3 - \phi_1)\ell_p\left(h_w - \frac{\ell_p}{2}\right) \tag{1.2}$$

As can be observed, the displacement capacity and thus displacement ductility are strongly influenced by the wall curvature capacity. Curvature may be limited in a RM structural wall by tensile strains in the reinforcement associated with a

fracturing failure of the reinforcement. However, it is much more likely in RM structural walls that the compressive strain capacity of the masonry, ε_{mu}, would be the limiting factor. The practical limit of ε_{mu} can further be exasperated for the case of seismic loading by the potential for vertical reinforcement to buckle when subjected large reversals of strain in tension and compression. This mechanism can cause an overall loss of wall stability in the plastic hinge region leading to undesirable failure imposed by the buckling rebar against the faceshell of the masonry.

1.3.5 Experimental Studies of RM Structural walls Failing in Flexure

As with many other aspects of RM design, there is a substantial difference in the quantity of RM structural wall test data available compared to RC structural walls. Nevertheless, early tests on fully-grouted RM structural walls were done by Priestley (1976), who reported the results of six walls. The purpose of these tests was to establish that existing shear strength limits were overly conservative, which was confirmed by the observed flexural failure of the walls when they were anticipated to fail in shear. The walls possessed a height of 1.6 m and a length of 2.4 m, with a total level of applied axial stress that varied from 0 MPa- 0.7 MPa, vertical reinforcement ratios that ranged from 0.36%- 0.48% and horizontal reinforcement ratios that ranged from 0.71%- 1.02%. The effects of base slip as well as shear cracking towards hysteretic energy dissipation were noted along with analysis presented to quantify the displacement ductility and stiffness of the walls. The post-peak behavior of the walls and their ability to delay the onset of vertical compression cracking was impeded with the use of steel confinement plates placed in the bed joints at the compression toes of three of the walls tested.

Priestley and Elder (1982) tested three fully-grouted RM slender structural walls along with a series of assemblages to study their seismic behavior structural walls and the effects of confinement plates on wall performance. All walls had a height of 6.0 m and a length of 2.4 m and a vertical and horizontal reinforcement ratios of 0.72% and 0.40%, respectively. The level of applied axial stress was selected to be 1.90 MPa for two of the walls and 0.74 MPa for the third, with one of the former walls also detailed with confinement plates. Ductility of the walls was strongly influenced by the presence of lap splices in the lower portion of the walls, however the addition of the confinement plates increased the displacement ductility capacity of the walls from 2.8 to 4.3.

Within the TCCMAR program, several researchers testing RM piers reported on the formation of flexural mechanisms, although, the primary interest of these test programs was to investigate the shear failure. However, of the cantilever walls tested by Shing et al. (1991) a total of seven walls were reported as failing principally in flexure, with four of the walls failing in a mixed flexural, shear and/or base sliding failure mechanisms. Top drifts of these walls at 50% degradation from peak strength ranged from 1.8%- 2.8% and ductilities that were reported to range from 9.0- 18.0.

Eikanas (2003) tested six fully-grouted RM structural walls to study the effects of changing height to length (aspect) ratios (A_R) on wall behavior. The walls ranged in length from 1.0 m to 1.8 m corresponding to effective heights that varied from 1.3 m to 2.1 m with vertical reinforcement ratios of 0.31%- 0.57%, a horizontal reinforcement ratio of 0.17% and applied level of axial stress of 0.19 MPa. Ultimate drifts, determined at a 20% degradation from the peak strength (Δ_{u80}), ranged from 1.44% for A_R = 0.72 to 2.41% for A_R = 2.1. In addition, it was noted that toe crushing in the conventionally detailed walls occurred at strains higher than the design level of ultimate strain, ε_{mu} = 0.0025. Failure in these walls was described to occur as follows: face shell spalling which progressed to crushing of the block and grout core in combination with buckling of vertical reinforcement.

Shedid et al. (2008) tested six fully-grouted reinforced concrete block structural walls with heights of 3.6 m and lengths of 1.8 m to quantify their energy dissipation and ductility characteristics. Vertical reinforcement ratios ranged from 0.29%- 1.31%, horizontal reinforcement ratios ranged from 0.08%- 0.26% and applied levels of axial stress were provided up to 1.5 MPa. Drifts were reported at a 20% degradation from peak strength to range from 1.22%- 2.21% corresponding to displacement ductility levels of 2.3- 7.8. Shedid et al. (2008) noted that typical failure patterns of the walls included: compressive strains well in excess of 0.0025, ductile, rather than brittle, strength degradation leading to toe crushing and buckling of vertical reinforcement. Shedid et al. (2009) reported that following yielding of the vertical reinforcement, a dramatic drop in stiffness occurs, representing less than 20% of initial elastic stiffness. In addition, the equivalent viscous damping was found to increase proportionally to the increase in displacement ductility.

Most recently, Ahmadi Koutalan (2012) tested 21 shear wall specimens as both cantilever (15) and fixed-fixed (6) elements along with two full-scale masonry

buildings on a shake-table. The cantilever shear walls were tested over a range of heights of 3.6m- 2.4m, lengths of 0.8m- 2.4m, axial load levels of 0%- 15% of f'_m and vertical reinforcement ratios of 0.16%- 1.2%. Ultimate drifts were reported to range from 1.31%- 4.47% with average displacement ductilities from both directions of loading were found to range from 4.66- 17.04. The research program ultimately validated displacement-based design for use on masonry structures, and suggested that was a better approach towards design of irregular structures, when force-based procedures cannot be applied.

These research programs indicate that conventional RM structural wall construction is capable of high levels of drift as well as substantial ductility. With respect to the MSJC classification, the walls reported mostly fall under the *Intermediate Reinforced Masonry Structural walls* (R = 3.5) SFRS (MSJC 2011). A survey of existing experimental data on RM structural walls conducted by Vaughan (2010) indicated an overall average idealized displacement ductility capacity of this wall type of μ_Δ = 4.93. However, the performance of walls which fit into this category is often hindered by the effects of spalling and lateral instability associated with the buckling of reinforcement in the compression toes. To address the limited compressive strain of the masonry, Priestley (1976) and Priestley and Elder (1982) introduced steel confinement plates in the bed joints of the compression toes in RM structural walls. To improve post-peak behavior, a number of other researchers developed and tested ways to confine the masonry located in the compression toes of RM walls which will be described in the subsequent section.

1.3.6 Confinement of Masonry

The majority of the available research on buckling of vertical reinforcement when subject to large reversed strains is focused on RC columns under cyclic and monotonic loading. However, the relatively small size and high compressive stresses in the compression zone of structural walls lends itself well to comparison with column behavior. Bresler and Gilbert (1961) established that lateral stirrups around vertical reinforcement in RC columns can act to inhibit and delay the tendency for vertical reinforcement to buckle under compressive stress. The potential for inelastic buckling of reinforcement in the plastic hinge region of RC columns has been studied extensively by Pantazopoulou (1998), Moyer and Kowalsky (2003) and Berry and Eberhard (2005) leading to detailed prescriptive requirements for RC columns as well as structural walls. Whereby, the ends of

special (ACI 2011) or *ductile* (CSA 2004b) RC structural walls are detailed according to the requirements of confined columns containing a minimum of two layers of reinforcement with lateral confinement stirrups.

RM structural walls, however, are restricted on the space available to place vertical reinforcement and typically can only be detailed with a single layer of vertical reinforcement as illustrated by the cross-section that was shown in Fig. 1.3. Paulay and Priestley (1993) presented an analytical model with suggested limits towards the unsupported height of structural walls due to the potential for out-plane wall instability after yielding of reinforcement related to the thickness of the compression region of the wall. Azimikor (2012) tested five very slender RM walls in an effort to quantify this phenomenon, but proved inconclusive, as the effects contributing to local buckling of vertical reinforcement are difficult to replicate within laboratory testing. Nevertheless, increasing the compressive strain of masonry, ε_{mu}, through confinement will invariably increase the likelihood that vertical reinforcement may buckle.

Early methods of confining masonry did not diverge greatly from a conventional wall layout of a rectangular cross-section detailed with a single layer of vertical reinforcement. Instead, research was focused on alternative materials which could be placed in the masonry units themselves to provide confining effects. For instance, one of the earliest means to confine masonry were stainless steel plates placed on the mortar bed on the faceshell and web of the units as depicted in Fig. 1.5. Tests on structural walls detailed with confinement plates were first conducted by Priestley and Bridgeman (1974) in brick walls and later by Priestley (1976) and Mayes et al. (1976) in concrete block walls and piers, respectively. In these early tests, it was observed that the confinement plates acted as a mechanism to delay the vertical splitting tension failure of the compression toes, thus increasing the effective compressive strain of the masonry. Tests on a series of walls and prisms reported by Priestley and Elder (1982) and Priestley and Elder (1983) were used to evaluate the design characteristics necessary to predict confined wall behavior. It was suggested that a modified Kent-Park stress strain relationship, adopted from concrete behavior, could be used to estimate the confining effects on the masonry. It was also noted, that although the ultimate strain of the wall could be improved upon though the addition of confinement plates, it had a minimal effect on influencing the peak strength or strain corresponding to peak strength in the masonry as compared to concrete confinement techniques. Currently, the New Zealand masonry design code

(SANZ 2004) adopts confinement plates for their Ductile walls category allowing for an ultimate compressive strain in the masonry of ε_{mu} = 0.008.

As part of the TCCMAR program, Hart et al. (1988), Hart et al. (1989) and Sajjad (1990) presented experimental and analytical work related to the testing of 114 RM prisms with a total of seven different types of confinement. The confinement schemes tested included lateral stirrups placed in cores around a single vertical bar in the centre, steel confinement plates in the bed joints, a steel "confinement comb" placed in the bed joints, steel mesh in the bed joints, and various circular or spiral tie configurations around four bars placed in the cells as indicated in Fig. 1.5.

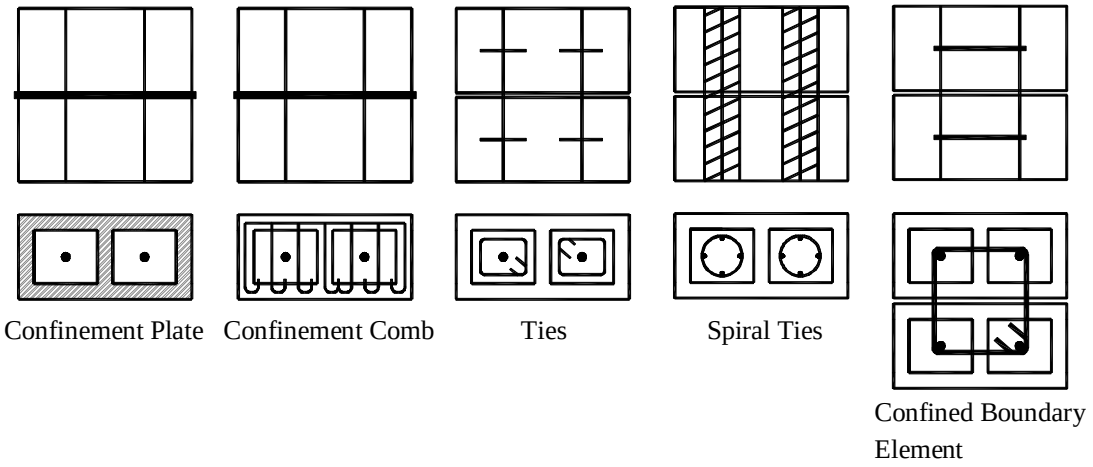

Figure 1.5 – Examples of Confinement Techniques for Masonry

The confinement schemes tested generally had a negligible effect on altering peak stress or strain characteristics of the masonry but did soften the descending branch of the stress-strain curve after peak loading. In addition, six walls with confinement were also tested, and based on these results a constitutive model was created to predict wall behavior based on the stress-strain relationship for each particular confinement scheme. Further analysis related to masonry confinement includes two walls reported by Shing et al. (1991) and Shing et al. (1993) as well as another analytical model developed and presented by Nazir and Hart (2001). As late as 1997, the Uniform Building Code (UBC) (ICBO 1997) allowed for compressive masonry strains up ε_{mu} = 0.006 for walls confined with #3 (9.5 mm) stirrups at an 8" (203 mm) spacing. However, in lieu of the many confinement possibilities, the MSJC (2011) no longer specifies any one methodology, but

rather leaves the onus on a designer to select and detail an appropriate confinement technique.

More recent work on confinement of unreinforced grouted concrete block by Dhanasekar and Shrive (2002) employed two types of welded wire mesh to confine the grouted cells in unreinforced concrete block prisms. The wire mesh proved to be an effective means of increasing the peak compressive strength by 29% and 38%, respectively for the two configurations tested. In addition, the steel mesh also increased the strain at the peak compressive stress by 20% and 36%, respectively. Softening of the post-peak stress-strain relationship was also reported to be proportional to the increase in strain at peak stress.

The majority of recent work on masonry confinement has come from an extensive test program at Washington State University. Malmquist (2004) tested 45 concrete block and brick prisms with steel confinement plates and combs. The reported strains at 50% of the peak stress in the confined concrete block prisms were measured to be 0.0055 and 0.006 for confinement plates and combs, respectively, compared to an unconfined value of 0.004. Hervillard (2005) tested 30 concrete block and brick prisms which contained fibre reinforced grout. Strains reported for the block prisms corresponding to a drop to 50% of the peak stress were 0.0039 and 0.0047, for different amounts of fibre reinforcement, compared to 0.0032 in the control prisms. Finally, Snook (2005) incorporated three different types of bed joint confinement techniques into large scale RM wall tests with an A_R = 0.93 and 1.5: steel plates, steel confinement comb and fibre wraps. The top drift corresponding to a drop in resistance to 80% of the peak had the following deviations from the unconfined conventional wall tested: the confinement plates resulted in a -9.3% and +5.4% change in drift, the confinement combs resulted in a +6.2% and +1.4% change in drift and the fibre wraps resulted in a +35.8% and +15.4% change in drift, for A_R = 0.93 and 1.5, respectively.

To investigate the behavior of RM structural walls possessing different end configurations, Shedid et al. (2010a) tested seven fully-grouted RM structural walls constructed of half-scale block units. The length of the walls was fixed at 1.8 (3.6 m in full-scale) with two different heights of 2.7 m and 4.0 m (5.4 m and 8.0 m in full-scale) selected. This test program was aimed at comparing the seismic behavior of walls with three different end configurations: a conventional rectangular wall cross-section, a flanged wall and a wall with confined boundary elements at its ends depicted in Fig. 1.5. The three walls detailed with a confined

boundary element at the ends allowed for 4 vertical reinforcement bars placed in two layers and confined with steel reinforcement stirrups placed in every course. Tests of boundary element prisms reported by Shedid et al. (2010b) indicated an increase in the compressive strain by 51% over unreinforced and unconfined boundary elements. Shedid et al. (2010a) reported that an increase in ductility of at least 39% and 106% was achieved in walls with the addition of flanges and confined boundary elements, respectively. Additionally, the measured drift for rectangular, flanged and boundary element wall configurations at a drop of 20% from peak load was observed to be at least 1.0%, 1.5% and 2.0% drift, respectively.

1.3.7 Experimental Studies of RM Structural Walls Failing in Shear

There is a relatively limited number of tests of RM structural walls that meet the conditions imposed for regions of moderate seismic risk within Canada (i.e. fully-grouted, standard concrete block units with vertical and horizontal reinforcement). The design expressions and detailing requirements currently found in the U.S.A. and Canada masonry design codes are largely based on the results of a large-scale, multiple-institute, test program in the 1970's and 1980's: The U.S. - Japan Joint Technical Coordinating Committee for Masonry Research (TCCMAR). The objectives of this program was to quantify a wide range of material, assemblage, member and structural properties of masonry in an effort to modernize masonry construction and design.

A majority of the isolated structural walls tested as a part of TCCMAR focused on relatively small-size walls (essentially masonry piers) depicted in Fig. 1.6a (Yancey et al. 1991). These elements are characterized as the contributing mechanism towards the failure of RM frame structures (Paulay and Priestley 1992) and arise from instances when structural walls contain openings. For instance, Leiva and Klinger (1994) tested six RM walls with openings and established that following a weak beam strong column approach to design, adequate seismic resistance is possible. However, as a result of this detail the relatively stiff connections above and below the piers cause double curvature in the piers as indicated in Fig. 1.6a. Therefore, when subjected to lateral loads masonry piers tend to be governed by a shear failure mechanism. By contrast, cantilever structural walls subject to single curvature are generally more typical of modern construction detailing as indicated in Fig. 1.6b, whereby movement joints are used to isolate piers and preserve simply supported beam connections

(Drysdale and Hamid 2005). Pier B, indicated in Fig. 1.6b, is much more likely to controlled by flexure, rather than shear.

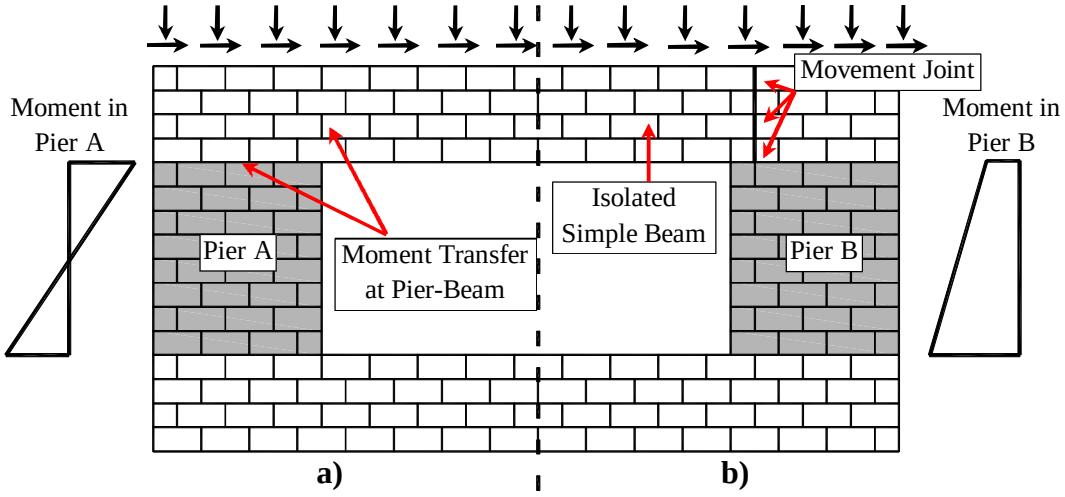

Figure 1.6 - Masonry Piers as They Appear in Structural walls in: a) Masonry Frames; and b) Masonry Structural wall with Isolated Openings

Nevertheless, testing of piers under double curvature conditions form a significant portion of the test data used to formulate masonry shear strength expressions used over the last 20 years (Fattal and Todd 1991, Anderson and Priestley 1992, Voon and Ingham 2007 and Davis 2008).

As a part of the TCCMAR, a number of tests on concrete block and clay brick piers with various grouting patterns and reinforcement schemes were conducted at the Earthquake Research Center of the University of California at Berkeley. A total of 63 piers were tested by Chen et al. 1978, Hidalgo et al. 1978 and Hidalgo et al. 1979. However, due to recognized errors in the testing due to the flexibility of the test frame and uncertainties related to the application of axial loads, the results from these programs are largely omitted from shear strength expression derivations. Nevertheless, Sveinsson et al. (1985) tested ten fully-grouted reinforced concrete block piers 1.2 m long and 1.4 m tall. The effects of different horizontal (shear) reinforcement types (reinforcing bars and wire mesh), different horizontal reinforcement percentages (0.075%- 0.394%), horizontal reinforcement anchorage conditions (90° and 180° bends around extreme vertical reinforcement) and applied levels of axial load (1.7- 3.0 MPa) were studied. It was concluded that horizontal reinforcement was effective in increasing shear strength, but found that there was a limit to its effectiveness and higher amounts of reinforcement did not

correspond to a proportional gain in strength. It was also recommended that only 180° hooks on horizontal reinforcement bars around vertical reinforcement be used for seismic resistance, as they produced the best energy dissipation characteristics and were best able to develop full strength over the short wall lengths studied.

Tests on fully-grouted reinforced concrete block piers in Japan as part of TCCMAR include five piers tested by Okamoto et al. (1987) and 14 piers tested by Matsumura (1987). Although many other specimens were tested, only those constructed of fully-grouted concrete block masonry that demonstrated a shear failing mechanism are reported here, as Matsumura was primarily focused on the behavior of partially-grouted piers (29 tested). The results from Matsumura (1987) were used to develop an empirical shear strength expression presented by Matsumura (1988). The fully-grouted piers were all 1.8 m tall and had lengths of 0.8 m- 1.6 m, with the majority possessing a length of 1.2 m. The parameters of interest included the horizontal reinforcement ratio (0.12%- 0.67%) and the level of applied axial stress (0.5- 2.0 MPa). The piers tested by Okamoto et al. (1987) also had a height of 1.8 m and lengths that varied from 0.8 m to 2.0 m. Although horizontal reinforcement was held constant (0.17%) the level of applied axial stress was varied from 0 to 5.9 MPa. It was noted by Fattal and Todd (1991) that, at the time, the strengths from Okamoto et al. (1987) were unexpectedly high, and predictive shear strength expressions available at the time proved to be excessively conservative. As a consequence, the results from this test program have generally been conspicuously omitted from more recent shear strength expression development (Voon and Ingham 2007, Davis 2008).

Of the tests completed from TCCMAR, only Shing et al. 1991 tested cantilever (i.e. under single curvature) fully-grouted reinforced concrete block structural walls. A total of eight walls that failed in shear dominated modes were reported, of which all the walls shared the height and length of 1.8 m. The parameters that varied between the shear failing walls include the vertical reinforcement ratio (0.38%- 0.74%), the horizontal reinforcement ratio (0.12%- 0.22%) and the applied level of axial stress (0 MPa- 1.9 MPa). The results from this test program were used to quantify the stiffness degradation effects of structural walls as well as their energy dissipation properties. Shing et al. (1991) noted that the level of reinforcement and orientation of shear cracking played a significant role in the energy dissipation qualities of the walls and that shear ductility is improved with increased levels of axial load. Displacement ductilities for the idealized load-

displacement envelope (to 50% load degradation) ranged from 4.0- 11.0 with top drifts that ranged from 0.9%- 1.7%.

Following the conclusion of TCCMAR program, Ibrahim (1995) tested five fully-grouted RM cantilever structural walls with a height of 1.4 m and lengths that varied from 1.4 m to 3.0 m. Horizontal reinforcement ratios were fixed at 0.20% while vertical reinforcement ratios of the walls varied from 0.40%- 0.60% and the level of applied axial stress varied from 0.7 MPa- 1.7 MPa. A model was created that adopted a modified compression field theory (MCFT) approach towards estimating the shear strength of the walls within a finite element program. Idealized displacement ductilities of the walls measured to a load degradation of 50% ranged from 4.4- 11.4 corresponding to levels of top drift that ranged from 0.7%- 1.8%.

Voon and Ingham (2006) reported on the behaviour of seven fully-grouted RM cantilever structural walls failing in shear towards the development of the next edition of the New Zealand masonry design standard (SANZ 2004). The walls had heights that ranged from 1.8 m to 3.6 m and lengths that ranged from 1.8 m to 3.0 m. The vertical reinforcement ratio was varied from 0.59%- 0.97% and horizontal reinforcement was varied from 0.0%- 0.062% with levels of applied axial stress that ranged from 0.0 MPa- 0.5 MPa. The walls all demonstrated significant levels of stable hysteretic response, with drifts corresponding to a drop to 80% of the peak load reported to range from 0.33%- 0.67%. The results from this test program were subsequently used to propose an improved shear strength expression in Voon and Ingham (2007). As part of this analysis the effect that increased levels of displacement ductility can have on the shear strength of masonry was quantified based on Fig. 1.7 proposed by the ATC-6 document related to seismic design of bridge columns (ATC 1981). It has been recognized for RC design that within the highly strained plastic hinge region of beams, columns or walls, there will progressive widening of cracks and damage along the shear interface such that concrete is no longer effective at transmitting shear stresses via aggregate interlock. As depicted in Fig. 1.7, a RM wall behaves in a similar manner. In Case (1), a wall is shown which will possess a shear failure prior to reaching its flexural strength, where the masonry maintains its full shear strength (V_m). In Case (2), a wall has reached its full flexural strength and has begun inelastic deformation, reducing the effectiveness of the masonry to resist shear causing a shear mechanism to control wall ductility capacity. Case (3)

represents a wall where shear strength offered by the reinforcement alone is sufficient to ensure a full flexural mechanism can develop.

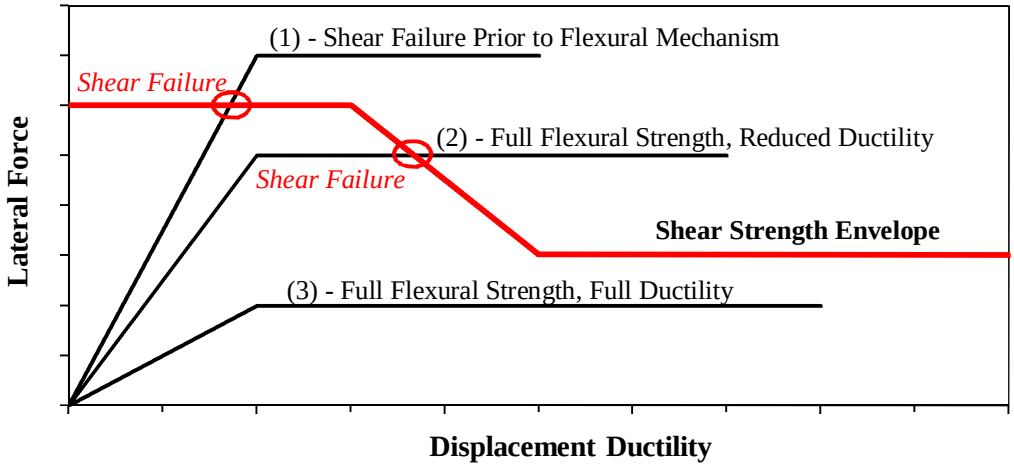

Figure 1.7 – Shear Failure Envelope as Expressed as a Function of Displacement Ductility

Finally, El-Dakhakhni et al. (2012) reported on the results of eight fully-grouted RM cantilever structural walls which possessed a range of different sizes and reinforcement configurations. These walls were designed to address perceived deficiencies within the Canadian shear strength expression in the CSA S304.1 developed by Anderson and Priestley (1992) which led to a reduction factor of 60% applied to the strength contribution of the reinforcement in the CSA S304.1 (CSA 2004a). The walls varied in height and length from 2.0 m – 3.0 m and possessed vertical reinforcement ratios of 0.79%- 1.31% and horizontal reinforcement ratios of 0.07%- 0.13% with levels of applied axial stress that varied from 0 MPa- 1.0 MPa. The walls possessed idealized displacement ductilities that ranged from 3.8- 9.0 corresponding to levels of top drift that ranged from 0.51%- 0.95% at a degradation to 80% of the peak load. Within this study, the effectiveness of various shear strength expressions were compared and found to produce generally inaccurate and widely variable results. It was observed, however, that the shear strength expression of the CSA A23.3 (CSA 2004b) concrete design standard, based on a simplified modified compression field theory (SMCFT) approach (Bentz et al. 2006), gave the most accurate prediction of RM wall strength.

In conclusion, it is evident from the literature that RM walls failing in shear can possess significant levels of inelastic drift and ductility. In addition, there also appears a need to address current deficiencies within the current shear force expression used by design codes. In particular, the adoption of a capacity design philosophy for flexurally failing structural walls, whereby flexural failure mechanisms are strived for over shear failure, would benefit twofold from an improved approach to estimating the inclination of the shear crack angle and shear strength of walls as follows.

1. Using an overly conservative shear strength expression with purely empirical, rather than theoretically justified, reductions to the strength offered by horizontal reinforcement would lead to excessively costly or impractical designs for low aspect ratio walls.

2. The current methodology to predict shear strength does not have any means to account for shear strength degradation with increased ductility nor does it properly account for the contributions of shear deformations to top drift of the shear spread of plasticity within the plastic hinge. All of these parameters play important roles within seismic design and ultimately, the behavior of RM structural walls.

1.3.8 Summary and Conclusions

The current study aims at establishing a prescriptive confinement detailing scheme of the susceptible vertical reinforcement within the plastic hinge zone of the walls using existing masonry materials and construction practices. The proposed confinement approach is selected as the detailing adopted by Shedid et al. (2010a), and was selected due to several important observations regarding modern RM construction practice. One such observation is that confinement strategies involving steel confinement plates, fiber materials or other forms of non-traditional reinforcement, which typically require the use of specialized materials and/or expertise, may render such a strategy as cost prohibitive or impractical to apply in many situations. Another observation is that, whenever there is an overall lack of explicit design code guidance pertaining to new systems, there will be a subsequent lack of experience, interest and comfort amongst the design community to attempt the use of these systems. Finally, from the regulatory point of view, in order to integrate new construction materials and components within traditional systems, there will always be a need for ancillary

tests regarding the combined behavior regarding other, non-structural performance aspects, such as durability or fire rating. Therefore, the use of masonry boundary elements detailed as confined columns which does not deviate from conventional construction practice presents the best opportunity for real world application and formalized prescriptive design code requirements.

Finally, current force-based seismic design codes blend ductility-based and strength-based requirements within design. As such, providing a new masonry SFRS category is only useful within the design world, if it is actually feasible to carry-out a design using standardized construction techniques. A potential hindrance in the design of ductile shear walls is the potential for shear failure within the region of plastic hinging. Therefore, in combination with the study aimed at improving ductile shear wall behavior, it is necessary to also address deficiencies in the current shear strength expression used in design. A new shear strength expression is derived from stress equilibrium expressions originating from the development of the Modified Compression Field Theory (MCFT) in concrete design. Such a method has been illustrated to more accurate with regards to concrete member design, and its application with regard to masonry member design would represent a significant advancement away from empirically derived equations. It is the goal of the work presented in this dissertation to illustrate that when special care is taken, masonry can be a highly ductile and effective from of seismic construction.

1.4 Notation for Chapter 1

A_g = gross-cross-section area of wall (mm^2);
A_R = aspect ratio of wall (h_w / ℓ_w);
c = depth of neutral axis (mm);
d_b = diameter of rebar (mm);
f_c = cylinder strength of concrete (MPa);
f_y = yield strength of reinforcement (MPa);
f_u = ultimate strength of reinforcement (MPa);
h_w = height of a wall in (mm);
ℓ_p = length of plastic hinge (mm);
ℓ_w = length of wall (mm);
M = moment applied to the critical cross-section of a wall (kN·m);
P = total level of axial stress (MPa);
R = seismic force modification factor adopted by ASCE 7-11;

R_d = seismic force modification factor related to SFRS ductility;
R_o = seismic force modification factor related to SFRS overstrength;
V = lateral design shear force (N);
V_m = shear strength of shear wall associated with masonry (N);
V_n = total shear strength of shear wall (N);
Δ_p = inelastic top displacement of wall (mm);
Δ_y = top displacement of wall at first yield of reinforcement (mm);
ε_m = compressive strain of masonry;
ε_{mu} = ultimate compressive strain of masonry;
ε_{su} = ultimate strain of reinforcement;
μ_Δ = displacement ductility;
ϕ = curvature of a wall (rad/mm).

1.5 References for Chapter 1

Ahmad, N., Crowley, H., Pinho, R. and Ali, Q. (2010). "Derivation of displacement-based fragility functions for masonry buildings." *Proc., 14th European Conference on Earthquake Engineering*, Ohrid, Macedonia, Paper #327.

Ahmadi Koutalan, F. (2012). "Displacement-based Seismic Design and Tools for Reinforced Masonry Shear-Wall Structures." Ph. D. Thesis, The University of Texas at Austin, U.S.A.

American Concrete Institute (ACI). (2011). "Building code requirements for structural concrete and commentary." *ACI Committee 318-11*, American Concrete Institute, Farmington Hills, MI, USA.

Anderson, D. L., and Priestley, M. J. N. (1992). "In-plane shear strength of masonry walls." *Proc., 6th Canadian Masonry Symposium*, Saskatoon, Canada, 223–234.

American Society for Civil Engineers (ASCE). (2006). "Seismic Rehabilitation of Existing Buildings." *ASCE 41-06*, ASCE, Reston, Va.

Applied Technology Council. (ATC). (1981). "Seismic design guidelines for highway bridges." *ATC-6*, Berkeley, CA, USA.

Applied Technology Council. (ATC). (1998). "Evaluation of earthquake damaged concrete and masonry wall buildings." *Federal Emergency Management Agency FEMA-306*, Washington D.C., USA.

Applied Technology Council. (ATC). (2007). "Interim testing protocols for determining the seismic performance characteristics of structural and non-structural components." *Federal Emergency Management Agency FEMA-461*, Washington D.C., USA.

Applied Technology Council. (ATC). (2009). "Quantification of building seismic performance factors." *Federal Emergency Management Agency FEMA-P695*, Washington D.C., USA.

Applied Technology Council (ATC). (2011). "Seismic performance assessment of buildings volume 1 - methodology." *ATC-58-1 75% Draft*, ATC, Redwood City, California.

Azimikor, N. (2012). "Out-of-plane stability of reinforced masonry shear walls under seismic loading: cyclic uniaxial tests." Master of Applied Science-Thesis, The University of British Columbia, Vancouver, Canada.

Banting, B. R. and El-Dakhakhni, W. W. (2012). "Force- and Displacement-Based Seismic Performance Parameters for Reinforced Masonry Structural Walls with Boundary Elements." *ASCE Journal of Structural Engineering* Vol. 138(12), 1477-1491.

Banting, B. R. and El-Dakhakhni, W. W. (2013a). "Seismic Performance Quantification of Reinforced Masonry Structural Walls with Boundary Elements." Submitted to *ASCE Journal of Structural Engineering*, Accepted with Revisions for 2nd Round of Review on Feb. 11, 2013.

Banting, B. R. and El-Dakhakhni, W. W. (2013b). "Seismic Design Parameters for Special Masonry Structural Walls Detailed with Confined Boundary Elements." Submitted to *ASCE Journal of Structural Engineering* on Dec. 12, 2012.

Banting, B. R. and El-Dakhakhni, W. W. (2013c). "Normal Strain-Adjusted Shear Strength Expression for Reinforced Masonry Structural Walls." Submitted to *ASCE Journal of Structural Engineering* and Accepted with Revisions for Revise for Editor Only on Dec. 14, 2012.

Bentz, E. C., Vecchio, F. J. and Collins, M. P. (2006). "Simplified modified compression field theory for calculating shear strength of reinforced concrete elements." *ACI Journal*, 103(4), 614-624.

Berry, M., P., and Eberhard, M., O. (2005). "Practical performance model for bar buckling." *J. Struct. Eng.*, 131(7), 1060-1070.

Bohl, A., and Adebar, P. (2011). "Plastic hinge lengths in high-rise concrete shear walls." *ACI Structural Journal*. 108(2), 148-157.

Bresler, B., and Gilbert, P. H. (1961). "Tie requirements for reinforced concrete columns." *ACI Structural Journal*, 58(5), 555-570.

Canadian Standards Association (CSA). (2004a). "Design of masonry structures." *CSA S304.1-04 (R2010)*, CSA, Mississauga, Canada.

Canadian Standards Association (CSA). (2004b). "Design of concrete structures." *CSA A23.3-04 (R2010)*, CSA, Mississauga, Canada.

Chen, S. J., Hidalgo, P. A., Mayes, R. L., Clough, R. W. and McNiven, H. D. (1978). "Cyclic loading tests of single masonry piers – Volume 2: Height to width ratio of 1." *Report No. UCB/EERC-78-28*, Earthquake Engineering Research Center, University of California Berkeley, USA.

Davis, C. L. (2008). "Evaluation of design provisions for in-plane shear in masonry walls." Master of Science in Civil Engineering-Thesis, Washington State University, Washington, USA.

Dhanasekar, M., and Shrive, N., G. (2002). "Strength and deformation of confined and unconfined grouted masonry." *ACI Structural Journal*, 99(6), 819-826.

Drysdale, R., and Hamid, A. (2005). *Masonry Structures- Behavior and Design.* 3ed., Canada Masonry Design Centre, Mississauga, Canada.

Eikanas, I. K. (2003). "Behavior of concrete masonry shear walls with varying aspect ratio and flexural reinforcement." Master of Science in Civil Engineering-Thesis, Washington State University, Washington, USA.

El-Dakhankhni, W. W., Banting, B. R. and Miller S. C. (2012). "Seismic performance parameters quantification of shear-critical reinforced concrete masonry squat walls." Submitted and accepted for publication, *J. Struct. Eng.*

Fattal, S. G. and Todd, D. R. (1991). "Ultimate strength of masonry shear walls: prediction vs. test results." *NISTIR 4633*, Building and Fire Research Laboratory, Gaithersburg, USA.

Hart, G. C., Noland, J. L., Kingsley, G. R., Englekirk, R. E. and Sajjad, N. A. (1988). "The use of confinement steel to increase the ductility in reinforced masonry shear walls." The Masonry Society Journal, 7(2)

Hart, G. C., Sajjad, N., Kingsley, G. R., and Noland, J. L. (1989). "Analytical stress-strain curves for grouted concrete masonry." *The Masonry Society Journal*, 8(1), T21-T34.

Hervillard, T. P. C. (2005). "Effectiveness of polymer fibers for improving the ductility of masonry structures." Master of Science-Thesis, Washington State University, Washington, U.S.A.

Hidalgo, P. A., Mayes, R. L., McNiven, H. D. and Clough, R. W. (1978). "Cyclic loading tests of single masonry piers – Volume 1: Height to width ratio of 2." *Report No. UCB/EERC-78-27*, Earthquake Engineering Research Center, University of California Berkeley, USA.

Hidalgo, P. A., Mayes, R. L., McNiven, H. D. and Clough, R. W. (1979). "Cyclic loading tests of single masonry piers – Volume 3: Height to width ratio of 0.5." *Report No. UCB/EERC-78-12*, Earthquake Engineering Research Center, University of California Berkeley, USA.

Housner, G. W. (1956). "Limit design of structures to resist earthquakes." *Proceedings of the 1st World Conference on Earthquake Engineering*: Earthquake Engineering Research Institute, Berkeley, CA, USA, 5-1 – 5-13.

Ibrahim, K. S. (1995). "Inelastic behaviour of reinforced masonry shear walls: an experimental and analytical study." Ph. D. Thesis, Carleton University, Ottawa, Canada.

International Council of Building Officials (ICBO). (1997). *Uniform Building Code (UBC)*. International Council of Building Officials, Whittier, California, U.S.A.

Krawinkler, H., Parisi, F., Ibarra, L., Ayoub, A. and Medina, R. (2002). "Development of a testing protocol for woodframe structures." *Consortium of*

Universities for Research in Earthquake Engineering (CUREE) No. W-02, Richmond Ca, USA.

Leiva, G. and Klinger, R. E. (1994). "Behavior and design of multi-story masonry walls under in-plane seismic loading." *The Masonry Society Journal*, 13(1), 15-24.

Li, J. and Weigel, T. A. (2006). "Damage states for reinforced CMU masonry shear walls." *Advances in Engineering Structures, Mechanics and Construction*, 140(2), 111-120.

Malmquist, K. J. (2004). "Influence of confinement reinforcement on the compressive behavior of concrete block masonry and clay brick masonry prisms." Special Report, Washington State University, Washington, USA.

Masonry Standards Joint Committee. (MSJC). (2008). "Building Code Requirements for Masonry Structures." *TMS 402/ASCE 5/ACI 530*, The Masonry Society, American Society of Civil Engineers, Boulder, New York/American Concrete Institute, and Detroit, USA.

Matsumura, A. (1987), "Shear strength of reinforced hollow unit masonry walls." *Proceedings of the 4th North America Masonry Conference*, Paper No. 50, Los Angeles, USA, 50-1 - 50-16.

Matsumura, A. (1988). "Shear strength of reinforced masonry walls." *Proc., 9th World Conf. on Earthquake Engineering*, Vol. 7, Tokyo, 121–126.

Mattock A. H. (1967). Discussion of "Rotational capacity of reinforced concrete beams" by W.G. Corley. *J. Struct. Eng.*, 93(2), 399-412.

Mayes, R. L., Omote, Y. and Clough, R. W. (1976). "Cyclic shear tests of masonry piers Volume 1: Test Results." *Report No. UCB/EERC-76-8*, Earthquake Engineering Research Center, University of California Berkeley, USA.

Mitchell, D., Tremblay, R., Karacabeyli, E., Paultre, P, Saatcioglu, M. and Anderson, D. (2003). "Seismic force modification factors for the proposed 2005 edition of the National Building Code of Canada," *Canadian Journal of Civil Engineering*, NRC Canada, 30 (2), 2003, 308-327.

Murcia-Delso, J., and Shing, B. (2011). "Fragility curves for in-plane seismic performance of reinforced masonry walls." *Proc., 11th North American Masonry Conference*, Minneapolis, Minnesota, Paper #2.04-3.

National Building Code of Canada: Institute for Research in Construction (NBCC). (2010). *National Building Code of Canada 2010*., National Research Council of Canada, Ottawa, Canada.

National Institute of Standards and Technology (NIST). (2010). "Evaluation of the P-695 methodology for quantification of building seismic performance factors." *NIST GCR 10-917-8*., NIST, Gaithersburg, MD, USA.

Nassar, A. A., and Krawinkler, H. (1991). "Seismic Demands for SDOF and MDOF Systems." *Report No. 95*, The John A. Blume Earthquake Engineering Centre, Stanford University, California, U.S.A.

Nazir, N. A. and Hart, G. C. (2001). "Analytical stress strain curves for confined and reinforced concrete masonry." *The Masonry Society Journal*, 19(1), 9-20.

Okamoto, S., Yamazaki, Y., Kaminosono, T., Teshigawara, M. and Hirashi, H. (1987). "Seismic capacity of reinforced masonry walls and beams." *Proceedings of the 18th Joint Meeting of the U.S.-Japan Cooperative Program in Natural Resource Panel on Wind and Seismic Effects: NBSIR 87-3540*, National Institute of Standards and Technology, Gaithersburg, USA, 307-319.

Pantazopoulou, S., J. (1998). "Detailing for reinforcement stability in RC members." *J. Struct. Eng.*, 124(6), 623-632.

Park, Y. J. and Ang, A. H. S. (1985). "Mechanistic seismic damage mdoel for reinforced concrete." *J. Struct. Eng.*, 111(4), 722-739.

Park, Y. J., Ang, A. H. S. and Wen, Y. K. (1985). "Seismic damage analysis of reinforced concrete buildings." *J. Struct. Eng.*, 111(4), 740-757.

Park, R., and Paulay, T. (1975). *Reinforced Concrete Structures*. John Wiley & Sons, Inc., New York and Toronto.

Paulay, T., and Priestley, M., J., N. (1992). *Seismic Design of Reinforced Concrete and Masonry Buildings*, John Wiley & Sons, Inc., New York and Toronto, 139-142.

Paulay, T., and Priestley, M., J., N. (1993). "Stability of ductile shear walls." *ACI Structural Journal*, 90(4), 385-392.

Paulay, T., and Uzumeri, S. M., (1975). "A Critical Review of the Seismic Design Provisions for Ductile Shear Walls of the Canadian Code and Commentary." *Canadian Journal of Civil Engineering*, 2(4), 592-600.

Priestley, M. J. N. (1976). "Cyclic testing of heavily reinforced concrete masonry shear walls." *Research Report 76-12*, Department of Civil Engineering, University of Canterbury, Christchurch, New Zealand.

Priestley, M. J. N. (2000). "Performance-based seismic design" Keynote Address, *Proceedings of the Twelfth World Conference on Earthquake Engineering*. Earthquake Engineering Research Institute, Auckland, New Zealand, Paper #2831.

Priestley, M., J., N. and Bridgeman, D., O. (1974). "Seismic resistance of brick masonry walls." *Bulletin of the New Zealand National Society for Earthquake Engineering*, 7(4), 167-187.

Priestley, M., J., N., and Elder, D., M. (1982). *Seismic Behaviour of Slender Concrete Masonry Shear Walls*. Research Report, University of Canterbury, Christchurch, New Zealand.

Priestley, M. J. N. and Elder, D. M. (1983). "Stress-strain curves for unconfined and confined concrete masonry." *ACI Journal*, 80(3), 192-201.

Priestley, M. J. N., and Kowalsky, M. J. (1998). "Aspects of drift and ductility capacity of rectangular cantilever structural walls." *Bulletin of the New Zealand National Society for Earthquake Engineering*, 31(2), 73-75.

Priestley, M. J. N., Calvi, G. M., and Kowalsky, M. J. (2007). *Displacement-Based Seismic Design of Structures*, IUSS Press, Pavia, Italy.

Riddell, R. (2008). "Inelastic response spectrum: Early history." *Earthquake Engineering and Structural Dynamics*, 37(8), 1175-1183.

Sajjad, N. A. (1990). "Confinement of concrete masonry." Ph. D. Thesis, University of California, Los Angeles, CA, USA.

Shedid, M. T. (2009). "Ductility of concrete block shear wall structures." Ph.D. Thesis, McMaster University, Hamilton, Canada.

Shedid, M. T., Drysdale, R. G. and El-Dakhakhni, W. W. (2008). "Behavior of fully grouted reinforced concrete masonry shear walls failing in flexure: experimental results." *J. Struct. Eng.*, 134(11), 1754-1767.

Shedid, M. T., El-Dakhakhni, W. W. and Drysdale, R. G. (2010a). "Alternative strategies to enhance the seismic performance of reinforced concrete-block shear wall systems." *J. Struct. Eng.*, 136(6), 676-689.

Shedid, M. T., El-Dakhakhni, W. W. and Drysdale, R. G. (2010b). "Characteristics of confined and unconfined masonry prisms for seismic performance enhancement of structural walls." *Masonry International.*, 23(2), 69-78.

Shibata, A. and Sozen M. A. (1974). *The Substitute Structure Method for Earthquake-resistant Design of Reinforced Concrete Frames*. University of Illinois at Urbana-Champaign, U.S.A.

Shing, P. B., Noland, J. L., Spaech, H., Klamerus, E. and Schuller, M. (1991). "Response of single-storey reinforced masonry shear walls to in-plane lateral loads." *U.S. – Japan Coordinated Program for Masonry Building Research Report No. 3.1(a)-2*, University of Colorado at Boulder, USA.

Shing, P., B., Carter, E., W., and Noland, J., L. (1993). "Influence of confining steel on flexural response of reinforced masonry shear walls." *The Masonry Society Journal*, 11(2), T21-T34.

Standards Association of New Zealand (SANZ). (2004). "Design of reinforced concrete masonry structures." *New Zealand Standards Association* (*NZS) 4230:2004*, CEN, Wellington, New Zealand.

Structural Engineers Association of California (SEAOC). (1995). *Vision 2000: Performance-Based Seismic Engineering of Buildings*. Structural Engineers Association of California, Sacramento, US, 1995.

Snook, M. K. (2005). "Effects of confinement reinforcement on the performance of masonry shear walls." Master of Science in Civil Engineering-Thesis, Washington State University, Washington, USA.

Sveinsson, B. I., McNiven, H. D., and Sucuoglu, H. (1985). "Cyclic loading tests of masonry piers – Volume 4: Additional tests with height to width ratio of 1." *Report No. UCB/EERC-85-15*, Earthquake Engineering Research Center, University of California Berkeley, USA.

Tabinashi, R.(1956). "Studies on the nonlinear vibrations of structures subjected to destructive earthquakes." *Proceedings of the 1st World Conference on Earthquake Engineering*, Earthquake Engineering Research Institute, Berkeley, CA, 6-1 – 6-16.

Tomaževič, M. (1999). "Seismic resistance verification of structural walls" *Earthquake-Resistant Design of Masonry Buildings*, Imperial College Press, London, 127-141.

Vaughan, T. P. (2010). "Evaluation of masonry wall performance under cyclic loading." Master of Science in Civil Engineering-Thesis, Washington State University, Washington, USA.

Veletsos, A. S. and Newmark, N. M. (1960). "Effect of inelastic behaviour on the response of simple systems to earthquake motions." *Proceedings of the 2nd World Conference on Earthquake Engineering*: Science Council of Japan, Japan, Vol. 2, 895-912.

Veletsos A. S. and Newmark N. M. (1964). "Response spectra for single-degree-of-freedom elastic and inelastic systems." *Volume 3 of design procedures for shock isolation systems of underground protective structures. Report No. RTD-TDR-63-3096*, Air Force Weapons Laboratory, Kirkland Air Force Base, Albuquerque, NM, USA.

Voon, K. C. and Ingham, J. M. (2006). "Experimental in-plane shear strength investigation of reinforced concrete masonry walls." *J. Struct. Eng.*, 132(3), 400-408.

Voon, K. C. and Ingham, J. M. (2007). "Design expression for the in-plane shear strength of reinforced concrete masonry." *J. Struct. Eng.*, 133(5), 706-713.

Yancey, C. W. C., Fattal, S. G. and Dikkers, R. D. (1991). "Review of research literature on masonry shear walls." *NISTIR 4512*, Building and Fire Research Laboratory, Gaithersburg, USA.

CHAPTER 2: EXPERIMENTAL PROGRAM

2.1 Introduction

In this chapter an experimental program regarding the testing of masonry walls possessing confined boundary elements is presented. The information in this chapter is the sole work of the author with Dr. El-Dakhakhni acting in an advisory and editorial role to prepare two manuscripts for journal submission. This chapter consists of information from two separate journal articles that have been integrated together for the purposes of providing better flow within the context of a thesis. The information contained in this chapter can be found in the articles:

Banting, B. R. and El-Dakhakhni, W. W. (2012). "Force- and Displacement-Based Seismic Performance Parameters for Reinforced Masonry Structural Walls with Boundary Elements." *ASCE Journal of Structural Engineering* Vol. 138(12), 1477-1491

Banting, B. R. and El-Dakhakhni, W. W. (2013). "Seismic Performance Quantification of Reinforced Masonry Structural Walls with Boundary Elements." Submitted to *ASCE Journal of Structural Engineering*, Accepted with Minor Revisions for 2nd Round of Review Feb. 11, 2013.

2.2 Wall Specimen Details

A total of nine half-scale walls with confined boundary elements were tested, with results reported in this section. These nine walls fit into a larger test matrix of eleven walls total indicated by Table 2.1 and Fig. 2.1. Detailed experimental results from Walls 5 and 6 are reported by Shedid et al. 2010a but have integrated within this chapter and overall thesis for comparison purposes. The parameters that were compared between the half-scale specimens are highlighted in Table 2.1 and include the wall height (h_w), wall length (ℓ_w), the height to length (aspect) ratio (A_R), the number of inter-story floor slabs ($IS^{\#}$), discontinuity of confinement detailing above the plastic hinge, the level of applied axial load (P_a), and the vertical reinforcement ratio (ρ_v) of the web of the wall. In addition, the horizontal reinforcement ratio in the plastic hinge region (ρ_h) is also given in Table 2.1, which was detailed to ensure a flexural failure of the walls. The same reinforcement bar sizes were used for all the walls, consisting of No. 10 bars (A_s = 100 mm^2, d_b = 11 mm) as the vertical reinforcement with a yield strength ($f_{y,v}$) of 496 MPa and ultimate strength ($f_{u,v}$) 720 MPa. The horizontal reinforcement and lateral stirrups were comprised of D4 bars (A_s = 25.4 mm^2, d_b = 5.7 mm) which possessed a yield strength ($f_{y,h}$) of 582.5 MPa.

Table 2.1 – Half-Scale Wall Design Details

		Wall										
		1	**2**	**3**	**4**	**5**	**6**	**7**	**8**	**9**	**10**	**11**
h_w	**(mm)**	1,900	2,660	2,660	3,990	2,660	3,990	3,990	3,990	3,990	3,990	3,990
ℓ_w	**(mm)**	1,235	1,235	1,235	1,235	1,805	1,805	1,805	1,805	1,805	1,805	2,665
A_R		**1.53**	**2.15**	2.15	**3.23**	1.48	2.21	2.21	2.21	2.21	2.21	1.5
ρ_v	**(%)**	0.69	0.69	1.17	0.69	0.56	0.56	0.56	0.56	0.56	0.56	0.51
ρ_h	**(%)**	0.6	0.6	0.6	0.3	0.6	0.3	0.3	0.3	0.3	0.3	0.3
P_a	**(MPa)**	0.89	0.89	0.89	0.89	0.89	0.89	0.45	0.45	1.34	0.45	0.89
IS#		**0**	1	1	2	1	2	2	0	2	2	**0**

Walls 1 and 11 were each constructed with a height-to-length (aspect) ratio, A_R, of 1.5 to match a third wall tested by Shedid et al. (2010a) and labelled as Wall 5. However, each of these walls were detailed with the same boundary element, thus producing different relative lengths of boundary element (ℓ_b) to wall length (ℓ_w). Walls 1, 2 and 4 were each detailed with identical cross sections and possessed the same vertical reinforcement spacing (s_v) and total applied axial stress (P_a) but varied by their h_w of 3,990 mm, 2,660 mm and 1,900 mm as shown in Table 2.1. This corresponds to full-scale wall heights of 8.0 m, 5.3 m and 3.8 m, respectively. Varying these three wall heights will result in altering the shear force and moment gradients at failure as their cross-sectional moment capacities were expected to be the same, but would correspond to different lateral loads (Q_u). Walls 2 and 3 were each detailed with the same gross dimensions, but possessed different levels of vertical reinforcement in the web. This would cause a shift in the neutral axis depth (c) and thus would alter the ratio with wall length (c/ℓ_w), which is commonly applied in design codes as prescriptive measure of curvature ductility capacity.

For a mid-rise RM structure ranging between three and eight stories in height, the axial compressive stresses caused by gravity loads would be expected to normally range below 10% the compressive strength of the concrete block unit. The axial compressive load carried by an RM structural wall is a function of the occupancy loads, tributary areas and load distributions that may change during a seismic event. Varying the level of axial load also alters the depth of the neutral axis (c) as well as the rate of stiffness degradation under seismic loads. In boundary elements or flange-shaped cross-sections a shift in c is compounded by the abrupt change in member width beyond the wall web boundary. Two wall specimens, Walls 7 and 9 were detailed and constructed identically to a previously tested 3-storey wall described by Shedid et al. (2010a) (Wall 6). The applied level of axial compressive stress in Walls 7 and 9 was 50% and 150% that of Wall 6 in order to

shift *c*, at the theoretical ultimate capacity, from laying solely within the confined zone (low axial load) into the wall web (high axial load).

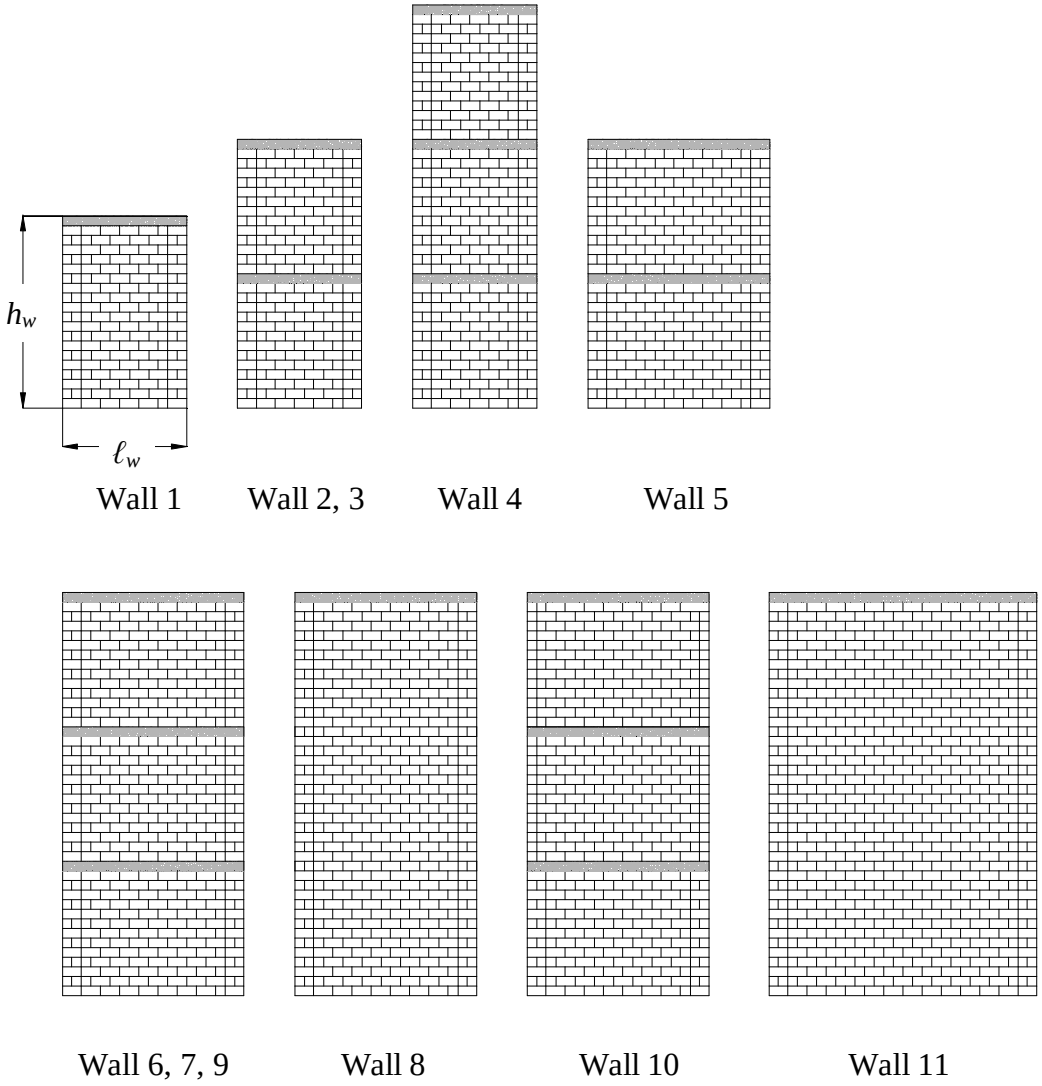

a)

Figure 2.1 – Design Details of Walls: a) Elevation View

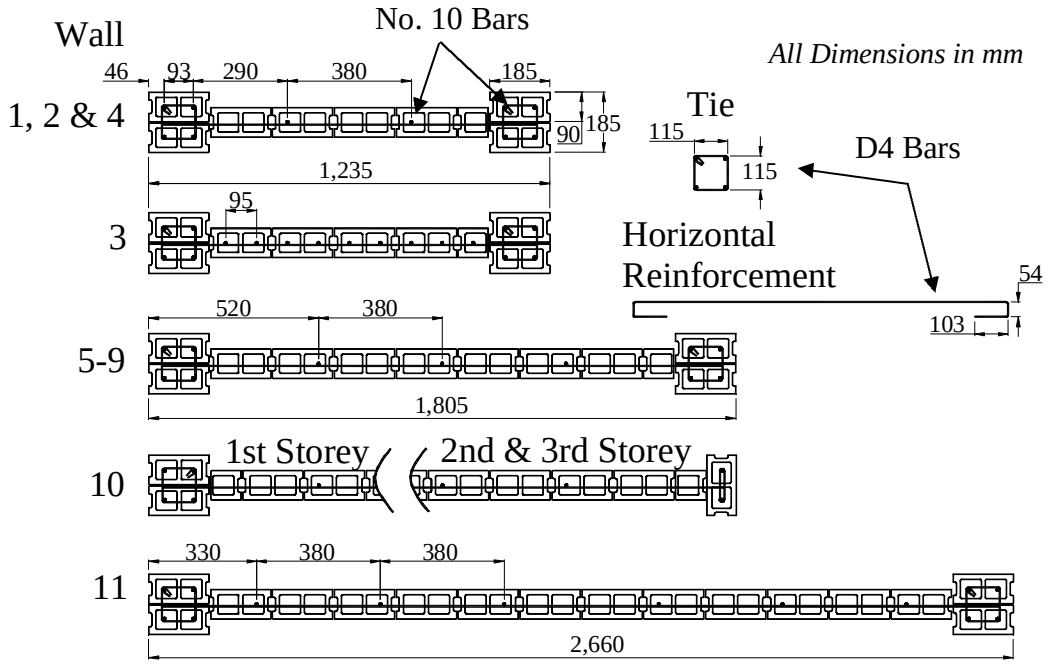

b)

Figure 2.1 Continued... – Design Details of Walls: b) Cross-Section Details

In actual buildings, inter-storey floor slabs serve to transfer seismic loads to structural walls and also act as a supporting diaphragm against out-of-plane wall instability. Areas required to provide several stories of clear head room, such as a lobby or atrium, are common in many types of buildings where intersecting floor diaphragms would not be present. Given that design codes do not differentiate between these configurations, Wall 8 was detailed in the same fashion as Wall 7, with the same level of applied axial stress, but without any RC floor slabs at the 1st and 2nd storey levels. The CSA S304.1 (2004a) does, however, limit the ratio of unsupported RM wall height to wall thickness for moderately ductile shear walls (R_d = 2.0), as given by Eq. 2.1:

$$\frac{h}{(t+10)} \leq 14 \qquad (2.1)$$

Where h in mm, is the unsupported height of the wall and t in mm, is the width of the compression zone. A boundary element cross-section would be a desirable design option since it would effectively double the maximum unsupported height over conventional construction (since the boundary element is two units wide). In addition, it had also been observed, but not quantified, by Shedid et al. (2010a) that simulated floor slabs tended to alter cracking patterns within RM structural

walls which may have a net effect on the spread of plasticity in the wall. Wall 8 served as a direct comparison to Wall 7 to observe this effect. Walls 1 and 11 are also detailed without RC slabs due to constructability issues of their irregular height (Wall 1) and to prevent excessive plasticity around the slab (Wall 11).

Given the added material and labor expense of having a specially detailed boundary element extend the entire height of a wall, a more economic design would then aim at having the boundary element curtailed above the critical plastic hinge region. In this regard, Wall 10 had a boundary element within the 1st storey that transitioned into an "I-shaped" flanged cross-section above the 1st floor slab at a height of 1,335 mm (one-third the wall height) as shown in Fig. 2.2. The modular nature of masonry units typically prevents curtailment of flexural reinforcement within the wall itself, however, the space offered by the 1st floor slab makes it a feasible region to curtail the excess flexural reinforcement from the 1st storey. A lateral load (Q) was applied across the top of each wall resulting in a triangular moment distribution. Therefore, the moment capacity of the flanged cross-section (located one-third of the wall height above the base) required a moment capacity greater than two-thirds that of the boundary element cross-section (located at the base of the wall). Consequently, the flanged cross-section was designed to sustain a maximum lateral load (Q_u) of 148.2 kN (i.e. the top force that will cause flexural failure at the bottom of flanged section), which exceeded Q_u of the confined boundary element cross-section located at the base of the wall which equalled to 141.2 kN (i.e. the force that will cause flexural failure at the bottom of the boundary element wall).

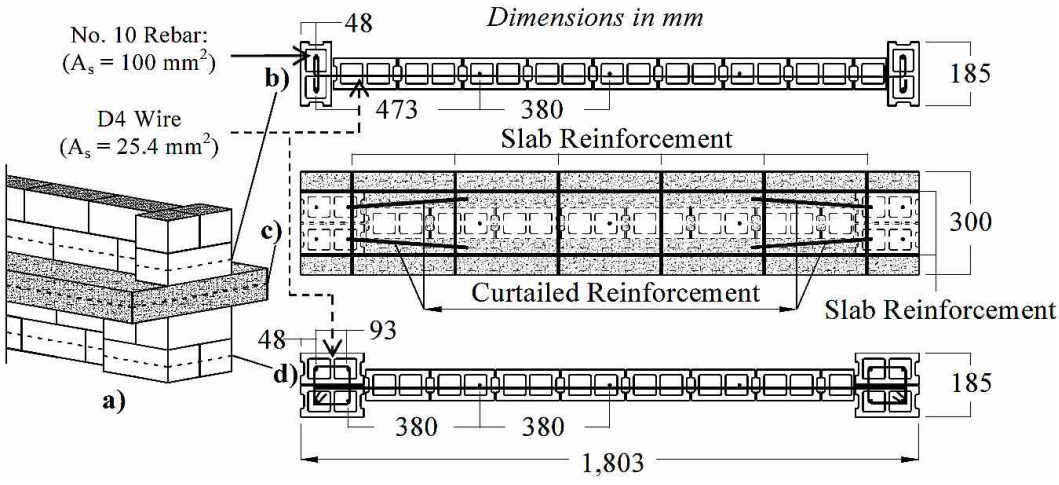

Figure 2.2 – Wall 10 Curtailment Details: a) 1st Floor Slab Transition Point, b) Flanged Cross-section, c) RC Slab Reinforcement Details and Curtailed Bars, d) Confined Boundary Element Cross-Section

2.3 Wall Construction

A half-scale version of the standard 190 mm x 190 mm x 390 mm concrete block stretcher unit (typical to North American construction) was specified for construction. The half-scale units chosen have been previously used by other researchers at McMaster University such as Long (2006) and Shedid et al. (2010a) with success in efforts to correlate reduced-scale component behavior with that of full-scale. The 90 mm x 90 mm x 185 mm half-scale blocks were laid with a 5 mm scaled mortar joint in a half running bond by professional masons. The boundary elements were comprised of two units laid together resulting in an overall boundary element cross sectional size of 185 mm x 185 mm as depicted in Fig. 2.3. The boundary elements contained two layers of vertical reinforcement bars with two bars each (four bars in total) of No. 10 size (A_s = 100 mm^2, boundary element reinforcement ratio (ρ_b) = 1.17%) and placed in the centre of each of the two block cells that comprised the boundary element. Square shaped lateral stirrups with outer dimensions of 115 mm × 115 mm were placed at each course resulting in a vertical stirrup spacing of s_s = 95 mm as depicted in Fig. 2.3. The stirrups and horizontal shear reinforcement were each comprised of D4 deformed bars (A_s = 25.4 mm^2) corresponding to No. 10 size (A_s = 100 mm^2) bar in full-scale.

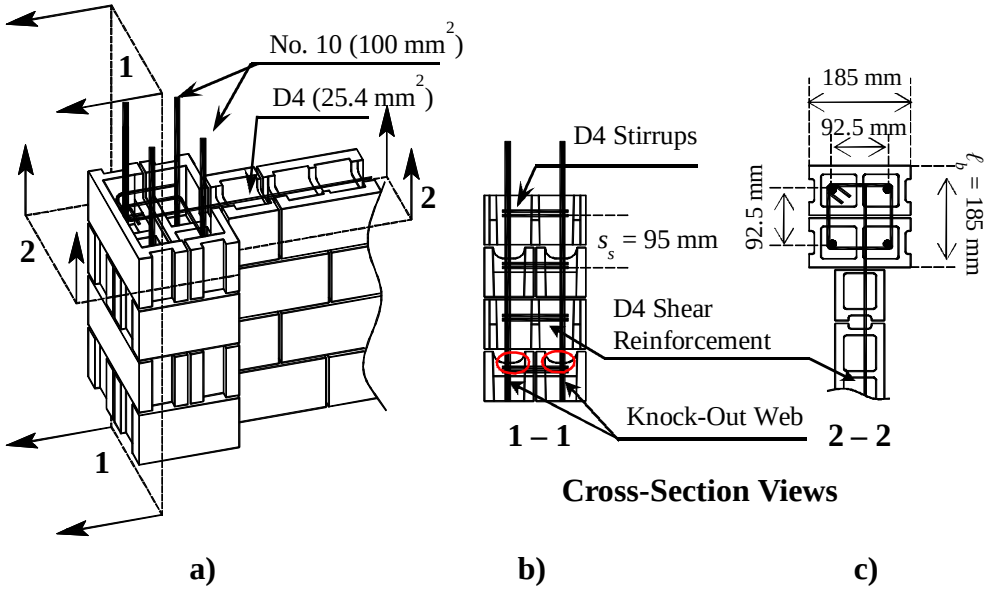

Figure 2.3 – Boundary Element Detailing: a) Boundary Element Tied into Web of a RM Wall, b) Elevation View (Section1-1) and c) Plan View (Section 2-2)

Construction of each specimen began with pouring a footing measuring 400 mm high × 500 mm wide with lengths that varied from 1,800 mm to 3,000 mm depending on the wall length. All vertical wall reinforcement was tied within the RC footing. Each specimen was constructed to a height of seven courses as shown in Fig 2.4a at which point all cells were fully-grouted up to 6½ courses above the footing as shown in Fig. 2.4b to facilitate the formation of a shear key and avoid the formation of a cold joint and sliding plane in the wall. After 13 courses were constructed to a height of 1,235 mm above the footing, the remaining 6½ courses were fully grouted. The RC slabs in walls which contained them as indicated in Fig. 2.1, were cast-in-place atop the 13th course in Walls 2-7, 9 and 10 and shored up for the subsequent storey to be constructed above with the process repeated for the 2nd and 3rd stories in those walls if applicable. All walls had RC slabs cast at the top to facilitate connection with the lateral loading beam used in the test set-up. Vertical reinforcement ran continuously up the height of each specimen. Lap splices were avoided to reduce the number of test variables and to ensure that full inelastic strains are developed in the vertical reinforcement. Horizontal reinforcement was placed by the mason within the knock-out web area of the unit in each course (i.e. at 95 mm spacing). Horizontal reinforcement was hooked around the vertical bars with a 180° hook in the boundary element as shown in Fig. 2.4c prior to grouting and Fig. 2.4d after grouting. A summary of the constituent properties of the materials used to construct the different elements of each wall were determined from standardized testing methods and is given in Table 2.2.

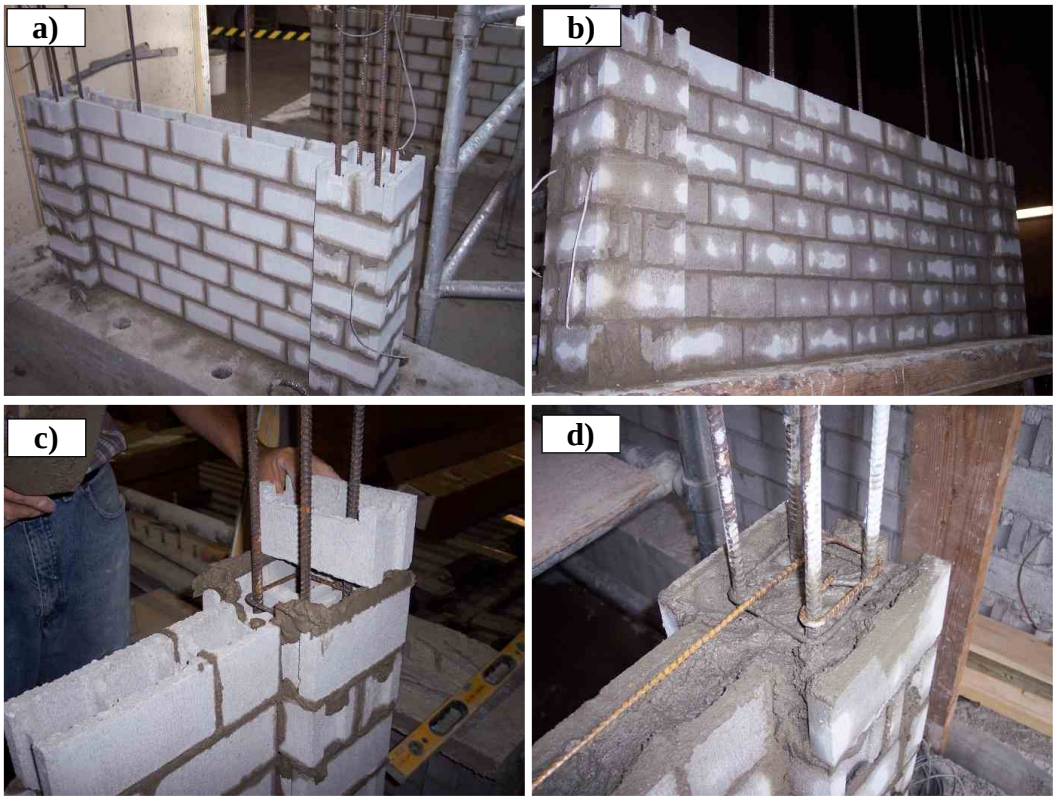

Figure 2.4 – Construction of Wall Specimens: a) Seven Courses Laid Prior to Grouting of Wall 1, b) Water Absorbed after Grouting of 6 ½ course in the 2nd Storey in Wall 7, c) Construction of the Confined Boundary Element and d) Horizontal Reinforcement and Lateral Stirrup Placement after 6 ½ courses Grouted

Table 2.2 – Material Properties

Material Test	Strength (C.O.V.)	Reference
Type S Mortar (CSA A179-04 2004)	16.6 MPa (16.2%)	Cube Compressive Strength ASTM C780-09
	128.7% (1.8%)	Flow Table Test ASTM 1437-07
Half-Scale Concrete Block	26.5 MPa (13.2%)	Block Strength ASTM C140-10
Fine Grout (CSA A179-04 2004)	18.5 MPa (17.1%)	Cylinder Strength ASTM C476-10
Inter-Storey Floor Slab Concrete	30.4 MPa (10.0%)	Cylinder Strength ASTM C39-10
Footing Concrete	27.8 MPa (22.1%)	Cylinder Strength ASTM C39-10
4-Course Running Bond Prism	14.9 MPa (13.7%)	Prism Strength CSA S304.1-04
4-Course Running Bond Prism with Correction Factor of 1.16	17.3 MPa (13.7%)	Prism Strength ASTM C1314-10
	11,300 MPa (16.4%)	Young's Modulus ASTM E111-04
D4 Steel Reinforcement	582.5 MPa (1.3%)	Yield Strength ASTM A615-09
No. 10 Steel Reinforcement	496.3 MPa (2.3%)	Yield Strength ASTM A615-09

2.3.1 Test Set-up

The test set-up consists of a reusable RC base measuring 600 mm tall × 1,100 mm wide × 4,200 mm long that is prestressed with 63 mm high strength bolts at 920 mm spacing to a strong floor at the McMaster University Applied Dynamics Laboratory as depicted in Fig. 2.5 and Fig. 2.6. The RC footing for each wall is mounted atop the reusable base, orientated in the E-W direction, and leveled with a layer of mortar before being prestressed with 25 mm high strength threaded steel rods. Mortared to the RC slab at top of each wall is a rigid steel loading beam designed to transfer lateral loads across the top of the wall using two outward facing C150 × 16 channel sections welded to a 20 mm thick × 200 mm wide steel plate. Vertical reinforcement in the wall was left protruding above the RC slab and steel dowels were cast in open cells of the wall where no vertical reinforcement was placed. These protruding bars were subsequently welded to holes in the loading beam prior to each test to facilitate a continuous fixed connection between the wall and the loading beam.

Spanning laterally across the loading beam (N-S orientation) are two HSS 127×127×13-350 mm long steel box sections. Atop these are two HSS 203×203×13-870 mm long steel box sections (N-S orientated) resting on a 45 mm steel roller positioned at their mid-span as shown in Fig. 2.5. Each end of the HSS 203×203×13 sections has attached to it a 16 mm diameter high strength threaded rod. On the South face of the wall this rod is fixed to the reusable base and on the North face of the wall the threaded rod is rigged to a 100 mm stroke hydraulic actuator which is used to maintain a constant axial load during testing as shown in Fig. 2.5. As the wall moves in the E-W direction during the test, these actuators are extended or retracted as needed to maintain a constant tension in the threaded rod which causes the specified compressive reaction force in the wall which is monitored by two 100 kN load cells.

Bolted to the lateral loading beam at the top of the wall in Fig. 2.5 is a ±500 kN hydraulic actuator. Whereby "–" is interpreted as a retracting force on the actuator and a load applied in the East direction of the wall and "+" is interpreted as an extension force on the actuator and a load applied in the West direction of the wall. The actuator has a total stroke of 500 mm and is mounted to a stiff reaction frame. To ensure the wall displaces along its major axis (in-plane in the E-W direction) a series of out-of-plane supports were pinned to the wall over its height as shown in Fig. 2.5. At the inter-storey slab heights, two HSS 76×76×9.5 steel box sections are pin connected to the wall and to a reaction frame (not shown) that runs parallel to the South side of the test set-up. The pin connection is designed to resist out-of-plane displacements and torsional rotation of each wall while not influencing in-plane wall movements and allowing free vertical movement. The out-of-plane support at the top of each wall consists of two orthogonally orientated HSS 89×89×4.8 steel box sections welded to the lateral loading beam as shown in Fig. 2.5 that protrude out the South side of the wall. These are attached to a HSS 102×102×4.8 steel box section that runs parallel to the test set-up and is fixed to the South reaction frame. The protruding arms are attached to the parallel HSS section with a specially designed rig containing greased rollers which allow for frictionless in-plane movements and use slotted pin-connections that allow vertical movements while preventing any torsion in the wall.

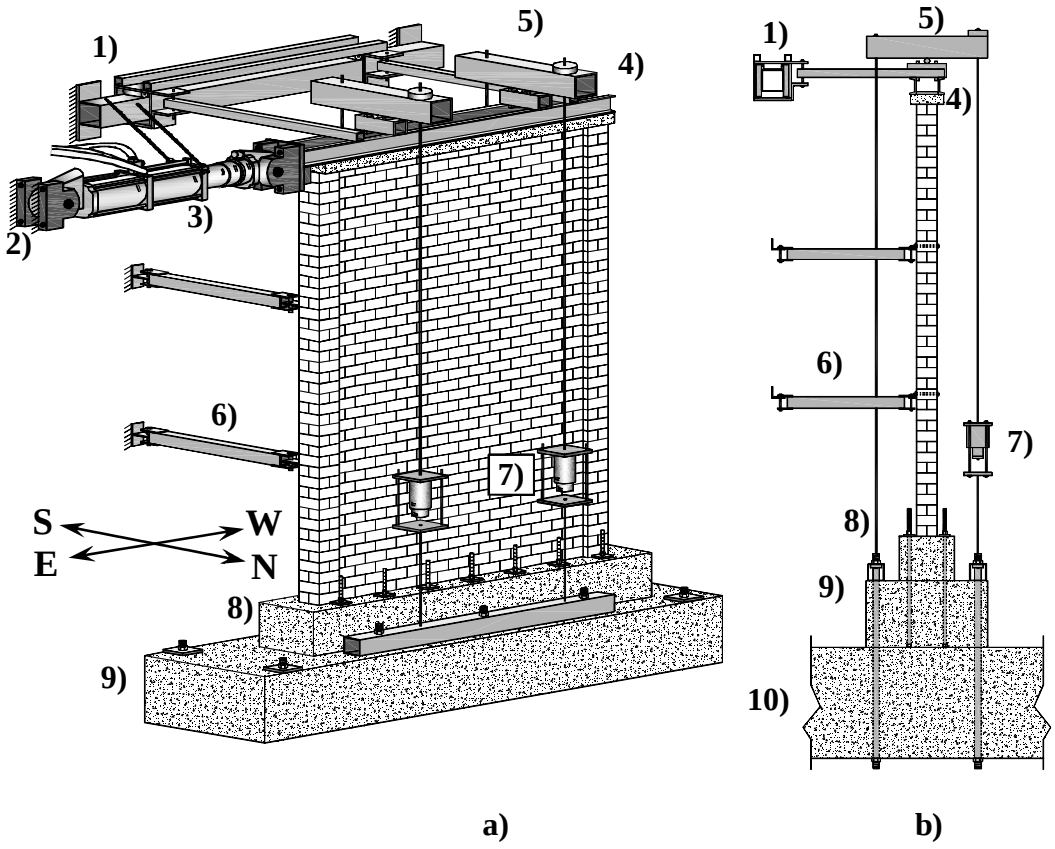

Figure 2.5 – Test Set-Up with Wall 11: a) Isometric View and b) Elevation View: 1) Top of Wall Out-of-Plane Support, 2) Reaction Frame (Not Shown), 3) ± 500 kN & 500 mm Stroke Hydraulic Actuator, 4) Rigid Steel Loading Beam fixed to Top of Wall, 5) 2 × Axial Loading Beams with ± 100 kN Load Cell, 6) 4 × Inter-Storey Out-of-Plane Supports, 7) 2 × 100 mm Stroke Axial Load Hydraulic Actuators, 8) RC Wall Footing, 9) Reusable RC Base, 10) Strong Floor

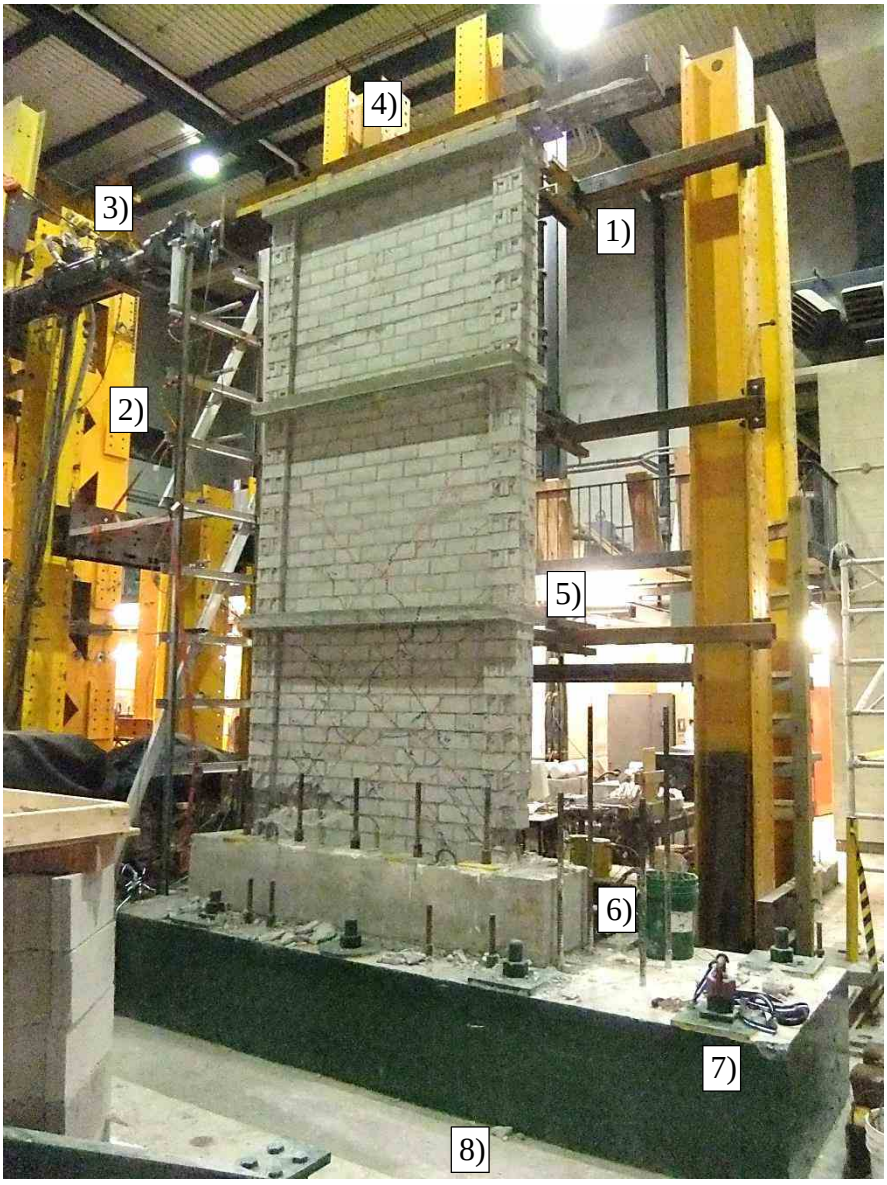

Figure 2.6 – Photo of Test Set-Up with Wall 9 at End of Test: 1) Top of Wall Out-of-Plane Support, 2) Reaction Frame, 3) ± 500 kN & 500 mm Stroke Hydraulic Actuator, 4) Rigid Steel Loading Beam fixed to Top of Wall, 5) 4 × Inter-Storey Out-of-Plane Supports, 6) RC Wall Footing, 7) Reusable RC Base, 8) Strong Floor

2.3.2 Instrumentation

Each wall was instrumented with 22 vertically mounted linear variable displacement transducers (LVDTs) with strokes that varied between 12.5 mm and 50 mm. The LVDT were fixed to the East and West wall ends to measure vertical displacements necessary to determine average curvatures in the wall. Lateral displacements were recorded with ten LVDTs and String potentiometers with 25 mm to 250 mm stroke positioned along the height of each wall at a regular spacing of 443 mm (one-third of a storey). Relative sliding was recorded along the base of each wall as well as along the 1st floor grout connection as a precautionary measure. Finally, the two outermost reinforcement bars in each of the boundary elements had five-5 mm strain gauges to record strains in the reinforcement along the wall height and strain penetration into the RC footing. The strain gauges were located at heights of -200 mm, 0 mm, +200 mm, $+\ell_w/2$ and $+\ell_w$, relative to the wall-footing interface, in an effort to quantify the extent of inelastic strains in the reinforcement within the expected plastic hinge region.

2.3.3 Test Protocol

Testing was conducted for each wall through load-control protocol with initial lateral loads applied at increments of 25% of the theoretical yield load. During this phase of loading, the experimental yield load was determined based on the strain gauge located at the wall-footing interface reaching the yield strain level, which was identified as the first yielding of the reinforcement. The top displacement of the wall measured at this point was averaged from both directions of loading and is defined as the experimental yield displacement (Δ_{ye}). Further displacement-controlled loading cycles of the wall were then applied at increasing multiples of Δ_{ye} representing values of the experimental displacement ductility ($\mu_{\Delta e}$). A full displacement cycle consists of the displacement measured at the top of a wall from a zero load starting position to the target displacement in the West direction (+) then reversed to the same displacement in the East direction (–) and subsequently brought back to the point of zero load. Two displacement cycles were completed for each target displacement increment. Failure of a wall was defined as the point where the lateral resistance dropped to below 50% of that measured as the peak lateral load (Q_u). In the following section the qualitative and quantitative observations made during each of the loading cycles for each wall are presented.

2.4 Detailing of Confined Boundary Element

To determine the stress-strain properties of the masonry, a series of four-course single unit fully-grouted prisms (height to thickness ratio (h/t) of 4.0) and a series of four-course double unit boundary elements (h/t = 2.0) similar to those tested by

Shedid et al. (2010b) were tested under uniaxial compression with their stress-strain behavior presented in Fig. 2.7. The blocks and grout used were consistent with those used for the wall tests. The prisms had an average peak strength of f'_m = 16.0 MPa, whereas the boundary elements recorded a significant (25%) reduction in strength over the prisms, recording an average f'_m = 12.0 MPa. However, the prisms only achieved a maximum strain of ε_{mu} = 0.0033 (based on the strain at 50% f'_m on the descending branch), whereas the boundary elements achieved a significant increase (94%) in the strain with an average ε_{mu} = 0.0064 (based on the strain to 50% f'_m) as shown in Fig. 2.7. It should be noted that these assemblages did not contain reinforcement and were not instrumented in the same manner as those reported by Shedid et al. (2010b), which only reported strains to 30% f'_m. Nevertheless, the *unreinforced* boundary element configuration has a dramatic effect on softening the descending branch of stress-strain and avoiding the sudden and brittle failure observed with the standard prism configuration. The tendency for this softened behavior, along with reduction in strength of the masonry, can be attributed to the way the boundary element is constructed. Whereby, units laid parallel would result in regions where grout is likely to be ineffective (i.e. between adjacent face shells). In addition to this, the typical failure mechanism of fully-grouted masonry prisms is characterized by an expansion of the grout leading to spalling and separation of the face shell as shown in Fig. 2.8a. Such a mechanism would be impeded in the boundary element by the intersecting units above and below each course as indicated in Fig. 2.8b, which would act as a means to restrain the face shell against expansive stresses imposed by the grout columns. Because the boundary element acts to reduce the anisotropy of the masonry assemblage its behavior may also be considered more amenable to that of concrete.

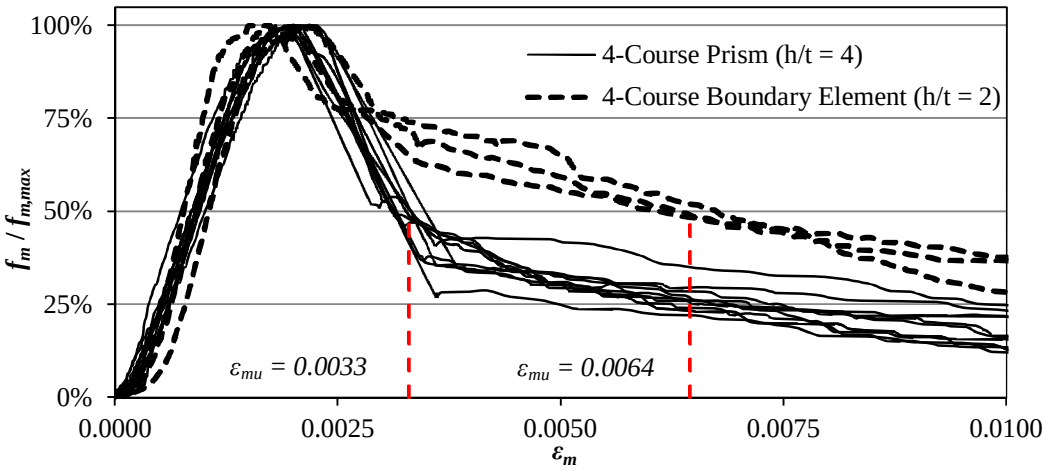

Figure 2.7 – Normalized Stress-Strain Relationship of Prism (*h/t* = 4.0) and Boundary Element (*h/t* = 2.0)

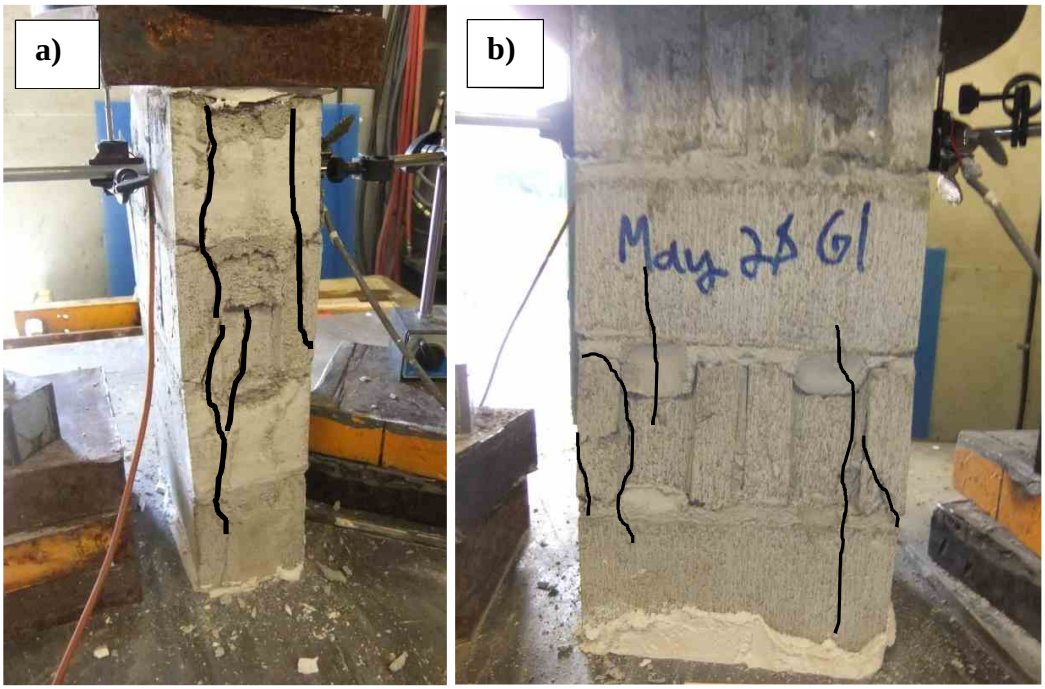

Figure 2.8 – Photos from Prism Testing: a) Face Shell Separation and Vertical Cracking at ε_m = 0.003 (h/t = 4.0) and b) Minor Vertical Cracking at ε_m = 0.005 (h/t = 2.0)

Therefore, due to the lack of any prescriptive detailing available for masonry confined with lateral stirrups, the requirements set out by the concrete structures design standard CSA A23.3 for design of ductile RC walls (CSA 2004b) has been selected as a basis to theoretically estimate ε_{mu} in confined boundary elements. The boundary element detailed in Fig. 2.9 can be considered as the *area of concentrated reinforcement* defined in Fig. 2.10 with an effective gross length (ℓ_b) = 185 mm and a width (b_b) = 185 mm for an overall net area (A_g) = 32,610 mm^2 (after accounting for the loss of area from the frogged ends of the units). Four No. 10 vertical reinforcement bars (A_s = 100 mm^2, d_b = 11 mm) are placed in the centre of the open webs of the overlapping units, which results in a centre-to-centre spacing of 92.5 mm. Lateral stirrups were bent from D4 bars (A_s = 25.4 mm^2, d_b = 5.7 mm) into square stirrups around the vertical bars. The outside-to-outside dimension of the confined core is therefore calculated as: 92.5 mm + (d_b of No. 10) + (2 × d_b of D4) = 115 mm, which represents a confined area (A_c) = 13,225 mm^2, equivalent to 38.6% of the gross boundary element area. Stirrups were placed at each course with a spacing (s_s) = 95 mm and, thus, ε_{mu} can be estimated from Eq. 2.2 derived from the CSA A23.3 (CSA 2004b).

$$\varepsilon_{mu} = \frac{A_s A_c f_{y,h}}{15 k_n A_g f'_m s_s h_c} - \frac{1}{300} \tag{2.2}$$

Where: A_s is the area of reinforcement of the stirrup along either axis (50.8 mm^2), h_c is the dimension of the confined core (115 mm) and k_n is a factor accounting for the number of bars in contact with the stirrup (for a square stirrup of four bars, k_n = 2.0 (CSA 2004b)) as indicated in Fig. 2.9.

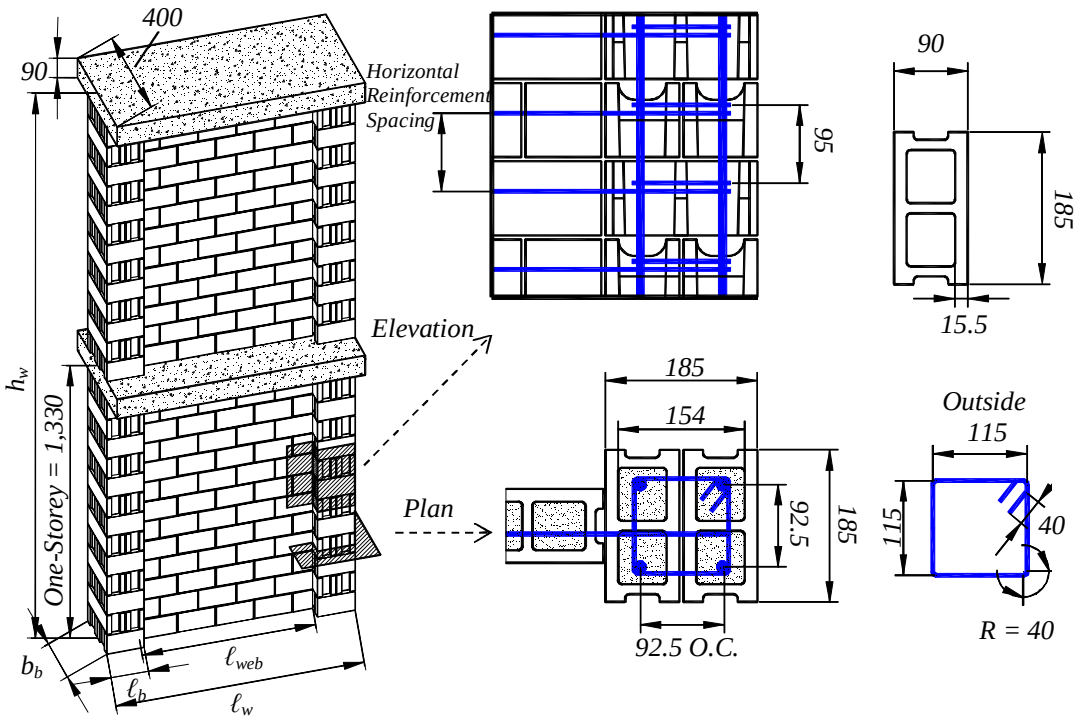

Figure 2.9 – Typical Wall Specimen and Boundary Element Detailing (*Dimensions are in mm*)

Eq. 2.2 can be solved with a f'_m = 12.7, as was reported by Shedid et al. (2010b), to yield a value of ε_{mu} = 0.0039. Comparing the results of Eq. 2.2 with those reported by Shedid et al. (2010b) indicates that Eq. 2.2 provides a reasonably conservative result amenable to the reported data. Finally, as with RC design, the value of ε_{mu} determined from Eq. 2.2 would have to be limited within the confined boundary element of a wall to prevent against web crushing. Thus a check is required to ensure that the unconfined region is not subject to strains in excess of the unconfined strain limit ε_{mu} = 0.0025 as verified from similar triangles in Eq. 2.3.

$$\frac{\ell_b}{c} \geq \frac{\varepsilon_{mu} - 0.0025}{\varepsilon_{mu}} \tag{2.3}$$

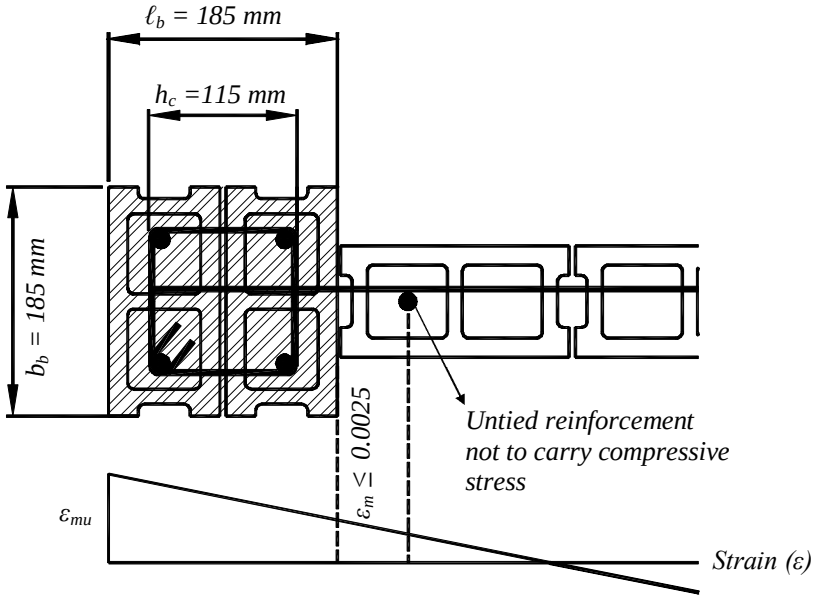

Figure 2.10 – Definition of Area of Concentrated Reinforcement as Applicable to RM Walls

Ultimately, the appropriate value of ε_{mu} for design of structural walls must be made with consideration of actual wall behavior with regard to displacement calculations since ε_{mu} must also be considered to act over an equivalent plastic hinge region, rather than just a the base of a wall. In conclusion, it is evident that the thickened boundary element would reduce and delay the typical failure mechanisms observed in traditional single wythe grouted masonry, whether unreinforced or reinforced. In the following sections, the appropriate value of ε_{mu} as it pertains to predicting wall behavior will be validated as it relates to actual wall test data.

2.5 Theoretical Properties of Wall Specimens

The theoretical wall strengths and top drifts discussed in this section have been determined using standard design methods as described in Drysdale and Hamid (2005) and are summarized in Table 2.3. Wall 8 has been omitted, however, given that it shares the same theoretical properties as Wall 7. Wall 10 has also been omitted because the critical cross-section details at the base of the wall do not deviate from Wall 7 and its ultimate failure was not governed by the performance

of the boundary element, as will be discussed in the subsequent chapter. The yield load (Q_y), depth of neutral axis (c_y), yield curvature (ϕ_y) and yield displacement (Δ_y), as a normalized top drift for each wall, has been determined and is given in Table 2.3 assuming elastic behavior of the masonry and steel. The theoretical ultimate strength of the wall (Q_u) is determined using the equivalent stress-block method described by the CSA S304.1 (2004a) and employing a limiting compression strain of 0.0025 in the masonry. Strain hardening of the vertical reinforcement is also considered in this calculation and is based on the material properties presented earlier. In addition, all tied vertical reinforcement in the boundary element is assumed to carry compressive forces, while, untied vertical reinforcement in the web of the wall is not. The resulting neutral axis depth ($c_{0.0025}$) and curvature ($\phi_{0.0025}$) at ε_{mu} = 0.0025 are also determined and given in Table 2.3. Displacement calculations, however, have been made assuming different values for ultimate strain, ε_{mu} = 0.0025, 0.004 and 0.006 with the limit given by Eq. 2.3. The theoretical ultimate top displacement (Δ_u) is determined using Eq. 2.4 assuming a plastic hinge of $\ell_p = \ell_w$, $\ell_w/2$ and $\ell_w/2 + 0.1h_w$ as three possible design values.

$$\Delta_u = (\phi_u - \phi_y)\ell_p(h_w - \ell_p/2) \tag{2.4}$$

Table 2.3 – Theoretical Predictions of Strength and Top Drift of Walls

		Wall 1	Wall 2	Wall 3	Wall 4	Wall 5	Wall 6	Wall 7	Wall 9	Wall 11
$Q_{y\ (kN)}$		143.2	103.6	127.4	69.7	175.2	112.6	102.9	122.7	188.2
$c_{y\ (mm)}$		351.3	337.6	384.3	326.7	420.7	463.8	404.9	514.8	725.5
$\phi_{y\ (\times 10^{-6}\ rad/mm)}$		3.0	2.9	3.1	2.9	1.9	1.9	1.8	2.0	1.3
Δ_y		0.19%	0.26%	0.28%	0.39%	0.17%	0.26%	0.25%	0.27%	0.18%
$Q_{u\ (kN)}$		193.8	133.7	185.0	91.9	243.8	156.1	146.5	176.8	301.0
$c_{0.0025\ (mm)}$		180.0	213.8	292.7	183.4	226.1	282.7	213.4	281.1	419.7
c/ℓ_w		0.146	0.173	0.237	0.149	0.125	0.157	0.118	0.156	0.158
$\phi_{0.0025\ (\times 10^{-6}\ rad/mm)}$		13.9	11.7	8.5	13.6	11.1	8.8	11.7	8.9	6.0
$\ell_p = \ell_w$	$\Delta_{0.0025}$	1.10%	1.09%	0.79%	1.51%	1.04%	0.98%	1.28%	0.99%	0.66%
	$\Delta_{0.004}$	1.86%	1.85%	1.28%	2.44%	1.71%	1.61%	2.05%	1.61%	1.04%
	$\Delta_{0.006}$	2.76%	2.79%	1.61%	3.56%	2.54%	2.34%	2.99%	2.35%	1.13%
$\ell_p = \ell_w/2$	$\Delta_{0.0025}$	0.75%	0.74%	0.57%	1.00%	0.85%	0.81%	1.04%	0.82%	0.69%
	$\Delta_{0.004}$	1.22%	1.17%	0.86%	1.51%	1.38%	1.29%	1.63%	1.30%	1.09%
	$\Delta_{0.006}$	1.78%	1.72%	1.04%	2.12%	2.04%	1.85%	2.35%	1.86%	1.19%
$\ell_p = \ell_w/2+0.1h_w$	$\Delta_{0.0025}$	0.88%	0.91%	0.56%	1.34%	1.00%	1.25%	1.32%	0.99%	0.80%
	$\Delta_{0.004}$	1.46%	1.49%	0.88%	2.13%	1.65%	2.03%	2.13%	1.61%	1.30%
	$\Delta_{0.006}$	2.15%	2.23%	1.07%	3.09%	2.45%	2.98%	3.11%	2.34%	1.41%
$\Delta_{ASCE\ 41,CP}$		0.36%	0.40%	0.40%	0.40%	0.35%	0.40%	0.41%	0.40%	0.34%
Assumptions: Strain hardening, only tied reinforcement carries compression										

Finally, the level of top drift related to a collapse prevention limit state ($\Delta_{ASCE\ 41,\ CP}$), as interpolated from the ASCE 41 Standard for the Seismic Rehabilitation of Existing Buildings (ASCE 2006) for reinforced masonry wall systems, is also presented. It is clear that there exists a very wide range of possibilities for the predicted top displacement for a boundary element wall depending on the design assumptions of strain and plastic hinge length made. However, the suggested drifts appearing in the ASCE 41 appear overly conservative by a wide margin for this wall type. In the next section, the assumptions required to make an accurate prediction of the theoretical wall strength and displacement behavior will be validated based on the experimental results and the formulation of a basis that can be used for design and analysis will be presented.

2.6 Summary and Conclusions

In this chapter the test program which was carried out is described regarding the test set-up, methodology and the selected test parameters. In addition, theoretical predictions regarding the strength and displacement properties of each wall are also presented, which also includes the two walls tested by Shedid et al. (2010a) integrated for comparison purposes.

Observations made from both unreinforced and reinforced prism testing indicate that the confined boundary elements offer an improvement to the ultimate strain in the compression toes of the walls. The expression which appears in the concrete structures standard CSA A23.3 (CSA 2004b) was used to estimate this strain and the subsequent theoretical estimates for top displacement are presented. In addition, the stirrup spacing selected also meets the requirements for tied reinforcement in the masonry standard CSA S304.1 (2004a) and has been used in strength and displacement calculations. Wall 3, which possess the highest reinforcement ratio was found to possess the lowest range of theoretical top drifts while Wall 4, which possessed the greatest aspect ratio also possessed the highest range of theoretical top drifts. The values obtained from the ASCE 41 Standard (ASCE 2006) were markedly less than those derived from first principal calculations (less than one-half of the most conservative estimates of drift). The analysis of each wall's behavior which appears in Chapter 4 will be compared with the theoretical predictions offered in this chapter, and their validity will be used towards the development of set of design expressions applicable towards this wall type.

2.7 Notation for Chapter 2

A_c = area of confined core in boundary element (mm^2);
A_g = gross-cross-section area of a boundary element (mm^2);
A_R = aspect ratio of wall (h_w / ℓ_w);
A_s = area of reinforcement (mm^2);
b_b = width of boundary element (mm);
c = depth of neutral axis (mm);
c_y = depth of neutral axis at the yield strength (mm);
$c_{0.0025}$ = depth of neutral axis calculated with limiting strain in masonry of 0.0025 (mm);
d_b = diameter of rebar (mm);
f'_m = prism strength of grouted masonry unit (MPa);
$f_{y,h}$ = yield strength of horizontal reinforcement (MPa);
$f_{y,v}$ = yield strength of vertical reinforcement (MPa);
$f_{u,v}$ = ultimate strength of vertical reinforcement (MPa);
h = unsupported height of a wall in (mm);
h_c = dimension of confined core (mm);
h/t = height to length ratio of prism;
h_w = height of wall (mm);
$IS^{\#}$ = number of intersecting floor slabs in wall;
k_n = parameter accounting for number of bar in contact with stirrups;
ℓ_b = Length of confined boundary element (mm);
ℓ_w = length of wall (mm);
P_a = total level of axial stress applied to each wall including self-weight (MPa);
Q = load applied at the top of the wall (kN);
Q_u = theoretical peak load (kN);
R_d = seismic force modification factor;
s_s = vertical spacing between lateral confinement stirrups (mm);
s_v = horizontal space between vertical reinforcing bars (mm);
t = width of the compression zone of a wall (mm);
$\Delta_{ASCE41,CP}$ = collapse prevention drift derived from the ASCE 41 document;
Δ_u = theoretical top drift of wall at ultimate load (%);
$\Delta_{0.0025}$ = theoretical ultimate top displacement with a limitng compressive strain of 0.0025;
$\Delta_{0.004}$ = theoretical ultimate top displacement with a limitng compressive strain of 0.004;
$\Delta_{0.006}$ = theoretical ultimate top displacement with a limitng compressive strain of 0.006;
Δ_y = theoretical yield displacement of wall (mm);
Δ_{ye} = experimental yield drift of wall (%);

ε_m = compressive strain of masonry;
ε_{mu} = ultimate compressive strain of masonry;
$\mu_{\Delta e}$ = experimental displacement ductility;
ρ_b = percent of vertical reinforcement of gross boundary element area;
ρ_h = percent of horizontal reinforcement of gross wall area;
ρ_v = percent of vertical reinforcement of gross cross-sectional area;
ϕ_y = theoretical yield curvature of wall (rad/mm);
$\phi_{0.0025}$ = theoretical curvature with limiting strain in masonry of 0.0025 (rad/mm);

2.8 References for Chapter 2

American Society for Civil Engineers (ASCE). (2006). "Seismic rehabilitation of existing buildings." *ASCE 41-06*, ASCE, Reston, Va.

American Society for Testing and Materials (ASTM). (2011). "Standard test methods for sampling and testing concrete masonry units and related units." *C140-11*, ASTM International, West Conshohocken, Pa.

American Society for Testing and Materials (ASTM). (2007). "Standard test method for flow of hydraulic cement mortar." *C1437-07*, ASTM International, West Conshohocken, Pa.

American Society for Testing and Materials (ASTM). (2009). "Standard test method for preconstruction and construction evaluation of mortars for plain and reinforced unit masonry." *C780-09*, ASTM International, West Conshohocken, Pa.

American Society for Testing and Materials (ASTM). (2010). "Standard specification for grout for masonry." *C476-10*, ASTM International, West Conshohocken, Pa.

American Society for Testing and Materials (ASTM). (2010). "Standard test method for compressive strength of masonry prisms." *C1314-10*, ASTM International, West Conshohocken, Pa.

American Society for Testing and Materials (ASTM). (2004). "Standard test method for Young's modulus, tangent modulus, and chord modulus." *E111-04*, ASTM International, West Conshohocken, Pa.

American Society for Testing and Materials (ASTM). (2009). "Standard specification for deformed and plain carbon-steel bars for concrete reinforcement." *A615/A615M-09b*, ASTM International, West Conshohocken, Pa.

American Society for Testing and Materials (ASTM). (2010). "Standard test method for compressive strength of cylindrical concrete specimens." *C39/C39M-10*, ASTM International, West Conshohocken, Pa.

Banting, B. R. and El-Dakhakhni, W. W. (2012). "Force- and Displacement-Based Seismic Performance Parameters for Reinforced Masonry Structural Walls with Boundary Elements." *ASCE Journal of Structural Engineering* Vol. 138(12), 1477-1491

Banting, B. R. and El-Dakhakhni, W. W. (2013). "Seismic Performance Quantification of Reinforced Masonry Structural Walls with Boundary Elements." Submitted to *ASCE Journal of Structural Engineering*, Accepted with Minor Revisions for 2nd Round of Review Feb. 11, 2013.

Canadian Standards Association (CSA). (2004a). "Design of masonry structures." *CSA S304.1-04 (R2010)*, CSA, Mississauga, Canada.

Canadian Standards Association (CSA). (2004b). "Design of concrete structures." *CSA A23.3-04 (R2010)*, CSA, Mississauga, Canada.

Drysdale, R., and Hamid, A. (2005). *Masonry Structures- Behavior and Design.* 3rd ed., Canada Masonry Design Centre, Mississauga, Canada.

Long, L., M. (2006). "Behaviour of half-scale reinforced concrete masonry shear walls." Master of Applied Science-Thesis, McMaster University, Hamilton, Canada.

Shedid, M. T., El-Dakhakhni, W. W. and Drysdale, R. G. (2010a). "Alternative strategies to enhance the seismic performance of reinforced concrete-block shear wall systems." *Journal of Structural Engineering*, 136(6), 676-689.

Shedid, M. T., El-Dakhakhni, W. W. and Drysdale, R. G. (2010b). "Characteristics of confined and unconfined masonry prisms for seismic performance enhancement of structural walls." *Masonry International.*, 23(2), 69-78.

CHAPTER 3: TEST OBSERVATIONS AND RESULTS

3.1 Introduction

In this chapter the observations made during the experimental testing of masonry walls possessing confined boundary elements is presented. The information in this chapter is the sole work of the author with Dr. El-Dakhakhni acting in an advisory and editorial role to prepare two manuscripts for journal submission. This chapter consists of information from two separate journal articles that have been integrated together for the purposes of providing better flow within the context of a thesis. The information contained in this chapter can be found in the articles:

Banting, B. R. and El-Dakhakhni, W. W. (2012). "Force- and Displacement-Based Seismic Performance Parameters for Reinforced Masonry Structural Walls with Boundary Elements." *ASCE Journal of Structural Engineering* Vol. 138(12), 1477-1491

Banting, B. R. and El-Dakhakhni, W. W. (2013). "Seismic Performance Quantification of Reinforced Masonry Structural Walls with Boundary Elements." Submitted to *ASCE Journal of Structural Engineering*, Accepted with Minor Revisions for 2nd Round of Review Feb. 11, 2013.

3.2 Observations Related to Force-Based Design

The hysteretic loops generated for each wall are presented in the following section along with a summary of experimentally recorded strength and displacement properties. The hysteresis load-displacement loops generated by each wall is presented in Fig. 3.1, Walls 5 and 6 were reported by Shedid et al. 2010 and are shown for comparison purposes. Overall, the hysteresis loops were generally symmetrical, indicating similar behavior in the reversed directions of loading, until failure mechanisms were initiated. The load displacement envelopes for all of the confined boundary element walls are given in Fig. 3.2. Force-based experimental measurements for ductility and strength reported include the experimental yield load (Q_{ye}), experimental yield displacement (Δ_{ye}), experimental displacement ductility ($\mu_{\Delta e}$), the peak lateral load (Q_{ue}), the top displacement at the peak lateral load (Δ_{Que}), the displacement ductility at the peak load ($\mu_{\Delta Que}$), the ultimate displacement defined as a drop in wall capacity to 80% of Q_{ue} ($\Delta_{80\%Que}$) and the corresponding ultimate displacement ductility ($\mu_{\Delta ue}$). Top displacements are also normalized by wall height and given as a percentage drift ($\Delta_{\%}$). A summary of the force-based results is given in Table 3.1, including the displacement ductility corresponding to the drift limit of 1.0% ($\mu_{\Delta e1\%}$).

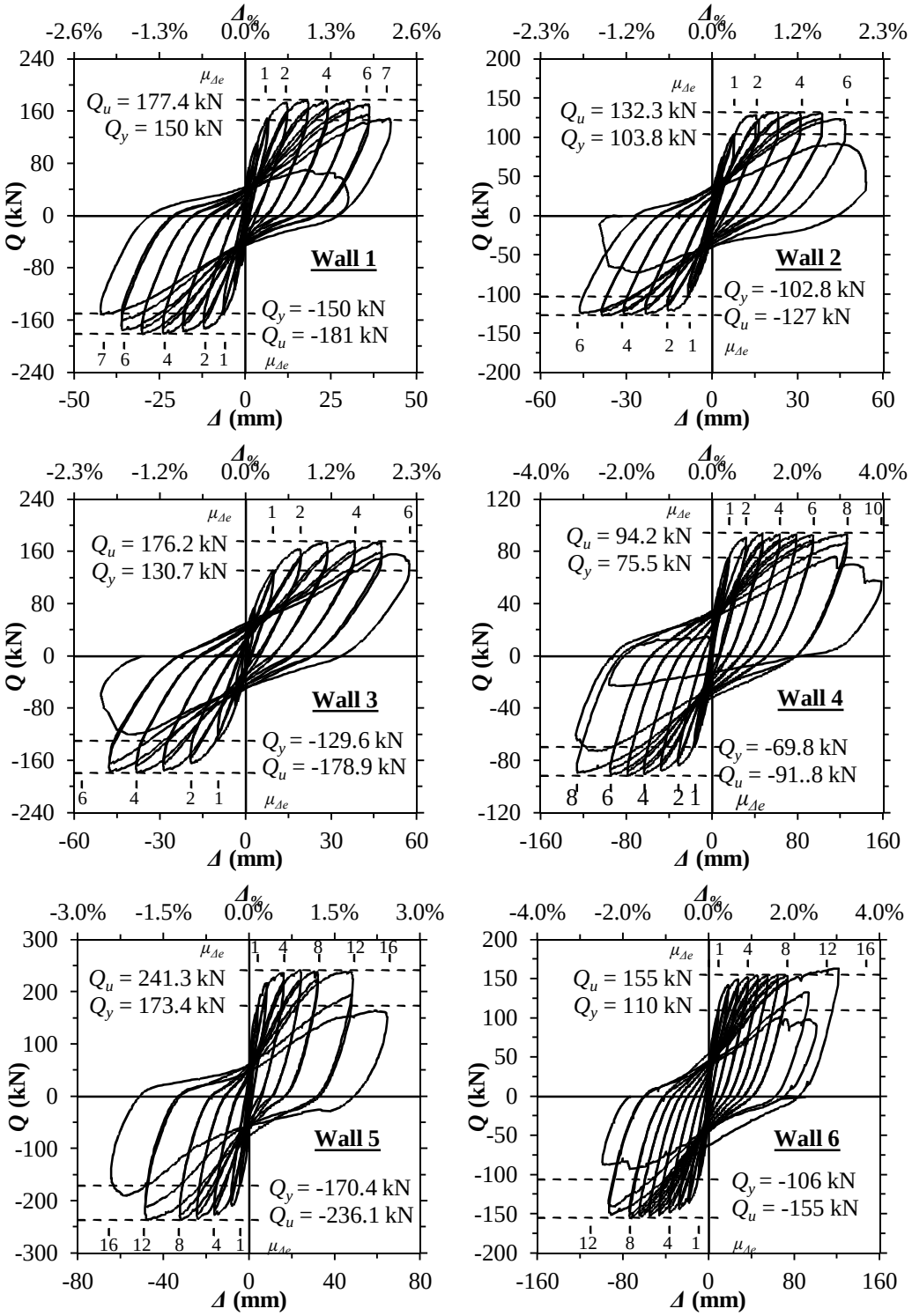

Figure 3.1 – Hysteretic Load-Displacement Response of Walls 1-6 (*Walls 5 and 6 also reported by Shedid et al. (2010)*)

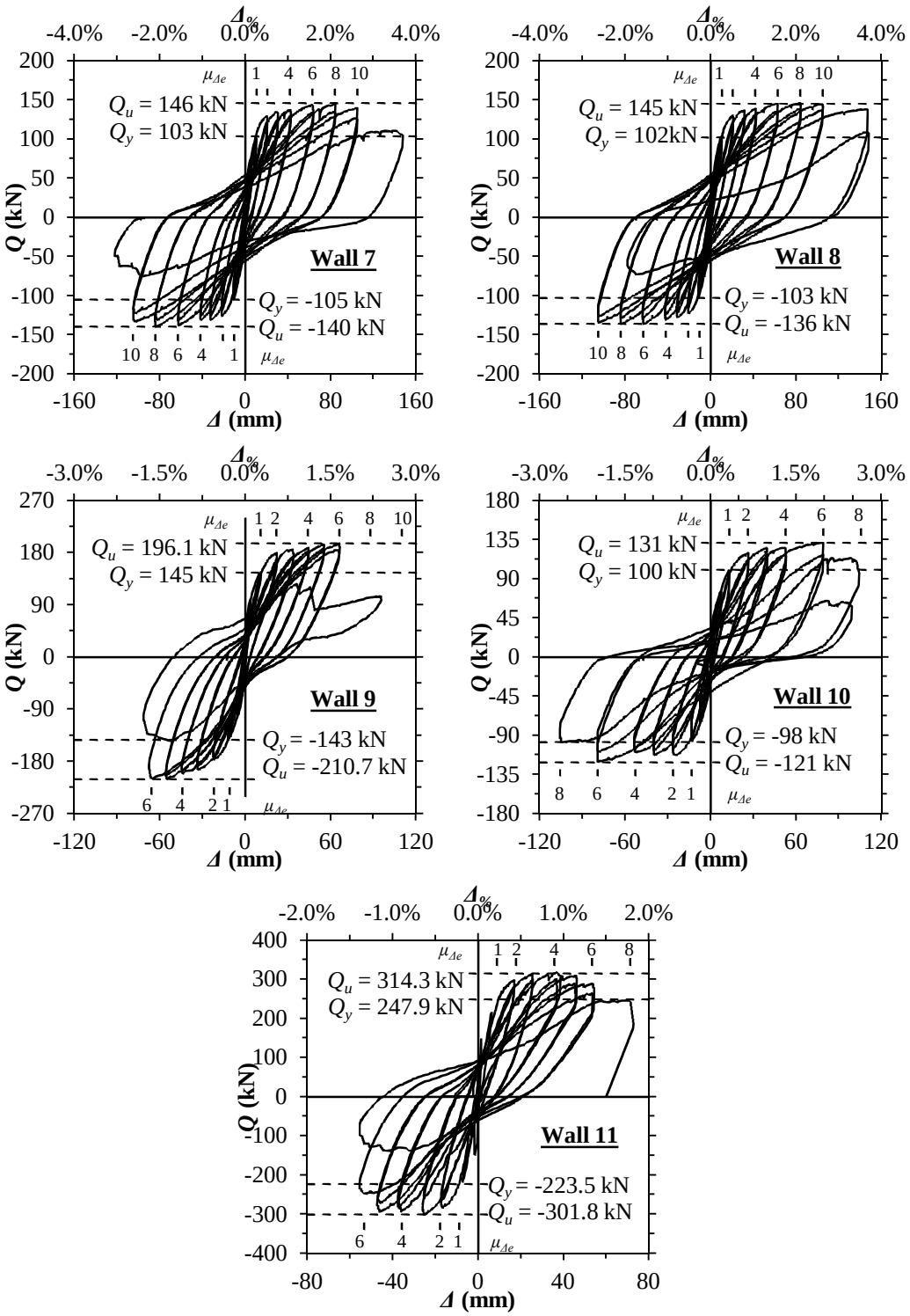

Figure 3.1 Continued... – Hysteretic Load-Displacement Response of Walls 7-11

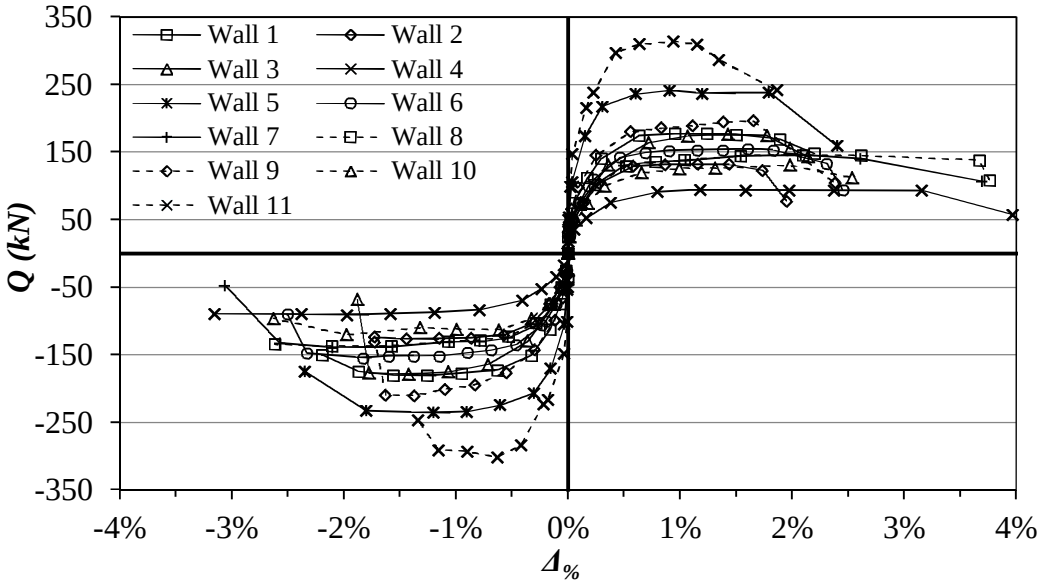

Figure 3.2 – Load-Displacement Envelope of all Walls (*Walls 5 and 6 reported by Shedid et al. (2010)*)

Table 3.1 – Summary of Experimental Loads and Displacements of Walls

	Wall Specimen										
	1	**2**	**3**	**4**	**5**	**6**	**7**	**8**	**9**	**10**	**11**
$Q_{ye\ (kN)}$	145.6	103.3	130.2	72.7	171.9	108	103.4	102.5	143.9	99.0	216.3
Δ_{ye}	0.31%	0.30%	0.36%	0.39%	0.15%	0.23%	0.25%	0.24%	0.27%	0.33%	0.17%
$Q_{ue\ (kN)}$	179.2	129.7	177.6	92.7	238.7	155	142.8	141.0	203.4	126.0	308
Δ_{Que}	1.53%	1.58%	1.78%	3.16%	1.80%	2.08%	2.59%	2.35%	1.64%	1.98%	1.25%
$\Delta_{80\%Que}$	2.20%	1.78%	1.98%	3.36%	2.19%	2.37%	3.03%	3.11%	1.82%	2.63%	1.54%
$\mu_{\Delta eQu}$	4.9	5.3	4.9	8.1	12.0	9.0	10.4	9.8	6.1	6.0	7.4
$\mu_{\Delta ue}$	7.1	5.9	5.5	8.6	14.6	10.3	12.1	13.0	6.7	8.0	9.1
$\mu_{\Delta e1\%}$	3.2	3.3	2.8	2.6	6.7	4.3	4.0	4.2	3.7	3.0	5.9

3.2.1 Extent of Inelastic Curvature

Average vertical wall strains measured over each externally mounted LVDTs were divided by the wall length to get the average curvature (ϕ) of a wall and are plotted in Fig. 3.3. Each wall has their experimentally measured values of yield curvature (ϕ_{ye}) determined from the average curvature measured over the bottom 150 mm of each wall. The extent of height over which the average wall curvature exceeds ϕ_{ye} is presented as the experimental extent of inelastic curvature ($\ell_{p\phi}$). The experimental plastic hinge length (ℓ_{pe}) is defined here as the average measured height up each wall from its base where inelastic curvatures, greater than the yield curvature, occurred. This is different than the *idealized* plastic hinge used to estimate the top displacement of a wall commonly used in design codes which represents the height over which a *constant* curvature is assumed. Rather, ℓ_{pe} is an indicator of the height over which special seismic detailing would be required. The curvature measured up to the peak load is also given as, ϕ_{ue}, and is determined over the bottom distance of each wall equal to $\ell_w/2$ and ℓ_w, for analysis purposes to be discussed in subsequent sections. The curvature profiles measured over the height of each wall is depicted in Fig. 3.3 and summarized in Table 3.2. The results from Wall 8 have been omitted due to the similarity in response with that of Wall 7. However, the results of Wall 9 have been omitted due to the formation of a plastic hinge at the second storey which will be described separately.

Table 3.2 – Wall Curvatures

	Wall 1	**Wall 2**	**Wall 3**	**Wall 4**	**Wall 5**	**Wall 6**	**Wall 7**	**Wall 9**	**Wall 11**
At Yield									
$\phi_{ye\ (\times 10^{-6}\ rad/mm)}$	4.46	3.90	3.76	3.45	2.04	1.91	2.01	1.58	1.65
Δ_{ye}	0.31%	0.30%	0.36%	0.39%	0.15%	0.23%	0.25%	0.27%	0.17%
At Ultimate Conditions									
$\phi_{Que\ (\times 10^{-6}\ rad/mm)}$ $(\ell_w/2)$	16.1	21.7	17.0	36.1	10.3	14.7	16.2	13.8	9.3
$\phi_{Que\ (\times 10^{-6}\ rad/mm)}$ (ℓ_w)	11.8	14.8	10.6	26.0	6.4	9.0	10.5	7.1	5.0
$\ell_{p\phi}$ $(\%\ell_w)$	60.0%	87.8%	88.5%	100%	60.9%	66.5%	98.5%	77.4%	53.1%

Wall 11 attained a $\ell_{p\phi}$ = 1,410 mm which is equivalent to 53.1% ℓ_w. This represents the smallest experimental plastic hinge of the walls tested as a proportion of wall length. By contrast, Wall 1, which also shared an A_R = 1.5, attained a $\ell_{p\phi}$ = 60.0% ℓ_w. Whereas, Walls 2 and 3, which differed by the amount of vertical reinforcement in the web of the wall, achieved nearly identical $\ell_{p\phi}$ = 87.9% ℓ_w and 88.7% ℓ_w, respectively. Finally, Wall 4 which represented the most slender and ductile wall tested attained the highest $\ell_{p\phi}$ = 100% ℓ_w. Comparison between all the walls indicates that the extent of plastic hinging is more strongly related to aspect ratio, rather than wall length, since Wall 4 achieved a $\ell_{p\phi}$ nearly

double that of Walls 1 and 11 independent of the reinforcement ratios tested. by contrast, it was observed that Wall 8 (ϕ_{ye} = 1.87 E-6 rad/mm) had a lower ϕ_{ye} than Wall 7 (ϕ_{ye} = 2.01 E-6 rad/mm) and also measured a greater extent of inelastic curvature as shown in Fig. 3.3, despite otherwise possessing similar behavior. Whereby, $\ell_{p\phi}$ was found to be 98.5% ℓ_w and 109.6% ℓ_w (not shown in Table 3.2), respectively for Walls 7 and 8. Contrastingly, Wall 9 exhibited lower values of ϕ_{ye} = 1.57E-6 rad/mm, $\ell_{p\phi}$ = 77.4% ℓ_w compared to similar walls.

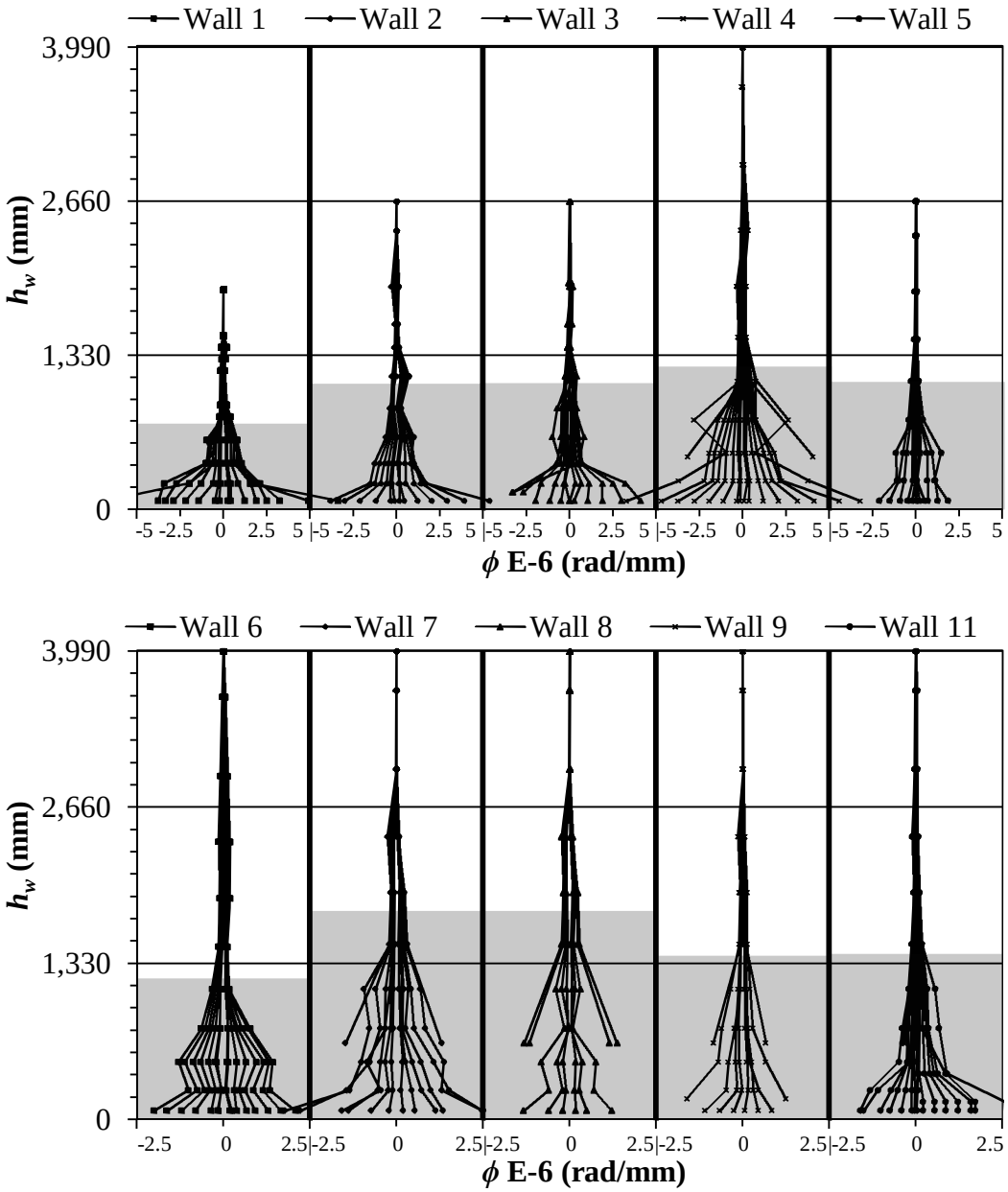

Figure 3.3 – Average Curvature Profiles of Walls Indicating $\ell_{p\phi}$ (Shaded)

Wall 10 experienced yielding in the second storey prior to yielding at the base of the wall. Although yielding occurred in the 2nd storey at a lower top displacement than the 1st storey it was decided that subsequent cycling and analysis be based on the response of the wall-footing interface. Large diagonal and horizontal cracks formed with increased displacements concentrating in the upper half of the 1st storey and lower half of the 2nd storey indicating that plasticity was simultaneously spreading downward from the 2nd storey and upward from the 1st. This in effect resulted in the formation of two plastic hinges in the wall. Two separate yield curvatures were determined for Wall 10, one corresponding to the plastic hinge that formed in the 1st storey (i.e. boundary element) cross-section (ϕ_{ye} = 2.00 E-6 rad/mm) and the second corresponding to the hinge that formed in the 2nd storey (i.e. flanged) cross-section (ϕ_{ye} = 1.81 E-6 rad/mm). By altering the layout of Wall 7 to that of Wall 10 a second plastic hinge formed about the 1st floor slab as demonstrated by the curvature profile in Fig. 3.4 caused by the lack of confinement of the flanged cross-section.

Due to the coupling effect between the two hinges that formed it is not possible to isolate the spread of the plastic hinge located at the 1st floor slab. However, it is possible to determine the *net effect* that the transition to a flanged cross-section has on the overall wall behavior by considering the change curvature from a similar wall with continuous boundary elements. In this regard, the second hinge affected the cracking pattern of Wall 10 resulting in shear cracks that more closely resembled that of Wall 8, rather than that of Wall 7. Therefore, effect of the flanged cross-section on a wall with continuous boundary elements is best represented by the difference in curvature between Walls 10 and 8. At points of equal load the curvature profile of Wall 8 was subtracted from Wall 10 as shown in Fig. 3.4. The results indicate nearly equal propagation of inelastic curvature above (676 mm) and below (692 mm) the 1st floor slab (equivalent to 75.9% ℓ_w) corroborating the observations of cracking damage made during the test.

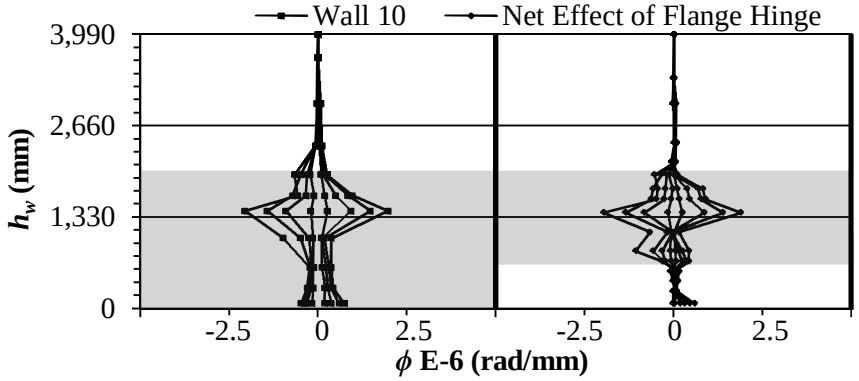

Figure 3.4 -Net Effect of Flanged Hinge Formation in Wall 10 with $\ell_{p\phi}$ (Shaded)

3.2.2 Experimental Elastic Stiffness and Ductility

Experimentally measured values for stiffness are summarized in Table 3.3 and determined as given by Fig. 3.5 from the experimental load-displacement envelope of the walls as the gross uncracked tangential stiffness (K_{ge}) measured up to 50% Q_{ye} or until cracking was observed, the cracked tangential stiffness (K_{cre}) measured after cracking occurs until Q_{ye} and the yield secant stiffness (K_{ye}) determined from the experimental yield displacement. The load-displacement envelopes for the tested walls do not resemble an elastic perfectly-plastic relationship as would be required with the equal displacement assumption. Therefore, an idealization is necessary to establish an equivalent bilinear relationship such that the idealized displacement ductility can be established. There have been several different idealization approaches proposed for use with masonry structural walls based on differing interpretations of the yield stiffness and displacement (Shing et al. 1989; Tomaževič 1999 and Shedid et al. 2008). For this analysis, the recent definition offered by Priestley et al. (2007) will be adopted, whereby the idealized yield displacement (Δ_y*) is determined as the intersection of a line passing from the origin through the experimental yield displacement (slope K_{ye} in Fig. 3.5) with a horizontal line defined by Q_{ue}. Based on the idealized relationship, the displacement ductility capacity of each wall ($\mu_{\Delta i}$) is determined up to the ultimate displacement defined as $\mu_{\Delta i} = \Delta_{80\%Que}/\Delta_y$* and presented in Table 3.3. In addition, the displacement ductility at the drift limit specified by the NBCC (2010) for post-disaster structures (1.0%) is also presented in Table 3.3 as $\mu_{\Delta i1\%}$. The values of $\mu_{\Delta i}$ are 4.0 and 10.2 for Walls 3 and 5, respectively, whereas, with the drift limit of 1.0% is applied, the idealized displacement ductility drops to 2.0 and 4.8 for Walls 3 and 5, respectively.

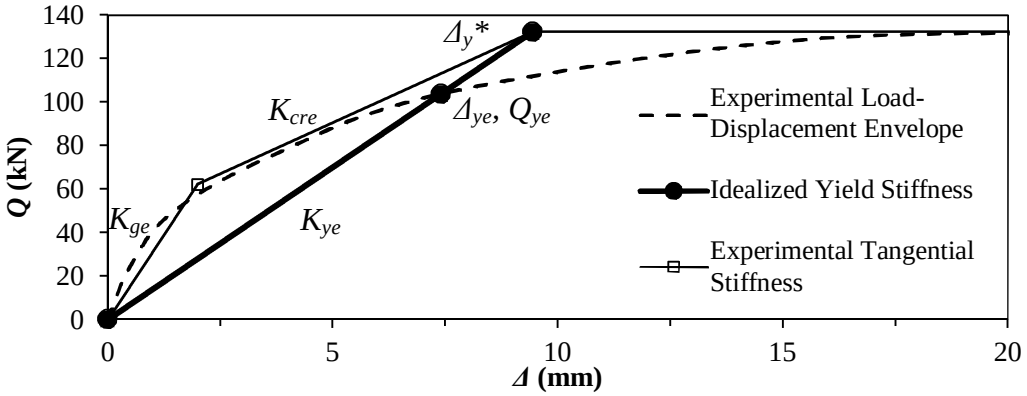

Figure 3.5 – Stiffness Definitions shown here for Wall 3 in Push as an Example

Table 3.3 – Experimentally Determined Stiffness of Walls and Idealized Displacement Ductility

	Wall 1	**Wall 2**	**Wall 3**	**Wall 4**	**Wall 5**	**Wall 6**	**Wall 7**	**Wall 8**	**Wall 9**	**Wall 10**	**Wall 11**
	Experimentally Measured Properties (Stiffness in kN/mm)										
K_{ge}	65.2	30.4	46.5	14.2	270.5	31.3	29.6	43.2	42.9	18.8	132.7
K_{cre}	14.7	4.2	5.4	1.7	14.6	6.5	3.2	3.2	4.3	2.2	13.9
K_{ye}	24.7	12.9	13.6	4.7	43.1	11.8	10.4	9.9	13.4	7.5	31.9
Δ_y*	0.38%	0.37%	0.49%	0.50%	0.21%	0.33%	0.35%	0.36%	0.39%	0.42%	0.24%
$\mu_{\Delta i}$	5.7	4.8	4.0	6.6	10.2	7.1	8.7	8.8	4.7	6.2	6.4
$\mu_{\Delta i1\%}$	2.6	2.7	2.0	2.0	4.8	3.0	2.9	2.8	2.6	2.4	4.2

3.2.3 Flexure-Shear-Sliding Contributions to Wall Top Displacements

The top displacement of each wall results from of a combination of flexural, shear and base sliding displacements. Employing techniques adopted by Massone et al. (2004), flexural displacements are isolated by integrating the experimentally measured curvature along the height of each specimen and subtracting it and the base sliding from the top drift to determine the shear contribution. The hysteresis loops generated from each mode of deformation are presented in Fig. 3.6. All walls demonstrated large loops generated by flexural deformations, indicating high levels of energy dissipated by flexural yielding of the vertical reinforcement. Under low levels of top wall displacements, shear deformations are nearly linear elastic. Similar observations were made by Shing et al. (1989) under low levels of top displacement. However, once diagonal cracking occurs, shear forces are redistributed and resisted by the horizontal reinforcement and grout-block-mortar friction as described in Tomaževič (1999) and shown by the growing size of loops. Progressively larger hysteresis loops were produced for base sliding which is characterized by a purely plastic behavior, whereby the maximum displacement is maintained during unloading. All Walls exhibited sliding displacements only at the interface of the 1st course with the footing. In the following sections comparisons are drawn between the behavior of each wall in terms of the relative proportion of each deformation mode.

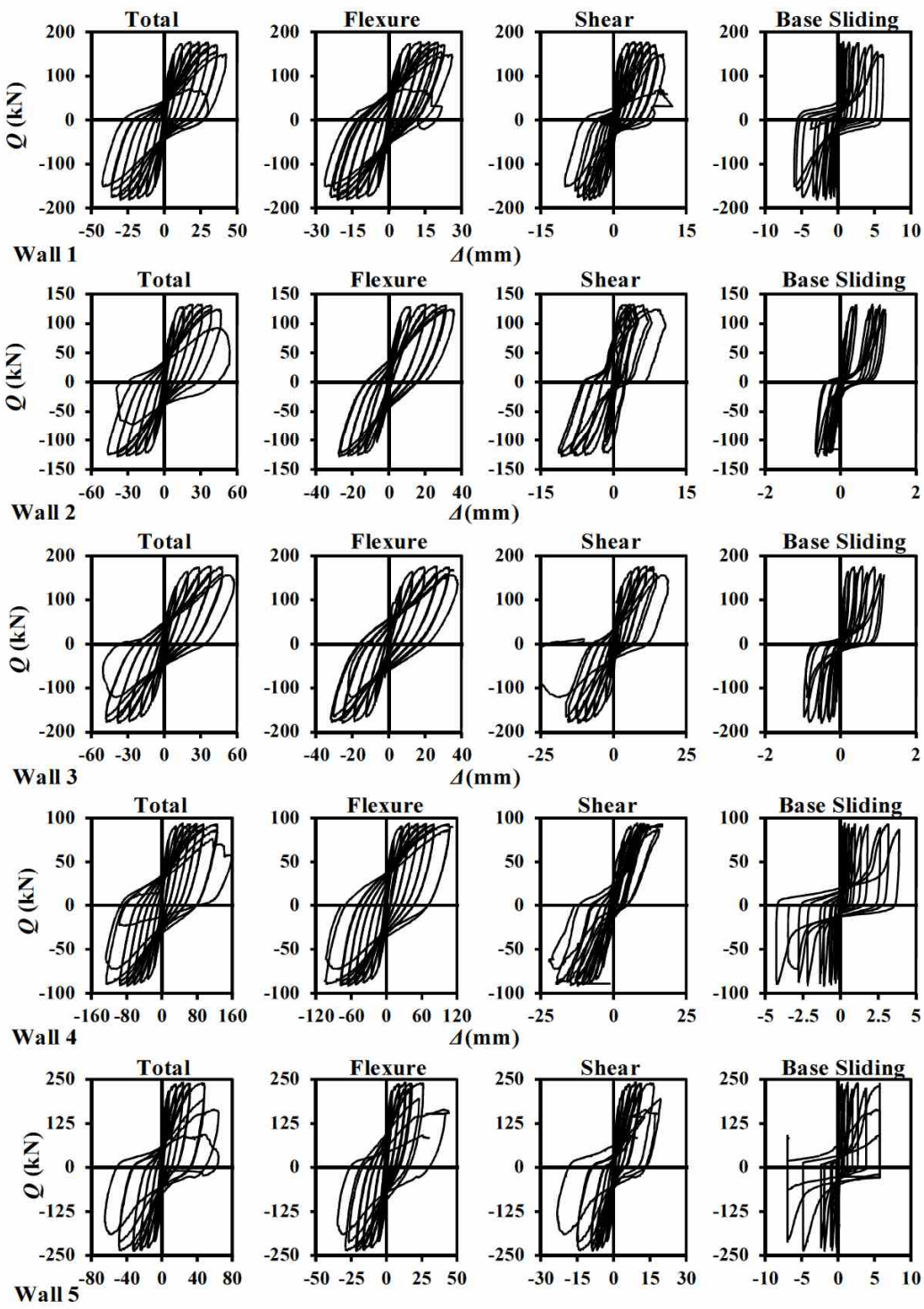

Figure 3.6 – Deformation Hysteresis Loops of Walls (Flexure, Shear and Base Sliding) Walls 1-5

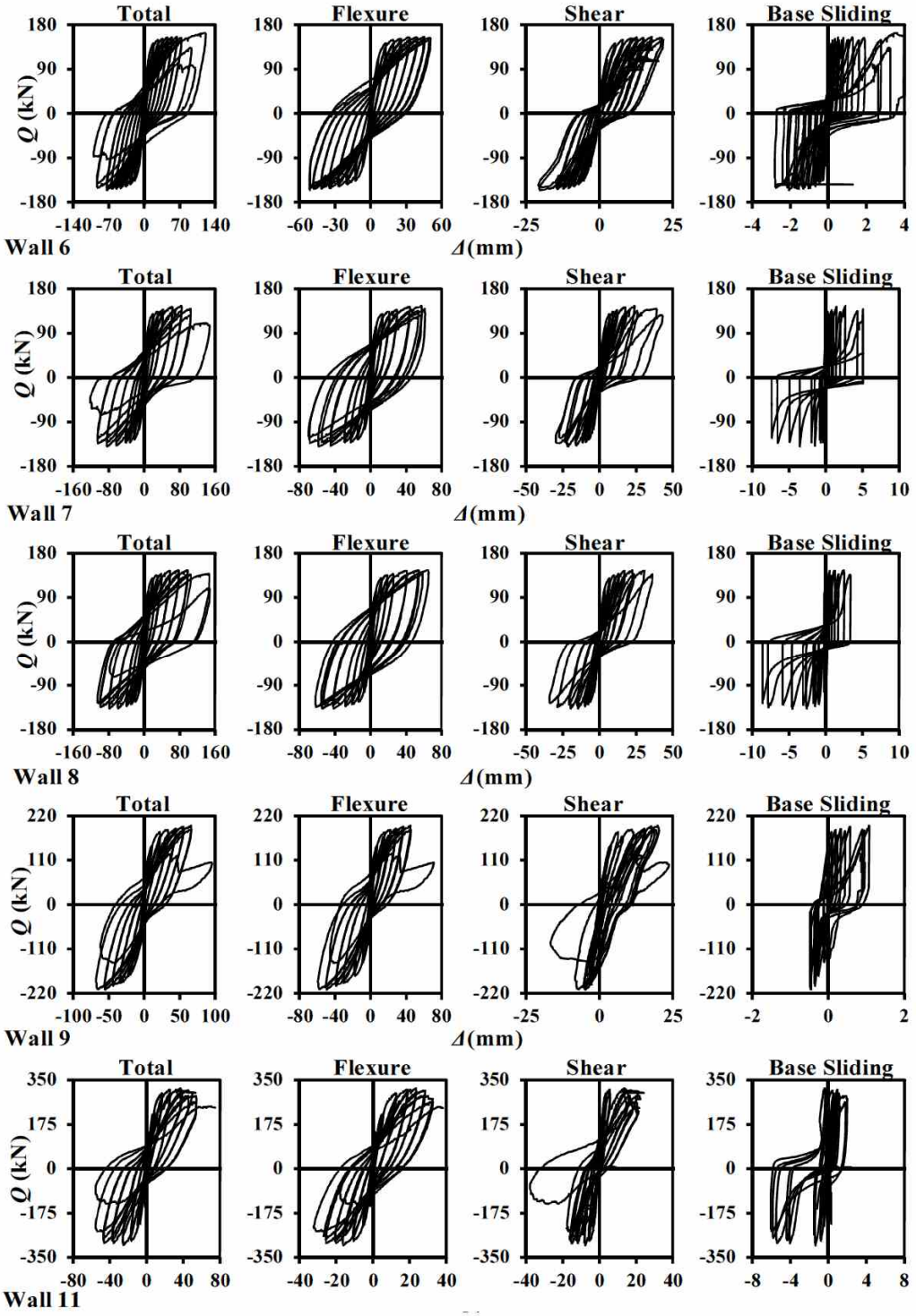

Figure 3.6 Continued ... – Deformation Hysteresis Loops of Walls (Flexure, Shear and Base Sliding) Walls 6-11

Overall, flexure was the dominant form of behavior for the walls, however, comparison between Walls 1 and 11 (Aspect Ratio (A_R) = 1.5) indicate that Wall 11 possessed significantly larger shear deformations than that measured in Wall 1, an average of 36.0% of the total top displacement compared to 15.8%, respectively, as indicated in Fig. 3.7. This difference between these walls, with the same A_R but differ in their sizes and ratio of boundary element length (ℓ_b) to wall length (ℓ_w), may be attributed to the improved post-peak response of Wall 1 compared to the critical web crushing that occurred outside the boundary element in Wall 11 that will further be discussed in the section dedicated to performance-based design.

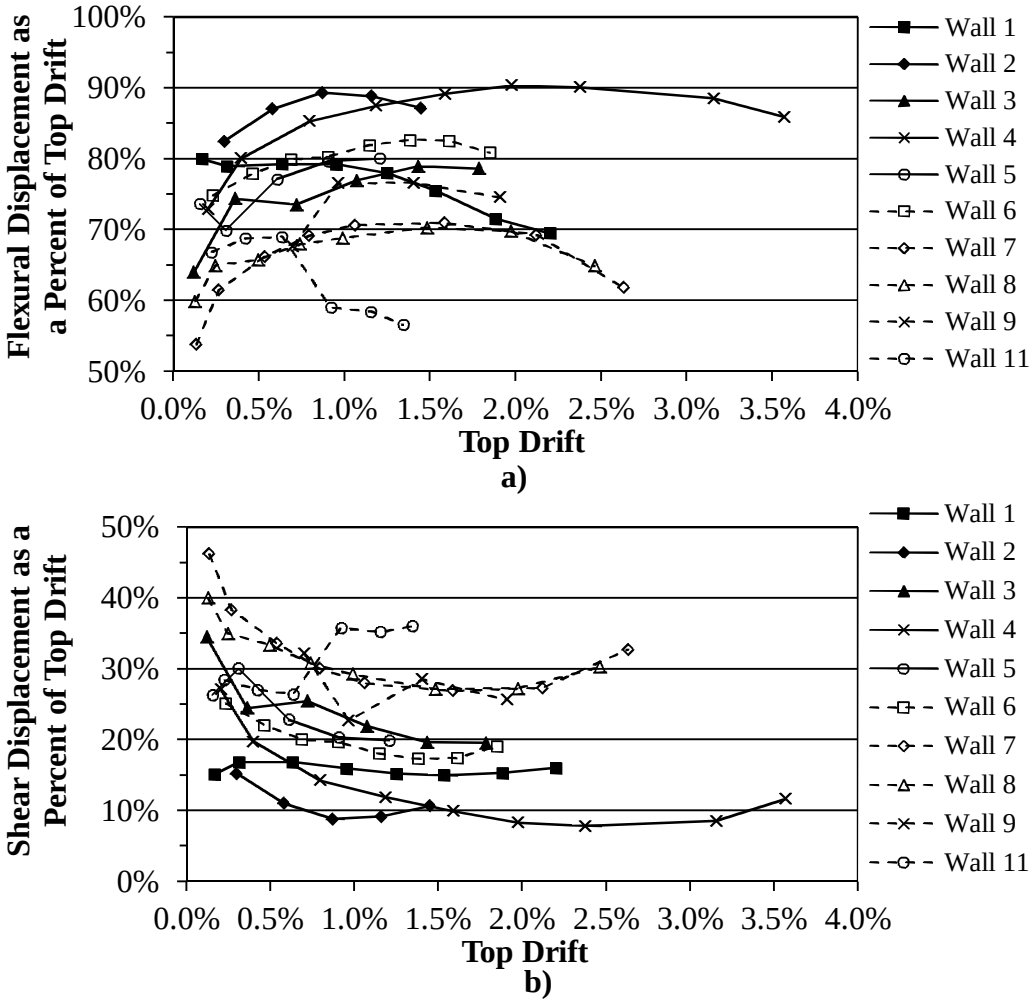

Figure 3.7 - Experimentally Determined Proportion of Top Displacement attributed to: a) Flexure and b) Shear

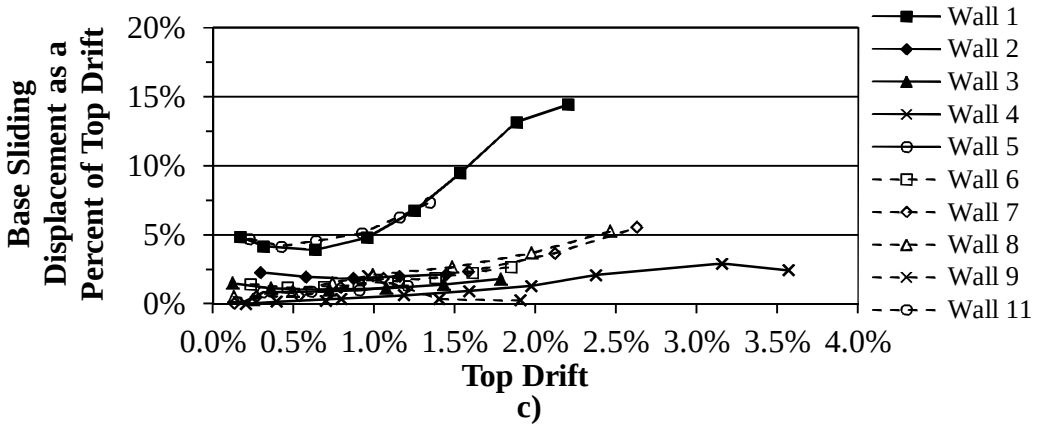

c)

Figure 3.7 Continued... - Experimentally Determined Proportion of Top Displacement attributed to: c) Base Sliding

It is also postulated that the size effects between the walls may have also contributed to the reduction in shear stiffness and thus the increased shear displacement of Wall 11. The relatively thickened and stiffer boundary elements in the walls can be considered as a contributing mechanism in the resulting diagonal crack spacing in a similar manner to how concentrated reinforcement in RC beams is by the modified compression field theory (MCFT) (Vecchio and Collins 1986) a topic that will be explored in greater detail in Chapter 5.

The added web reinforcement in Wall 4 had the effect of increasing Δ_{ye} by 23%%, while also increasing Q_u by 36.9% compared to Wall 2 based on the results reported in Table 3.1. As a result of the higher shear forces experienced by Wall 3, the proportion of shear deformation to total wall drift was on average 24%, more than double the average of 10.9% measured for Wall 2 referring to the results of Fig. 3.7.

Finally, the effect of altering A_R of Walls 1, 2 and 4, which each share the same cross-section details and applied axial stress, are considered. The behavior of Wall 1 was significantly more dominated by shear (15.8%) and a stable base sliding mechanism which peaked at 14.5% of overall top drift. By contrast, Walls 2 and 4 possessed predominantly flexural deformations accounting for an average of 85.5% and 87.0% of total top drift, respectively. As a result, and contrary to a purely flexural analysis, Wall 2 achieved a lower level of top drift than Wall 1 despite having similar ultimate curvatures, Wall 1 experienced a stable shear/sliding mechanism that did not inhibit wall strength. It is concluded that although flexure dominates behavior in high aspect ratio walls, flexural failing walls with aspect ratios between 1.5 and 2.2 may possess other deformation modes that may contribute significantly and positively to overall seismic behavior.

3.3 Observations Related to Displacement-Based Design

Displacement-based seismic design, unlike force-based design, uses the non-linear behavior of a structure and changing stiffness and ductility and damping properties that occur with increased levels of top drift directly in the analysis procedure (Priestley et al. 2007). In the following sections, the degradation of wall stiffness and the changes to the equivalent viscous damping with increased levels of top wall drift will be presented.

3.3.1 Equivalent Viscous Damping

Within the context of displacement-based design, the effective level of damping generated by a RM structure is expected to increase with progressive yielding of reinforcement and the opening of cracks or crushing of grout and masonry. To estimate the damping properties of a quasi-statically loaded system, such as the current walls, Chopra (2007) provides a means to estimate the equivalent viscous damping of a dynamic system from the hysteric response of one displacement cycle under quasi-static loading by Eq. 3.1.

$$\zeta_{eq} = \frac{1}{4\pi}\frac{E_D}{E_s} \tag{3.1}$$

$$\zeta_{\Delta i} = \frac{1}{4\pi}\frac{E_{D\Delta i}}{Q \times \Delta \times 0.5} \tag{3.2}$$

Since hysteretic behavior is observed for all deformation types, the contributions of flexure, shear and base sliding to the overall equivalent viscous damping ratio ($\zeta_{\Delta i}$) can be determined with Eq. 3.2. Where the energy dissipated from one displacement cycle of the wall (E_D) can be divided into each of the deformation types ($E_{D\Delta i}$) and divided by the maximum strain energy of the equivalent elastic system (E_S). The peak load (Q) and displacement (Δ) are also defined here for each load cycle, rather than over the entire load history. The equivalent viscous damping of each wall is plotted in Fig. 3.8 against the idealized displacement ductility determined in Table 3.3. It is suggested by Priestley et. al (2007) that RM wall structures have similar damping properties to RC wall structures and both can typically assume 5% elastic damping that will increase with greater levels of displacement ductility as given by Eq. 3.3 and also plotted in Fig. 3.8. Overall, the simplification proposed by Eq. 3.3 offers a conservative estimate of the equivalent viscous damping of the statically loaded walls, which demonstrate similar behavior, characterized with a gradual increase in damping as yield strains in the reinforcement and cracking of the masonry increase.

$$\zeta_{eq} = 0.05 + 0.444\left(\frac{\mu_\Delta - 1}{\mu_\Delta \pi}\right) \tag{3.3}$$

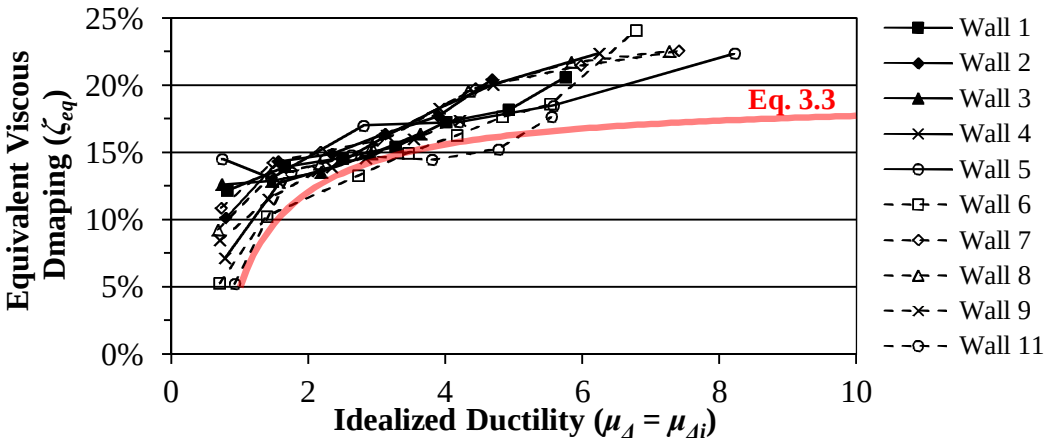

Figure 3.8 – Equivalent Viscous Damping of the Walls versus Idealized Displacement Ductility

Furthermore, the hysteresis loops generated by each of the deformation modes plotted in Fig. 3.6 indicates that hysteretic damping may also be possessed by each deformation mode, contributing to the overall wall behavior, which is plotted in Fig. 3.9.

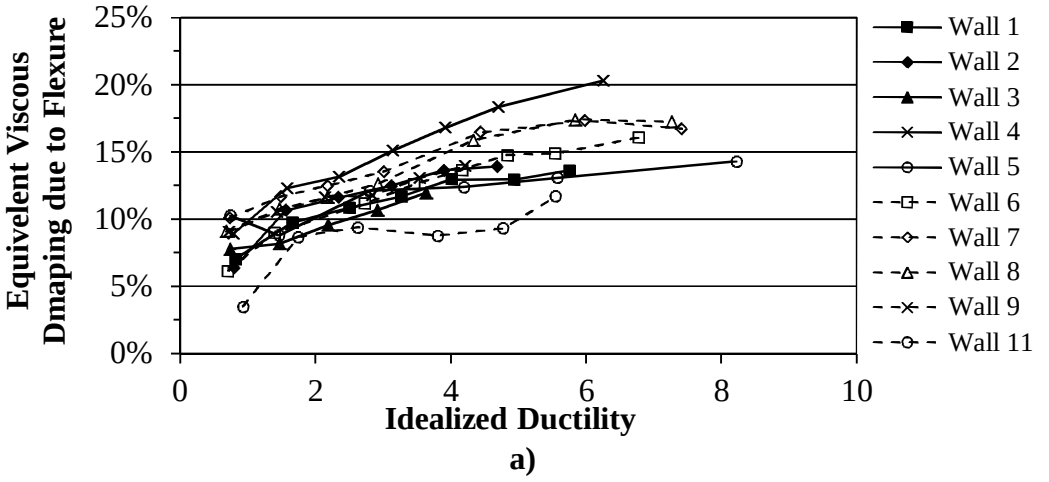

Figure 3.9 – Equivalent Viscous Damping Deformation Mode Contributions from: a) Flexure

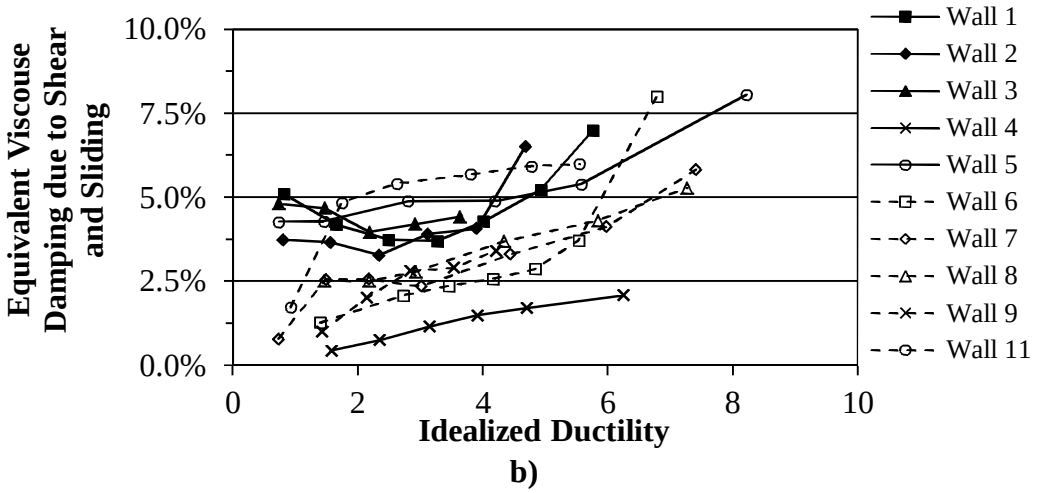

b)

Figure 3.9 Continued... – Equivalent Viscous Damping Deformation Mode Contributions from: b) Shear plus Sliding Deformations

Overall, flexure is the dominant contributor to the equivalent viscous damping at all ductility levels, for all walls, while contributions from shear and sliding deformations generally lie below ζ_{eq} = 10.0%. For instance, Wall 2 has the highest levels of damping attributed to flexure, however, it does not offer a significantly larger overall damping ratio over its load history compared to other walls. In fact, all walls demonstrated very similar overall damping behavior, and distinctive differences are apparent only when flexure versus shear and sliding deformations are considered.

3.3.2 Effective Stiffness Degradation

The use of an elastic or equivalent cracked stiffness for RC and RM structures to estimate the natural period of a structure will tend to be overly conservative when yielding of reinforcement and high levels of ductility are considered. To overcome this, the use of an effective secant stiffness ($K = Q/\Delta$) determined from the load-displacement response of the inelastic structure at the desired level of top displacement is suggested by Priestley et al. (2007) as a more accurate estimate of the effective (design) period for the structure. The values of K for each wall is based on the load-displacement response plotted in Fig. 3.10a against the top drift and Fig. 3.10b against the idealized displacement ductility.

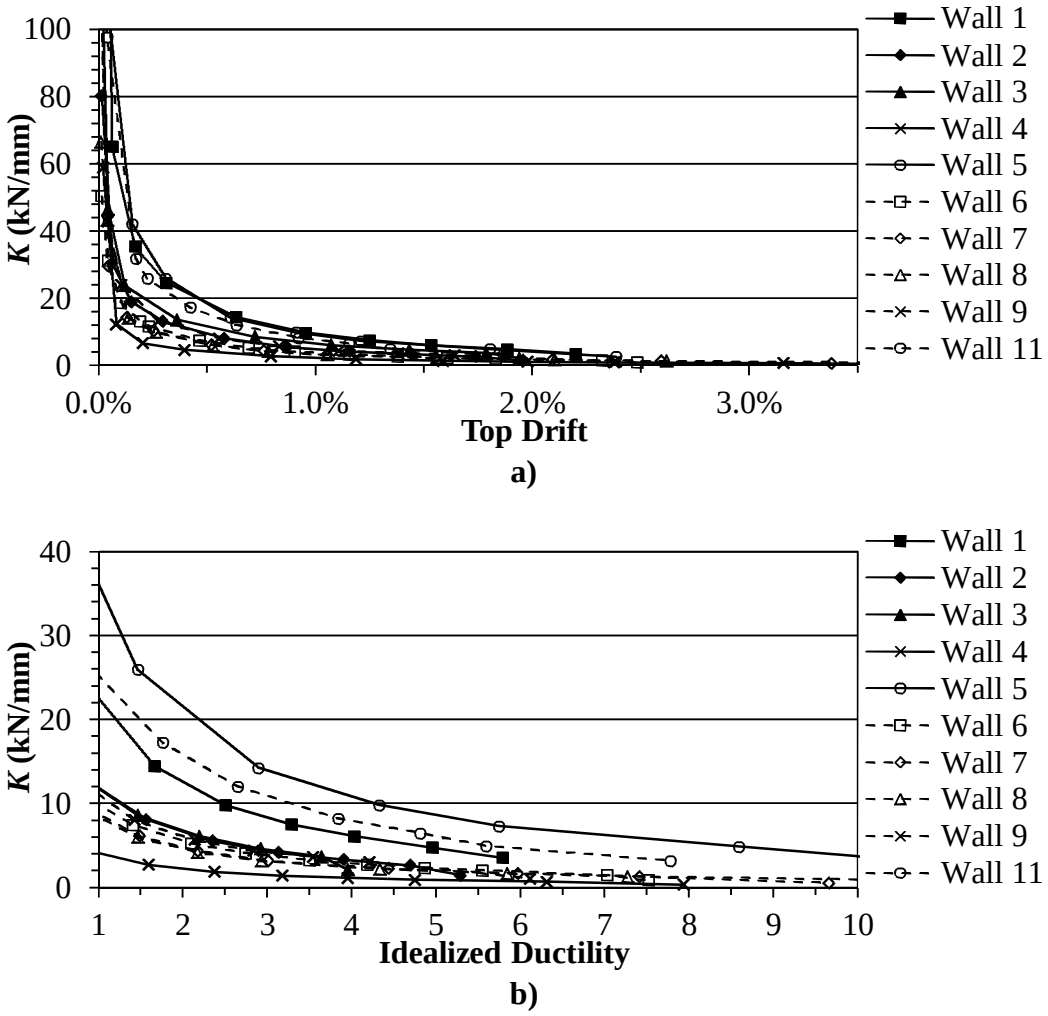

Figure 3.10 – Secant Stiffness Degradation of Walls versus: a) Top Drift and b) Displacement Ductility

It is clear that there is a significant reduction in stiffness of each of the walls relative to increased levels of top displacement. The Walls with the lowest aspect ratio, Walls 1, 5 and 11, possess the highest absolute levels of stiffness, while, Wall 4 which was the most slender, was the least stiff. This observation corresponds with elastic beam theory, and thusly, is also typically observed in seismic design with respect to the long periods of tall (slender) structures compared to the short periods of short (squat) structures. However, unlike elastic theory, Fig. 3.10 indicates that by the design level of ductility or drift, all walls have significantly degraded in stiffness, and also natural period.

3.4 Observations Related to Performance-Based Design

Wall 1: Minor horizontal cracking damage (< 2 mm) during the yield cycle appeared in the bed joints of the boundary elements extending up nine courses from the base. In addition, several stepped and straight-line diagonal cracks concentrated between the 2nd and 13th courses formed in the web of the wall during the Δ_{ye} displacement cycle. Cracks continued to form in this manner as depicted by the crack pattern in Fig. 3.11 until peak load was reached. During the 1st displacement cycle to a target displacement of Δ = ±35.9 ($\Delta_{\%}$ = ±1.89%), the first signs of face shell spalling were observed in the bottom two courses in the boundary elements at both wall toes. After the 2nd displacement cycle vertical cracking and spalling of the face shell exposed the vertical reinforcement and grout core causing a drop in strength. By the conclusion of the 2nd displacement cycle at Δ = ±35.9 mm ($\Delta_{\%}$ = ±1.89%) there was evidence that buckling of the outermost vertical reinforcement in both boundary elements was occurring. The buckling was localized between the base of the wall and the 1st lateral tie, although spalling of the face shell extended into the 2nd course of each boundary element as depicted by the photo inserts in Fig. 3.11. Crushing of the grout core and severe buckling of the reinforcement was observed in the 1st course of the boundary elements during the 1st displacement cycle at Δ = ±41.8 mm ($\Delta_{\%}$ = ±2.20%) as depicted by the photo insert in Fig. 3.11. While attempting a second displacement cycle at Δ = +41.8 mm ($\Delta_{\%}$ = +2.20%), crushing in the West toe spread into the web of the wall which caused a drop in strength and stability leading to the termination of the test.

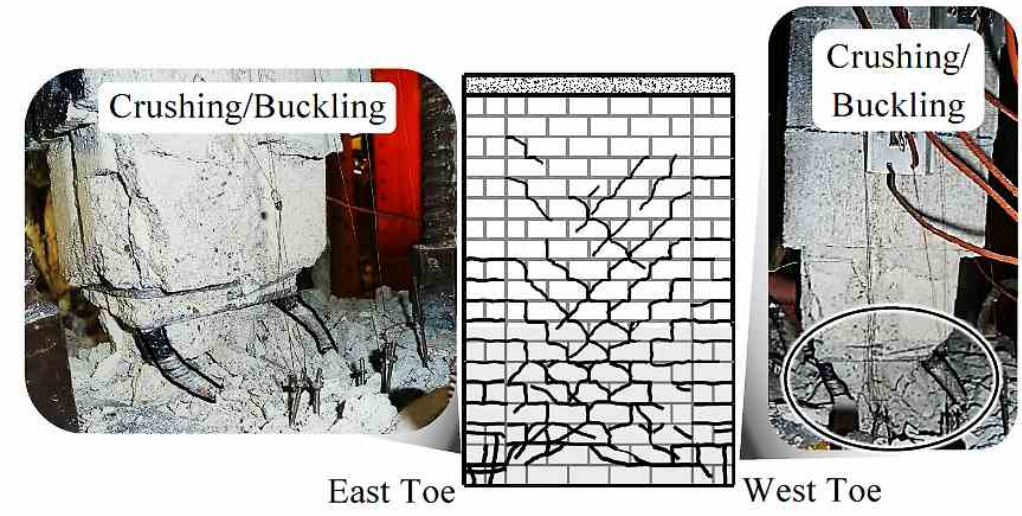

Figure 3.11 – Crack Pattern and Failure Mechanisms of Wall 1

Wall 2: The first signs of cracking damage was observed by the experimental yield displacement cycle and consisted of horizontal bed joint cracks (< 2 mm) in the boundary elements that spanned over nine courses and in the web of the wall over five courses. There were four major stepped and straight-line diagonal cracks in the web of the wall within the 1st storey as well. The crack pattern for Wall 2 is depicted in Fig. 3.12 and indicates that the spread of diagonal shear cracking up the wall appeared to be inhibited by the presence of the 1st floor slab. Failure mechanisms in Wall 2 initiated at Δ = +46.8 mm ($\Delta_{\%}$ = +1.76%) when the spalling of the face shell in the West toe boundary element penetrated the block, exposing the vertical reinforcement over the bottom two courses. Vertical cracks in the West toe became evident at this point but no crushing was observed. In the reversed direction of loading at Δ = -46.1 mm ($\Delta_{\%}$ = 1.73%) face shell spalling progressed to expose the grout core in the East toe boundary element, however, no significant loss of strength was observed. During the second displacement cycle to a target displacement of Δ = +46.8 mm ($\Delta_{\%}$ = +1.76%), crushing of the bottom two courses in the West toe began, which then spread into the web of the wall, as shown by the photo insert in Fig. 3.12. Loading in the West direction was stopped at this point due to the severe drop in strength, which left a significant residual drift of +44.0 mm ($\Delta_{\%}$ = +1.65%) in the wall. Loading in the reversed direction led immediately to crushing of the grout core and buckling of the vertical reinforcement in the East toe boundary element as depicted by the photo insert in Fig. 3.12. It was evident at this point that buckling of the exposed vertical reinforcement in the wall toes was causing out-of-plane displacements and a loss of overall wall stability.

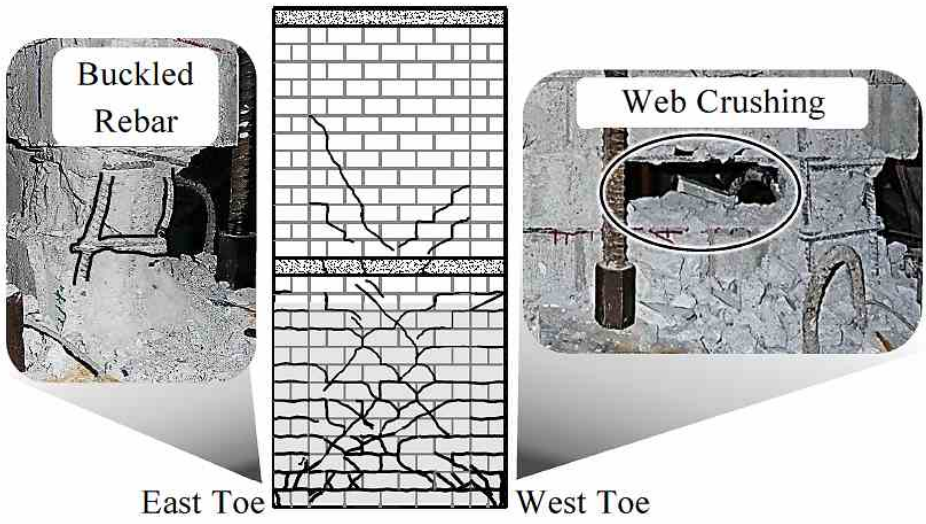

Figure 3.12 – Crack Pattern and Failure Mechanisms of Wall 2

Wall 3: The diagonal cracking damage observed in Wall 3 was substantially greater than that of Wall 2 over its load history as indicated by Fig. 3.13. Failure mechanisms in Wall 3 were observed to initiate during the second displacement cycles at Δ = ±47.4 mm ($\Delta_{\%}$ = ±1.78%). Spalling of the face shell in the bottom two courses of the boundary element in both wall toes penetrated to the grout core exposing the vertical reinforcement. While attempting to reach a target displacement of Δ = +57.2 mm ($\Delta_{\%}$ = +2.15%), crushing of the grout core and buckling of the vertical reinforcement in the West toe occurred, as shown by the photo insert in Fig. 3.13. Upon loading in the reversed direction, crushing of the East boundary element was observed over the 2nd and 3rd course, which spread into the web of the wall as depicted by the photo insert in Fig. 3.13. The test was terminated at this point due the buckling of vertical reinforcement in the web of the wall causing a drop in capacity and an overall loss of wall stability. The final crack pattern of Wall 3 is depicted in Fig. 3.13, and unlike Wall 2, shows that shear cracks were able to pass through the 1st storey slab, also depicted in Fig. 3.14. A similar effect was observed between Walls 7 and 9 which differed in level of applied axial load.

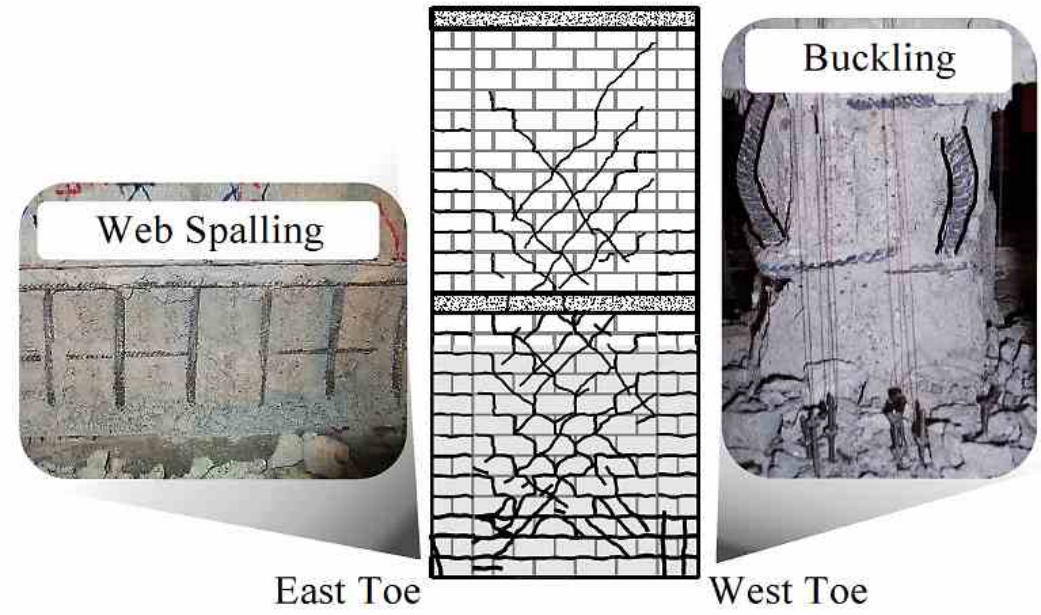

Figure 3.13 – Crack Pattern and Failure Mechanisms of Wall 3

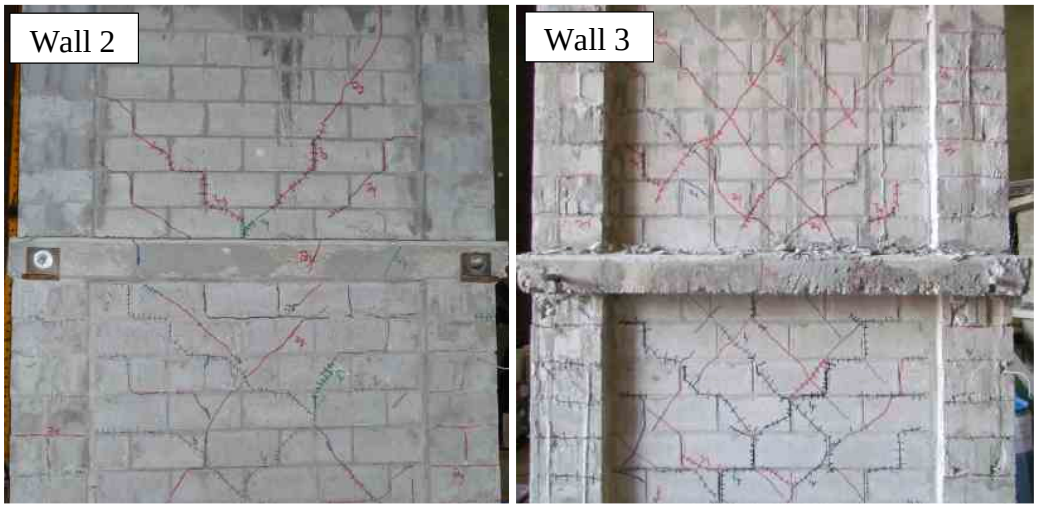

Figure 3.14 – Photos of Shear Crack Penetration in Walls 2 and 3

Wall 4: Initial cracking damage sustained at the yield cycle consisted of horizontal web cracks (< 2 mm) spread over six bed joints in the 1st storey and in two courses in the 2nd storey. Horizontal cracks in the boundary elements appeared in nine courses in the 1st storey. Cracking damage during increased top displacements were predominantly flexural in nature as indicated by Fig. 3.15. Failure mechanisms in Wall 4 initiated on the second displacement cycle at Δ = +125.9 mm ($\Delta_{\%}$ = +3.16%) in the form of face shell spalling as shown in Fig. 3.16. This was followed by crushing of the grout core and severe buckling of the vertical reinforcement within the East toe (depicted by the photo inserts in Fig. 3.15). While attempting the first cycle to a target displacement of ± 158 mm ($\Delta_{\%}$ = ±3.96%) one of the outermost vertical reinforcement bars in the East toe boundary element fractured at Q = +76.2 kN and Δ = +114 mm ($\Delta_{\%}$ = +2.86%). This led to crushing of the grout core and buckling of the vertical reinforcement in the West toe. At Q = +69.5 kN and Δ = +137.0 mm ($\Delta_{\%}$ = +3.43%) the second outermost vertical reinforcing bar in the East toe *fractured* (depicted in Fig. 3.15). At the target displacement of Δ = +158 mm ($\Delta_{\%}$ = +3.90%), the wall reached a Q = +57.3 kN (62% Q_u). Based on the photographic evidence shown in Fig. 3.15, the points where the reinforcement fractured was localized to where concentrated bends due to bar buckling was observed in the prior displacement cycle. Cycling the wall in the reversed direction caused crushing of the East toe, which spread into the web of the wall leading to the termination of the test. The cracking pattern of Wall 4 (depicted in Fig. 3.15) demonstrates small diagonal shear cracks throughout the 1st and, to a lesser extent, 2nd stories. Despite this, the high aspect ratio (A_R = 3.23) and observed behavior indicates a primarily flexural response of the wall. Also, unlike Wall 11, failure due to fracture of the rebar suggests that very high curvature demands were reached and a more fully developed plastic hinge mechanism was achieved.

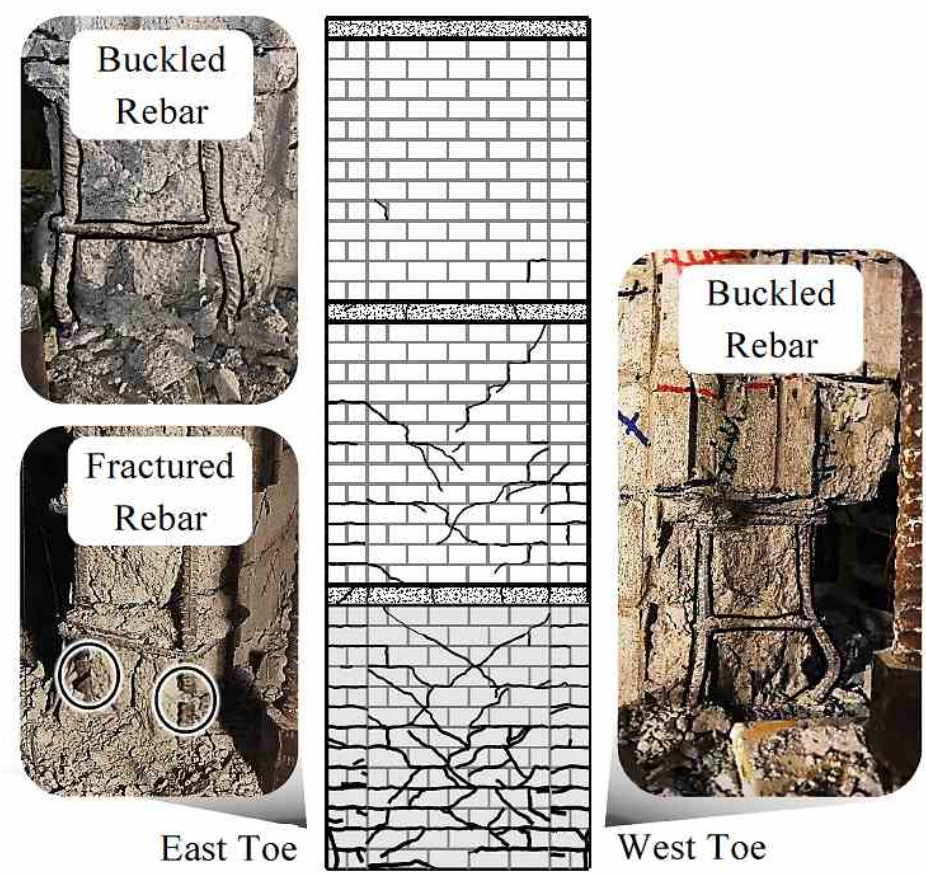

Figure 3.15 – Crack Pattern and Failure Mechanisms of Wall 4

Figure 3.16 – First Signs of Face Shell Spalling in Wall 4 ($\Delta_{\%}$ = +3.16%)

Wall 7: At Δ = ±105 mm ($\Delta_{\%}$ = ±2.63%) there was a minimal drop in capacity (4.2% in the West and 4.7% in the East) and the first vertical compression cracks appeared in the wall boundaries as shown in Fig. 3.17. Face shell spalling extended up to four courses high in the East and three courses high in the West wall toes, respectively, with the second displacement cycle. Large cracks and openings in the compression toes indicated that the block shell and the parts of the grout that lay outside the vertical reinforcement (confined region) in the boundary element were no longer effective in carrying compressive stress. The grouted core (area within the lateral ties) remained intact until buckling of vertical reinforcement started to become visible between the lateral ties during the second displacement cycle. Fracture of an outer bar in the East toe occurred at +100 mm top displacement. The fracture occurred at an equivalent top drift of +2.8% at the point on the rebar where signs of buckling were previously identified as indicated in Fig. 3.18. This resulted in a 27% drop in capacity to +106 kN at Δ = +147 mm ($\Delta_{\%}$ = +3.68%). The West toe of Wall 7 showed signs of compression failure characterized by crushing of the grouted core and severe buckling of vertical reinforcement between the wall footing and 1st lateral tie as indicated in Fig. 3.18. Upon load reversal, crushing failure of the East toe initiated at Δ = -98.5 mm ($\Delta_{\%}$ = -2.5%) followed by fracture of a single tension reinforcement bar at Δ = -116.5 mm ($\Delta_{\%}$ = -2.9%). Crushing of the grouted core and buckling of the vertical reinforcement was localized between the 1st and 2nd course lateral ties in the East toe with face shell spalling now extending to the 4th course and into the web of the wall. The lateral reinforcing ties displayed signs of deformation but did not fracture.

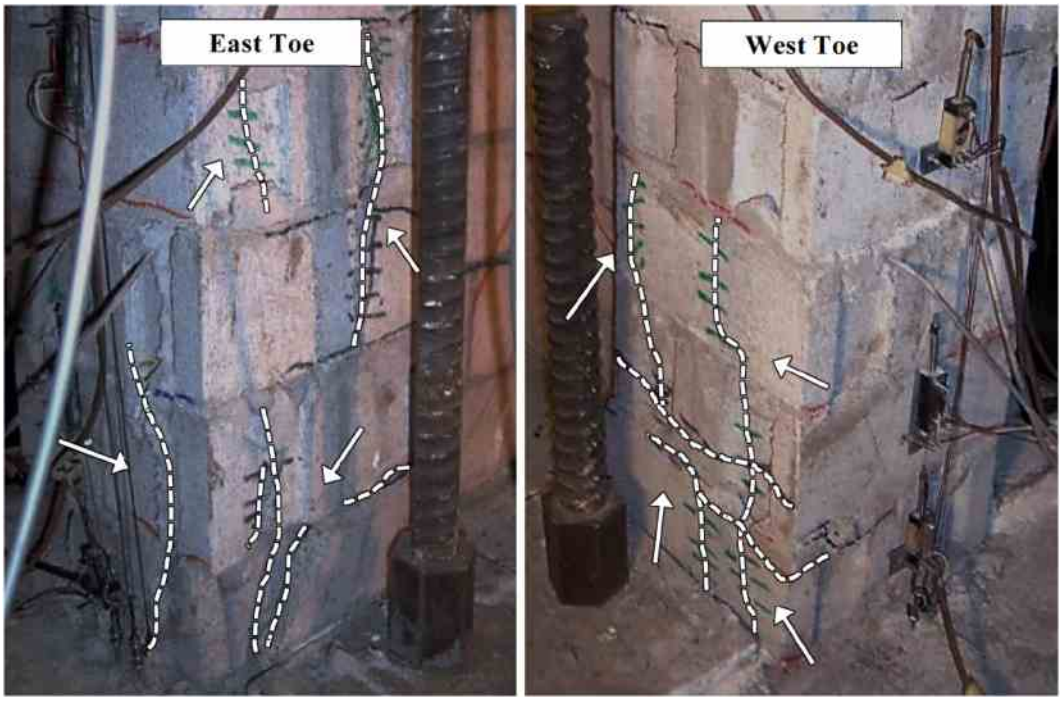

Figure 3.17 – Appearance of Vertical Cracking in Wall 7 ($\Delta_{\%}$ = ±2.63%)

Figure 3.18 – Eventual Fracture of Reinforcement and Failure of Wall 7 in East Toe (Left Photo: $\Delta_{\%}$ = -2.63% second cycle, Right Photo: $\Delta_{\%}$ = +3.68% first cycle, grout core removed)

Wall 8: The crack pattern of Wall 7 and 8 are presented in Fig. 3.19, and indicates that shear cracking was inhibited by the presence of the inter-storey slab in Wall 7, but allowed to propagate over the height of Wall 8. Overall, however, this did not result in a significant difference in strength or displacement characteristics. A small drop in capacity was observed at Δ = ±105 mm ($\Delta_{\%}$ = ±2.63%) in the East direction (135 kN) while the West direction experienced a marginal increase. Vertical cracking initiated during this displacement cycle in both the West and East toes as indicated in Fig. 3.20. Spalling of the face shells initiated on the second cycle (compared to the 1st cycle in Wall 7) at Δ = +105 mm ($\Delta_{\%}$ = +2.63%) and extended up four courses in the West toe and three courses in the East toe in a similar manner to Wall 7. At Δ = +147 mm ($\Delta_{\%}$ = +3.68%) buckling of vertical reinforcing bars around the intact grouted core became evident between ties over the bottom three courses in the West toe. In the reversed direction, a top displacement of only -72 mm ($\Delta_{\%}$ = -1.8%) was reached before crushing initiated in the East toe and spread into the web of the wall buckling a vertical reinforcing bar located in the web. Upon the 2nd cycle at Δ = +147 mm ($\Delta_{\%}$ = +3.68%) in the West direction the test was terminated as the opening and closing of cracks in the West toe initiated crushing which spread along the entire length of the specimen from both ends. Nevertheless, it should be appreciated that such excessive damage occurred at a very high level of drift (3.7%), well beyond any usable drift limit.

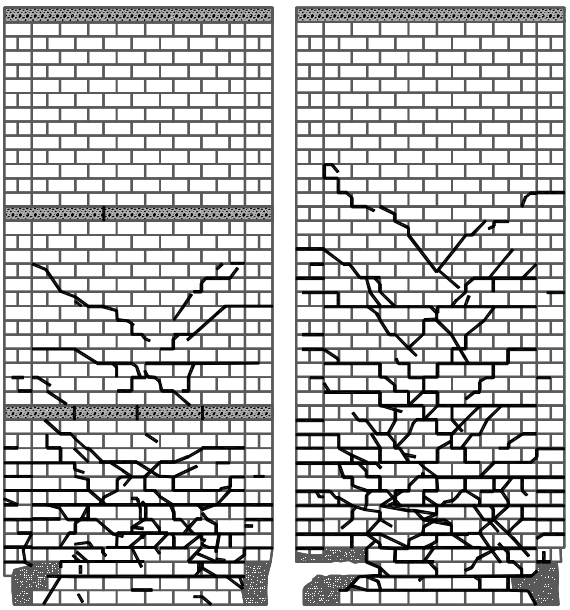

Figure 3.19 – Crack Patterns of Wall 7 and Wall 8 Illustrating the Influence of Inter-storey slabs on Crack Patterns

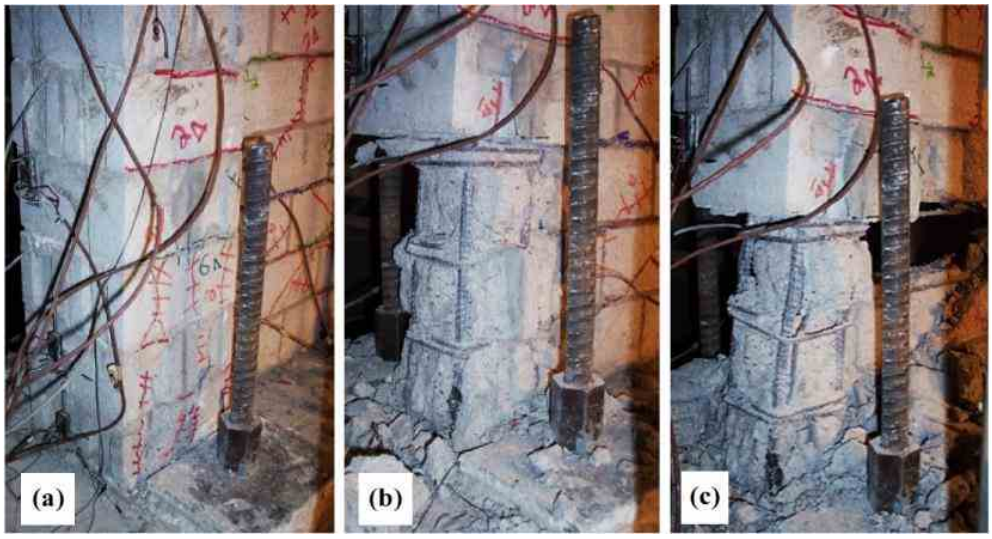

Figure 3.20 – Progression of Failure of East Toe in Wall 8: a) Vertical Cracks Observed ($\Delta_{\%}$ = -2.63%), b) Loss of Face shell in Tension ($\Delta_{\%}$ = +3.68% 2nd cycle), c) Final Failed State with Crushing in Web and Buckling of Confined Reinforcement

Wall 9: At Δ = ±33.0 mm ($\Delta_{\%}$ = ±0.83%) signs of vertical cracks appeared in both East and West toes extending over the bottom two courses. During the 2nd displacement cycle at Δ = ±44.0 mm ($\Delta_{\%}$ = ±1.10%) face shell spalling initiated in both compression toes with minimal loss of grout outside the confined core. Cycling Wall 9 at Δ = ±55.0 mm ($\Delta_{\%}$ = ±1.38%) continued to cause minor spalling of the face shell at both toes shown in Fig. 3.21 and resulted in the East side attaining its peak load. The peak load was sustained by Wall 9 in the West direction of loading to Δ = +66.0 mm ($\Delta_{\%}$ = +1.65%) and also coincided with the point when the vertical reinforcement first became exposed. At this displacement cycle the East toe maintained its resistance. By Δ = ±66.0 mm ($\Delta_{\%}$ = ±1.65%) both compression toes had sustained face shell spalling up to two courses in the West and three courses in the East exposing the vertical reinforcement and the lateral ties. Upon the second displacement cycle at $\Delta_{\%}$ = -1.65% in the East direction crushing of the exposed grouted core initiated in the East toe over the 2nd and 3rd course and extended into the web of the wall. Three vertical reinforcement bars in the East boundary element buckled between the 1st and 2nd lateral ties while one of the vertical bars buckled between the 2nd and 3rd ties. When cycling the wall in the reversed direction one bar fractured in the East toe at Δ = -35.1 mm ($\Delta_{\%}$ = -0.88%) and the other three boundary element reinforcement bars fractured at Δ = -44.8 mm ($\Delta_{\%}$ = -1.12%), each fracturing at the location where buckling was previously observed. The test was continued to Δ = +95.2 mm ($\Delta_{\%}$ = +2.4%) in the West where a lateral resistance of +104.2 kN (47% drop from the peak) was measured before concluding the test. Overall, the crack pattern of Wall 9, depicted

in Fig. 3.22, indicates that the higher shear force due to the greater axial load, caused shear cracks to penetrate through the inter-storey floor slab. This behavior is similar to that observed in Wall 8, rather than Wall 7, which possessed crack angles different than Wall 9 as well as less visible cracking in the 2nd storey.

Figure 3.21 – Initiation of Face Shell Spalling in Wall 9 ($\Delta_{\%}$ = ±1.38%) with Grouted Core Intact

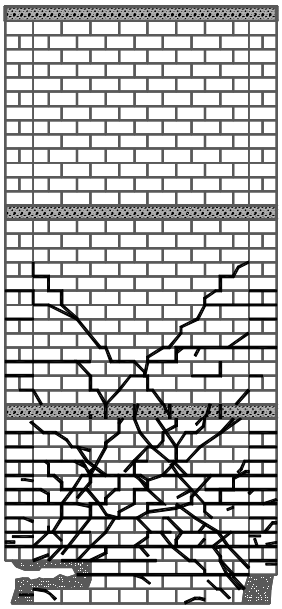

Figure 3.22 – Crack Pattern of Wall 9

Wall 10: Yielding of the outermost vertical reinforcement was first measured at the interface of the 2nd storey with the 1st floor slab in the flanged cross-section at a lateral load of 90 kN and Δ = +10.2 mm ($\Delta_{\%}$ = +0.25%) as well as -95 kN and Δ = -12.3 mm ($\Delta_{\%}$ = +0.31%). The measured yield load of the flanged section was an average of 5.1 kN (5.2%) less than the theoretical prediction. Yielding initiated in the steel within the boundary element in the 1st storey at a load of +100 kN indicated by the dashed line Q_y in Fig. 3.1, and Δ = +13.1 mm ($\Delta_{\%}$ = +0.33%) and -98 kN and Δ = -13.3 mm ($\Delta_{\%}$ = -0.33%) resulting in Δ_{ye} = 13.2 mm. Although yielding occurred in the 2nd storey at a lower drift than the 1st storey it was decided that subsequent cycling and analysis be based on the response of the wall-footing interface. The transition to a flanged boundary in the 2nd storey reduced the yield stiffness by 26% from Wall 7 and formed two distinct plastic hinge locations in Wall 10. Large diagonal and horizontal cracks formed with increased displacements concentrating in the upper half of the 1st storey and lower half of the 2nd storey indicating that plasticity was simultaneously spreading downward from the 2nd storey and upward from the 1st. The flanged cross-section displayed significant sliding and a wide opening (≈ 25 mm) formed between the 1st floor slab and the wall at peak loads as shown in Fig. 3.23. Curtailing vertical reinforcing bars in the slab appeared to fix the relative rotation of the slab to that of the 1st storey causing the concentration of sliding and flexural rotation at the interface between the flanged cross-section and the 1st floor slab.

A peak strength of Q_{ue} = +131 kN and -121 kN were recorded, respectively, at Δ = ±79 mm ($\mu_{\Delta e}$ = 6.0, $\Delta_{\%}$ = ±1.98%) as was indicated in Fig. 3.1. This measured peak lateral resistance was governed by crushing of the flanged cross-section and occurred at a lateral load that was 15.0% lower than that predicted theoretically for the capacity of the flanged cross-section. Vertical cracks appeared in the West flange and extended up to three courses above the 1st floor slab. Spalling also initiated at the East flange and extended up to two courses high from the 1st floor slab and formed a crack down through the slab itself as shown in Fig. 3.24. The West and East flange toes initially lost approximately half of the units' cross-sectional area due to bar buckling and spalling of the faces hell and grout, effectively reducing the wall length to approximately 1,700 mm. This reduction in length corresponds to the lower than predicted values for yield and ultimate loads that contributed to the formation of a second plastic hinge within the wall that ultimately governed failure. At Δ = ±105 mm ($\mu_{\Delta e}$ = 8.0, $\Delta_{\%}$ = ±2.63%) lateral resistances of +112 kN and -97 kN were recorded, respectively, representing a 14.5% and 19.8% drop from the peak capacity in both directions. The test was terminated after crushing spread into the web of the wall in the 2nd storey and buckling of web reinforcement became evident. As no confinement was offered by the flange to the vertical reinforcement, the former was unable to sustain large reversed inelastic strains without buckling.

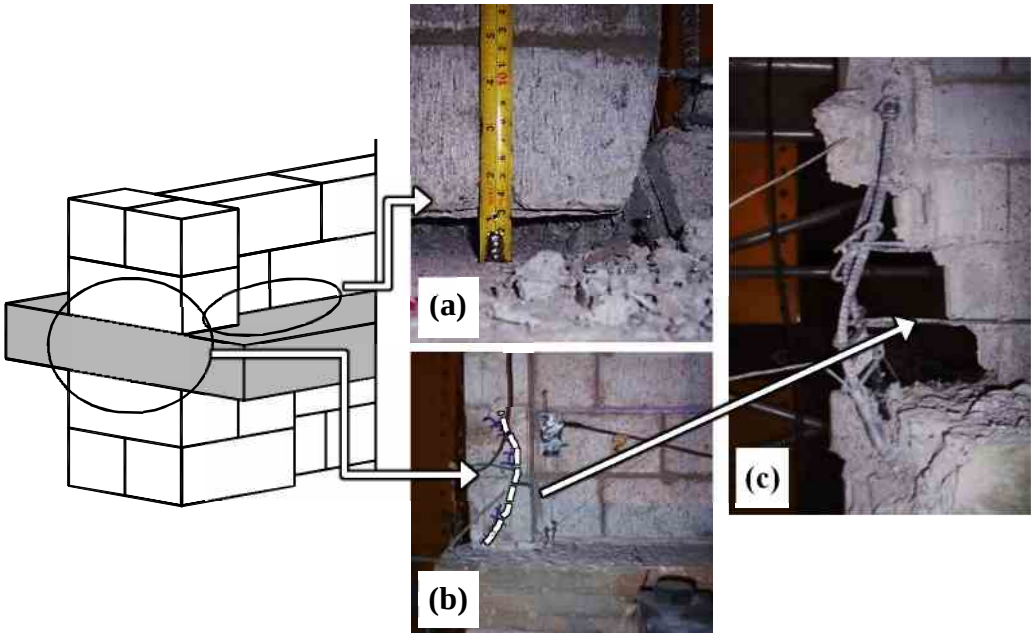

Figure 3.23 - Post-Failure of Wall 10: a) Rocking of above 1st Floor Slab, b) Vertical Cracking in Flange, c) Exposed Vertical Reinforcement Due to Buckling

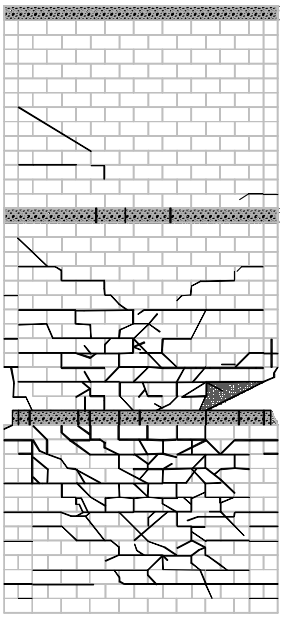

Figure 3.24 - Crack Pattern of Wall 10 at Failure

Wall 11: Initial cracking observed at the experimental yield displacement consisted of six hairline cracks (< 2 mm wide) which penetrated across the web of the wall. The cracks originated in the boundary elements and formed in a horizontal orientation in the bed joints indicating they were caused by flexural bending. The cracks that continued into the web of the wall transitioned into a diagonal orientation indicating inelastic shear deformations. Wall 11 was able to maintain a lateral resistance within 5% of Q_{ue} from Δ = ±16.9 mm ($\Delta_{\%}$ = +0.42%) to Δ = ±46.0 mm ($\Delta_{\%}$ = +1.15%) despite extensive diagonal cracks which penetrated up to the top course of the wall as depicted by the crack pattern in Fig. 3.25. Failure mechanisms in Wall 11 initiated at Δ = -53.4 mm ($\Delta_{\%}$ = -1.34%), when face shell spalling of the East toe occurred as shown in the photo insert of Fig. 3.25. The face shell *spalling* extended up the bottom two courses of the wall toes, exposing the boundary element reinforcement and stirrups. This led to *buckling* of reinforcement in the boundary element as shown in the photo insert in Fig. 3.25. During the second displacement cycle at Δ = -53.4 mm ($\Delta_{\%}$ = -1.34%), *crushing* of the grout core initiated which reduced wall strength to 60% of Q_{ue}. Loading in the reversed direction led to crushing of the grout core in the West toe which spread to *web crushing* of the wall, as indicated by the photo insert of Fig. 3.25. The subsequent loss of capacity and wall stability led to the termination of the test at this point. The distinct diagonal orientation of the crushed region in the West toe depicted by the photo insert in Fig. 3.25 suggests influence from a shear compression strut. However, the definitive failure mode of Wall 11 was by flexural yielding and subsequent buckling of reinforcement combined with crushing of the masonry and grout core.

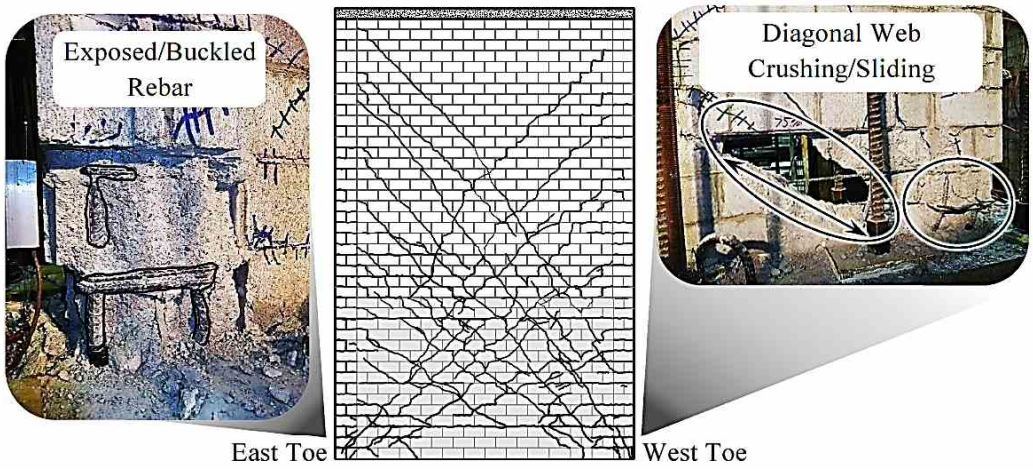

Figure 3.25 – Crack Pattern and Failure Mechanisms in Wall 11

3.5 Summary and Conclusions

The confined boundary element offers resistance against buckling of the vertical reinforcement and confinement of the grouted core. The appearance of vertical cracking, face shell spalling and exposure of the vertical reinforcement in the compression toes did not result in a decrease in strength or imply an imminent failure of the boundary element. Generally, failure (as defined previously) of each wall was instigated by crushing of the grouted core in combination with buckling of vertical reinforcement between ties and eventual fracture of the reinforcement. However, such failures occurred at very high top drift levels that ranged from 2.4% in Wall 9 to 3.7% in Wall 8. The investigated tie spacing, selected as one tie per course, offered the minimum level of resilience in the compression toes that could be improved upon by decreasing the tie spacing.

The cast-in-place RC floor slabs had a measureable effect on the propagation of cracking. Walls 7 and 8 demonstrated that the effect of altering the propagation of shear cracks inhibited the extent of inelastic curvature. In Wall 9, increased moment resistance, due to the increase in axial stress, caused the slab to crack at multiple points rendering it ineffective either in resisting the crack propagation in the wall or altering the crack inclinations. These results suggest that the cracking pattern of a wall is influenced by several factors including the presence and detailing of inter-storey slabs, the load conditions on the wall and the location and extent of the plastic hinge region.

Observations from walls governed by boundary element failure indicated that at the point of ultimate top displacement, the boundary element experienced face shell spalling and loss of grout outside the confined core but vertical reinforcement remained confined by the lateral ties. The performance of the boundary element for each of the walls was marked by an ability to delay the buckling of reinforcement as well as crushing of the grout core, such that the occurrence of face shell spalling in the compression toes did not correspond with an abrupt drop in resistance. Failure by fracture of the vertical reinforcement was observed in Walls 4, 7, 8 and 9, while failure of Wall 11 was precipitated by crushing of the web of the wall outside the boundary element. It is clear that the effectiveness of masonry wall confinement is strongly correlated to: the ability of the wall to fully develop its plastic hinge, the relative size of the flexural compression region to the boundary element as well as the contributions of shear stresses and deformations on the overall wall behavior. The walls tested, aside from Wall 4, possess very low aspect ratios when considering flexural wall design, since an A_R below 2.0 is typically considered squat, but each still demonstrated that a ductile flexural failure mechanism can be designed for and the boundary element is an effective means of confined the compression toe.

All walls were predominantly governed by flexural deformations; however the contribution from shear to the top wall displacement and equivalent viscous damping ratio indicate that shear deformations should be considered in analysis. The relative boundary element size to wall length appeared to play a critical role in the force-based response of Walls 1 and 11, respectively. Experimental (6.9 and 7.1) and idealized (6.4 and 5.8) ductilities did not differ significantly between the walls, although the manner by which each wall achieved this differed significantly. The ultimate curvature measured was greater for Wall 1 compared to Wall 11 (43.4 E-6 rad/mm versus 15.5 E-6 rad/mm), as was the ultimate drift (2.20% versus 1.55%), the extent of inelastic curvature (60.0% ℓ_w versus 53.1% ℓ_w) and the overall proportion of shear deformation to total top deformation (36.0% versus 15.8%). It is inferred from the failure mechanisms in Wall 11 that a shear compression strut combined with the relative small boundary element led to a web crushing failure, indicating that Wall 1 had an improved post-peak performance attributed to the relatively large boundary element it possessed. It is also inferred from crack patterns that the greater level of shear deformation sustained by Wall 11 could be linked to the larger shear crack spacing parameter based on the modified compression field theory. It is thus clear that shear deformations play a critical role in the overall wall response and that it would be prudent to consider size effects in calculations regarding shear stiffness and strength.

The effect of changing the aspect ratio between Walls 4, 2 and 1 (A_R = 3.23, 2.15 and 1.5) had a direct impact on the plastic hinge length. This was observed with the extent of inelastic curvature $\ell_{p\phi}$ = 100%, 87.9% and 60.0% of ℓ_w for Walls 4, 2 and 1, respectively. This in turn, result in a substantial levels of top drift ($\Delta_{80\%Que}$ = 3.36%) and $\mu_{\Delta ue}$ = 8.5 for Wall 4. Whereas, Walls 2 and 1 attained different drifts of = 1.78% and 2.20% as well as $\mu_{\Delta ue}$ = 6.0 and 7.1, respectively. It is inferred from the measured contributions from shear and sliding deformations, that Wall 1 was able to sustain a stable shear and base sliding response at levels greater than Wall 2, likely attributed to the higher shear forces. The implication of this would be that neglecting these effects, as is common within design, may lead to overly conservative predictions of actual behavior.

The increase in the reinforcement ratio from Wall 2 to Wall 3 resulted in an increase in top drift ($\Delta_{80\%Que}$ = 1.78% to 2.00%) however caused a significant drop in displacement ductility ($\mu_{\Delta ue}$ = 6.0 to 5.5 and $\mu_{\Delta i}$ = 4.8 to 4.0), respectively. Although Wall 3 gained an increase in Q_{ue} over Wall 2 by 36.9% this also caused an increase to Δ_{ye} by 23.0%. It can be inferred from the observed difference in crack patterns and measured proportion of shear deformation between the walls (10.9% for Wall 2 and 24.0% for Wall 3) that in a similar way that the responses of Wall 1 and 2 differed from flexural theory due to shear contributions, so did the responses of Walls 2 and 3.

In the following Chapter, a thorough analysis of the results and observations presented here will be provided with respect to force-, displacement and performance-based seismic design parameters.

3.6 Notation for Chapter 3

A_R = height-to-length aspect ratio of wall;
E_D = energy dissipated from one full hysteretic loop (kN×mm);
$E_{D\Delta i}$ = energy dissipated from an isolated deformation type (kN×mm);
E_S = peak strain energy from an equivalent elastic system (kN×mm);
K = experimental secant stiffness of the load-displacement envelope (kN/mm);
K_{cre} = experimental tangential stiffness of a cracked wall (kN/mm);
K_{ge} = experimental uncracked tangential stiffness of a wall (kN/mm);
K_{ye} = experimental secant yield stiffness of wall (kN/mm);
ℓ_b = Length of confined boundary element (mm);
ℓ_{pe} = experimental extent of inelastic curvature;
$\ell_{p\phi}$ = experimental plastic hinge measured as extent of inelastic curvature;
ℓ_w = length of wall (mm);
Q = lateral load applied to a wall (kN);
Q_{ue} = experimental peak load (kN);
Q_{ye} = experimental yield load (kN);
Δ = top displacement of a wall (mm);
Δ_{Que} = the top displacement at the peak lateral load (mm);
$\Delta_{80\%Que}$ = experimental top drift of wall at 80% of peak load (%);
Δ_{ye} = experimental yield drift of wall (%);
Δ_y* = idealized yield displacement of wall (%);
$\Delta_{\%}$ = top drift measured as the top displacement divided by the all height (%);
ζ_{eq} = equivalent viscous damping given as a percent of critical;
$\zeta_{\Delta i}$ = equivalent viscous damping of an isolated deformation type;
μ_Δ = displacement ductility used to calculate damping taken as $\mu_{\Delta i}$;
$\mu_{\Delta e}$ = experimental displacement ductility;
$\mu_{\Delta Que}$ = experimental displacement ductility at peak lateral load;
$\mu_{\Delta ue}$ = experimental displacement ductility at 80% peak lateral load;
$\mu_{\Delta e1\%}$ = experimental displacement ductility 1% drift;
$\mu_{\Delta i}$ = idealized displacement ductility of wall;
$\mu_{\Delta i1\%}$ = idealized displacement ductility of wall at 1% drift;
ϕ = average curvature measured along the height of each wall (rad/mm);
ϕ_{ye} = experimental yield curvature of wall (rad/mm).

3.7 References for Chapter 3

Banting, B. R. and El-Dakhakhni, W. W. (2012). "Force- and Displacement-Based Seismic Performance Parameters for Reinforced Masonry Structural Walls with Boundary Elements." *ASCE Journal of Structural Engineering* Vol. 138(12), 1477-1491

Banting, B. R. and El-Dakhakhni, W. W. (2013). "Seismic Performance Quantification of Reinforced Masonry Structural Walls with Boundary Elements." Submitted to *ASCE Journal of Structural Engineering*, Accepted with Minor Revisions for 2nd Round of Review Feb. 11, 2013.

Chopra, A., K. (2007). *Dynamics of Structures: Theory and Applications to Earthquake Engineering*. 3ed., Pearson Prentice Hall, Upper Saddle River, New Jersey, USA.

Massone, L., M., and Wallace, J., W. (2004). "Load-deformation responses of slender reinforced concrete walls." *ACI Structural Journal*, 101(1), 103-113.

National Building Code of Canada: Institute for Research in Construction (NBCC). (2010). *National Building Code of Canada 2010*. National Research Council of Canada, Ottawa, Canada.

Priestley, M. J. N., Calvi, G. M., and Kowalsky, M. J. (2007). *Displacement-Based Seismic Design of Structures*, IUSS Press, Pavia, Italy.

Shedid, M. T., Drysdale, R. G. and El-Dakhakhni, W. W. (2008). "Behavior of fully grouted reinforced concrete masonry shear walls failing in flexure: experimental results." *J. Struct. Eng.*, 134(11), 1754-1767.

Shedid, M. T., El-Dakhakhni, W. W. and Drysdale, R. G. (2010a). "Alternative strategies to enhance the seismic performance of reinforced concrete-block shear wall systems." *J. Struct. Eng.*, 136(6), 676-689.

Shing, P., B., Schuller, M., and Hoskere, V., S. (1989). "In-plane resistance of reinforced masonry shear walls." *J. Struct. Eng.*, 116(3), 619-640.

Tomaževič, M. (1999). "Seismic resistance verification of structural walls" *Earthquake-Resistant Design of Masonry Buildings*, Imperial College Press, London, 127-141.

Vecchio, F. J., Collins, M. P. (1986). "The modified compression-field theory for reinforced concrete elements subjected to shear." *ACI Journal*, 83(2), 219-231.

CHAPTER 4: ANALYSIS OF WALL TEST DATA

4.1 Introduction

In this chapter analysis is presented from the experimental program and results Chapters 3 and 4 for masonry walls possessing confined boundary elements. The information in this chapter is the sole work of the author with Dr. El-Dakhakhni acting in an advisory and editorial role to prepare the manuscript for journal submission. This chapter consists primarily of information from a single journal article that has been integrated together with some analysis presented in the articles for which the previous chapters were based on. This was done with the intention of providing better flow within the context of a thesis. The information contained in this chapter can be found in:

Banting, B. R. and El-Dakhakhni, W. W. (2012). "Seismic Design Parameters for Special Masonry Structural Walls Detailed with Confined Boundary Elements." Submitted to *ASCE Journal of Structural Engineering* Dec. 12, 2012.

4.2 Comparison with Experimental Strengths and Displacements

The experimental results related to the strength, displacements and curvature of the walls tested were provided in Tables 3.1 and 3.2, and were presented in terms of an average taken from both directions of loading on each wall. Theoretical predictions for wall strength and displacement at yield were also given in Table 2.3, which are subsequently compared with the experimentally measured values and plotted in Fig. 4.1 as a ratio between the experimental result and the theoretical prediction. Despite the influence of shear and sliding deformations, not considered in theoretical predictions, a good overall agreement is observed with respect to the ratio of yield strengths Q_{ye}/Q_y = 104% (coefficient of variation (c.o.v.) = 7.3%) and displacements Δ_{ye}/Δ_y = 104% (c.o.v. = 12.5%). Whereby, Wall 1 was omitted from the average displacement calculation due to its exceptionally high yield displacement (Δ_{ye}/Δ_y = 164.5%) caused by a high proportion of sliding displacement. Walls 5 and 6 are included for comparison purposes but are derived from information presented by Shedid et al. (2010).

With respect to the ultimate conditions possessed by the Walls, Fig. 4.1 presents a comparison between the average experimental peak lateral resistance for the walls (Q_{ue}) (given in Table 3.1) to the theoretical strength predictions (Q_u) (given in Table 2.3). An average ratio of peak strength Q_{ue}/Q_u = 100% (c.o.v. = 6.7%) is determined, validating the assumption that the tied vertical reinforcement is

effective in carrying compression stresses as stated in Chapter 2. By contrast, neglecting compression steel would result in a Q_{ue}/Q_u = 108% (c.o.v. = 7.8%). The average curvatures (ϕ_{ue}) in the walls were presented in Table 3.2 based on measurements corresponding to a distance equal to ℓ_w and $\ell_w/2$ above the wall base. This height is chosen because it is indicative of where the effective plastic hinge would be assumed to extend for the purpose of the predictive design expressions development. The measured top drifts associated to where the peak lateral strength was maintained to (allowing for a 3% variation from Q_{ue}) were given in Table 3.1 as Δ_{Que}. The most accurate estimates of theoretical top drift at the peak load are shown in Fig. 4.1. The first prediction of top drift selected was estimated with $\ell_p = \ell_w$ and ε_{mu} = 0.004 and was represented as $\Delta_{u0.004}$ in Table 3.1. The ratio between the experimental and theoretical drifts is indicated in Fig. 4.1 with an average of $\Delta_{Que}/\Delta_{u0.004}$ = 113% (c.o.v. = 17.9%). By contrast, adopting the reduced plastic hinge of $\ell_p = \ell_w/2$ and a limiting strain of ε_{mu} = 0.006 yielded a better average with greater scatter relative to the experimental data as indicated in Fig. 4.1 with $\Delta_{Que}/\Delta_{u0.006}$ = 111% (c.o.v. = 26.8%). Finally, adopting the plastic hinge expression of $\ell_p = \ell_w/2 + 0.1\ h_w$ yielded the least accurate results relative to the experimental data as indicated in Fig. 4.1 with $\Delta_{Que}/\Delta_{u0.004}$ = 120% (c.o.v. = 20.3%). Clearly, there is a significant amount of variation in the ratio of predicted to experimental wall behavior. As such, in the following sections, a new method of estimating the effective plastic hinge will be developed and validated with the experimental data. However, in the next section the effect of shear spread of plasticity and its relationship to degrading shear strength, plastic hinge development and overall displacement ductility will be considered.

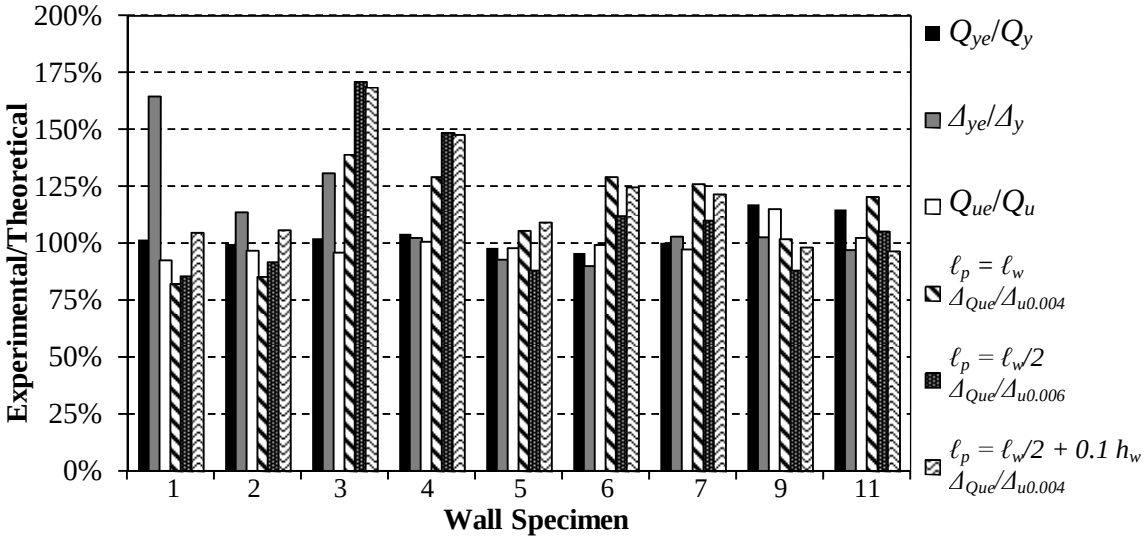

Figure 4.1 – Ratio of Experimental to Theoretical Predictions for Strength and Displacement

4.3 Shear Strength Degradation Effects on Flexural Walls

As part of this analysis the effect that increased levels of displacement ductility can have on the shear strength of masonry is quantified based on the relationship proposed by the ATC-6 document related to seismic design of bridge columns (ATC 1981) and later described by Priestley et al. (1996). It has been recognized for RC design that within the highly strained plastic hinge region of beams, columns or walls, there will be progressive widening of cracks and damage along the shear interface such that concrete is no longer effective at transmitting shear stresses via aggregate interlock. This may lead to a premature shear failure in flexurally controlled walls even when full flexural strength is reached. Such ductility-based modification factors to the masonry component of shear resistance have been adapted for use with masonry design of shear-critical walls (Voon and Ingham 2006; Davis 2008). However, these values have been determined through empirical curve fitting with experimental data of RM walls dominated by shear mechanisms. In Chapter 5 a derivation will be presented which considers the anisotropy and material characteristics of RM structural walls to estimate the angle of shear cracking. The Normal Strain-adjusted Shear Strength Expression (NSSSE) that is provided in Chapter 5 is shown here with regard to estimating the shear strength degradation effects in flexural walls undergoing plastic hinging. By applying the NSSSE approach the shear strength can be directly related to the normal strain (ε_n) determined from curvature measurements of each wall at the critical shear location in the plastic hinge, corresponding to a distance of $d_v/2$ above the base, where d_v is taken as the effective shear depth of the section, taken as the distance between the centroid of boundary elements as indicated in Eq. 4.1.

$$\varepsilon_n = \phi_{dv/2}\left(\ell_w/2 - c\right) \tag{4.1}$$

The shear resistance (V) can thus be estimated with Eq. 4.2 from the crack inclination angle (θ) given in Eq. 4.3 and the masonry compression strut contribution factor (β) given in Eq. 4.4 which will be derived in Chapter 5:

$$V = \beta\sqrt{f'_m}\,b_w d_v + A_s f_y \frac{d_v \tan\theta}{s_h} \tag{4.2}$$

$$\theta = \left(\frac{2000J + 4000 - \lambda}{50(18J + 75)}\right)\left(\frac{50}{\left(1 + 220\varepsilon_n\right)}\right) \tag{4.3}$$

$$\beta = \left(\frac{4000J + 2000 - \lambda}{500(3.5J + 1.5)}\right)\left(\frac{1}{4\left(1 + 1800\varepsilon_n\right)}\right) \tag{4.4}$$

Where b_w is taken as the width of the web (mm), s_h is the vertical spacing between horizontal reinforcing bars (mm), A_s is the area of horizontal reinforcement (mm^2), f_y is the yield strength of horizontal reinforcement (MPa) the factor J accounts for differences between constituent material strengths and assemblage compressive strength and λ is a crack spacing factor.

Walls 1 and 11 are considered here for analysis because each Wall possesses an aspect ratio (A_R) of 1.5, and thus shear forces would most likely govern behavior. In addition, Walls 1 and 11 do not possess inter-storey floor slabs that would cross a shear crack and potentially act to strengthen the wall.

The shear strength envelope for Walls 1 and 11 is given in Fig. 4.2 which is also plotted on the same axis as the experimentally recorded load-displacement envelope. Because each wall was over reinforced for shear, the shear compression failure limit adopted as $0.15f'_m b_w d_v$, described in Chapter 5, governed the shear envelope as indicated by the horizontal line in Fig. 4.2. However, as normal strains increased with increased plastic curvature, the effective shear crack angle becomes smaller, further reducing the effectiveness of reinforcement and compression strut, reducing the shear strength. Solid and dashed lines shown in Fig. 4.2 represent the shear strengths considering the contributions of the masonry and reinforcement (solid line) and the reinforcement alone (dashed line). The intersection between the shear envelope and the hysteresis loop would indicate the point where a shear failure would be expected to occur. Fig. 4.2 suggests the potential for shear failures at very high drifts for both walls, which was confirmed from observations made during the testing of both walls in Chapter 3 which indicated that increased sliding and shear deformations coincided with a significant drop in resistance. Fig. 4.2 also depicts the measured increase in shear and sliding displacements as a percentage of the total top displacement plotted along the secondary vertical axis. From both walls there is a noticeable trend of increased shear and sliding displacements when the shear strength envelope moves closer to the hysteresis loops. However, as also observed during testing, intersection of the flexural strength envelope of the walls with the shear strength envelope does not necessarily result in a diagonal tension shear failure, since the flexural capacity also degrades at high drifts when spalling and crushing commences.

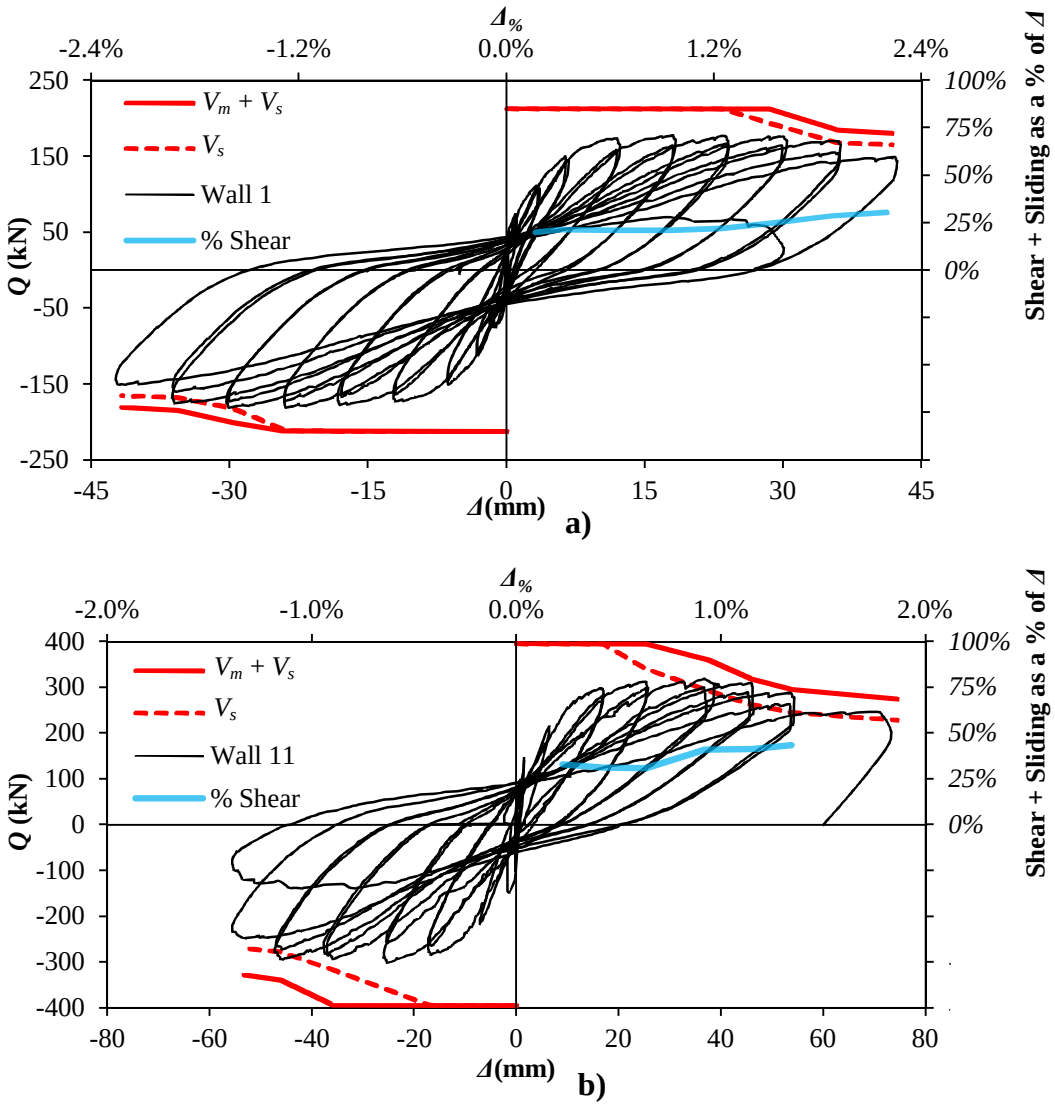

Figure 4.2 – Shear Strength Envelopes for: a) Wall 1 and b) Wall 11: (Primary Axis) also Indicating the Increase in Shear plus Sliding Displacement as a Percent of Top Drift (Secondary Axis)

4.4 Effective Elastic Stiffness

Force-based design relies on the assumption that seismic loads attracted by an elastically behaving structure can be reduced for a substitute structure possessing the same initial stiffness but a reduction in strength if the latter still possess the same displacement capacity. The theoretical elastic stiffness (K_{gt}), and thus natural period, of a structure is dependent of the stiffness of individual walls that comprise the SFRS. The elastic stiffness of a cantilever RM wall subject to a point

load at its top considering both flexure and shear deformations can be determined according to Eq. 4.5.

$$K_g = \frac{1}{\frac{h_w^{\ 3}}{3E_m I_e} + \frac{kh_w}{0.4E_m A_e}} \tag{4.5}$$

Whereby, I_e is the effective moment of inertia of the wall reduced from the gross member properties (I_g) such as to consider the effects of cracking (m^4), E_m is the Young's modulus of the masonry in MPa, A_e is the effective area of the member (m^2), reduced from the effective gross area (A_g) in shear when cracking occurs (m^2), and k is a shape factor accounting for the distribution of shear stresses across a cross section. The value of k is typically taken as 1.2 for rectangular cross-sections, however, none of the walls tested meet this criteria. Therefore, adopting Hooke's law and assuming an isometric elastic material, k can be estimated with Eq. 4.6.

$$k = \frac{A_g}{I_g^{\ 2}} \iint \frac{Q_m^{\ 2}}{t^2} dxdz \tag{4.6}$$

Where, Q_m is the first moment of area and t is the width of the cross-section. Since Q_m and t are discontinuous along the wall cross-section due to the protruding boundary elements, solution to the double integral in Eq. 4.6 becomes quite cumbersome. Nevertheless, k can be solved for with Eq. 4.6 as 1.44, 1.35 and 1.29 for wall lengths of 1,235 mm, 1,805 mm and 2,660 mm, respectively. The theoretical gross section stiffness for flexure (K_{ft}) and shear (K_{st}) are given in Table 4.1 along with the total theoretical elastic stiffness (K_{gt}) determined from Eq. 4.5. Furthermore, a simplified approach to estimate the reduced cross-section stiffness is suggested by both Paulay and Priestley (1992) and the Canadian concrete structures design code CSA A23.3 (CSA 2004) based on the gross-section properties. The former suggests a reduction factor (α) given by Eq. 4.7 while the latter is based on an upper and lower bound of α given by Eqs. 4.8 and 4.9, respectively, where $I_e = \alpha I_g$ and $A_e = \alpha A_g$.

$$\alpha = \left(\frac{100}{f_y} + \frac{P_a}{f'_m A_g} \right) \tag{4.7}$$

$$\alpha = \left(0.6 + \frac{P_a}{f'_m A_g} \leq 1.0 \right) \tag{4.8}$$

$$\alpha = \left(0.2 + 2.5\frac{P_a}{f'_m A_g} \le 0.7 \right) \tag{4.9}$$

Whereby, the yield strength of the vertical reinforcement (f_y) is given in MPa, the total applied axial load on the wall (P_a) is given in MN and the compressive prism strength of the masonry (f'_m) is given in MPa and the gross area of the wall cross-section (A_g) is given in m^2. The theoretical stiffness of the cracked section representing an effective yield stiffness (K_{yt}) is determined with Eq. 4.7 ($K_{y4.7}$), 4.8 ($K_{y4.8}$) and 4.9 ($K_{y4.9}$)for each wall is presented in Table 4.1, with Wall 10 omitted due to the failure mechanism occurring outside of the confined boundary element and results of Walls 5 and 6 derived from information reported by Shedid et al. 2010 and shown for comparison purposes.

Table 4.1 – Effective Elastic Stiffness

	Wall 1	**Wall 2**	**Wall 3**	**Wall 4**	**Wall 5**	**Wall 6**	**Wall 7**	**Wall 8**	**Wall 9**	**Wall 11**
	Stiffness in kN/mm									
K_{gt}	72.1	31.3	31.3	10.4	105	30.2	28.4	28.4	28.4	65.8
K_{st}	219.6	156.8	156.8	104.6	320.7	169.8	159.4	159.4	159.4	218.7
K_{ft}	107.4	39.1	39.1	11.6	156.2	36.8	34.5	34.5	34.5	94.1
$K_{y4.7}$	18.6	8.1	8.1	2.7	27.0	7.8	6.5	6.6	8.5	17.0
$K_{y4.8}$	47.5	20.6	20.6	6.9	69.0	19.8	17.9	18.0	19.8	43.3
$K_{y4.9}$	24.9	10.8	10.8	3.6	36.0	10.3	7.8	8.0	12.6	22.7

Based on a comparison of the experimentally measured stiffness reported in Table 3.3 with theoretical values given in Table 4.1, the following conclusions can be made. The average ratio of experimental stiffness K_{ge} to theoretical stiffness K_{gt} is determined as K_{ge} / K_{gt} = 1.44 (c.o.v. = 36.3%), representing a significant variation between observed and predicted stiffness of the walls prior to cracking. However, it is speculated that this likely due to the sensitivity of the instrumentation used to measure lateral displacements as well as the difficulty in establishing when cracked behavior occurs. Nevertheless, the use of Eq. 4.9 proved to be an accurate means of estimating the effective yield stiffness, yielding a ratio of $K_{ye}/K_{y4.9}$ = 1.21 (c.o.v. = 10.3%) which is reasonable for 'back of the envelope' calculations given the simplification of the approach. By normalizing the lateral stiffness degradation (K) presented in Chapter 3.3.2 by the theoretical yield stiffness $K_{y4.9}$, further defined simply as K_y, scatter in the behavior of the walls is significantly reduced, as evidenced by Fig. 4.3a for wall drift, and in Fig. 4.3b for the idealized ductility.

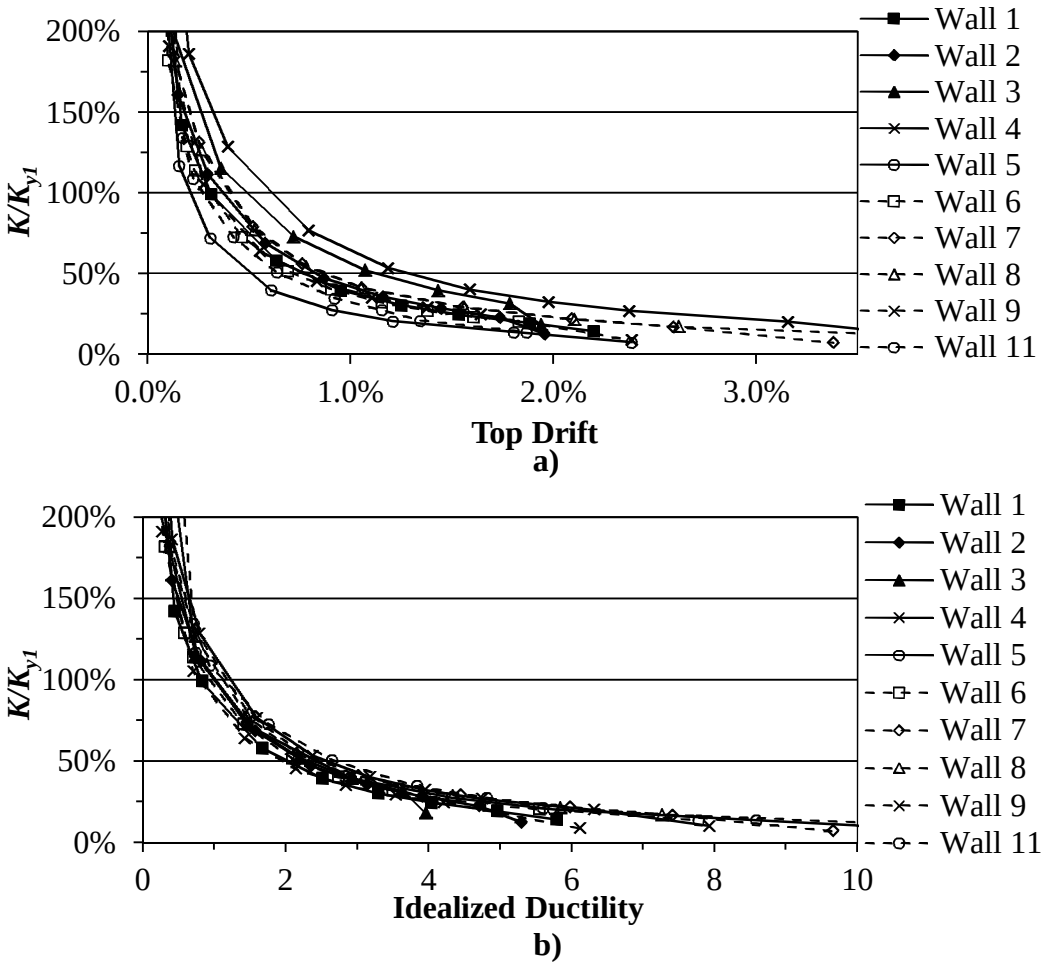

Figure 4.3 – Normalized Experimental Stiffness (*K*) by Theoretical Yield Stiffness versus: a) Top Drift and b) Idealized Displacement Ductility

4.5 Effective Yield Displacement

The experimentally measured yield displacement (Δ_{ye}) was presented in Table 3.1 and the idealized yield drift (Δ_y*) based on the definition offered by Priestley et al. (2007) was given in Table 3.3. For design purposes and initial wall sizing, it is useful to have an estimate of the yield drift without requiring the extraneous work of conducting a thorough push-over analysis needed to solve for Δ_y* when experimental data is not available. Therefore, three theoretical values for the idealized yield drift, necessary for ductility calculations, are proposed in this section.

The first simplified estimate of Δ_y*, referred to as Δ_{y1}*, can be arrived at based on the secant yield stiffness, K_{y1}, which passes through the experimental yield drift at

load Q_{ye}. On average, the ratio of Q_{ye}/Q_{ue} = 75% (c.o.v. = 5.5%), such that Δ_{y1}* can be solved for with the theoretical yield stiffness and theoretical ultimate strength, Δ_{y1}* = Q_u/K_{y1}, as given in Table 4.2. This gives a reasonable and conservative estimate of the yield drift, with an average ratio of Δ_y*/Δ_{y1}* = 92.1 % (c.o.v. = 16.1%).

Alternatively, Priestley et al. (2007) provides an even simpler means to estimate Δ_y* based on a yield curvature equal to $2.10\varepsilon_y/\ell_w$, where ε_y is the yield strain of the vertical reinforcement of 0.0025. The resulting idealized yield drift is thus determined as Δ_{y2}* and given in Table 4.2 with a resulting ratio of Δ_y*/Δ_{y2}* = 101.0 % (c.o.v. = 19.5%). The final estimate of Δ_y* given in Table 4.2 is based on the theoretical yield drift (Δ_y) given in Table 2.3. Whereby, an idealized yield drift (Δ_{y3}*) is determined by dividing Δ_y by the ratio of Q_{ye}/Q_{ue} = 75%, resulting in Δ_y*/Δ_{y3}* = 112.6 % (c.o.v. = 17.5%).

In conclusion, for the extra effort required to estimate the yield drift considering moment equilibrium of a cracked section (Δ_{y3}*) there is little benefit over adopting a more simplified approach such as given by Δ_{y1}* *and* Δ_{y2}*.

Table 4.2 – Theoretical Estimates of the Effective Yield Displacement

	Wall 1	**Wall 2**	**Wall 3**	**Wall 4**	**Wall 5**	**Wall 6**	**Wall 7**	**Wall 8**	**Wall 9**	**Wall 11**		
	Effective Yield Displacement ($\Delta_{\%}$)											
Δ_y*	*0.38%*	*0.37%*	*0.49%*	*0.50%*	*0.21%*	*0.33%*	*0.35%*	*0.36%*	*0.39%*	*0.42%*	**Avg.**	**c.o.v.**
Δ_{y1}*	0.41%	0.43%	0.55%	0.64%	0.25%	0.40%	0.47%	0.35%	0.35%	0.35%		
Δ_y*/ Δ_{y1}*	*92.7%*	*86.0%*	*89.1%*	*78.1%*	*84.0%*	*82.5%*	*74.5%*	*102.9%*	*111.4%*	*120.0%*	**92.1%**	**16.1%**
Δ_{y2}*	0.27%	0.38%	0.38%	0.57%	0.26%	0.39%	0.39%	0.39%	0.39%	0.39%		
Δ_y*/ Δ_{y2}*	*140.7%*	*97.4%*	*128.9%*	*87.7%*	*80.8%*	*84.6%*	*89.7%*	*92.3%*	*100.0%*	*107.7%*	**101.0%**	**19.5%**
Δ_{y3}*	0.25%	0.35%	0.36%	0.52%	0.23%	0.35%	0.33%	0.33%	0.36%	0.33%		
Δ_y*/ Δ_{y3}*	*152.0%*	*105.7%*	*136.1%*	*96.2%*	*91.3%*	*94.3%*	*106.1%*	*109.1%*	*108.3%*	*127.3%*	**112.6%**	**17.5%**

4.6 The Effective Plastic Hinge Length

With regard to the seismic design of structural walls the definition of the plastic hinge will vary depending on the goals of a designer. For instance, the plastic hinge region may be defined as a conservative upper bound if confinement or shear strength detailing considerations are being made, or as a conservative lower bound if drift and ductility capacity calculations are made (CSA 2004). The plastic hinge region over which inelastic curvatures extend ($\ell_{p\phi}$) reflects the height over which special detailing would be required, and was given in Table 3.2. Within this context, it is evident from Table 3.2 that Wall 4 and Wall 7, representing the highest aspect ratio and lowest axial load, respectively, also possess the greatest extent of $\ell_{p\phi}$ above the base of the wall. By contrast, walls

possessing an aspect ratio of 1.5 showed significantly reduced values of $\ell_{p\phi}$ suggesting that wall height, rather than length, is a better indicator of plasticity. It is evident then from Table 3.2 then that the equivalent plastic hinge length (ℓ_p) needed to predict top drift would also not be considered as a fixed proportion of ℓ_w, but rather as a function of other wall parameters.

Expressions developed to determine ℓ_p available in current texts (Paulay and Priestley 1992) or based on analysis of test data (Paulay and Uzumeri 1975; Bohl and Adebar 2011) have largely been developed with consideration of RC behavior. Whereas, with RM there is a tendency for flexural cracks to be concentrated in the bed joints, compared to RC walls which contain no such inherent planes of weakness and tend to localize rotations near the wall base. In addition, the reduced compressive and tensile strength of masonry, relative to RC, would make masonry more susceptible to the propagation of shear cracks causing an increased effect of the shear spread of plasticity. The load application to the walls results in a triangular moment distribution as depicted in Fig. 4.4, such that when the ultimate moment (M_u) occurs at the base of the wall the yield moment (M_y) would occur at approximately 25% h_w above the base. This would represent the expected extent of inelastic curvature, without considering the effects of shear cracking and development lengths of the reinforcement.

It has been well established that the tension shift phenomenon (Paulay and Priestley 1992) will cause yield strains in the vertical reinforcement to extend further than that established from flexural stresses. The distance by which the yield strain extends is defined here as the shear spread of plasticity. To estimate this effect that the shear spread of plasticity has on the plastic hinge, the crack angle (θ) must be established. The first assumption is that at a distance of 25% h_w above the base where M_y is assumed to occur, the neutral axis depth of the wall is taken to be the mid-depth of the wall ($0.5\ell_w$). The plastic hinge is therefore taken as the vertical projection of this crack as depicted in Fig. 4.4. Therefore, the plastic hinge can be defined as:

$$\ell_p = 0.25h_w + 0.5\ell_w \tan\theta \tag{4.10}$$

The derivation of the crack angle θ depends on a number of different parameters that vary within a wall and a complete solution is presented in Chapter 5 of this dissertation. However, for the purposes of estimating the plastic hinge length such a complex solution is neither desired nor necessary.

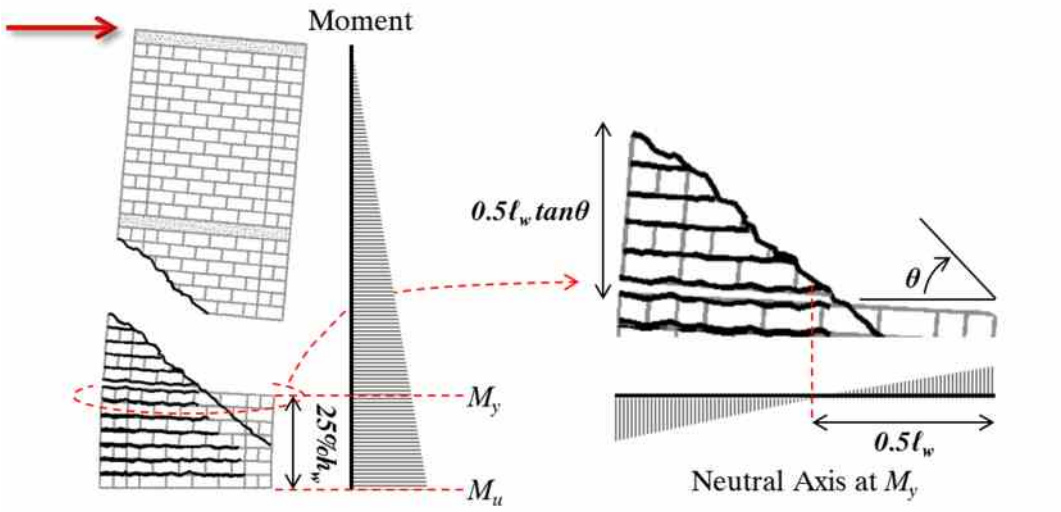

Figure 4.4 – Extent of Plastic Hinge Considering Shear Crack Angle, θ

Rather, an approximate solution to θ can be determined based on the unique circumstances that arise within a wall undergoing plastic hinging. Through equilibrium of stresses the following relationship can be determined relating the shear strength of the wall to the shear in the masonry and the stress in the horizontal reinforcement, and is completely derived in Chapter 5 as Eq. 5.28 of this dissertation:

$$v = v_{mi} + \rho_{sh} f_{yh} \tan\theta \tag{4.11}$$

Where, v is the shear stress, the average stress in the horizontal reinforcement is represented by $\rho_{sh}f_{sh}$ and v_{mi} is the shear stress transferred through aggregate interlock across the crack by the masonry.

Within the plastic hinge region the contribution of masonry towards shear resistance may be conservatively neglected, and thus Eq. 4.11 reduces to a function of the horizontal reinforcement and θ. This relationship can be described considering equilibrium of the cracked masonry macro-element Fig. 4.5. By a similar process, the resultant shear stress along the vertical axis can also be related to the stress in the vertical reinforcement. Similar to the derivation of Eq. 4.11, this requires the assumption of no horizontal or vertical stress applied, which may be reasonably assumed at the mid-depth of the wall where close to the neutral axis.

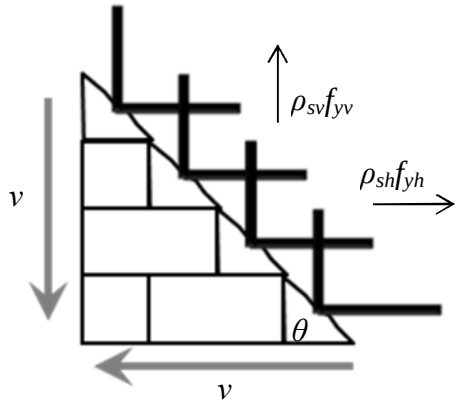

Figure 4.5 –Stress Equilibrium Neglecting Shear Resisted by Masonry

Equilibrium of forces must be maintained between the resultant shear forces and the resultant forces carried by the reinforcement at a crack. Therefore, the area of vertical reinforcement that spans over a crack that must be considered, which can be determined to be proportional to cos θ. Similarly, the area of horizontal reinforcement spanning a crack would be proportional to sin θ. Therefore Eq. 4.11 can be written along either axis neglecting the contribution from masonry in Eq. 4.12 which can be rearranged in terms of θ in Eq. 4.13:

$$v = \rho_{sv} f_{yv} \cot\theta = \rho_{sh} f_{yh} \tan\theta \tag{4.12}$$

$$\tan^2\theta = \frac{\rho_{sv} f_{yv}}{\rho_{sh} f_{yh}} \tag{4.13}$$

Substitution of Eq. 4.13 back into Eq. 4.10 will yield the following approximate solution of the plastic hinge:

$$\ell_p = 0.25h_w + 0.5\ell_w\sqrt{\left(\frac{A_{sv} f_{yv}/s_v}{A_{sh} f_{yh}/s_h}\right)} \le \min(1.5\ell_w, h_w) \tag{4.14}$$

Whereby, the practical limits to the possible extent of plastic hinge are given as $1.5\ell_w$ and h_w based on the observed response of the walls. The reinforcement characteristics are indicated as the area of vertical reinforcement (A_{sv}), area of horizontal reinforcement (A_{sh}) with respective yield strengths (f_{yh}, f_{yv}) and spacing (s_v and s_h). The estimated top drift for each of the walls based on Eq. 4.14 has been determined in Table 4.3. Of the total four possible plastic hinge lengths have been assumed for the walls (the previous three presented in Chapter 2 of $\ell_p = \ell_w$, $\ell_w/2$ and $\ell_w/2 + 0.1h_w$ and Eq. 4.14), each was used to back-calculate the required

strain in the masonry (ε_{mu}) needed to achieved the recorded ultimate displacement with results plotted in Fig. 4.6.

Table 4.3 – Theoretical Top Drifts Determined with Eq. 4.14 Compared with Table 2.3

		Wall 1	Wall 2	Wall 3	Wall 4	Wall 5	Wall 6	Wall 7	Wall 9	Wall 11
$\ell_p = \ell_w$	$\Delta_{0.0025}$	1.10%	1.09%	0.79%	1.51%	1.04%	0.98%	1.28%	0.99%	0.66%
	$\Delta_{0.004}$	1.86%	1.85%	1.28%	2.44%	1.71%	1.61%	2.05%	1.61%	1.04%
	$\Delta_{0.006}$	2.76%	2.79%	1.61%	3.56%	2.54%	2.34%	2.99%	2.35%	1.13%
$\ell_p = \ell_w/2$	$\Delta_{0.0025}$	0.75%	0.74%	0.57%	1.00%	0.85%	0.81%	1.04%	0.82%	0.69%
	$\Delta_{0.004}$	1.22%	1.17%	0.86%	1.51%	1.38%	1.29%	1.63%	1.30%	1.09%
	$\Delta_{0.006}$	1.78%	1.72%	1.04%	2.12%	2.04%	1.85%	2.35%	1.86%	1.19%
$\ell_p = \ell_w/2+0.1h_w$	$\Delta_{0.0025}$	0.88%	0.91%	0.56%	1.34%	1.00%	1.25%	1.32%	0.99%	0.80%
	$\Delta_{0.004}$	1.46%	1.49%	0.88%	2.13%	1.65%	2.03%	2.13%	1.61%	1.30%
	$\Delta_{0.006}$	2.15%	2.23%	1.07%	3.09%	2.45%	2.98%	3.11%	2.34%	1.41%
$\Delta_{ASCE\ 41,CP}$		0.36%	0.40%	0.40%	0.40%	0.35%	0.40%	0.41%	0.40%	0.34%
ℓ_p = Eq. 4.14	$\Delta_{0.0025}$	0.92%	1.00%	0.85%	1.73%	1.05%	1.23%	1.64%	1.14%	0.89%
	$\Delta_{0.004}$	1.53%	1.68%	1.40%	2.86%	1.72%	2.08%	2.68%	1.90%	1.45%
	$\Delta_{0.006}$	2.26%	2.53%	1.77%	4.20%	2.56%	3.07%	3.95%	2.80%	1.58%
Assumptions: Strain hardening, only tied reinforcement carries compression										

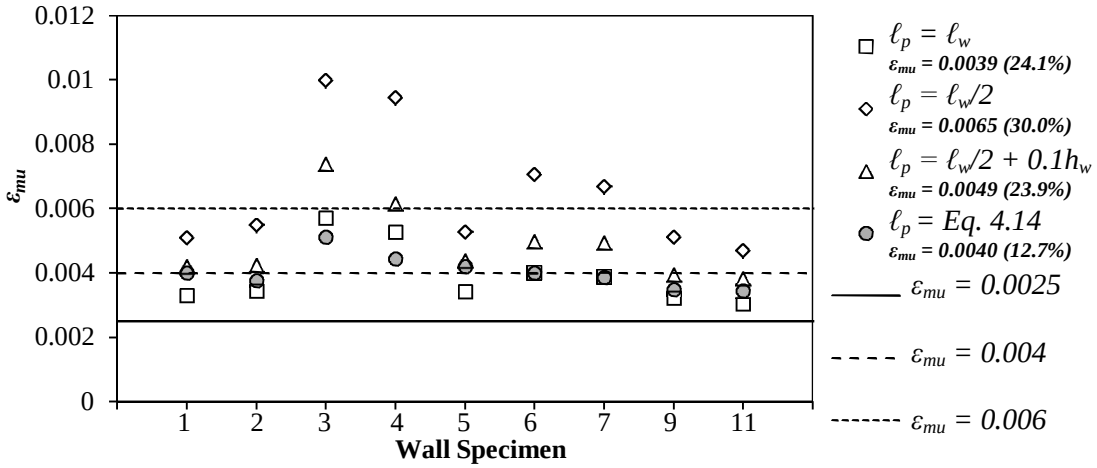

Figure 4.6 – Required Strain of Masonry for Different Values of ℓ_p to Achieve Δ_{Que} (*Average ε_{mu} and (c.o.v.) given for each*)

Fig. 4.6 indicates that Eq. 4.14 is the best means to account for the response of the walls (ε_{mu} = 0.0040, c.o.v. = 12.7%), whereas assuming a constant ℓ_p based only on wall length, would require significantly different and highly variable values of ε_{mu} to achieve the experimentally measured drift.

In conclusion, the following design procedure is suggested towards estimating the displacement ductility capacity of RM walls with boundary elements. Firstly, an idealized yield curvature (ϕ_y*) can be estimated by Eq. 4.15.

$$\phi_y^* = 2.10\varepsilon_y / \ell_w \tag{4.15}$$

Once known, ϕ_y* can be used to determine the idealized yield drift (Δ_y*) in Eq. 4.16.

$$\Delta_y^* = \phi_y^* \frac{h_w^2}{3} \tag{4.16}$$

The ultimate curvature (ϕ_u) in the wall can be determined by dividing the limiting strain determined from Eq. 2.2 of ε_{mu} = 0.004 by the depth of the neutral axis solved for adopting the compression block theory and considering tied compression reinforcement in Eq. 4.17.

$$\phi_u = 0.004 / c \tag{4.17}$$

Using the plastic hinge defined in Eq. 4.14, the displacement corresponding to the peak load of the walls (Δ_{Qu}) is determined from Eq. 4.18.

$$\Delta_{Qu} = \frac{\phi_y h^2}{3} + (\phi_u - \phi_y)(\ell_p)(h_w - \ell_p/2) \tag{4.18}$$

To account for the increase in displacement capacity allowing for a degradation in strength to 80% of Q_u it was found that on average this occurred at a displacement equal to Δ_{ye} past Δ_{Que} as shown for solution to $\Delta_{80\%Qu}$ in Eq. 4.19.

$$\Delta_{80\%Qu} = \Delta_{Qu} + \Delta_y \tag{4.19}$$

Whereby, the theoretical yield displacement (Δ_y) is readily estimated as 75% of Δ_y*. Comparison between the theoretical top drift (Δ_{Qu}) determined with these theoretical assumptions yield very good results for all walls, with a ratio of Δ_{Que} /Δ_{Qu} = 99.3 % (c.o.v. = 12.7 %). Furthermore, adding, Δ_y to Δ_{Qu} yields a ratio between experimental and theoretical drifts of $\Delta_{80\%Qu}$ / (Δ_{Qu} + Δ_y) = 98.7% (c.o.v. 13.5%). Finally, the ductility, $\mu_{\Delta i}$, can be determined by Eq. 4.20.

$$\mu_\Delta = \Delta_{80\%Qu} / \Delta_y^* \tag{4.20}$$

Based on this simplified approach summarized in Table 4.4, it is possible to quickly establish estimates of the parameters needed to for an idealized load-displacement curve that could be used towards a force-based seismic design.

Table 4.4 – Theoretical Estimate of Wall Drift

	Wall 1	**Wall 2**	**Wall 3**	**Wall 4**	**Wall 5**	**Wall 6**	**Wall 7**	**Wall 8**	**Wall 9**	**Wall 11**	**Avg.**	**c.o.v.**
Δ_{Que}	1.53%	1.58%	1.78%	3.16%	1.80%	2.08%	2.59%	2.35%	1.64%	1.25%	Δ_{Que}/Δ_{Qu}	
Δ_{Qu}	1.53%	1.68%	1.40%	2.86%	1.72%	2.08%	2.68%	2.68%	1.90%	1.45%	**99.3%**	**12.7%**
$\Delta_{80\%Que}$	2.20%	1.78%	1.98%	3.36%	2.19%	2.37%	3.03%	3.11%	1.82%	1.54%	$\Delta_{80\%Que}/\Delta_{80\%Qu}$	
$\Delta_{80\%Qu}$	1.80%	2.06%	1.78%	3.43%	1.98%	2.47%	3.07%	3.07%	2.29%	1.84%	**98.7%**	**13.5%**

4.7 Displacement- and Performance-Based Seismic Design Parameters

This test program was designed in accordance with the objectives set out by the Federal Emergency Management Agency (FEMA) document 461 (ATC 2007) and P695 (ATC 2009) for the quantification of performance-based seismic behaviour of structural components. The wall test results are intended to serve as a basis in the future development of high quality fragility functions for RM walls with boundary elements as set out by the ATC-58-1 (ATC 2011). Recent studies into the performance of conventional RM structural walls by Li and Weigel (2006) and Murcia-Delco and Shing (2011) have focused on qualitative assessment of performance-based damage states of historical wall test data.

Currently, the FEMA 306 document (ATC 1998) outlines five possible damage categories for RM intended to differentiate between the method of repair (MOR) needed to remediate a RM structure. These, or similar damage states, are related to a demand parameter such as top drift, which can be used as a metric to evaluate the anticipated costs associated with a seismic event. Although many damage-based indices are related to drift, other indices have been suggested, such as: hysteretic energy, number of load cycles, energy dissipation and curvature-based strain measurements (Park and Ang 1985; Pagni and Lowes 2004; Priestley et al. 2007). More recently, Gulec and Whittaker (2009) developed drift-based fragility functions from a database of 434 RC squat walls based on four identified MORs associated with different damage states. Although it is outside the scope of this study to evaluate or develop MOR categories for RM construction, in the following sections a suggested set of damage states will be identified for this wall category adapted from those proposed in the literature reviewed by the authors.

4.7.1 Digital Image Correlation Analysis

Residual crack widths in masonry may require remediation for aesthetic, water penetration or even strength or stiffness purposes depending on the width of the

crack opening and the wall's exposure. Because residual crack width depends greatly on the residual drift in the wall, Gulec and Whittaker (2009) conservatively assumed crack widths based on the peak loading conditions during displacement cycles. Based on the FEMA 306 document (ATC 1998), the five damage states of RM walls with boundary elements have been defined in Table 4.5 and are related to crack width size (δ), the lateral load (Q) and visual observations of damage. Firstly, to establish δ in a consistent manner that may also be applied to walls where direct measurements were not taken, digital image correlation (DIC) computer analysis was used to measure surface strain in Walls 1, 2 and 3. This, in turn will be related back to curvature measurements and a method of estimating crack widths in flexurally-dominated walls will be proposed.

The use of DIC has long been associated with measuring the deformation and fracture of metallic materials, but has found more recent applications towards concrete and masonry materials testing. Choi and Shah (1997) tested prismatic concrete specimens under compression and indicated a good correlation between DIC and typical displacement transducer (LVDT) measurement techniques towards measuring compressive strains. In their study, DIC was also used to measure surface strains on the concrete specimens including quantifying the formation of cracks within the cement matrix. Lawler and Keane (2001) measured deformations in concrete subject to compression using 3-D DIC analysis. Similarly, Raffard et al. (2001) applied DIC towards the testing of historical stone masonry materials, however, as with the previous authors' work, specimens were of a relatively small size compared to structural elements. More recently, Tung et al. (2008) applied DIC towards compression test of brick panels and both Tusini and Willam (2008) and Citto et al. (2011) reported using DIC analysis in tests on brick prism compression tests. Much of the research related to masonry materials which has documented use of DIC has focused on small scale compression testing, although Smith et al. (2010) reported using DIC towards the analysis of full-scale testing of precast concrete shear walls subjected to lateral loads. In addition, Destrebecq et al. (2010) used DIC towards crack detection of reinforced concrete beams. DIC has demonstrated to be an accurate technique of measuring surface deformations at the small scale, but with improvements in technology and the availability of high resolution of digital cameras it has been expanded to full-size structural elements.

Table 4.5 – Damage States Definition for RM Shear Walls with Boundary Elements

Damage State	Description	Crack Widths $\delta \leq$	Lateral Resistance $Q \leq$	Associated Observations
Insignificant	Surface finishes, retooling of mortar joints	1.6 mm (1/16")	Q_{cr}	First signs of cracking
Light	Initiation of reinforcement yielding, limited cracks requiring epoxy injection	1.6 mm (1/16")	$\approx Q_y$	Several small cracks visible localized in only the bottom few courses (horizontal), yielding of vertical reinforcement localized to the bottom few courses
Moderate	Extensive yielding of reinforcement and cracks requiring epoxy injection over much of the lower portion of the wall	3.2 mm (1/8")	First achieved Q_u	Cracking can be observed throughout the wall and likely extends throughout the plastic hinge region (horizontal and diagonal)
Heavy	Partial wall replacement/patching required	4.8 mm (3/16")	Nominal drop from Q_u	Boundary element exhibits spalling of faceshell and vertical splitting cracks but are not to such an extent to cause a significant drop in lateral resistance
Severe	Wall replacement	6.4 mm (1/4")	Resistance drops to 80%Q_u	Significant drop in strength and stiffness caused by crushing of the compression toe and grout core of boundary element including the exposure and potential buckling or fracture of vertical reinforcement

4.7.2 DIC Instrumentation and Calibration

Preparation of the walls for analysis required a black and white random speckle pattern to be painted on one side of the walls as shown in Fig. 4.7. A 14 mega-pixel camera was fixed in place and used to take black and white digital photographs of the wall during testing at each displacement cycle. The size of the walls, speckle pattern and resolution of the cameras resulted in an effective image size of 1 pixel equivalent to an average area of 0.25 mm^2. For a successful analysis, black speckles should be between 10 – 30 pixels in size (Cintron and Saouma 2008), which is required for the default settings in the software. The software selected was Vic 2-D (2009), which analyzes the pattern within a grid size of 27 pixels × 27 pixels. Pictures of each wall were taken just prior to testing to act as the reference image, with subsequent photos taken at the peak displacement of each displacement cycle. The DIC algorithms then trace the

relative movement of pixels over the load history of a test specimen as it deforms. This is accomplished by first assigning a grid of nodes to the area of interest defined on the reference image, as depicted in Fig. 4.7. Analysis begins with a pixel pattern, acting as a point of reference on the walls, which subsequent images are compared to. Analysis of the nodes within the reference grid is then compared to the adjacent grid of pixels, which is defined based on the step size chosen, the default is 5 pixels. From this, the software maps the location and intensity of the pixels in the reference image and compares them to the deformed image as indicated in Fig. 4.8. The use of the default settings results in a confidence level of deformation measurements of 0.1 pixels (0.05 mm). Acceptability of a DIC analysis is verified by the number of calculation iterations required, whereby analysis of the walls with the default settings resulted in an average of 1.9 to 2.3 iterations, a number less than five indicates an accurate measurement (Cintron and Saouma 2008).

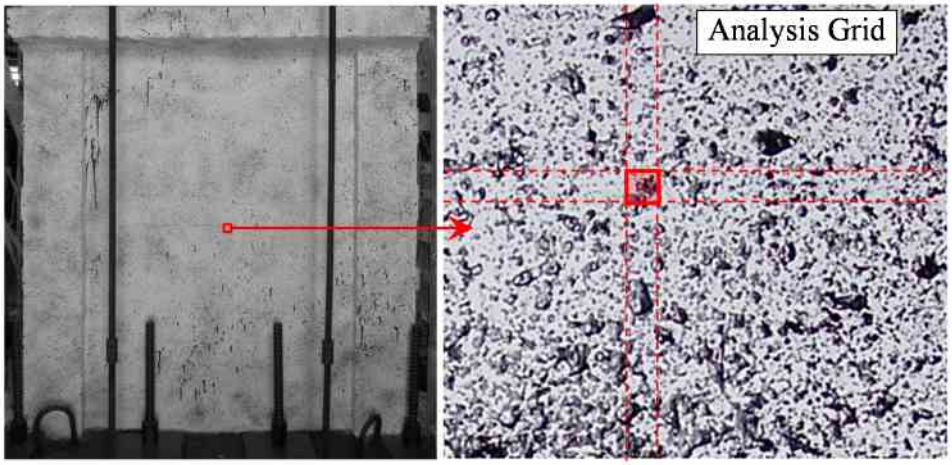

Figure 4.7 - Random Black and White Painted Speckle Pattern

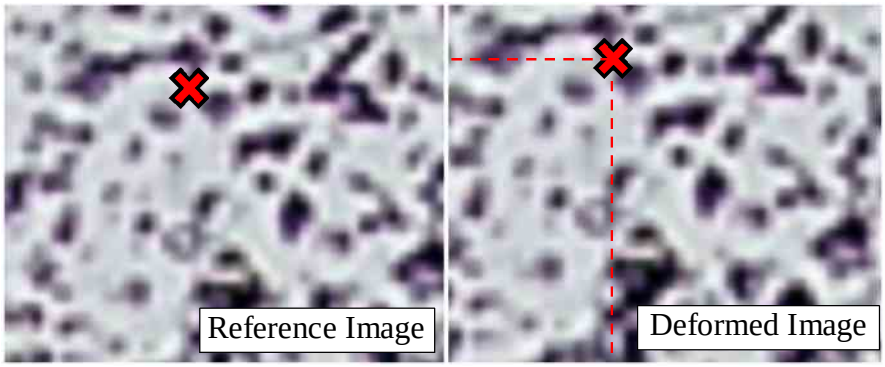

Figure 4.8 - Tracking the Movement of Pixels from the Reference Image

Since the walls were also measured using conventional LVDTs mounted on the walls during testing, calibration and comparison of the DIC measurements to the

LVDTs was conducted. During early load cycles of the walls it became evident that as a result of the resolution of the paint speckle pattern as well as digital cameras used to record pictures of the walls, it was not possible to gather reliable measurements of very low elastic strains on the surface of the wall. However, because these walls were considered to be highly ductile, and the main objectives of the DIC analysis was in damage analysis, measurements at such very low load levels that masonry remains uncracked were not of interest within this study. DIC analysis returns relative surface strains and displacements of the walls' surface in terms of relative pixel size. To facilitate comparison with LVDT measurements, the reference image for each wall, taken prior to loading, is used to calibrate between pixel size and physical dimension. To reduce lens effects and due to limitations with digital cameras and laboratory space, Walls 2 and 3, were recorded by two separate cameras, with one trained only on the lower storey of the wall (1.3 m tall) and the second trained on the upper storey. This was selected since the concentration of plastic hinging and cracking damage was anticipated to be contained within the lower storey only. The DIC images were then calibrated based on physical markers of a known physical dimension on the walls and the area of the wall is selected for analysis (omitting components of the test set-up that are in the field of view) as indicated in Fig. 4.9a, which on average resulted in a calibrated pixel size of 0.5 mm × 0.5 mm. The deformations interpreted from DIC could be plotted as either vertical displacement (indicative of flexural curvature) in Fig. 4.9b or as horizontal displacement (indicative of lateral deformations) in Fig. 4.9c.

The exact locations of the LVDTs were subsequently mapped on the DIC reference image for each test wall as shown in Fig. 4.10a and the vertical displacements were exported over the load histories for each wall. Comparison between physical LVDT and DIC measurements for wall displacement revealed that at high levels of displacement, the upper floors of Wall 2 began to show deviation from LVDT measurements. This was later attributed to play within the out-of-plane support system in the test set-up which caused slight movements in the wall, normal to the wall's lateral movements being recorded. Nevertheless, such erroneous readings were limited to the top of the aforementioned wall only, and were absent from Walls 1 and 3.

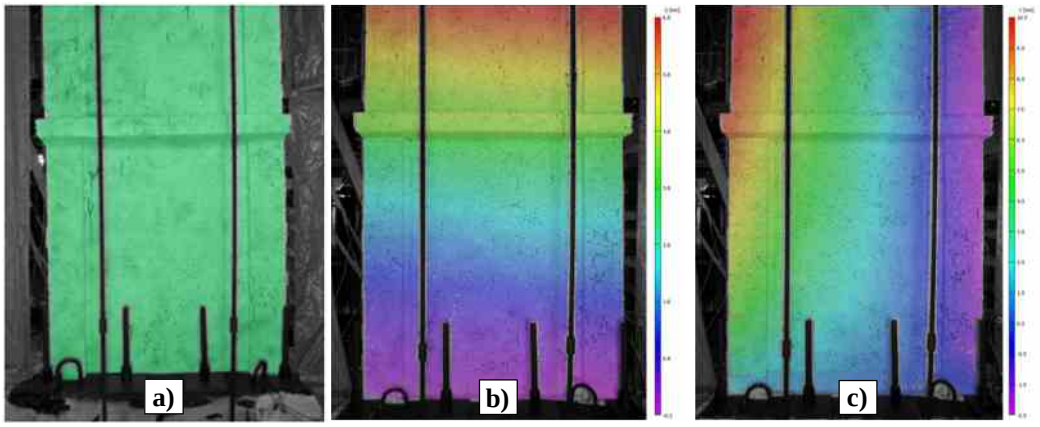

Figure 4.9 - Results of DIC Analysis: a) Area of Interest Defined as the Surface of the Wall, b) Indicating Lateral Displacements in the Wall, and c) Indicating Vertical Displacements in the Walls

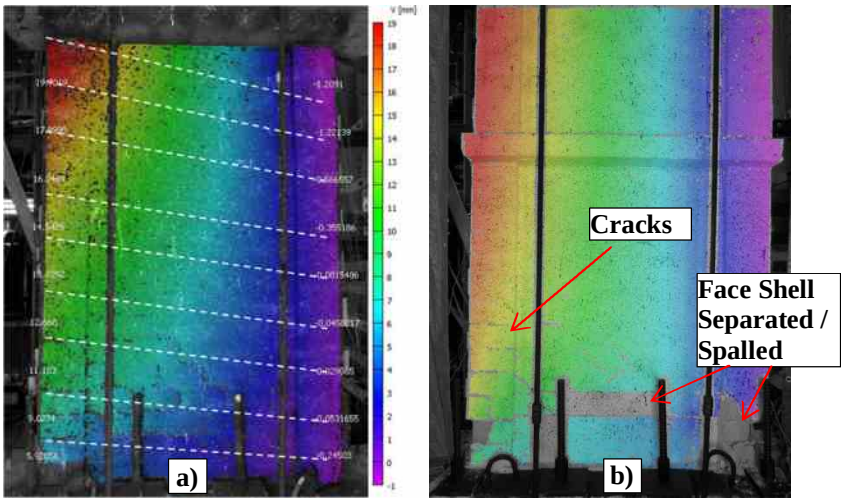

Figure 4.10 - DIC Measurements of Walls: a) Vertical displacement readings as LVDT Locations Indicating Flexural Curvature in the Walls (Dashed Lines), and b) Loss of DIC Measurements at Very High Drifts (>2.5%) when Crushing and Spalling has Occurred

Overall, DIC and LVDT measurements were within ± 0.1 mm to each other however, the use of DIC at very high displacement cycles was hindered by the occurrence of face shell spalling and separation. It was observed that DIC became ineffective in areas where the heaviest damage occurred, a similar issue with surface-mounted LVDTs as indicated in Fig. 4.10b.

4.7.3 Crack Measurements

The DIC analysis produced average strains on the surface of each wall over its load history, whereby, crack widths could be mapped directly by the software at areas where tensile flexural and shear strains were concentrated. This process is expedited within masonry because of the tendency for tensile strains to be concentrated in the inherent planes of weakness formed by the mortar joints. It was made evident during testing that crack damage was predominantly characterized by horizontal cracks along the bed joints due to flexural bending. The graphical analysis produced by DIC of vertical strains illustrates this observation, as indicated in Fig. 4.11, which depicts the first observed formation of flexural cracking at a top drift of ± 0.15% and load equal to 75% the yield load in Fig. 4.11a and 4.11b for Wall 2. This can be compared with the increase in crack penetration at a top drift of ± 1.2% and at peak lateral resistance in Fig. 4.11c and 4.11d. Vertical strain concentrations, illustrated as yellow and red, are localized at each bed joint in the boundary elements. The peak tensile strains in Fig. 4.11a and 4.11b were recorded as a strain of 0.8%, increasing to 3.0%, in Figures 4.11c and 4.11d. It is evident from the previous figure that as cracks develop portions of the mortar or faceshell will spall away and the DIC analysis will no longer be able to measure strains, indicated by small grey patches also indicated in Fig. 4.11c and 4.11d.

To account for this, cracks are measured by the relative displacement of adjacent segments above and below a crack as illustrated in Fig. 4.12 using the software's crack measuring tool. Based on the image correlation analysis as well as observations made during testing, the maximum crack widths over the load history for Walls 1, 2 and 3 were contained within the boundary element and web of wall adjacent to the boundary element in the lower courses of the walls. These cracks were predominantly associated with flexure, however, shear crack widths were also measured, and were found to be the largest, although still smaller than flexural crack widths, in the web of the walls somewhere between the middle of the wall and the tension boundary element. The median crack width (δ_c) of the largest crack was selected as the parameter of interest for each walls' load cycle to be incorporated with damage state definition. The median, rather than mean, was chosen due to the potential for abrupt changes in the crack width due to the irregular cack surface. These peaks of troughs in crack width, illustrated in Fig. 4.11b, tended to disproportionately skew mean crack measurements.

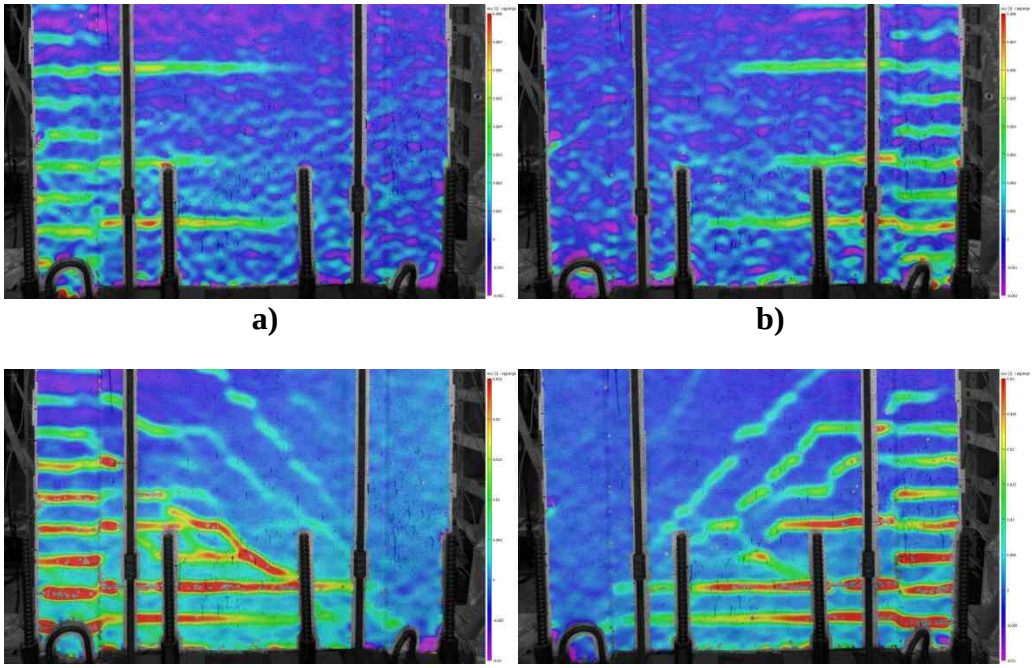

a) **b)**

c) **d)**

Figure 4.11 - Vertical Strain Concentration in Bed Joints of Wall 2: a) 75% Yield Load in +ve Load Direction, b) 75% Yield Load in -ve Load Direction, c) Peak Lateral Resistance in +ve Load Direction and d) Peak Lateral Resistance in –ve Load Direction

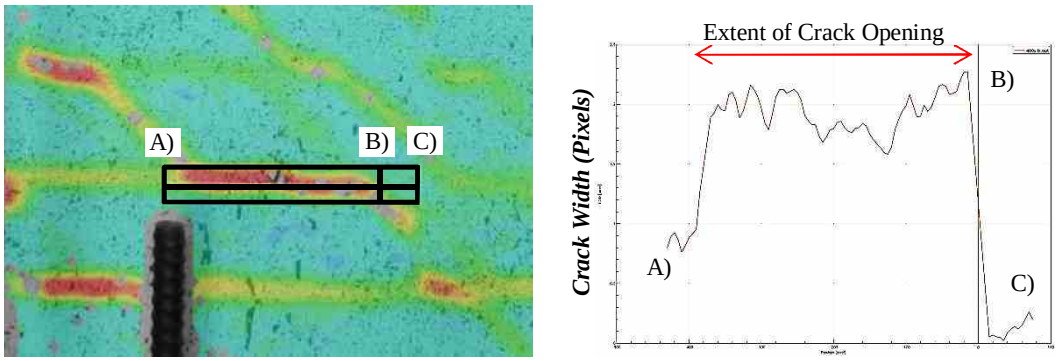

a) **b)**

Figure 4.12 - Determining Crack Widths in Walls: a) Close Up of a Crack Formation with Crack Measuring Tool, and b) Plot of Measured Relative Deformation over Crack Length Indicating Crack Width

4.7.4 Idealized Crack Widths

The benefit of knowing exactly where cracks will form in masonry walls is that crack spacing, and thus crack width, can be readily determined from curvature measurements. For instance, the typical curvature profile for a RM wall ascertained by average strain measurements by externally mounted displacement transducers as discrete locations is depicted in Fig. 4.13a for Wall 2. Whereas, digital image correlation analysis allows for a significantly smaller threshold of measurements which is better suited to pick up the concentrations of curvature that exist at the crack openings in the bed joints as illustrated by Fig. 4.13b. Curvature can be seen to be localized at a spacing of approximately 95 mm corresponding with the spacing between bed joints in the wall in Fig. 4.13b. Overall, good comparison between both methods is observed in Fig. 4.13c, with the exception at the base of the wall, due to difficulty in measuring base uplift with digital image correlation during the test.

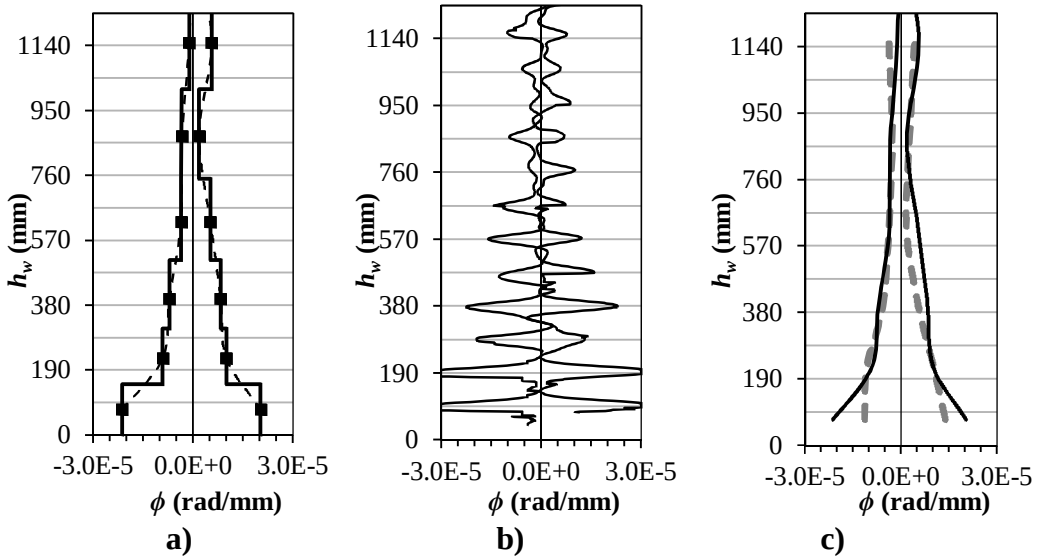

Figure 4.13 – Average Curvature Profiles of Wall 2 as Measured: a) As an Average from External Displacement Transducers, b) Directly from Digital Image Correlation (DIC) Analysis ($3 \times \Delta_{ye}$) and c) Comparison between the Averaged Values of both (DIC represented by the Dashed Line)

Based on the image correlation analysis as well as observations made during testing, the maximum crack widths over the load history for Walls 1, 2 and 3 were contained within the boundary element and web of wall adjacent to the boundary element in the lower courses of the walls. By contrast, shear crack widths were found to be the largest, although still smaller than flexural crack widths, in the web of the walls somewhere between the middle of the wall and the tension

boundary element. The median width (δ_c) is plotted in Fig. 4.14a for each of the 3 walls with the calibration error of ± 0.1 mm. Following the same procedure the median width of the maximum shear crack was also measured, with the results plotted in Fig. 4.14b. Overall, flexural cracks appeared in greater numbers and with wider openings than shear cracks. In addition, the width of flexural cracking is shown to be strongly correlated with the level of top drift as indicated by the R^2 values of the lines of best fit, since it would be directly related to wall curvature in the flexurally-dominated walls as indicated by Fig. 4.14a.

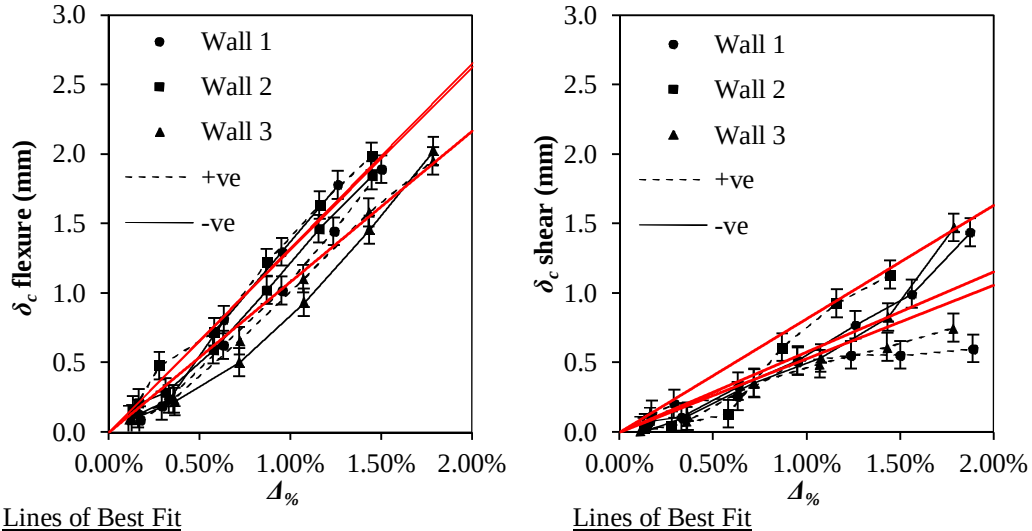

Lines of Best Fit
Wall 1: $\delta_c = 140\Delta_{\%} - 0.17$ ($R^2 = 0.97$)
Wall 2: $\delta_c = 135\Delta_{\%} - 0.05$ ($R^2 = 0.98$)
Wall 3: $\delta_c = 116.5\Delta_{\%} - 0.16$ ($R^2 = 0.98$)

a)

Lines of Best Fit
Wall 1: $\delta_c = 53.6\Delta_{\%} - 0.01$ ($R^2 = 0.74$)
Wall 2: $\delta_c = 92.1\Delta_{\%} - 0.21$ ($R^2 = 0.95$)
Wall 3: $\delta_c = 63.8\Delta_{\%} - 0.12$ ($R^2 = 0.84$)

b)

Figure 4.14 – Median Crack Widths Determined from Image Correlation Analysis: a) Flexural Cracks and b) Shear Cracks (+ve and –ve displacement cycles ±0.1 mm)

Therefore, it is possible to establish a theoretical basis to measure crack widths based on curvature readings and taking advantage of the knowledge of crack locations being at the mortar joints. The crack width to be determined from the average curvature measurements is done so from externally-mounted displacement transducers which measured vertical strains over the bottom four courses of the walls (4 mortar joints in total) and is defined as δ_ϕ. Two conservative assumptions are made to estimate δ_ϕ: no tensile strains are carried in the masonry between cracks which are concentrated at the bed joints (neglecting tension stiffening) and crack widths are evenly distributed between the bottom four mortar joints. Therefore, δ_ϕ is determined from the curvature measurement at

the base of the wall (ϕ), the depth of neutral axis (c) and a crack spacing of 95 mm (s_c), based on the half-scale nominal unit height, from Eq. 4.21.

$$\delta_\phi = \phi(\ell_w - c)s_c \tag{4.21}$$

The ratio between observed cracks from the image correlation analysis and those calculated from curvature measurements (δ_c / δ_ϕ) for Walls 1, 2 and 3 is plotted in Fig. 4.15. Overall, an average ratio between curvature and digital image correlation crack width measurements of δ_c / δ_ϕ = 0.88 (c.o.v. = 14.9%) was determined, indicating a fairly good correlation between the two methods. With test data from all the walls Eq. 4.21 is applied and the resulting critical crack widths are plotted in Fig. 4.16a.

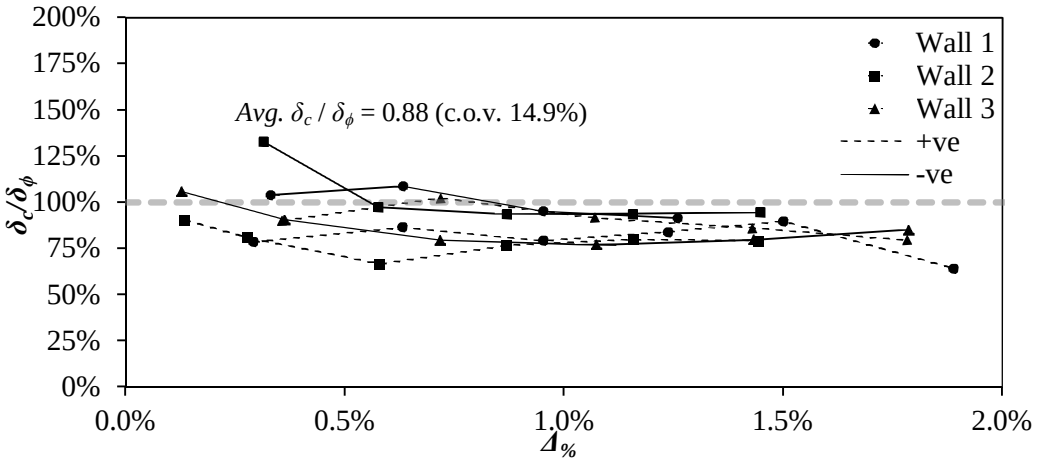

Figure 4.15 – Comparison between Crack Widths Determined from Image Correlation Analysis and from Curvature Measurements

It can be observed that based on Eq. 4.21 these crack widths are strongly related to the anticipated crack spacing parameter, which is determined from the nominal masonry unit height. Therefore, to relate this data to full-scale masonry construction, for which the FEMA 306 crack limits and those presented in Table 4.5 have been established for, the data given in Fig. 4.16a will have to be scaled to consider the increased spacing. It is expected that curvatures will not differ from half-scale to full-scale walls, since material strain limits are assumed to be constant and the depth of neutral axis remains as a constant proportion of wall length (Harris and Sabnis, 1999). However, the space between flexural cracks (s_c) would be increased to reflect the increased height of units, set to a nominal height of 200 mm. Applying these modifications to Eq. 4.21 for the walls provides a representative estimate of the equivalent full-scale crack width. From the perspective of performance-based design, only the minimum top drift from either direction of loading that is associated with the first occurrence of one of the

predefined crack limits given in Table 4.5 is of interest. As such, Fig. 4.16b has been created to indicate the drift associated with the occurrence of the crack width limits given in Table 4.5. In the subsequent sections, the occurrence of the remainder of the damage states identified in Table 4.5 will be presented.

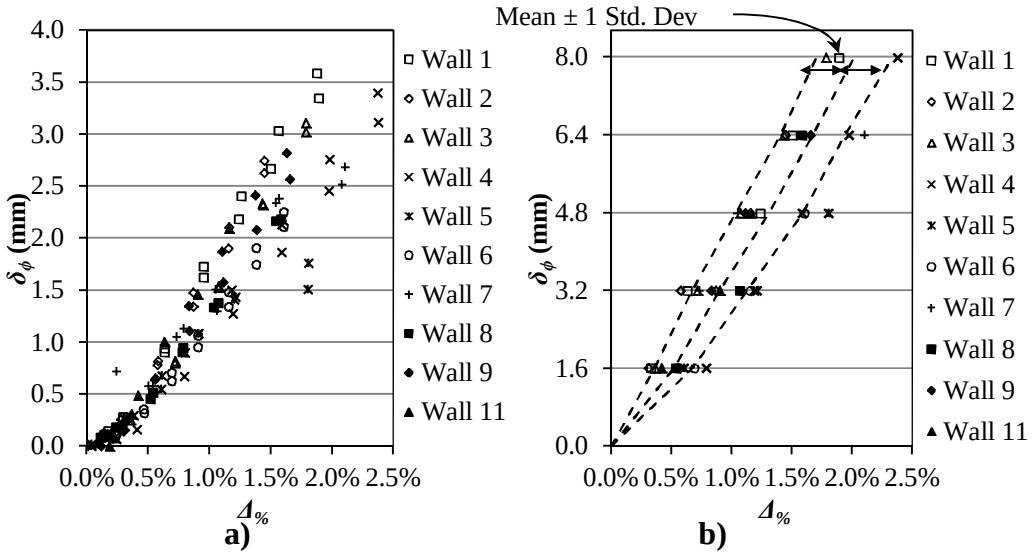

Figure 4.16 – Crack Widths Determined from Tensile Strains: a) Actual Widths for Each wall Over the Respective Load History and b) Values Representative of a Full-Scale Crack Spacing Discretized into Predefined Limits

4.7.5 Load- and Strain-Based Damage States

The first occurrence of cracking damage as part of the insignificant damage state of the walls can be established from observations made during the test as well as from the measured load-displacement response of the walls at the cracking load (Q_{cr}). With increased top drift, the occurrence of plastic straining in the vertical reinforcement can lead to residual crack openings and residual drift in a wall after it is unloaded. As such, the damage state associated with yielding of the vertical reinforcement leading to significant residual cracking is defined by the drift associated with the first occurrence of yield strains in the extreme reinforcement measured by strain gauges to a height of $\ell_w/2$ above the base. Furthermore, the significant drift over which the peak load is maintained, precludes the selection of a single point or damage state associated with this condition, as had been defined in previous studies. Rather, moderate and heavy damage states are related back to the drifts where peak resistance is first achieved and to the drift where it drops to a certain percentage of peak, respectively. In recognition that the walls can possess significant displacement capacity after attaining the peak load, the severe damage state is related to a drop in resistance to 80%Q_u. Finally, two

supplemental damage states are also recognized as were identified by Gulec and Whittaker (2009) based on the overall load-displacement behavior of the walls, but remain separate from those identified in Table 4.5. The first is based on forming a collapse mechanism at the maximum drift attained by the walls at a drop in lateral resistance of 50%Q_u, if applicable. Secondly, a residual drift limit of 1.0% has been selected and determined from the intersection of the load-displacement hysteresis with a lateral load equal to zero.

4.7.6 Occurrence of Visually Observed Damage States

The visual observation-based damage states are listed in Table 4.5 and include the first occurrence of visible crack damage, spalling of the face shell, vertical compression cracking, crushing of masonry and buckling of the vertical reinforcement. Since all walls were dominated by flexural mechanisms, crushing and spalling damages were localized to the boundary elements representing the compression toes of the walls. The occurrence of face shell spalling in the boundary elements of the walls was localized at the lowest three courses in the walls as depicted by the photos in Fig. 4.17a. The occurrence of vertical cracking was usually an indicator during testing that splitting of the face shell had occurred which is why both mechanisms are grouped in the heavy damage state in Table 4.5. After spalling of the masonry face shell initiated, there was no immediate drop in lateral resistance of the wall. Rather, it was typical that only upon further cycling would crushing of the block and grout core of the boundary element occur, to such an extent to expose the vertical reinforcement and cause a drop in lateral resistance as depicted by the photographs in Fig. 4.17b.

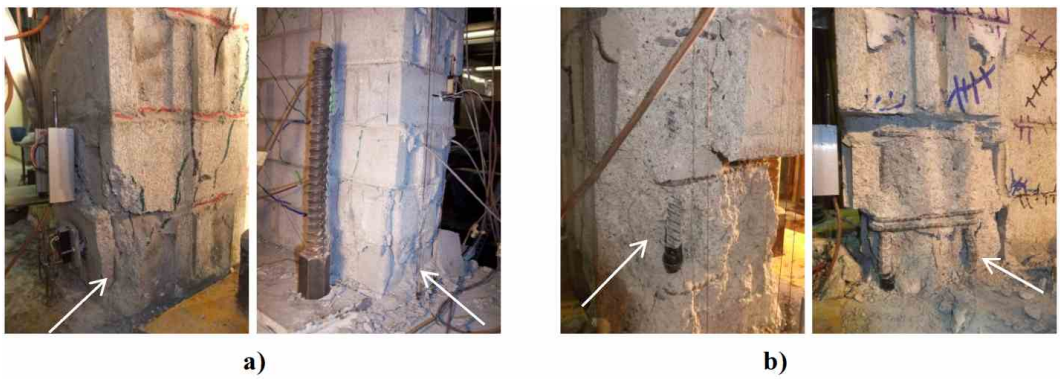

Figure 4.17 – Visual Observation-Based Damage States: a) Spalling of the Face Shell and Vertical Cracking and b) Crushing of the Masonry to Expose Reinforcement

4.7.7 Development of Fragility Curves

For each of the damage states identified in Table 4.5, the limiting level of top drift associated with the first occurrence of any of the criteria for damage state for a particular wall is presented in Table 4.6. The ATC-58-1 (ATC 2011) recommends the use of a cumulative probability function to generate fragility functions based on a log-normal probability distribution. The lognormal probability distribution function is given by Eq. 4.22 and requires determination of the median drift for each damage state, designated as θ_i in Eq. 4.23, as well as the logarithmic standard deviation (dispersion) designated as β_i in Eq. 4.24.

$$F(\Delta) = \Phi\left(\frac{\ln(\Delta/\theta_i}{\beta_i}\right) \tag{4.22}$$

$$\theta_i = e^{\left(\frac{1}{M}\sum_{i=1}^{M}\ln\Delta_i\right)} \tag{4.23}$$

$$\beta_i = \sqrt{\left(\frac{1}{M-1}\sum_{i=1}^{M}\left(\ln\left(\Delta_i/\theta_i\right)\right)^2\right)} \tag{4.24}$$

Whereby, the log-normal probability distribution (F) given by Eq. 4.22 is determined for any given level of top drift (Δ_i) with a standard normal (Gaussian) cumulative distribution (Φ). The drift associated for each wall for each damage state is given as Δ_i, the total number of wall specimens is given as M = 11 and the calculated values of θ_i and β_i are listed in Table 4.6. The dispersion of the test data is indicative of the quality of the fragility function and is highly dependent on material and construction variation that exists between specimens. The fragility function for each damage state is presented in Fig. 4.18.

Table 4.6 – Critical Drift Associated with Each Damage State

	Walls (Δ_i) (%)													
Damage State	**1**	**2**	**3**	**4**	**5**	**6**	**7**	**8**	**9**	**10**	**11**	***θ***	***β***	***D***
Insignificant	0.06	0.07	0.09	0.11	0.04	0.05	0.05	0.05	0.08	0.05	0.05	0.06%	0.32	0.11
Light	0.33	0.31	0.36	0.36	0.30	0.29	0.30	0.33	0.34	0.32	0.42	0.33%	0.11	0.19
Moderate	0.63	0.58	0.72	0.80	0.61	0.69	0.73	0.71	1.07	0.99	0.42	0.70%	0.25	0.22
Heavy	1.24	1.16	1.07	1.59	1.80	1.60	1.05	1.04	1.58	1.98	1.16	1.35%	0.23	0.23
Severe	1.50	1.45	1.43	1.98	2.19	2.37	2.10	2.08	1.58	2.53	1.54	1.85%	0.21	0.20
Supplemental	1.89	1.74	1.89	1.98	1.80	1.60	1.54	1.54	1.65	1.98	1.34	1.71%	0.12	0.15

The quality of the experimentally generated fragility functions may be quantified by the goodness-of-fit of the smoothed fragility function to the observed experimental demand values of each wall specimen. To evaluate the quality of the fragility function, a Lilliefors test for goodness-of-fit (Lilliefors, 1967) is carried out for a 95% confidence level according to the procedure described by Porter et al. (2007) and required by ATC-58-1 (ATC 2011). Each damage state passed the 95% confidence level test, with each corresponding to a Kolmogorov-Smirnov test parameter (D) given in Table 4.6 which were all less than the critical parameter: $D_{critical} = 0.26$ for the respective damage states selected. The procedure for this test is laid out in ATC-58-1 (ATC 2011) and the satisfaction of the criteria indicates high quality experimentally-based fragility functions for the walls reported.

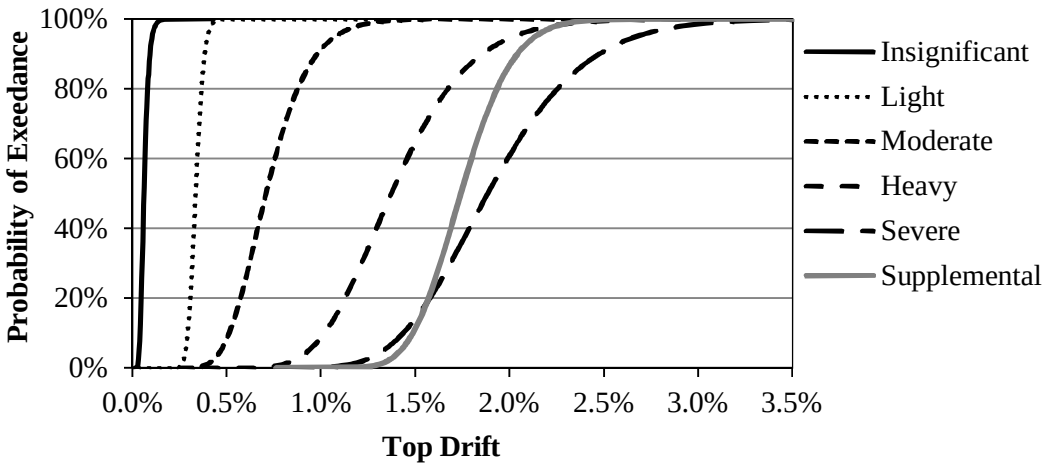

Figure 4.18 – Fragility Curves for Test Walls

4.8 Summary and Conclusions

Analysis related to the force-based and, next-generation, performance-based seismic design of RM structural wall containing confined boundary elements is presented. This analysis was conducted with the experimental results of eleven RM structural walls tested under reversed cycles of quasi-static loading which included two previously reported walls by Shedid et al. (2010). The following conclusions can be made about the analysis presented regarding the seismic design of *RM* walls with boundary elements.

Recognizing the effects that plastic flexural rotations in the plastic hinge region can have on the shear strength of the wall, a method was proposed to quantify and predict potential shear failure in the walls at high levels of ductility. This was accomplished by adopting a smeared crack model based on the normal strain-adjusted shear strength expression (NSSSE) developed for masonry shear design.

This method avoids empirical reductions in the contributing shear strength of masonry with increased ductility, and instead relates the masonry compression strut capacity and crack angel directly to the average curvature of the critical region in the wall. Furthermore, based on this approach, a new method to predict the plastic hinge length of masonry walls is also proposed. This method recognizes the inherent planes of weakness that exist within masonry construction as well as effects of different reinforcement schemes can have on the shear spread of plasticity as a result of changes to the shear crack angle.

Wall strength was best predicted by assuming that reinforcement tied in the boundary element is capable of carrying compressive forces, while existing expressions to estimate the effective yield stiffness and displacement proved to be readily applicable to this wall category. Overall, the idealized load displacement response of the walls could be accurately modeled with Eqs. 4.15 - 4.20 such that the ratio of experimental to theoretical displacement at peak loading was found to be $\Delta_{Que} / \Delta_{Qu}$ = 103.4 % (c.o.v. = 10.3 %). Furthermore, the ultimate drift in the wall corresponding to a drop to 80% of Q_u was also accurately predicted with a ratio of $\Delta_{80\%Qu} / (\Delta_y + \Delta_{Qu})$ = 105.5% (c.o.v. 11.4%). The walls also had idealized displacement ductility levels ($\mu_{\Delta i}$) that varied from 4.0 to 10.2, indicating that there is a justifiable need to provide for new categories of RM SFRS within current seismic design standards.

Based on the need to develop next-generation of performance-based seismic design codes, analysis related to the occurrence of drift-based damage states has been presented. First, a set of damage states have been defined for RM walls based on the existing literature for RM and RC structural walls. The damage states have further been refined to reflect the fact that, unlike previous studies, crack width data can be included towards the analysis. The use of image correlation software was used first as a method to measure crack widths and to develop a relationship between crack width, crack spacing and curvature measurements that are more easily measured with the use of externally mounted displacement transducers. The critical drifts for each damage state and for each wall were determined, and a series of fragility functions were generated and checked using a Lilliefors test for confidence, indicating they were of a high quality.

The analysis presented in this paper provides the necessary information for a designer to carry-out seismic analysis for RM structural walls with confined boundary elements. Although a significant emphasis was placed on determining the behavior of the tested wall specimens, the results from this analysis illustrate how seismic behavior will vary, even amongst walls such those tested. It is likely that a more efficient and accurate design is possible through some extra computation effort on behalf of a designer when empirical or overly conservative

methods are abandoned. When, such a philosophy is adopted, it is very clearly observed actual wall response can be tailored towards the design objectives, whether they be force-, displacement- or performance-based. It is the hope that this, and future work will lead towards the level of detail within design often encountered with RC structural walls, and as such, will come more efficient and safe masonry structures.

4.9 Notation for Chapter 4

A_e = effective across-section area of a wall accounting for cracking (mm^2);
A_g = gross-cross-section area of wall (mm^2);
A_R = aspect ratio of wall (h_w/ℓ_w);
A_s = area of reinforcement (mm^2);
A_{sh} = area of horizontal reinforcement (mm^2);
A_{sh} = area of vertical reinforcement (mm^2);
b_w = width of the web of a wall (mm);
c = depth of neutral axis (mm);
D = Kolmogorov-Smirnov test parameter used for confidence test;
$D_{critical}$ = limit of Kolmogorov-Smirnov test parameter;
d_v = effective depth of member resisting shear taken as 80% of ℓ_w (mm);
E_m = Young's modulus of elasticity of masonry (MPa);
F = log-normal probability distribution;
f'_m = prism strength of grouted masonry unit (MPa);
f_y = yield strength of reinforcement (MPa);
f_{yh} = yield strength of horizontal reinforcement (MPa);
f_{yv} = yield strength of vertical reinforcement (MPa);
h_w = height of wall (mm);
I_e = effective moment of inertia reduced from the gross section considering the effects of (mm^4);
I_g = moment of inertia of an uncracked gross section (mm^4);
J = parameter used in NSSSE analysis considering the effects of material strengths;
k = shape factor used to determine shear stiffness;
K_{ft} = theoretical flexural stiffness of a wall (kN/mm);
K_{st} = theoretical shear stiffness of a wall (kN/mm);
K_{gt} = theoretical gross section stiffness of a wall (kN/mm);
K_{ge} = experimental gross section stiffness of a wall (kN/mm);
K_{ye} = experimental yield stiffness of a wall (kN/mm);
K_{yt} = theoretical yield stiffness of a wall (kN/mm);
$K_{y4.7}$ = theoretical yield stiffness of a wall determined from Eq. 4.7 (kN/mm);
$K_{y4.8}$ = theoretical yield stiffness of a wall determined from Eq. 4.8

(kN/mm);
$K_{y4.9}$ = theoretical yield stiffness of a wall determined from Eq. 4.9 (kN/mm);
K_y = theoretical secant yield stiffness of a wall (kN/mm);
ℓ_p = equivalent plastic hinge corresponding to estimates of top dispalcement;
$\ell_{p\phi}$ = experimental plastic hinge measured as extent of inelastic curvature ($\%\ell_w$);
ℓ_w = length of wall (mm);
M = number of wall specimens considered in fragility function;
M_u = ultimate moment capacity of wall (kN·m);
M_y = yield moment of wall (kN·m);
P_a = total level of axial stress applied to each wall including self-weight (MPa);
Q = load applied at the top of the wall (kN);
Q_{cr} = cracking load (kN);
Q_m = first moment of area;
Q_u = theoretical peak load (kN);
Q_{ue} = experimental peak load (kN);
Q_y = theoretical yield load (kN);
Q_{ye} = experimental yield load (kN);
s_c = crack spacing taken as nominal unit height (95 mm);
s_h = vertical spacing between horizontal reinforcing bars (mm);
s_v = horizontal space between vertical reinforcing bars (mm);
t = width of the a wall in the area of interest;
V = shear strength of wall (kN);
α = reduction factor used to related between I_e and A_e to I_g and A_g, respectively;
β = masonry compression strut parameter;
β_i = logarithmic standard deviation (dispersion);
Δ = top drift of a wall (%);
Δ_{Qu} = the idealized top drift of each wall at the peak lateral load (%);
Δ_{Que} = the experimental top drift of each wall at the peak lateral load (%);
$\Delta_{80\%Qu}$ = theoretical top drift of wall at 80% of peak load (%);
$\Delta_{u0.004}$ = theoretical top drift of wall with a limiting strain in masonry of 0.004 (%);
$\Delta_{u0.006}$ = theoretical top drift of wall with a limiting strain in masonry of 0.006 (%);
Δ_y = theoretical yield drift of wall (%);
Δ_{ye} = experimental yield drift of wall (%);
Δ_y* = idealized yield drift of wall (%);
Δ_{y1}* = theoretical yield drift of wall based on K_{y1} (%);
Δ_{y2}* = theoretical yield drift of wall from Priestley et al. (2007) (%);

Δ_{y3}* = theoretical yield drift of wall determined from Q_{ye}/Q_{ue} ratio (%);
δ = crack width size (mm);
δ_c = median crack width (mm);
δ_c = theoretical crack width determined from curvature readings (mm);
ε_{mu} = ultimate strain in masonry;
ε_n = normal strain in wall at critical shear location;
ε_y = yield strain of vertical reinforcement taken as 0.0025;
θ = shear crack inclination angle measured relative to the bed joint;
θ_i = median drift associated with a damage state (%);
λ = parameter to account for size effects in shear;
$\mu_{\Delta i}$ = idealized displacement ductility of wall;
v = average shear stress in macro element (MPa);
v_{mi} = local shear stress transmitted by aggregate interlocking forces at cracks (MPa);
ρ_{sh} = percent area of reinforcement in the horizontal direction (%);
ρ_{sn} = percent area of reinforcement in the vertical direction (%);
ϕ = average curvature measured at eth base of the wall to estimate flexural cracking (rad/mm);
Φ = normal probability distribution;
$\phi_{dv/2}$ = curvature measured at critical shear location (rad/mm);
ϕ_{ue} = experimentally measured ultimate curvature measured at a distance of ℓ_w of $\ell_w/2$ from the base (rad/mm);
ϕ_y* = idealized yield curvature of wall (rad/mm);

4.10 References for Chapter 4

Applied Technology Council (ATC). (2011). "Seismic performance assessment of buildings volume 1 - methodology." *ATC-58-1 75% Draft*, ATC, Redwood City, California.

Applied Technology Council. (ATC). (2009). "Quantification of building seismic performance factors." *Federal Emergency Management Agency FEMA-P695*, Washington D.C., USA.

Applied Technology Council. (ATC). (2007). "Interim testing protocols for determining the seismic performance characteristics of structural and non-structural components." *Federal Emergency Management Agency FEMA-461*, Washington D.C., USA.

Applied Technology Council. (ATC). (1998). "Evaluation of earthquake damaged concrete and masonry wall buildings." *Federal Emergency Management Agency FEMA-306*, Washington D.C., USA.

Applied Technology Council. (ATC). (1981). "Seismic design guidelines for highway bridges." *ATC-6*, Berkeley, CA, USA.

Banting, B. R. and El-Dakhakhni, W. W. (2012). "Seismic Design Parameters for Special Masonry Structural Walls Detailed with Confined Boundary Elements." Submitted to *ASCE Journal of Structural Engineering* Dec. 12, 2012.

Bohl, A., and Adebar, P. (2011). "Plastic hinge lengths in high-rise concrete shear walls." *ACI Structural Journal*. 108(2), 148-157.

Canadian Standards Association (CSA). (2004). "Design of concrete structures." *CSA A23.3-04 (R2010)*, CSA, Mississauga, Canada.

Cintrón, R. and Saouma, V. (2008). "Strain measurements with digital image correlation system Vic-2D." *Report Cu-NEES-08-06*, University of Colorado, U.S.A.

Citto, C., Wo, S. and Willam, K. (2011). "Image correlation diagnostics of masonry assemblies." *Proc., 11th North American Masonry Conference*, Minneapolis, Minnesota, Paper #6.02-1.

Davis, C. L. (2008). "Evaluation of design provisions for in-plane shear in masonry walls." Master of Science in Civil Engineering-Thesis, Washington State University, Washington, USA.

Destrebecq, J. F., Toussaint, E., and Ferrier, E. (2010). "Analysis of Cracks and Deformations in a Full Scale Reinforced Concrete Beam Using a Digital Image Correlation Technique." *Experimental Mechanics*. 51(6), 879-890.

Gulec, C. K. and Whittaker, A. S. (2009). Performance-Based Assessment and Design of Squat Reinforced Concrete Shear Walls. Technical Report MCEER-09-0010, University at Buffalo, New York, U.S.A.

Harris, H. G. and Sabnis G. M. (1999). *Structural Modeling and Experimental Techniques*. 2nd ed., CRC Press, New York, U.S.A.

Lawler, J., and Keane, D. (2001). "Measuring three-dimensional damage in concrete under compression." *ACI Materials Journal*, 98(6), 465-475.

Li, J. and Weigel, T. A. (2006). "Damage states for reinforced CMU masonry shear walls." *Advances in Engineering Structures, Mechanics and Construction*, 140(2), 111-120.

Lilliefors, H. W. (1967). "On the Kolmogorov-Smirnov test for normality with mean and variance unknown." *Journal of the American Statistical Association*, 62(318), 339-402.

Murcia-Delso, J., and Shing, B. (2011). "Fragility curves for in-plane seismic performance of reinforced masonry walls." *Proc., 11th North American Masonry Conference*, Minneapolis, Minnesota, Paper #2.04-3.

Pagni, C. and Lowes, L. (2004). "Predicting earthquake damage in older reinforced concrete beam-column joints." *PEER Report 2003/17*, Pacific Earthquake Engineering Research Center, University of California, Berkeley, U.S.A.

Park, Y. J. and Ang, A. H. S. (1985). "Mechanistic seismic damage model for reinforced concrete." *J. Struct. Eng.,* 111(4), 722-739.

Paulay, T., and Priestley, M., J., N. (1992). *Seismic Design of Reinforced Concrete and Masonry Buildings*, John Wiley & Sons, Inc., New York and Toronto, 139-142.

Paulay, T., and Uzumeri, S. M., (1975). "A Critical Review of the Seismic Design Provisions for Ductile Shear Walls of the Canadian Code and Commentary." *Canadian Journal of Civil Engineering*, 2(4), 592-600.

Porter, K., Kennedy, R., Bachman, R. (2007). "Creating fragility functions for performance-based earthquake engineering." *Earthquake Spectra*, 23(2), 471-489.

Priestley, M. J. N., Calvi, G. M., and Kowalsky, M. J. (2007). *Displacement-Based Seismic Design of Structures*, IUSS Press, Pavia, Italy.

Priestley, M. J. N., Seible, F. and Calvi, G. M. (1996). *Seismic Design and Retro Fit of Bridges*. John Wiley & Sons, Inc., New York and Toronto

Raffard D., Ienny P., and Henry, J. P. (2001) "Displacement and strain fields at a stone/mortar interface by digital image processing." *J. Testing & Eval.,* 29(2), 115–122.

Shedid, M. T., El-Dakhakhni, W. W. and Drysdale, R. G. (2010). "Alternative strategies to enhance the seismic performance of reinforced concrete-block shear wall systems." *J. Struct. Eng.*, 136(6), 676-689.

Smith, B. J., McGinnis, M. J., and Kurama, Y. C. (2010). "Full-field lateral response investigation of hybrid precast concrete shear walls." *3rd fib International Congress*, Washington D.C., USA.

Tung, S., Shih, M., and Sung, W. (2008). "Development of digital image correlation method to analyse crack variations of masonry wall." *Sadhana*, 33(6), 767-779.

Tusini, E., and Willam, K. (2008). "Performance evaluation of reinforced concrete masonry infill walls." *Report CU-NEES-08-04*, Centre for Fast Hybrid Testing, University of Colorado, USA.

Vic 2-D. (2009). Vic 2-D Digital Image Correlation Software, *Correlated Solutions*, www.correlatedsolutions.com/index.php/products/vic-2d-2009

Voon, K. C. and Ingham, J. M. (2006). "Experimental in-plane shear strength investigation of reinforced concrete masonry walls." *J. Struct. Eng.*, 132(3), 400-408.

CHAPTER 5: NORMAL STRAIN-ADJUSTED SHEAR STRENGTH EXPRESSION FOR FULLY-GROUTED REINFORCED MASONRY STRUCTURAL WALLS

5.1 Introduction

In this final chapter an analytical model is developed and applied towards a more rational design expression to estimate the shear strength and behavior of fully-grouted reinforced masonry structural walls. This paper was originally written as two parts (Formulation and Verification) but was merged into one. It is the sole work of the author with Dr. El-Dakhakhni acting in an advisory and editorial role to prepare the manuscript for journal submission as the article:

Banting, B. R. and El-Dakhakhni, W. W. (2013). "Normal Strain-Adjusted Shear Strength Expression for Reinforced Masonry Structural Walls." Submitted to *ASCE Journal of Structural Engineering* and Accepted with Revisions for Revise for Editor Only on Dec. 14, 2012.

5.2 Background

Since the conclusion of the test programs carried out by the Joint U.S.-Japan Technical Coordinating Committee on Masonry Research (TCCMAR) during the 1970's and 1980's, there has been little progress made to enhance the shear strength expressions used for masonry design. The experimentally derived expressions currently employed by North American design codes are based on the 45° cracked member assumption and truss analogy, where shear strength is expressed as an algebraic summation of resistance offered by masonry, axial load and shear reinforcement. By contrast, the Modified Compression Field Theory (MCFT), which has gained a wide acceptance within the concrete design community, demonstrates that the 45° cracked member assumption can be overly conservative. Yet the MCFT or similar equilibrium-based approaches have often been thought of as incompatible with masonry due to the latter's complex anisotropic behavior. However, seismic design detailing requirements within North America typically require the highly susceptible plastic hinge region of structural (shear) walls to contain vertical and horizontal steel reinforcement in *fully-grouted* concrete block units. Under these circumstances, the anisotropic effects are greatly reduced and the development of a simplified approach to estimate the equilibrium conditions at the shear-critical zone of masonry structural walls is possible. Tests on masonry panels conducted at McMaster University in Canada are used with existing literature to define a set of constitutive relationships for cracked masonry subject to stress states that are typical in

reinforced masonry structural walls. Subsequently, a methodology is proposed to accurately estimate the angle of inclination of shear cracking and the shear resistance offered by the horizontal reinforcement and the masonry compression strut accounting for aggregate interlock effects. The proposed Normal Strain-adjusted Shear Strength Expression (NSSSE) was found to predict the shear strength of 57 wall tests reported in literature with a mean ratio of experimental to theoretical strengths of $V_{Experimental} / V_{Theory} = 1.16$ (C.O.V. = 11.4%) and a 95% percentile of $V_{Experimental} / V_{Theory} = 0.98$.

5.3 Background

Experimental investigations to quantify the in-plane shear strength of concrete block masonry structural walls have been conducted over the past 50 years, yet currently there exists a relatively small and fragmented database of relevant results. This situation resulted mainly from the fact that several experimental programs have been conducted with testing methods or construction materials that are not representative of modern North American construction or design code requirements. Presently, masonry design codes such as the Masonry Standards Joint Committee (MSJC) (2011) and the Canadian Standards Association (CSA) S304.1 (2004a) adopt expressions to estimate the shear strength of masonry that are based on the results from a series of test programs carried out during the late 1970's and 1980's in the U.S.A. and Japan. The Joint U.S.-Japan Technical Coordinating Committee on Masonry Research (TCCMAR) encompassed several research programs that aimed at quantifying the shear strength of reinforced masonry (RM) structural walls and piers. From the data collected through the TCCMAR program, only four test programs presented results that were relevant to the development of design expressions for shear strength of fully-grouted concrete block masonry (Fattal and Todd, 1991). The test programs of interest include three series of masonry piers subject to double curvature (Sveinsson et al., 1985; Okamoto et al., 1987; and Matsumura, 1987) and one series of masonry structural walls subject to single curvature (Shing et al., 1991). Based on these tests, empirical shear strength expressions were developed (Matsumura, 1988a; Shing et al., 1990; and Anderson and Priestley, 1992) that served as the basis for the current North American shear design provisions. A list of the masonry shear design expressions in the current North American codes and the New Zealand design code (which adopts similar construction techniques and materials to those in its North American counterparts) is presented in Table 5.1. It is not the intention of the writers to give a detailed review or account of the derivation these or similar expressions, for which, interested readers may refer to Fattal and Todd, 1991; Voon and Ingham, 2007; and Davis, 2008.

Table 5.1 – Masonry and Concrete Design Shear Strength Expressions

$V_n = \left(\left(0.16\left(2-\frac{h_e}{d_v}\right)\sqrt{f'_m}\right)b_w d_v + 0.25P_{axial}\right)\gamma_g + \left(0.6A_h f_y \frac{d_v}{s_h}\right); 0.25 \le \frac{h_e}{d_v} \le 1.0;$ $V_n \le 0.4\sqrt{f'_m}\, b_w d_v \left[2-(h_w/\ell_w)\right];\ \ 0.5 \le h_w/\ell_w \le 1.0$	CSA S304.1 (2004)
$V_n = \left(\left(0.083\left(4.0-1.75\left(\frac{h_w}{\ell_w}\right)\right)\sqrt{f'_m}\right)b_w \ell_w + 0.25P_{axial} + 0.5\left(\frac{A_h}{s_h}\right)f_y \ell_w\right);$ $0.25 \le \frac{h_e}{d_v} \le 1.0;$ $V_n \le \left(\left[4+2.67\left(1-\frac{h_e}{d_v}\right)\right]\sqrt{f'_m}\, b_w d_v\right);\quad 0.25 \le \frac{h_e}{d_v} \le 1.0$	MSJC (2011)
$V_n = \left[\left(\left((C_1+C_2)0.15\sqrt{f'_m}\right)\right)+\left(0.9\frac{P_{axial}}{b_w d_v}\tan\alpha\right)+\left(C_3\frac{A_h f_y}{b_w s_h}\right)\right]b_w d_v;$ $\frac{P_{axial}}{b_w d_v}\ \&\left(0.9\frac{P_{axial}}{b_w d_v}\tan\alpha\right) \le 0.1 f'_m;\ \ V_n \le 0.45\sqrt{f'_m}$	SANZ (2004)
$V_n = \beta\sqrt{f'_m}\, b_w d_v + \frac{A_h f_y d_v \cot\theta}{s_h};\ \beta = \frac{0.40}{(1+1500\varepsilon_x)} \times \frac{1300}{(1000+s_{ze})};\ \theta = 29+7000\varepsilon_x;$ $\varepsilon_x = \frac{V_n h_w/d_v + V_n - 0.5P_{axial}}{2E_s A_v};\ \ V_n \le 0.25 f'_m\, b_w d_v$	CSA A23.3 (2009)

A_h = area of a single horizontal reinforcing bar (mm^2); A_v = area of reinforcement in tension under flexure (mm^2); b = factor to account for block type; C_1 = constant taken as $33\rho_v f_{yv}/300$; C_2 = constant taken as $0.42 \times (4 - 1.75(h_w/\ell_w))$; C_3 = constant for bar anchorage taken as 0.8; d_v = effective depth taken as $0.8\ell_w$ (mm); E_s = Young's modulus of reinforcement taken as 200 GPa; f'_m = prism strength of masonry (MPa); f_y = yield strength of horizontal reinforcement (MPa); f_{yv} = yield strength of vertical reinforcement (MPa); h_w = height of wall (mm); ℓ_w = length of wall (m); P_{axial} = axial force (N); s_h = vertical spacing of horizontal reinforcing bars (mm); V_n = shear strength (N); α = angle between the applied axial load and the centroid of the compression zone in the wall; β = factor to account for compression strut in concrete; γ_g = factor to account for partial grouting; ε_x = strain at mid-depth of section; θ = angle of crack inclination measured from the vertical; ρ_v = area of vertical reinforcement as a percent of gross wall area.

More recently, Voon and Ingham (2006) tested a series of six RM structural walls towards the development of the New Zealand design code (SANZ) 4230:2004 (2004) and El-Dakhakhni et al. (2012) reported the experimental results of a series of eight RM structural walls to evaluate the current CSA S304.1 (2004a) design expressions. Both of the aforementioned studies indicated that North American codes were overly conservative when compared to the New Zealand code. In addition, the study by El-Dakhakhni et al. (2012) indicated that, although developed for reinforced concrete (RC), better prediction of masonry wall shear strengths was achieved by directly applying the Canadian concrete design code

CSA A23.3 (2004b) shear strength expression. The CSA A23.3 (2004b) shear strength expression was derived from the method described by Bentz et al. (2006), which was also proposed by Sarhat and Sherwood (2011) as a better predictor of the shear strength of RM beams.

The study presented herein focuses on addressing the deficiencies in the current empirically derived masonry shear strength expressions. This is achieved by developing a simplified mechanics-based approach to solve for force equilibrium and strain compatibility in cracked masonry macro elements. The next sections will present a brief summary of relevant literature pertaining to the shear behavior of concrete and masonry at the macro-level. This will be followed by a series of analytical derivations and simplifications to establish a relationship between a wall's peak shear strength and the normal strain at critical locations. The proposed Normal Strain-adjusted Shear Strength Expression (NSSSE) will be subsequently validated using experimental tests on masonry macro elements and full-scale structural walls and piers.

5.4 Shear Behavior of Reinforced Concrete at the Macro-Level

The state of stress and strain at any given point within a masonry structural wall will vary with the loading conditions on the wall and the location of the point of interest within the wall as depicted in Fig. 5.1a. Macro elements (or panels), which can be theoretically isolated for analysis or physically constructed for testing, represent regions of larger structural elements, such as a walls, that can be modeled and analyzed to gain a better understanding of composite material behavior. Physical concrete macro elements (panels) are comprised of the same materials as the large-scale structural wall of interest, but are constructed with smaller dimensions and tested under well-defined and controlled boundary and stress conditions. Based on tests of RC macro elements at the University of Toronto, Canada, Vecchio and Collins (1982) and (1986) developed a smeared crack model that could accurately predict the shear behavior of RC. Their Modified Compression Field Theory (MCFT) utilizes a series of material constitutive relationships, stress-strain compatibility equations and force equilibrium expressions to quantify the shear strength of RC elements. The MCFT was developed to encompass a wide range of design details and load conditions that lent the MCFT well towards finite element analysis (FEA) of much larger structures.

In such FEA models, the RC component is idealized as a series of 2-D homogenized membrane (macro) element with constant stress and strain similar to that which is shown in Fig. 5.1b for masonry. Forces in the element are expressed in terms of the average stresses that develop in the constituent materials (i.e. the concrete and the steel reinforcement). A smeared crack model is used to solve for

equilibrium of the element for a particular stress state considering the non-linearity of the constituent materials, whereby, the orientation of the principal stress axes are used to determine the orientation of the cracks within the concrete. In this model, the principal compression stress is assumed to be carried by a series of concrete compression struts of equal width separated by cracks that form normal to the principal tensile stress direction. Stress-strain compatibility is assumed between the reinforcement and concrete on either side of the cracks such that the angle formed by the principal stress is assumed to coincide with the angle of principal strain. Material models also consider the strength degradation effects that lateral tensile strains have on: the diagonal strut's compressive strength, the tension stiffening effect of reinforcement embedded in concrete and the shear stress transferred by aggregate interlock along the crack surface. The results of Walraven (1981) were used by Vecchio and Collins (1986) to develop a rational means to estimate the maximum shear force that can be transferred across an open crack based on the maximum aggregate size in the concrete and the crack opening width.

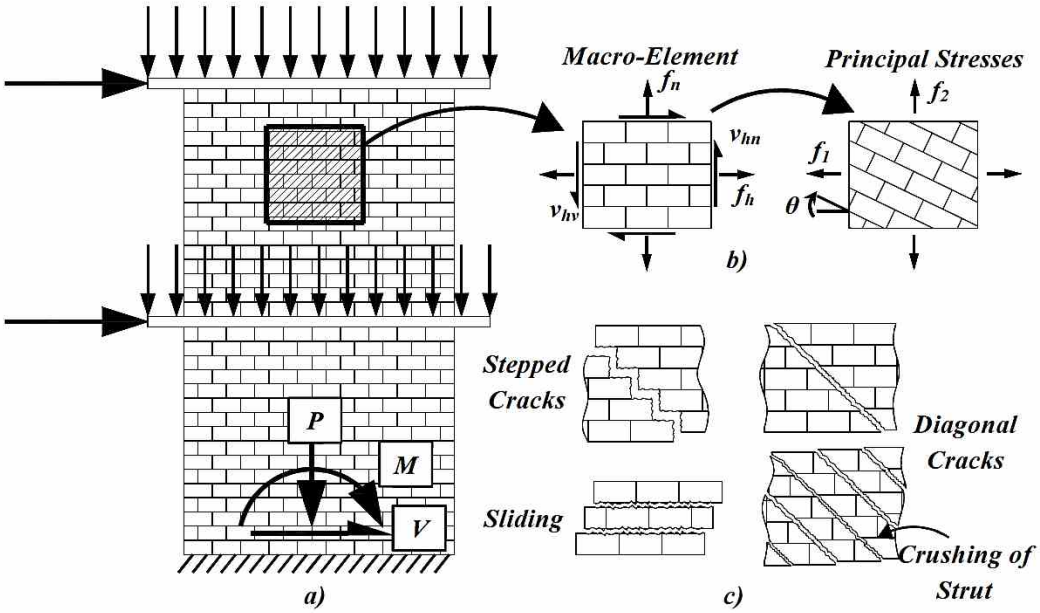

Figure 5.1 – Behavior of RM subjected to Combined Loading: a) A Typical RM Structural Wall subject to Axial and Shear Forces and an Applied Moment, b) Equivalent RM Macro-Element, c) Typical Shear Failure Modes in Masonry

Interested readers are directed to Vecchio and Collins (1986) and Collins and Mitchell (1991) for the full set of equilibrium equations required to analyze concrete elements subject to a general state of stress. Further work on the MCFT moved towards facilitating a simplified approach that is appropriate for design

applications and back-of-the-envelope calculations, where only the peak shear strength is typically required. Finally, Bentz et al. (2006) proposed the Simplified Modified Compression Field Theory (SMCFT) as a relatively simple, but accurate, means to estimate the peak shear strength in RC members with simple hand calculations and minimal iteration. This method has been adopted by the Canadian concrete design code CSA A23.3 (CSA 2004b) as the *General Method* for shear design. The SMCFT provides a rational means to estimate the crack angle (θ), which relates to the resistance offered by the shear reinforcement, and the concrete strength parameter (β) as described in Table 5.1. The following section will highlight the masonry-related experimental work that will be used to develop a similar set of constitutive equations to that of RC as described above.

5.5 Shear Behavior of Reinforced Masonry at the Macro-Level

Only a limited number of tests on concrete block macro elements are reported in the literature reviewed by the writers, with even fewer results that included steel reinforcement. However, in a comprehensive experimental program, Khattab (1993) and Drysdale and Khattab (1995) tested 36 unreinforced and reinforced concrete block macro elements under various bi-axial stress states at McMaster University, Canada. The macro elements were constructed as square panels measuring 1,200 mm × 1,200 mm × 190 mm. The test parameters included varying the following parameters: the angle θ between principal compression stress and the bed joint orientation, the area of and relative ratio between the vertical and the horizontal reinforcement, the presence of grout flues that run normal and parallel to the bed joints and the ratio of the applied principal stresses. These experimental results were used to derive the necessary constitutive properties to develop a macro element FEA model that was presented by El-Dakhakhni et al. (2006). It was concluded that the anisotropy of masonry was most pronounced in unreinforced panels, with grout flues that ran only normal to the bed joints. Within these panels the distribution of cracks and the ultimate failure mechanisms were strongly dependent upon the orientation of the average principal stresses to the bed joints. Failure of all unreinforced macro elements was generally contingent upon the existence of the masonry inherent planes of weakness (i.e. mortar joints). It was typical to have failure dominated by cracks that form in either a stepped or a straight-line path along the bed and/or head joints. By comparison, the degree of anisotropy in masonry macro element behavior was notably reduced by maintaining continuous grout flues in both orthogonal directions with the presence of vertical and horizontal reinforcement embedded within.

Tikalsky et al. (1995) tested eight RM panels of dimensions 800 mm tall × 1,200 mm wide × 140 mm thick under a simultaneous axial compressive stress applied normal to the bed joints and a lateral tensile stress applied parallel to the bed

joints. It was observed that with increased lateral tension, the peak compressive stress, and corresponding strain, were reduced in the masonry. Liu et al. (2006) also tested a total of 86 unreinforced fully-grouted concrete block masonry square panels of dimensions 800 mm × 800 mm × 190 mm and 1,000 mm × 1,000 mm × 190 mm. The panels were each tested under varying principal stress ratios as well different angles θ. In their study, Liu et al. (2006) developed material models for the uniaxial compressive and tensile strengths of masonry that account for its anisotropic characteristics.

5.6 Current Research and Focus

Although the MCFT and SMCFT were both experimentally validated using macro-level tests of RC panels, the MCFT and SMCFT compatibility equations have been derived assuming concrete to be an isotropic material at the macro-level. As a result, the MCFT and SMCFT are not directly applicable for use with RM structural walls for the following reasons:

1. Concrete block masonry construction is anisotropic or orthotropic at best. This is because of the internal structure of the units, the inherent weak planes within masonry construction formed by bed and head mortar joints and the interaction between masonry constituent materials.

2. Typical stress conditions, reinforcement details and cross-sectional properties in a loadbearing structural masonry wall differ significantly from those occurring in RC T-beams used to verify the MCFT and the SMCFT.

3. Masonry walls are highly composite and are constructed of several materials (i.e. concrete block, mortar, grout, and vertical and horizontal steel reinforcement). The interaction between these different materials when subjected to different types of load conditions (e.g. pure compression versus pure shear) causes a significant change in the behavior of RM when compared to RC. As a result, at the macro-level, masonry has different constitutive relationships that are heavily dependent on the angle of principal stresses relative to the bed joint.

4. RM walls also differ in construction and detailing from their RC counterparts. This situation has resulted from several fundamental and practical limitations in masonry construction including: bar spacing and arrangements (that must conform to the modular nature of masonry units), the potential for ungrouted cells and accidental voids in head joints within a wall, the use of different block geometries, the use of bed joint shear reinforcement or single-leg shear stirrups (as opposed to the standardized double-leg stirrups/horizontal reinforcement in RC wall construction) and the potential for cracking and sliding to form along mortar joints, to name but a few.

The difficulty in consolidating these inherent differences between RM and RC materials precludes a direct adoption of MCFT to masonry for macro elements. Nevertheless, the observations by Sarhat and Sherwood (2011) and El-Dakhakhni et al. (2012) indicated that at the larger (macro) scale of masonry beams and structural walls, respectively, the SMCFT has a potential for adoption in masonry shear design. Such adoption can be possible after accounting for the inherent differences between RM and RC as explained above, which is the focus of the current study. In the following sections, a set of constitutive relationships will be developed considering the equilibrium of a cracked masonry macro element to predict its shear strength. These relationships will be integrated into a NSSSE that will be verified using RM panels and structural (shear) wall test results.

5.7 Equilibrium of Cracked Masonry Macro Elements

Masonry structural (shear) walls are typically designed for a combination of compressive axial forces (P), lateral forces (V) and flexural moments (M) due to wind or seismic excitation as shown in Fig. 5.1a. This results in complex stress-strain interactions that are unique to the location of interest within a wall. For a particular stress state, a shear failure may occur in the form of one or more of the following: bed joint sliding, diagonal stepped cracking, the formation of a single diagonal crack (typically a brittle failure), the formation of several diagonal cracks (a pseudo-ductile failure) or a shear compression failure due to the crushing of masonry (Drysdale and Hamid 2005) as depicted in Fig. 5.1c. The occurrence of a shear failure mechanism depends upon several parameters related to the wall's cross-section detailing, boundary conditions and the relative levels of different straining actions. Shear failure mechanisms usually also develop in conjunction with inelastic material behavior such as the yielding of vertical and/or horizontal reinforcement, the opening of cracks as well as the possibility of masonry crushing or spalling.

North American shear strength expressions presented in Table 5.1 have been developed assuming a diagonal tension failure along a fixed 45° cracking plane in a masonry wall. The consequence of this assumption is an unconservative estimate of shear resistance offered by the reinforcement and the masonry when $\theta < 45°$ and overly conservative estimates when $\theta > 45°$, respectively. For the forthcoming analysis, θ is meant to represent the orientation of shear cracks and principal stresses relative to the bed joint as defined in Fig. 5.1b, based on strain compatibility as will be described in further sections. To overcome this, empirical reductions of 0.5 and 0.6 to the reinforcement strength have been applied to the shear design expressions in the MSJC (2011) and the CSA S304.1 (2004a), respectively. In addition, the shear resistance of the masonry has also been empirically derived based on the moment gradient effects occurring in walls of varying aspect ratio (given as h_e/d_v in Table 5.1) and the level of applied axial

load. Although it is widely recognized that aggregate interlock mechanisms, and thus the local conditions at the shear crack surfaces, contribute significantly to the masonry shear strength, differences in these mechanisms and conditions are not accounted for in the current masonry shear strength expression.

To develop a more rational expression to predict the shear strength of RM walls, it is necessary to account for the anisotropic characteristics of masonry when subjected to bi-axial states of stress along different orientations to the bed joint. It is also necessary to move beyond the assumption of a fixed 45° crack angle and apply a rational methodology to estimate the crack spacing and the shear transfer through aggregate interlock of masonry components at crack locations. In addition, the shear resistance of masonry should consider both the level of applied moment and contribution of axial forces by a rational determination of the level of normal strain at the critical location. However, prior to considering the above, the first step to develop a rational analysis is to establish the necessary equilibrium equations for masonry macro elements under different stress states.

A closer schematic view of a cracked masonry macro element is presented in Fig. 5.2a, where it is subjected to an average normal stress f_n along the axis normal to the bed joint (n), an average horizontal stress f_h along the axis parallel to the bed joint (or normal to the head joint) (h), and a shear stress v_{hn}. In the figure, the macro element is divided into identical crack-separated struts inclined at an angle θ to the bed joint at an average spacing of s_θ. The masonry struts are subjected to principal tensile stresses (f_1), which are oriented perpendicular to the cracks, and principal compressive stresses (f_2), which are oriented along the struts. In addition, the vertical and horizontal reinforcements that run along the n and h axes, respectively, of the macro element are smeared, resulting in reinforcement ratios of $\rho_{sn} = A_{sn} / s_n b_w$ and $\rho_{sh} = A_{sh} / s_h b_w$ where A_s, s_n, s_h and b_w are the area of a single bar (mm^2), the average spacing between the vertical bars (mm), the average spacing between the horizontal bars (mm) and the width of the masonry unit (mm), respectively. Finally, perfect bond conditions are assumed between the reinforcement and the grout and between the grout and the masonry units. As such, equilibrium can be based on the average stresses, which are assumed to be constant over each side area of the macro element as described by Eqs. 5.1 and 5.2. As such, looking along the horizontal axis, the average net force is determined by integrating the horizontal stresses on the masonry and reinforcement over their corresponding areas, respectively.

$$\int_{A_g} f_h dA = \int_{A_m} f_{mh} dA + \int_{A_s} f_{sh} dA \tag{5.1}$$

$$f_h = f_{mh} + \rho_{sh} f_{sh} \tag{5.2}$$

By neglecting the small area of masonry displaced by the reinforcement (i.e. $A = A_m - A_s \approx A_m$), and enforcing equilibrium, the stresses of the macro element (f_h), the masonry (f_{mh}) and the reinforcement (f_{sh}) can be obtained. As such, considering equilibrium under the stress state shown in Fig. 5.2b will yield the following:

$$f_h = \left(f_{m1} - \frac{v_{hn}}{\tan\theta} \right) + \rho_{sh} f_{sh} \tag{5.3}$$

$$f_n = \left(f_{m1} - v_{hn} \tan\theta \right) + \rho_{sv} f_{sv} \tag{5.4}$$

Where, the average stress transmitted by the reinforcement is limited to their yield strengths ($f_{sh} \leq f_{shy}$ and $f_{sn} \leq f_{sny}$) and the principal tension stress carried by the masonry is f_{m1}.

Finally, the average shear stress acting on the macro element can also be expressed in terms of the principal stresses in the masonry strut (f_{m1} and f_{m2}) as given in Eq. 5.5.

$$v_{hn} = \frac{\left(f_{m1} + f_{m2} \right)}{\left(\tan\theta + \frac{1}{\tan\theta} \right)} \tag{5.5}$$

The conditions shown in Fig. 5.2b represent the average stresses of the macro element. However, it would be anticipated that at each crack location there will be localized stress variations. At these points, reinforcement that crosses a crack will have to carry higher local stresses than the reinforcement embedded within the masonry due to the reduction in the resistance area (i.e. no tension will be carried by cracked masonry). The increased stress in the reinforcement is represented by local stresses $f_{sn,cr}$ and $f_{sh,cr}$. Although at each crack location no principal tensile stress can be transmitted by the masonry, it may be possible for shear stresses to be transmitted via aggregate interlock along the crack interface. This local shear stress is identified as v_{mi} in Fig. 5.2c and occurs as a result of the tendency of cracks in concrete-based materials (i.e. mortar, grout, and masonry units) to form in the cement matrix passing around the aggregates, thus resulting in a rough crack surface. A normal stress (f_{mi}), as identified in Fig. 5.2c, results in the following equilibrium equations given by Eqs. 5.6 and 5.7 for the parallel and normal to the bed joint axes, respectively, where, as previously stated, the stress carried by the reinforcement is limited by its yield strength along both axes ($f_{sh,cr} \leq f_{shy}$ and $f_{sn,cr} \leq f_{sny}$).

$$f_{sh}\rho_{sh}\sin\theta + f_{m1}\sin\theta = f_{sh,cr}\rho_{sh}\sin\theta - f_{mi}\sin\theta - v_{mi}\cos\theta \tag{5.6}$$

$$f_{sn}\rho_{sn}\cos\theta + f_{m1}\cos\theta = f_{sn,cr}\rho_{sn}\cos\theta - f_{mi}\cos\theta - v_{mi}\sin\theta \tag{5.7}$$

The preceding sets of equations can be used to solve for force equilibrium of a cracked masonry macro element. The next section will detail the strain compatibility of the macro element and how the stress-strain interaction is developed.

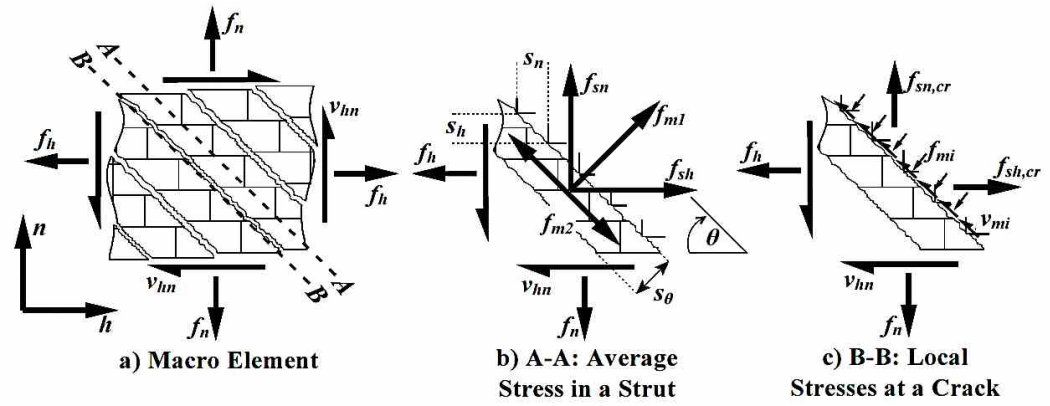

Figure 5.2 – State of Stress of a Cracked Masonry Macro-Element

5.8 Strain Compatibility in Cracked Masonry Macro Elements

Through the assumption of a perfect bond, the state of strain within the macro element constituent materials can be determined assuming that the angles of principal stresses and principal strains coincide and can both be represented by θ. This assumption has been experimentally verified by Khattab (1993) for masonry panels. The resulting state of strain of the macro element is expressed using Mohr's circle as depicted in Fig. 5.3. The principal tensile strain (ε_1) represents the average tension strain acting perpendicular to the masonry struts and across the cracks, the principal compressive strain (ε_2) acting along the compression strut of the cracked masonry and the average strains along the vertical and horizontal axes are represented by ε_n and ε_h, respectively. Finally, the average total shear strain of the element is given by γ_{hn} in Fig 5.3. The Mohr's circle analysis yields Eqs. 5.8-5.10, where compressive strains are taken as negative while tensile strains are considered positive.

$$\tan^2\theta = \frac{\varepsilon_h - \varepsilon_2}{\varepsilon_n - \varepsilon_2} \tag{5.8}$$

$$\varepsilon_1 = \varepsilon_h + \varepsilon_n - \varepsilon_2 \tag{5.9}$$

$$\gamma_{hn} = \frac{2(\varepsilon_h - \varepsilon_2)}{\tan\theta} \tag{5.10}$$

The preceding equilibrium and compatibility equations for of a masonry macro element under a general state of stress and strain depend on developing homogenized properties that account for the effect of different constituent materials on the overall behavior of the composite masonry macro element. However, before attempting this, it should be noted that the inclination of masonry compression struts by the angle θ means that, except for the special case of θ = 90°, the characteristics of the compression strut are unlikely to resemble that of the typical uniaxial prism tests, specifically their strength $f'_{m(90°)}$. Therefore, there is a need to consider the anisotropy of masonry construction in altering the compressive strength of masonry as a function of the load orientation with respect to the bed joint. The implications of this unique masonry characteristic will be discussed in the following section.

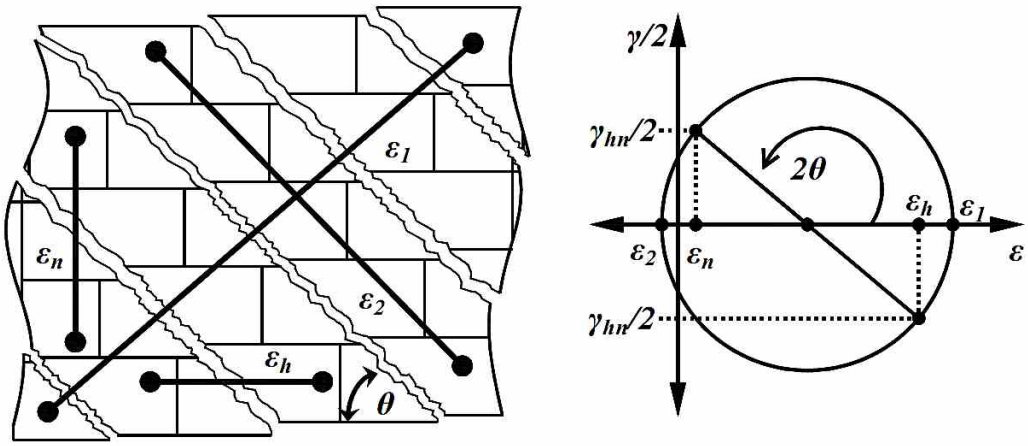

Figure 5.3 – State of Strain in a Masonry Macro-Element

5.9 Effects of the Principal Stress Orientation on the Masonry Compressive Strength

In practice, the typical means of establishing masonry strength is with uniaxial compression tests on masonry assemblages, in the form of prisms, which are constructed as a composite system representative of masonry wall properties (i.e. block laid in running bond with representative mortar and grouting). These tests subject a small masonry assemblage (prism) to a pure compression stress applied

perpendicular to the bed joint (θ = 90°) which represents a ratio of principal stresses of f_{m2}/f_{m1} = -1/0. The CSA S304.1 (2004a) suggests that a reduction in compressive strength from $f'_{m(90°)}$ is expected if compressive forces are applied parallel to the bed joint (i.e. f_{m2}/f_{m1} = 0/-1 and θ = 0°) by a factor χ. This reduction in strength varies from $f'_{m(0°)} = 0.5\ f'_{m(90°)}$ to $0.75\ f'_{m(90°)}$ depending on the degree of continuity of grout flues normal to the compressive forces. Similarly, compression tests on masonry assemblages where $0° < \theta < 90°$ have indicated that the compressive strength of masonry at different angles, $f'_{m(\theta)}$, can deviate significantly from the uniaxial prism strength $f'_{m(90°)}$. This well-documented anisotropic behavior in masonry assemblages has been known to be dependent on several key interacting factors including the masonry unit, grout and mortar strengths, the workmanship of construction and the failure mechanisms (Hamid and Drysdale 1980; Drysdale and Hamid 2005). However, wall boundary conditions, overall stress and strain states and ultimate failure mechanisms may be significantly different from those of small assemblages. Therefore, to establish a relationship between $f'_{m(90°)}$ and $f'_{m(\theta)}$, the results from tests on large masonry panels loaded under pure compression as shown in Fig. 5.4a with θ = 0°, 22.5°, 45°, 67.5° and 90° will be utilized. The limited experimental results from Liu et al. (2006) and Drysdale and Khattab (1995) are reproduced in Fig. 5.4b. Based on regression analysis, the writers propose the compressive strength-orientation interaction relationships for $f'_{m(\theta)}$ given in Eq. 5.11 and 12.

$$\frac{f'_{m(\theta)}}{f'_{m(90^o)}} = (4.74\times10^{-4})\theta^2 + (-2.43\times10^{-2})\theta + 0.883 \le 1.0 \qquad \left[\theta \le 45^o\right] \tag{5.11}$$

$$\frac{f'_{m(\theta)}}{f'_{m(90^o)}} = (2.66\times10^{-4})\theta^2 + (-3.04\times10^{-2})\theta + 1.58 \le 1.0 \qquad \left[\theta > 45^o\right] \tag{5.12}$$

It should be noted that the presence of grout voids or the disruption of grout continuity in panels, where knock-out web units are not used, can have a substantial effect on strength characteristics as evidenced by the reduction in strength when $\theta = 22.5^o$ and $\theta = 67.5^o$ in Fig. 5.4b. In addition, the combined effects of simultaneous axial and lateral stresses would also be expected to influence $f'_{m(\theta)}$. To solve for equilibrium for a given state of stress using Eqs. 5.3-5.12, it is necessary to develop a set of constitutive relationships that account for the effect of the angle θ as well as lateral tensile strains ε_1 on the masonry compression strut strength $f'_{m(\theta)}$. These will be developed in the following sections.

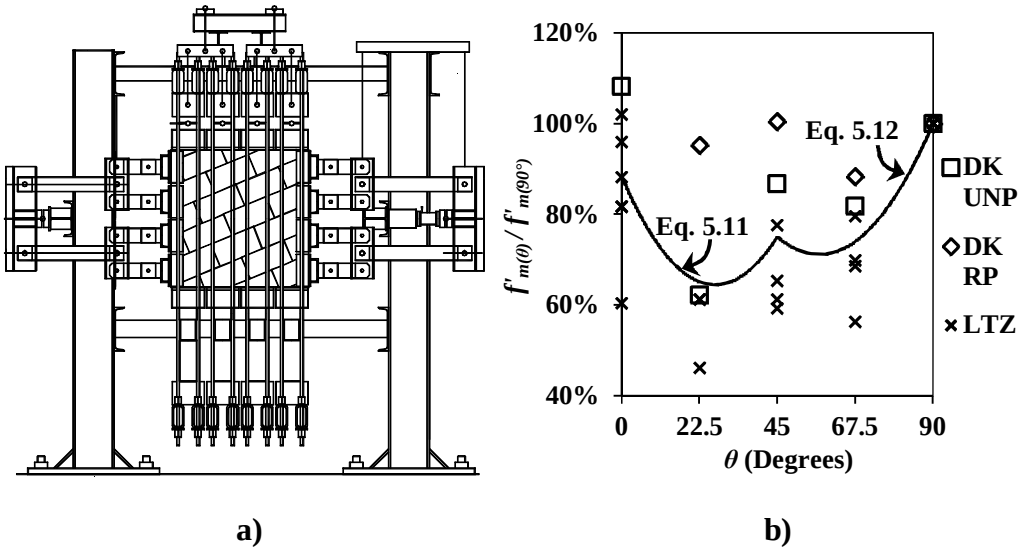

Figure 5.4 – Effect of Compressive Stress Angle on Peak Compressive Strength for Unreinforced Panels: a) Biaxial Test Set-up (El-Dakhakhni et al. (2006), b) Test Results by Drysdale and Khattab (1995) (DK UNP), Reinforced Panels by Drysdale and Khattab (1995) (DK RP) and Unreinforced Panels by Liu et al. (2006) (LTZ)

5.10 Constitutive Relationships

5.10.1 Cracked Masonry under Bi-axial Stress

Tikalsky et al. (1995) demonstrated that RM subject to axial compression shows a reduction in compressive strength capacity under the simultaneous application of lateral tensile forces. However, only masonry macro elements with axial stresses applied normal to the bed joint (θ = 90°) were tested. Drysdale and Khattab (1995) demonstrated that in addition to a reduction in strength caused by lateral tensile stresses, the angle by which the principal stresses are orientated will also cause a reduction in compressive strength. Therefore, to consolidate this complex behavior into a usable stress-strain relationship, the effect of θ as well as the lateral tension strains ε_1 must be considered within the compressive stress-strain relationship of the masonry compression struts within a macro element.

To establish this relationship for masonry, a Hognestad stress-strain model is adopted to represent masonry under compression as given by Eq. 5.13 and shown in Fig. 5.5a, where the strain corresponding to the peak compressive stress (ε_o) for masonry is taken to be -0.0018 (i.e. 0.0018 in compression) (Drysdale and Hamid, 2005).

$$f_{m2} = f_{m2,\max}\left(2\frac{\varepsilon_2}{-0.0018} - \left(\frac{\varepsilon_2}{-0.0018}\right)^2\right) \tag{5.13}$$

The relationship given by Eq. 5.13 will determine the value of the average compression stress carried by the masonry in the compression strut (f_{m2}) based on the peak compressive stress ($f_{m2,max}$). Under uni-axial compression, $f_{m2,max}$ would be the value of $f_{(\theta)}$ determined by Eqs. 5.11 or 5.12. However, in macro elements, the principal lateral strain (ε_1) must also be considered. To determine this effect, the principal stress ratios from ten RM panels reported by Drysdale and Khattab (1995) (DK) and five RM panels reported by Tikalsky et al. (1995) (TAH) at ultimate conditions are shown plotted in Fig. 5.5b against the lateral tensile strain ratio. Whereby, the peak compressive stress (f_{m2}) reported in the respective studies are normalized by the converted strength $f'_{m(\theta)}$ using Eqs. 5.11 or 5.12, as applicable. The normalized strength is plotted against the principal tensile strain (ε_1) normalized by ε_o defined previously. This provides an upper limit to the peak masonry compressive strength when subject to lateral strains. The best fit curve is shown in Fig. 5.5c and its equation is given by:

$$f_{m2,\max} = \frac{f'_{m(\theta)}}{0.41 + 0.33\frac{\varepsilon_1}{\varepsilon_o}} \leq f'_{m(\theta)} \tag{5.14}$$

It is evident from Fig. 5.5c that the compression stress-strain characteristics of a masonry strut, acting at an angle θ to the bed joint, which is simultaneously subjected to lateral tension strains, can differ significantly from the characteristics derived from prism tests.

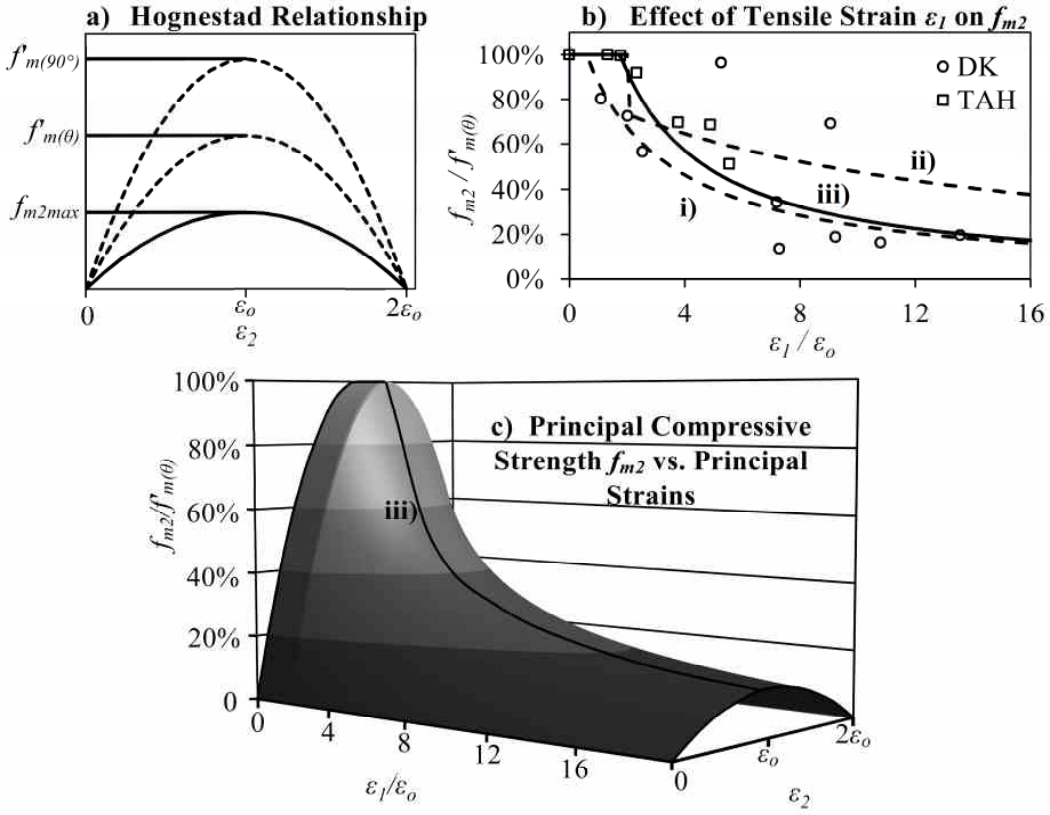

Figure 5.5 – Stress-Strain Relationship for Masonry: a) Hognestad Relationship, b) Masonry Subject to Lateral Tension: i) = Vecchio and Collins (1986) line of best fit, ii) = Tikalsky et al. (1995) line of best fit and iii) = Eq. 5.14 on Tests by Drysdale and Khattab (1993) (DK) and Tikalsky et al. (1995) (TAH), c) Compressive Strength versus Normal and Lateral Strains

5.10.2 Cracked Masonry under Uniaxial Tension

Prior to cracking, the tensile strength of masonry is assumed to act linearly elastic according to Eq. 5.15.

$$f_{m1} = E_m \times \varepsilon_1 \leq f_{cr(\theta)} \tag{5.15}$$

Where the average principal tensile stress in the masonry is given by f_{m1}, the Young's modulus of masonry is given as E_m and the cracking stress, $f_{cr(\theta)}$, is taken as a function of the angle of bed joint orientation, θ.

The failure plane of masonry under pure tension can occur along different paths that may or may not follow mortar joints as shown in Fig. 5.6a by the crack patterns i and ii, respectively. Due to this effect, a generalized cracking strength of

unreinforced masonry can be difficult to establish at different angles of θ. To determine an accurate model for measuring the effect of tensile stress at different angles, the experimental results from Drysdale and Khattab (1995) and Liu et al. (2006) will be utilized. To be consistent, only the panels where cracks form along paths normal to the applied tension will be considered. Therefore, the unreinforced panel results to be used are those reported by Drysdale et al. (1995) and Liu et al. (2006) with θ = 0° or 90° only as shown in Fig. 5.6a, crack pattern ii. To account for different values of θ, reinforced panels with θ = 22.5°, 45° and 67.5° reported by Drysdale and Khattab (1995) are also considered because they also tended to demonstrate cracking planes in straight lines as shown by Fig. 5.6a crack pattern ii. Reinforced panels are used in this analysis based on the observation that, up to the cracking stress, the reinforcement plays a negligible role in carrying tensile stresses. The experimental results for the aforementioned test programs are reproduced in Fig. 5.6b in terms of the cracking stress normalized by the square root of the prism strength versus the angle θ. Based on regression analysis, the writers propose the following relationship between the cracking strength $f_{cr(\theta)}$, the prism strength $f'_{m(90°)}$ (both in MPa) and θ (in degrees) as given by Eq. 5.16.

$$\frac{f_{cr(\theta)}}{\sqrt{f'_{m(90^o)}}} = \left(-3.93\times10^{-5}\right)\theta^2 + \left(3.49\times10^{-3}\right)\theta + 0.212 \tag{5.16}$$

After cracking occurs, the behavior of RM differs significantly from unreinforced masonry because of the ability of the reinforcement that crosses cracks to carry tensile stresses. The masonry macro element shown in Fig. 5.2a possesses cracks that were assumed to occur at discrete locations spaced at a distance s_θ (Fig. 5.2b). Between these locations it would be expected that uncracked masonry remains in perfect bond with the reinforcement, and thus, the former would still carry tensile forces. The redistribution of these tensile forces on the uncracked masonry results in a masonry tension stiffening effect as described by Attkinson and Hammons (1997). The capacity of the uncracked masonry strut to carry the tensile stress f_{m1} is expected to soften as tensile strains ε_1 increase. To account for this post-cracking effect, El-Dakhakhni et al. (2006) proposed Eq. 5.17 based on the test panels from Drysdale and Khattab (1995), which is also plotted in Fig 6c.

$$f_{m1} = \frac{f_{cr(\theta)}}{1+400\varepsilon_1} \le f_{cr(\theta)} \tag{5.17}$$

The preceding derivations presented the necessary constitutive relationships for a masonry macro element under the average state of stress shown in Fig. 5.2a. However, to maintain equilibrium across open cracks, a portion of the shear stress must be transferred via aggregate interlock as was shown in Fig. 5.2c. To account

for this phenomenon, the necessary relationships will be derived in the following section.

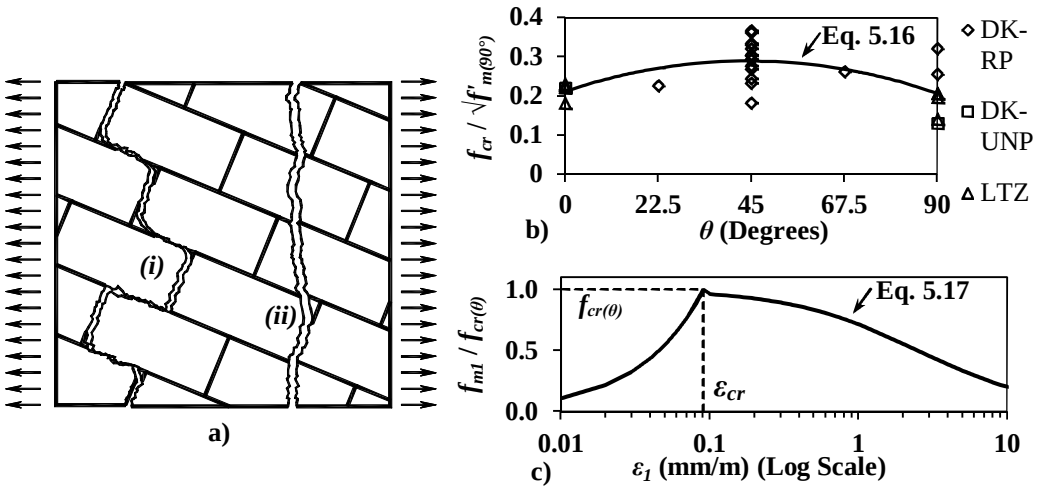

Figure 5.6 – Cracked Masonry Behavior: a) Comparison between Unreinforced and Reinforced Panel Crack Locations, b) Variation of Cracking Strength with θ generated for Drysdale and Khattab (1995) Reinforced Panels (DK-RP), Drysdale and Khattab (1995) Unreinforced Panels (DK-UNP) and Liu et al. (2006) (LTZ), and c) Tension Stiffening Effect of Masonry between Cracks

5.11 Shear Transfer via Aggregate Interlock in Cracked Masonry

Traditionally, experimental testing has focused on evaluating the capabilities of cracked unreinforced masonry to transmit shear stresses through bed joint sliding. Before and during crack initiation at the mortar-unit interface, shear resistance is obtained via internal friction generated by the applied axial load normal to the sliding plane. This phenomenon is dependent on the level of normal stress that acts against excessive openings of cracks. If the average crack width (w) exceeds the size of protruding aggregates along the crack surface, no contact, and hence no friction, will exist. It can be seen then that the aggregate interlock contribution of mortar along bed joint cracks, which is comprised of very fine aggregates, will be dwarfed by the contributions of the concrete block and grout which are comprised of larger aggregate sizes, when cracks penetrate the grout and the face shells of the masonry units. The writers are unaware of any studies that quantified the shear transfer via aggregate interlock forces over cracks of various widths for different combinations of mortar, block and grout (with different aggregate sizes). Nevertheless, Vecchio and Collins (1986) used the experimental work by Walraven (1981) to determine an upper bound ($v_{c,max}$) to the maximum shear that may be transferred across an open crack in concrete (v_{ci}) based on the maximum aggregate size (a_g), the crack width and cylinder strength of concrete (f'_c). The

expression given by Eq. 5.18 conservatively neglects the contribution of compressive normal stress f_{mi} shown in Fig. 5.2c.

$$v_{ci} \le v_{c,\max} = \frac{0.18\sqrt{f'_c}}{0.31 + \frac{24w}{(a_g + 16)}} \tag{5.18}$$

To adapt this expression for the composite nature of masonry materials, the interaction between the concrete block, grout and mortar must be considered. Subsequently, a_g will be taken as a weighted mean of the standard aggregate sizes in constituent masonry materials (coarse grout: $a_{g,gr}$ = 10 mm, fine grout: $a_{g,gr}$ = 2.5 mm, mortar: $a_{g,mo}$ = 2.5 mm and concrete block: $a_{g,bl}$ = 5.0 mm. These values were chosen based on the grading requirements specified by the mortar and grout standard CSA A179 (CSA 2004c) and the concrete materials standard CSA A23.1 (2009), respectively. Therefore, the contribution of each of these materials towards an average shear resistance will vary with the masonry block size selected, the type of grout used and the angle of inclination of the crack with respect to the bed joint and thus how much of each material passes through a crack. For simplicity the volumetric proportion of each of these materials contained within a representative masonry unit volume will serve as the basis for an estimate of a weighted mean aggregate size, $a_{g,av}$ given by Eq. 5.19.

$$a_{g,av} = \frac{V_{mo}a_{g,mo} + V_{bl}a_{g,bl} + V_{gr}a_{g,gr}}{V_{unit}} \tag{5.19}$$

Where the volume of mortar (V_{mo}) is the effective mortared area along one bed joint and one head joint multiplied by the standard mortar joint thickness of 10 mm, the block volume (V_{bl}) is based on the percent solids of the specified block and the total volume of the unit (V_{unit}) is based on the gross dimensions of the block accounting for mortar along the bed and head joints, respectively. The volume of grout (V_{gr}) can therefore be estimated as the difference between V_{unit} and $V_{bl} + V_{mo}$.

The compressive strength f'_c used in Eq. 5.18 is based on the cylinder strength of concrete used in the original analysis. Masonry, however, is a composite of different materials that not only mutually interact but each of which has individual mechanical properties that will differ significantly from the overall assemblage. For instance, grout is required by the CSA S304.1 (2004a) to have a cylinder strength of at least 10.0 MPa and 12.0 MPa for fine and coarse grouts, respectively, although actual strengths may be much higher. For a specified block strength of 20 MPa, the CSA S304.1 (2004a) limits the masonry design (prism) strength to 10 MPa, regardless of the grout strength. This perceived discrepancy

between the prism and individual material strengths is due to the unique mode in which uniaxial compression is resisted by masonry as a composite material. By contrast, aggregate interlock forces for each constituent material would depend on the bond between aggregate and the cement matrix, thus, being reflective of the individual constituent material properties rather than the composite assemblage (masonry) as a whole. In this context it is proposed that f'_c, as it appears in Eq. 5.18, is better represented by the weighted mean of the masonry material bond strength (f_{av}) given in Eq. 5.20 rather than the typical uniaxial prism strength $f'_{m(90°)}$ for masonry.

$$f_{av} = \frac{V_{mo} f_{mo} + V_{bl} f_{bl} + V_{gr} f_{gr}}{V_{unit}} \tag{5.20}$$

In the above equation, the compressive strength of mortar (f_{mo}), concrete block units (f_{bl}) and grout (f_{gr}) is determined by individual material tests. Replacing a_g and f'_c by $a_{g,av}$ and f_{av} respectively, from Eqs. 5.19 and 5.20 into Eq. 5.18 results is an upper bound expression for the shear transmitted via aggregate interlock as given by Eq. 5.21.

$$v_{mi} \le v_{m,\max} = \frac{0.18\sqrt{f_{m,av}}}{0.31 + \dfrac{24w}{(a_{g,av} + 16)}} \tag{5.21}$$

The final term required in the determination of shear transferred by aggregate interlock is the crack width ($w = s_\theta \times \varepsilon_1$). The average crack spacing within a masonry macro element (s_θ) can be estimated with Eq. 5.22 substituting in average crack spacing parameters s_{hc} and s_{nc}, measured along the horizontal and vertical axes, respectively.

$$s_\theta = \frac{1}{\dfrac{\sin(\theta)}{s_{hc}} + \dfrac{\cos(\theta)}{s_{nc}}} \tag{5.22}$$

Whereby, in Eq. 5.22, the average crack spacing measured as the vertical distance between horizontal cracks is given by s_{hc} and the horizontal distance measured between cracks forming normal to the bed joint is given by s_{nc}. The exact value of the crack spacing s_θ is a function of the potential planes of weakness within RM which may be related to the horizontally measured spacing between vertical reinforcement that runs normal to the bed joint (s_n). It also may be related to the measured space between head joints aligned within a running bond pattern (s_{hj}) taken as half the nominal block length. In the vertical direction these planes of

weakness may be dictated by the spacing between horizontal reinforcement that runs parallel to the bed joint (s_h) or the nominal bed joint spacing (s_{bj}) taken as the nominal block height. The exact nature of the cracking pattern will depend upon numerous factors such as the spacing and size of the reinforcement, the type of concrete units, the presence of grout flues that may only run normal and/or parallel to the bed joints, the occurrence of grout voids, the presence of cracks due to shrinkage or other load effects such as flexure as well as the overall workmanship quality of the construction, to name but a few. Because of the inherent difference in the detailing and loading conditions of masonry macro elements and RM structural walls, the exact values of the crack spacing parameters s_{hc} and s_{nc} will be described in the following sections relevant to the analysis of each.

5.12 NSSSE Verification: Masonry Panels (Macro Elements)

The equations derived above facilitate quantifying the stress state for a given set of strains in a RM macro element. However, it would be very time consuming to use the NSSSE developed equations (Eqs. 5.3-5.22) in hand calculations given the iterative solution process required. As a result, a spreadsheet has been created to carry out the necessary NSSSE calculations and to evaluate their effectiveness in predicting the behavior of 14 RM macro elements reported by Khattab (1993). Bearing in mind that the primary goal of the development of NSSSE is to predict the peak shear strength of RM structural walls, the selection of experimental results excluded those that were reported to suffer from a premature failure at the panel boundaries. Analysis was completed using the reported constitutive material properties derived from assemblage testing as well as the reported applied principal stress ratio and relative bed joint orientation. The calculation process will be briefly summarized here with reference to the NSSSE equations (Eqs. 5.3-5.22).

To begin the analysis of a RM macro element an arbitrary state of strain is defined as ε_h, ε_n, γ_{hn} with the corresponding Mohr's circle. The principal strains ε_1 and ε_2 are solved for, expedited by the fact that θ has already been defined for each macro element test given the nature of the loading conditions applied by Khattab (1993). The average tensile and/or compressive stresses carried by the reinforcement embedded normal and parallel to the masonry bed joint is then determined as $f_{sn} = \varepsilon_n \times E_s \leq f_{sny}$ and $f_{sh} = \varepsilon_h \times E_s \leq f_{shy}$, respectively. Based on the principal strains, the average compressive stress carried by the masonry compression strut (f_{m2}) is determined by Eqs. 5.11-5.14 and corresponding tensile stress across the strut (f_{m1}) is determined by Eqs. 5.15-5.17 while checking whether cracking has occurred.

If cracking has indeed initiated in the macro element, the tension stiffening effect of the masonry will have to be considered and f_{m1} will be limited by the local stress conditions at the crack surface. These local conditions will be governed by the amount of reserve strength in the reinforcement crossing the crack (i.e. how close it is to yield). For instance, if the average stress in the reinforcement embedded in the uncracked masonry is still within its elastic range, it will have significant reserve capacity at the crack to compensate for the abrupt reduction of cross-sectional area. The extent that there is sufficient reserve capacity in the reinforcement will depend on a number of factors, such as θ, ρ_{sh} and ρ_{sn} and, as such, Eq. 5.17 will govern the principal tensile stress. However, as the embedded reinforcement approaches its yield strength or the area of reinforcement in either direction is reduced, the reserve strength may govern the limiting value of f_{m1}. To determine this limit, the reserve strength can be solved for by assuming that $f_{sh,cr} = f_{shy}$ and $f_{sn,cr} = f_{sny}$, and back substitution into Eqs. 5.6 and 5.7, (and conservatively assuming $f_{mi} = 0$) will result in the following:

$$f_1 \le \left(f_{shy} - f_{sh}\right)\rho_{sh} + \frac{v_{mi}}{\tan\theta} \tag{5.23}$$

$$f_1 \le \left(f_{sny} - f_{sn}\right)\rho_{sn} + v_{mi}\tan\theta \tag{5.24}$$

Alternatively, if the crack width, w, is very small, and therefore v_{mi} is very large, but there is little reserve strength in the reinforcement, substitution of Eq. 5.24 into Eq. 5.23 also reduces to the following limit:

$$f_1 \le \left(f_{shy} - f_{sh}\right)\rho_{sh}\sin^2\theta + \left(f_{sny} - f_{sn}\right)\rho_{sn}\cos^2\theta \tag{5.25}$$

Finally, the shear transferred by aggregate interlock required for equilibrium can be determined by substituting Eq. 5.24 into Eq. 5.23 and solving for v_{mi} subject to the limit for $v_{m,max}$ (obtained from Eq. 5.21) as shown in Eq. 5.26.

$$v_{mi} = \frac{\left|\left(f_{shy} - f_{sh}\right)\rho_{sh} - \left(f_{sny} - f_{sn}\right)\rho_{sn}\right|}{\left(\tan\theta + \frac{1}{\tan\theta}\right)} \le v_{m,\max} \tag{5.26}$$

In conclusion, the principal stress f_1 can be selected as the minimum value resulting from Eqs. 5.17 and 5.23-5.25. In addition, the stresses f_h, f_n and v_{hn} can be all found using Mohr's circle. The final solution is achieved by iteratively solving for the appropriate strains ε_h and ε_n while keeping γ_{hn} constant until the final stresses match the known principal stress ratio from the experimental test. The process is repeated by gradually increasing the shear strain and solving for corresponding values of ε_h and ε_n that maintain the specified principal stress ratio.

Each of the macro elements tested by Khattab (1993) was detailed with vertical reinforcement in each cell (s_n = 200 mm) and horizontal reinforcement in each course (s_h = 200 mm). Based on the observations reported by Khattab (1993) these values were also selected as the crack spacing parameters s_{nc} and s_{hc}, respectively. Samples of the resulting theoretical average shear stress-shear strain relationship are shown in Fig. 5.7 for four masonry panels representing different values of θ and reinforcement ratios. Overall, the NSSSE predicts the response of the test panels fairly accurately, but, and perhaps more importantly; it was capable of more accurately predicting the peak shear strength of the panels. A summary of the theoretical predictions for peak strength using the NSSSE are presented with the experimental results in Table 5.2.

The average ratio of the theoretical strength to the measured strength is found to be v_{NSSSE}/v_{test} = 1.03 with a c.o.v. = 10.2%. Although an accurate prediction of strength was achieved, the computation process necessary is not appropriate for design purposes. Therefore, the following sections will outline a simplified design-oriented expression building on the aforementioned NSSSE approach to predict the average peak shear strength of RM structural walls and piers.

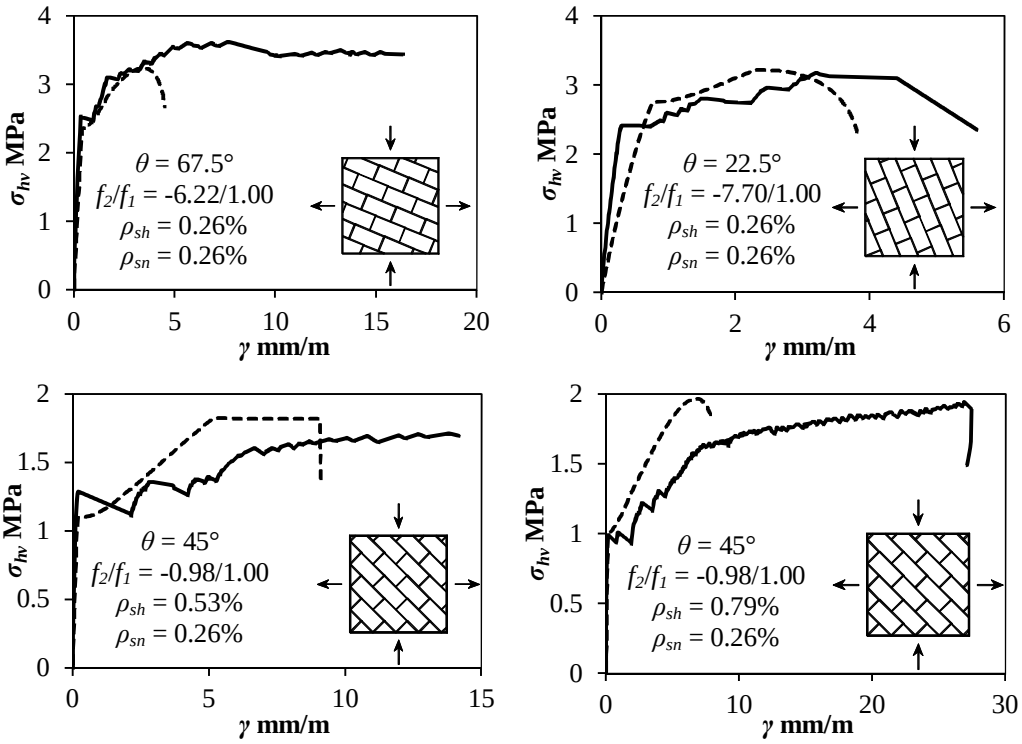

Figure 5.7 – Theoretical (Dashed) vs. Experimental (Solid) Shear Stress-Shear Strain of Masonry Macro Elements Tested by Khattab (1993)

Table 5.2 – Theoretical vs. Experimental Shear Strength for Masonry Panels (Macro Elements)

I.D.[1]	θ	f_2/f_1	$\rho_{sh(\%)}/\rho_{sn(\%)}$	v_{NSSSE}/v_{test}
RP1	0°	-7.08/1.00	0.26/0.26	1.14
RP2	67.5°	-6.22/1.00	0.26/0.26	1.12
RP3	45°	-6.49/1.00	0.26/0.26	1.09
RP4	22.5°	-7.70/1.00	0.26/0.26	0.99
RP6	45°	-13.5/1.00	0.26/0.26	0.90
RP7	0°	-0.98/1.00	0.26/0.26	1.21
RP8	45°	-1.08/1.00	0.26/0.26	0.90
RP9	45°	0.00/1.00	0.26/0.26	1.02
RP13	45°	-1.08/1.00	0.00/0.53	1.09
RP14	45°	-1.08/1.00	0.17/0.53	0.86
RP15	45°	-0.98/1.00	0.26/0.53	1.01
RP16	45°	-1.02/1.00	0.17/0.26	1.10
RP17	45°	-0.98/1.00	0.53/0.26	0.94
RP18	45°	-0.98/1.00	0.79/0.26	0.99
[1]Khattab (1993)			Overall Average	1.03
			C.O.V.	10.2%

5.13 NSSSE for Peak Shear Strength Prediction of RM Structural Walls

In the preceding section, a full NSSSE analysis could be applied to experimentally tested macro elements because the well-defined boundary and stress conditions they were subjected to reflect the basic assumptions used in the NSSSE derivation. However, such ideal conditions do not exist in RM structural walls that are subjected to combined shear, flexural and axial forces. It is therefore necessary to idealize the boundary and stress conditions and detailing of a RM wall by a representative macro element with similar shear behavior to that of the wall in order to accurately predict the RM wall peak shear strength.

For a RM structural wall, the material properties of concern such as: the prism strength ($f'_{m(90°)}$), average aggregate strength (f_{av}), average maximum aggregate size ($a_{g,av}$) and reinforcement detailing properties (ρ_{sh}, ρ_{sn}, s_{sh}, s_{sn}, f_{shy} and f_{sny}), may be determined, specified or predicted depending on the problem at hand (e.g. analysis or design). The average crack spacing parameters s_{nc} and s_{hc} of the macro element should reflect the anticipated behavior of the wall as a whole within its shear-critical region. Therefore, a distinction must be made between RM walls that will respond to lateral loads predominantly in a shear mode of

deformation versus those anticipated to respond predominantly in flexural mode of deformation.

In general, cantilever walls that would be expected to behave predominantly in flexure (i.e. $h_{eff}/\ell_w > 1.0$) can be assigned a vertical crack spacing parameter equal to the spacing of the vertical reinforcement such that $s_{nc} = s_n$ as vertical reinforcement in these walls will be highly stressed. By contrast, squat cantilever walls which are anticipated to behave predominantly in shear (i.e. $h_{eff}/\ell_w \leq 1.0$) as well as masonry piers (subject to double curvature) would be expected to have their horizontal reinforcement most highly stressed. As such, vertically orientated cracks would be expected to form at the planes of weakness created by the vertical reinforcement (s_n) as well as the head joints where the highly stressed horizontal reinforcement would cause cracks to concentrate (s_{hj}). To consolidate these effects, the cracks spacing parameter in this case will be taken as the average between the two contributing planes of weakness (i.e. $s_{nc} = (s_{hj} + s_n)/2$).

Regarding the horizontal crack spacing parameter (s_{hc}), a similar distinction must be made. Cantilever walls that would be considered to behave predominantly in flexure (i.e. $h_{eff}/\ell_w > 1.0$) will similarly be assigned a horizontal crack spacing parameter equal to the spacing of the horizontal reinforcement such that $s_{hc} = s_h$. Similarly, squat cantilever walls (i.e. $h_{eff}/\ell_w \leq 1.0$) as well as masonry piers (subject to double curvature) will also be assigned a horizontal crack spacing parameter of $s_{hc} = s_h$. However, to account for the possible effects of high levels of axial load on the crack pattern and overall shear strength, cases where $P_{axial} < 7.5\% f'_{m(90°)}A_g$ are assigned a crack spacing parameter as the bed joint spacing (i.e. $s_{hc} = s_{bj}$).

In lieu of a more complex analysis, the preceding limitations have been set out based on the engineering judgement of the writers based on qualitative observations made from experimental testing. The proposed crack spacing parameter values were selected for their ease of determination as well as their ability to adequately represent the observed behavior of different wall configurations. With the physical characteristics of the representative macro element for a structural wall now defined, the next step is to determine the critical loading conditions coincident with the peak shear strength.

To start, it is necessary to assume that the macro element representing the shear-critical region of a wall is not subjected to lateral confining pressures, such that $f_h = 0$. In addition, it is assumed for now that the peak shear strength of the masonry wall is reached when the horizontal reinforcement that crosses the cracks as well as that is embedded within the masonry have both yielded, such that $f_{sh} = f_{sh,cr} = f_{shy}$. Taking $f_h = 0$ and conservatively assuming $f_{mi} = 0$, Eq. 5.3 can be solved

directly, as given in Eq. 5.27. Similarly, the relationship given in Eq. 5.28 can also be determined by substituting Eq. 5.3 in Eq. 5.6.

$$v_{hn} = f_{m1} \tan\theta + \rho_{sh} f_{shy} \tan\theta \tag{5.27}$$

$$v_{hn} = v_{mi} + \rho_{sh} f_{shy} \tan\theta \tag{5.28}$$

It is clear that both Eqs. 5.27 and 5.28 express shear strength in the form of an algebraic summation of a masonry contribution and reinforcement contribution in a similar manner to existing design code equations. Therefore, to present the NSSSE in a format that designers are familiar with, it is useful to express the peak shear strength of the structural wall (v_n) in terms of a masonry stress component (v_m) and a horizontal reinforcement stress component (v_s) as given in Eq. 5.29. The necessary parameters for a solution to Eq. 5.29 can be reduced simply to a masonry strength parameter β and a crack inclination angle θ.

$$v_n = v_m + v_s = \beta \sqrt{f'_{m(90^o)}} + \rho_{sh} f_{shy} \tan\theta \tag{5.29}$$

With the appropriate substitutions, the masonry strength components: $f_{m1} \tan\theta$ of Eq. 5.27 and v_{mi} of Eq. 5.28, can both be rearranged to solve for the β parameter as given in Eq. 5.29. Expanding the f_{m1} term in Eq. 5.27 to that determined from Eq. 5.17 yields an explicit relationship to β given by the left side of the equality of Eq. 5.30. Similarly, it is also possible to express the masonry shear stress v_{mi} of Eq. 5.28 as the peak shear strength of the macro element limited by $v_{mi,max}$ (defined in Eq. 5.21), as given by the left side of the equality of Eq. 5.30.

$$\frac{f_{cr(\theta)} \tan\theta}{\sqrt{f'_{m(90^o)}}\left(1 + 400\varepsilon_1\right)} = \beta \le \frac{0.18\sqrt{f_{av}}}{\sqrt{f'_{m(90^o)}}\left(0.31 + \dfrac{24\varepsilon_1 s_\theta}{a_{g,av} + 16}\right)} \tag{5.30}$$

It is necessary to assume that the peak shear strength of the macro element coincides with the occurrence of $v_{mi,max}$ allowing for an explicit solution of Eq. 5.30. By substituting Eq. 5.16 for $f_{cr(\theta)}$ and explicitly solving for θ in Eq. 5.30, a relationship between $f_{av}/f'_{m(90^o)}$, s_{hc}, s_{vc} and $a_{g,av}$ is developed and is given by Eq. 5.31. This relationship is illustrated graphically in Fig. 5.8 for a typical range of physical characteristics of RM construction.

$$\theta = \tan^{-1} \frac{0.18\sqrt{f_{av}}\left(1+400\varepsilon_1\right)}{f_{cr(\theta)}\left(0.31+\frac{24\varepsilon_1 s_\theta}{a_{g,av}+16}\right)} \tag{5.31}$$

A full discussion of how the limits to these physical parameters have been determined (i.e. s_{nc}, s_{hc}, $a_{g,av}$, etc.) and integrated into the NSSSE for RM structural walls will be discussed further in the following section related to adoption of NSSSE for design codes. Nevertheless, it is clear from Fig. 5.8 that the crack spacing parameters, average maximum aggregate size and material strength ratio each have a significant effect on the crack angle θ, and, considering Eq. 5.30, on β as well. The principal tension strain ε_1 is the only variable in Eq. 5.30 (and Fig. 5.8) that cannot be explicitly determined from the physical characteristics of the macro element, as it is function of the load conditions of the RM wall. Since RM structural walls are typically subjected to bending and axial stresses which can be related to the level of normal strain, ε_n, it will be useful to define the strength parameters, β and θ, in terms of the level of ε_n rather than ε_1. Substituting Eq. 5.8 into Eq. 5.9 yields the following useful relationship between the principal tensile strain ε_1 and the normal strain ε_n:

$$\varepsilon_n = \frac{\varepsilon_1 - \varepsilon_2 \tan^2\theta}{\left(1+\tan^2\theta\right)} \tag{5.32}$$

For an explicit solution of Eq. 5.32, a masonry wall containing a very small amount of horizontal reinforcement such that $\rho_{sh}f_{sh} \approx 0$ is considered. Allowing for this extreme case, Eq. 5.5 can be substituted into Eq. 5.27 to yield the following relationship of the principal tensile stress:

$$f_{m1} = \frac{\nu}{\tan\theta} = \frac{\left(f_{m1}+f_{m2}\right)}{\left(\tan\theta+\frac{1}{\tan\theta}\right)} \tag{5.33}$$

For most cases, shear failure of a RM wall occurs prior to masonry crushing. As such, compression stresses in the masonry strut will be within the elastic range so that it is adequate to assume $f_{m2} = \varepsilon_2 \times E_m$, which can be back substituted into Eq. 5.33 and rearranged to yield:

$$\varepsilon_2 = \frac{f_{m1}\left(\tan\theta+\frac{1}{\tan\theta}-1\right)}{E_m} \tag{5.34}$$

Finally, substitution of Eq. 5.34 back into Eq. 5.32 will result in the following relationship between ε_n, ε_1 and θ:

$$\varepsilon_n = \frac{\varepsilon_1 - \left(\frac{f_{cr(\theta)}\left(\tan\theta + \cot\theta - 1\right)}{\left(1 + 400\varepsilon_1\right)E_m} \right) \tan^2\theta}{\left(1 + \tan^2\theta\right)} \tag{5.35}$$

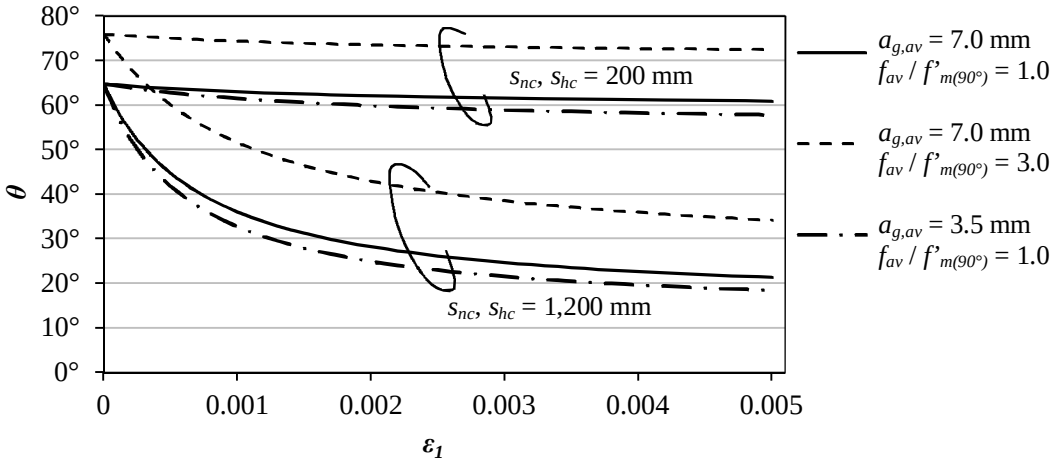

Figure 5.8 – Relationship between θ and ε_1 based on the solution of Eq. 5.31

With the relationship given by Eq. 5.34, a solution for β and θ is possible when the level of normal strain ε_n is known. To determine the anticipated level of normal strain ε_n in the representative macro element, a representative location within the RM wall must first be established. For simplicity, this location will be tentatively selected to be at the middle of the wall base cross-section (i.e. $\ell_w/2$). This location will be proven to be accurate enough later in the paper when the NSSSE is verified using RM wall test results. For a cantilever wall subjected to single curvature, shown in Fig. 5.9 as case i, the reaction forces within the wall can be idealized as a compression force carried by the masonry and a tensile force carried by the reinforcement. The resultant forces are shown by the thick arrows at the base of the wall separated by distance d_v in Fig. 5.9 and act in equilibrium with the applied loads. The applied compressive axial load acting concentrically on the wall can then be split into two forces, each of $0.5P_{axial}$ as shown on the wall base in Fig. 5.9 for case i. The wall must also remain in equilibrium with the resultant shear force transmitted by the compression struts. Therefore, each force at the wall base is also assigned a net tensile force of $0.5V \tan\theta$. Finally, the applied lateral load V acting at an effective height h_e will produce a net moment at the wall base. This will result in a net tensile and compressive force, respectively, of Vh_e/d_v as shown by the equilibrium equation at the base of the wall (Fig 9 case

i). The resultant tensile force is therefore taken as $Vh_e/d_v + 0.5V\tan\theta - 0.5P_{axial}$. By assuming the $d_v = 0.8\ell_w$ and for simplicity that the total area of vertical reinforcement in tension is $0.8\rho_{sn}A_g$, the average tensile strain in the reinforcement can be determined as ε_{sn} as shown in Fig 9. Finally, to translate this into the average strain in the middle of the cross-section the distance from the tension arm to the middle of the RM wall cross-section must be assumed, which is taken to be approximately $0.4\ell_w$ as shown in Fig. 5.9. The strain in the middle of the cross-section (ε_n) can be determined from similar triangles based on the distance from the resultant compressive force to the neutral axis (x) as given by:

$$\varepsilon_n = \frac{\left(Vh_e/d_v\right)+\left(0.5V\tan\theta\right)-\left(0.5P_{axial}\right)}{\sum A_{sn}E_s}\left(\frac{0.4\ell_w - x}{0.8\ell_w - x}\right) \tag{5.36-a}$$

RM piers which are subject to double bending, as shown by case ii in Fig. 5.9, are fixed against rotation along both the top and bottom edges. This has the effect of reducing the effective height h_e and resulting moment compared to cantilever walls (i.e. $h_e = h_w/2$). Due to the effects of double curvature, the resultant axial force acting on the bottom half of the pier will invariably be influenced by the bending effects of the upper half. This phenomenon is described by Priestley et al. (1994) for RC columns and is incorporated in the New Zealand masonry design code 4230:2004 (SANZ 2004) for RM piers, whereby, P_{axial} acts eccentrically as shown by case ii in Fig. 5.9. As a result, the tensile strain would be reduced resulting in the following modification to Eq. 5.36-a:

$$\varepsilon_n = \frac{\left(Vh_e/d_v\right)+\left(0.5V\tan\theta\right)-\left(P_{axial}\right)}{\sum A_{sn}E_s}\left(\frac{0.4\ell_w - x}{0.8\ell_w - x}\right) \tag{5.36-b}$$

The simultaneous solution of Eq. 5.36a or b (as applicable), Eq. 5.31 and Eq. 5.35 will yield a relationship between θ, β and ε_n facilitating a solution to the peak shear stress given by Eq. 5.29. Although an iterative process, these equations can be used to estimate the experimental peak shear strength of a RM wall for research purposes. For design purposes, however, further simplification is necessary and will thus be implemented in the following section that will present the NSSSE into a code-ready format.

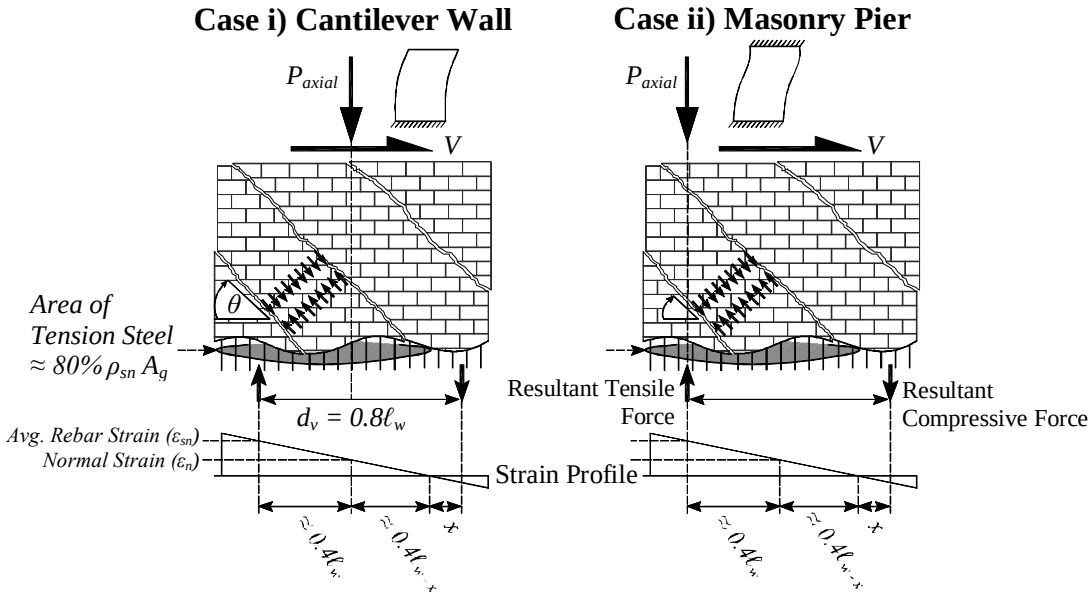

Case	Resultant Tensile Force	Resultant Compression Force
Cantilever (i)	$V\tan(\theta)+\left(V\frac{h_e}{d_v}\right)-\frac{P_{axial}}{2}$	$V\tan(\theta)-\left(V\frac{h_e}{d_v}\right)-\frac{P_{axial}}{2}$
Pier (ii)	$V\tan(\theta)+\left(V\frac{h_e}{d_v}\right)-P_{axial}$	$V\tan(\theta)-\left(V\frac{h_e}{d_v}\right)-P_{axial}$

Figure 5.9 – Normal Strain Conditions in a Masonry Cantilever Wall and Pier

5.14 Simplified NSSSE for Code Adoption

For design purposes, it would be beneficial to know f_{av} beforehand as a function of $f'_{m(90°)}$ since the latter is typically specified prior to the start of the design process. Therefore a new parameter, referred to as *the homogenized strength factor* (*J*), is proposed. The parameter gives the ratio between the average material strength of the aggregate interlock mechanism and the prism strength, and is given by:

$$J = \frac{f_{av}}{f'_{m(90^o)}} \tag{5.37}$$

A conservative estimate for the design value of *J* is readily accounted for using the specified strengths used by the CSA S304.1 (CSA 2004a), where: $10 \le f_{bl} \le 40$ MPa, $5 \le f'_{m(90°)} \le 25$ MPa and $f_{gr} \ge 10$ MPa or 12 MPa, for fine and coarse grout, respectively. Since prism strength is directly related to block strength in the CSA

S304.1 the design values for J can be calculated directly. As an example, this is carried out for Type A concrete block units in Table 5.3 considering two cases of grout strength: 10 MPa and 20 MPa. The values in Table 5.3 indicate that the range of design values using the CSA S304.1 (2004a) would range between J = 1.5 and J = 3.0. It should be noted that in cases where prism testing has been conducted to determine the actual value of $f'_{m(90°)}$, rather than assigning a value from the CSA S304.1, f_{av} should be based on a more thorough analysis considering actual material properties or can conservatively be taken as $f'_{m(90°)}$ (J = 1.0) instead.

Table 5.3 – Homogenized Material Design Strength Factor (J) using the CSA S304.1(2004a)

		Type A Block							
Block Size (mm)		140	190	240	290	140	190	240	290
f_{gr} (MPa)		10				20			
f_{bl} (MPa)	$f'_{m(90°)}$ (MPa)	$J = f_{av} / f'_{m(90°)}$							
40	17	1.61	1.58	1.52	1.49	1.86	1.84	1.80	1.78
30	13.5	1.60	1.57	1.53	1.50	1.91	1.90	1.87	1.86
20	10	1.58	1.56	1.53	1.51	2.00	2.00	2.00	2.00
15	7.5	1.72	1.71	1.69	1.67	2.28	2.29	2.31	2.33
10	5	2.00	2.00	2.00	2.00	2.84	2.88	2.94	2.98

To reduce the iterative nature of NSSSE, a second parameter, defined as *the crack spacing and aggregate size factor*, λ, is necessary and is given by the following:

$$\lambda = \frac{24(s_{nc} + s_{hc})}{a_{g,av} + 16} \tag{5.38}$$

Based on the volumetric proportions of masonry blocks to grout cells, and adopting the maximum aggregate sizes for masonry construction (coarse grout: $a_{g,gr}$ = 10 mm, fine grout: $a_{g,gr}$ = 2.5 mm, mortar: $a_{g,mo}$ = 2.5 mm and concrete block: $a_{g,bl}$ = 5.0 mm), the following values are suggested: $a_{g,av}$ = 7.0 mm (for RM with coarse grout) and $a_{g,av}$ = 3.5 mm (for RM with fine grout). The values of s_{hc} and s_{nc} have been defined previously based on the wall type and reinforcement detailing. However, the maximum possible values of s_{hc} and s_{nc} are limited to the maximum horizontal and vertical reinforcement spacing, taken to be 1,200 mm (CSA 2004a). For the simplified NSSSE, crack spacing parameter given by Eq. 5.22 has been reduced to simply the algebraic summation of the crack space parameters to avoid an iterative solution process involving θ.

Finally, to further reduce the iterations in the NSSSE solution process, the vertical projection of the shear strut acting along the wall is conservatively taken as V_f. To account for cases where flexural deformations are anticipated to be significant ($h_e/\ell_w > 1.0$), the normal strain can be taken directly as the tensile reinforcement strain ($\varepsilon_n = \varepsilon_{sn}$) as was previously defined in Fig. 5.9 and is given by:

$$\varepsilon_n = \frac{\left(Vh_e / d_v\right) + \left(V\right) - \left(0.5P_{axial}\right)}{0.8\rho_{sn} b_w \ell_w E_s} \qquad (h_e/\ell_w > 1.0) \tag{5.39-a}$$

When shear deformations are anticipated to be significant in cantilever walls ($h_e/\ell_w \leq 1.0$), Eq. 5.39-a can be modified assuming a general case of $x = 0.1\ell_w$ to yield the following:

$$\varepsilon_n = \frac{\left(Vh_e / d_v\right) + \left(V\right) - \left(0.5P_{axial}\right)}{2\rho_{sn} b_w \ell_w E_s} \qquad (h_e/\ell_w \leq 1.0) \tag{5.39-b}$$

Finally, for walls subject to double curvature Eq. 5.39-b can be modified to account for the increased influence of the applied axial load as such:

$$\varepsilon_n = \frac{\left(Vh_e / d_v\right) + \left(V\right) - \left(P_{axial}\right)}{2\rho_{sn} b_w \ell_w E_s} \qquad \text{(Piers with double curvature)} \tag{5.39-c}$$

In cases where the normal strain is determined to be a negative or where members are of a very low aspect ratio (i.e. piers of $h_e/\ell_w \leq 0.50$) such that the plane strain assumption used in Fig. 5.9 is no longer valid, ε_n may be conservatively taken to be zero. With the normal strain defined above, the simultaneous solution of: Eq. 5.31, Eq. 5.35 and Eq. 5.39a, b or c (as applicable), yields a relationship between θ and β in terms of level of normal strain ε_n and the parameters λ and J. This relationship is shown in Fig. 5.10, whereby through regression analysis using the range of variables specified in Fig. 5.10 the following relationships have been determined:

$$\theta = \left(\frac{2000J + 4000 - \lambda}{50(18J + 75)}\right)\left(\frac{50}{\left(1 + 220\varepsilon_n\right)}\right) \tag{5.40-a}$$

$$\beta = \left(\frac{4000J + 2000 - \lambda}{500(3.5J + 1.5)}\right)\left(\frac{1}{4\left(1 + 1800\varepsilon_n\right)}\right) \tag{5.40-b}$$

Incumbent upon the NSSSE analysis carried out for RM walls was the presumption that failure occurred upon yielding of the horizontal reinforcement. If

failure occurs prior to this, then the horizontal reinforcement would be assumed to have a tensile strain just below its yield strain (e.g. $\varepsilon_h \leq 0.002$ for 400 MPa reinforcement). Similarly, the principal compressive strain could be conservatively taken as just prior to the peak masonry strength (i.e. $\varepsilon_2 = \varepsilon_o = -0.0018$), then Eqs. 5.5-5.17 can be used to solve for a relationship between shear strength and normal strain ε_n. By also assuming a normal strain equal to that just prior to yielding of vertical reinforcement (e.g. $\varepsilon_n \leq 0.002$ for 400 MPa reinforcement) a limiting shear stress of $0.26f'_{m(90°)}$ can be determined directly. Accounting for the fact that reinforcement yield strengths may actually vary significantly from 400 MPa and possible ε_o deviation from -0.0018, a limit to the maximum design shear stress of $0.15f'_{m(90°)}$ is proposed. This is also consistent with the current maximum shear stress limit of $0.25f'_c$ adopted by the CSA A23.3 considering the reduction in compressive strength of masonry with the angle θ (i.e. the minimum masonry strength from Eq. 5.11 or 12 is approximately $0.6\ f'_{m(90°)}$ and $0.25\times0.6 = 0.15$). In the next section the preceding simplification of the NSSSE will be verified with the available database on RM structural wall tests.

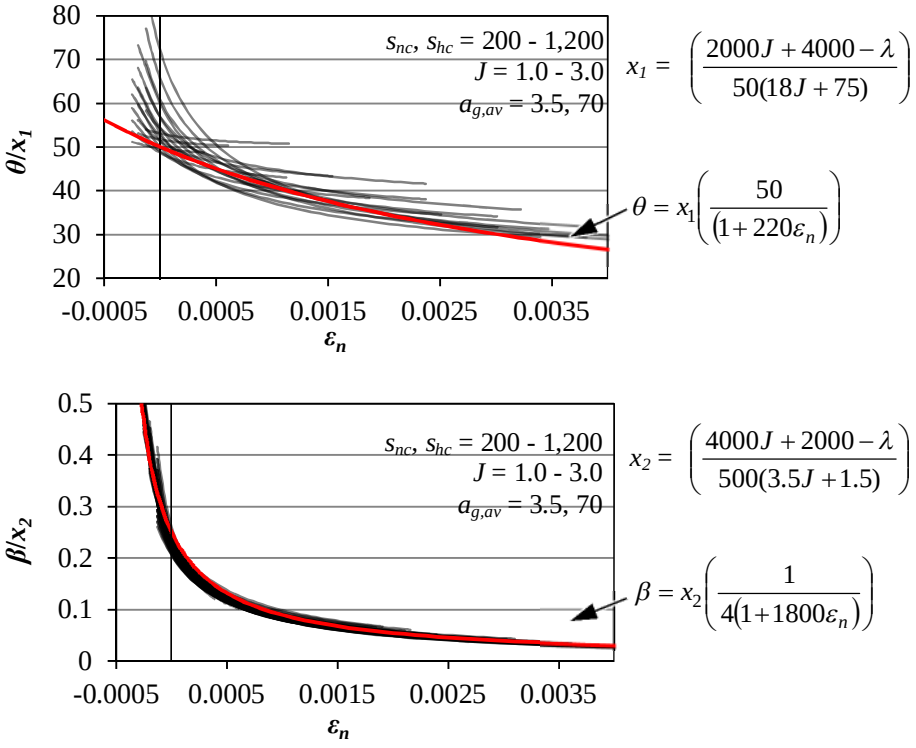

Figure 5.10 – Relationship between ε_n and the parameters θ and β

5.15 Simplified NSSSE Verification: RM Walls

A survey of the available literature has resulted in a total of 77 reliable RM wall and pier tests all subject to reversed cycles of quasi-static loading. However, unlike previous design code expressions, the NSSSE was explicitly derived for use with concrete block masonry and, as such, brick masonry construction will be considered only for comparison purposes to the existing shear strength expressions. This resulted in a total of 57 tests on concrete block masonry structural walls and piers collected from seven sources (Sveinsson et al. 1985; Okamoto et al. 1987; Matsumura 1987; Shing et al. 1991; Ibrahim and Suter 1999; Voon and Ingham 2006 and El-Dakhakhni et al. 2012). The physical parameters for each wall have been used as reported in literature, however, for cases where material testing data was not available a value of J = 1.5 was used. For each wall, the predicted shear strength was determined using Eq. 5.41 and was compared with the corresponding average peak shear strength from both directions of loading. To account for the fact that the angle may deviate from 45°, a check was also necessary to ensure that the assumed height of the crack does not exceed the height of the wall in determining the shear resistance of the reinforcement resulting in:

$$V_n = \beta\sqrt{f'_{m(90^o)}}\,b_w d_v + A_{sh} f_{shy} \frac{d_v \tan\theta}{s_h} \le 0.15 f'_{m(90^o)}\, b_w d_v; d_v \tan\theta \le h_w \tag{5.41}$$

The physical parameters for each wall were first identified based on the reinforcement detailing, aspect ratio and boundary conditions according to the procedures previously laid out. An arbitrary shear strength value is assumed to first solve Eq. 5.39, which is then substituted into Eq. 5.40 to determine the θ and β parameters. The shear strength (V_n) is solved for with Eq. 5.41, and substituted back into Eq. 5.39 to determine the normal strain. This process is repeated until the solution converges, normally after only a few iterations. To account for the anticipated reduction in the volume of grout and the reduction in aggregate size within the clay brick material a value of $a_{g,av}$ = 1.5 mm was assumed, and the same process was repeated for the brick wall specimens as with the concrete block wall specimens. The proposed Simplified NSSSE parameters and solution process for code adoption are summarized in Table 5.4 as it was applied to the test walls.

A summary of all the test walls' experimental strength values is presented in Table 5.5 as a ratio to existing design code expressions from the MSJC (2011), CSA S304.1 (2004a) and NZS 4230:2004 (SANZ 2004) as were described previously. It is not an easy task to directly compare each of these code expressions to NSSSE because of the way they were individually empirically calibrated. Since the applied axial load, and the steel and masonry experimental

strengths were known for the walls listed in the table, additional load or material strength reduction factors were not included in the Table 5.5 calculations. In addition, the shear strength reduction factors (ϕ) adopted by the MSJC (2011) and the NZS 4230 (2004) have also not been used so that the expressions may be compared to the CSA S304.1 (2004a) and the Simplified NSSSE.

For each experimental program listed in Table 5.5, the number of relevant wall specimens is listed along with the ratio ($V_{Experimetnal}/V_{Theory}$) between the average experimental shear strength and the theoretical strength predicted from the Simplified NSSSE (using the procedure laid out in Table 5.4). Due to a problem with grouting, the brick wall specimens presented by Matsumura (1987) were retested with the results published in Matsumura (1988b).

In general, for each individual test program, the Simplified NSSSE had an average $V_{Experimetnal}$ / V_{Theory} closer to 1.0 as well as a lower the coefficient of variation (C.O.V.) than that of other expressions. Of particular interest are the results from Okamoto et al. (1987), which have been discounted in some more recent shear expression derivations simply because of abnormally high strengths. While the Simplified NSSSE also observed a relatively high average strength ratio of 1.18, it was substantially lower than the other shear strength expressions. By contrast, the results from Ibrahim and Suter (1999) which were an example of RM wall construction that used a fine grout demonstrated unconservative predictions (i.e. $V_{Experimetnal}$ / V_{Theory} < 1.0) using the MSJC (2011) expression. Whereas, the Simplified NSSSE was able to conservatively and accurately predict the strengths by accounting for the reduction and aggregate size in these walls.

The overall average results from the concrete block wall specimens indicate that the Simplified NSSSE had the lowest shear strength ratio of $V_{Experimetnal}$ / V_{Theory} = 1.16 and the lowest C.O.V. of 11.4%. The 95th percentile strength ratios for the simplified NSSSE expression was around 1.0, indicating that no additional empirical reductions factors are required.

Although not specifically developed for brick wall specimens, it is evident from Table 5.6 that the Simplified NSSSE gave reasonably accurate predictions of brick wall peak shear strengths. However, as the NSSSE was not originally derived for reinforced brick walls, and as such, its use towards shear strength prediction of such walls would require further investigation and/or testing. It is of note that the other expressions, in which brick specimens were used in their derivations, had improved precision compared to the NSSSE evidenced by the low C.O.V. Nevertheless, as modern design and construction practices focus on utilizing reinforced fully-grouted concrete block walls in shear-critical regions of masonry buildings, the Simplified NSSSE presents an accurate, less variable and experimentally verified approach to predict the shear strength of such walls.

Table 5.4 – Simplified NSSSE in Design Code Formulation

Simplified NSSSE Expression	Comments
$f_{av} = \frac{V_{mo} f_{mo} + V_{bl} f_{bl} + V_{gr} f_{gr}}{V_{unit}}$	Average strength of constitutive materials used to determine aggregate interlock strength.
$J = \frac{f_{av}}{f'_{m(90^o)}}$	Homogenized strength factor, where $f'_{m(90°)}$ is the prism strength f'_m as described in the current CSA S304.1 (2004a). Design values of J can be determined from Table 5.3 absent of material testing data.
s_{nc}	Crack spacing parameter normal to bed joints. Walls subject to single curvature and $h_e/\ell_w > 1.0$ can be taken as spacing of vertical reinforcement (s_n), otherwise taken as an average of s_n and the head joint crack spacing factor s_{hj} taken as 200 mm.
s_{hc}	Crack spacing parameter parallel to the bed joints. Walls subject to single curvature and $h_e/\ell_w > 1.0$ or walls with axial load of $P_{axial} < 7.5\% f'_{m(90°)}$ can be taken as spacing of horizontal reinforcement (s_h), otherwise to be taken as the nominal spacing between bed joints (s_{bj}) of 200 mm.
$a_{g,av} = \frac{V_{mo} a_{g,mo} + V_{bl} a_{g,bl} + V_{gr} a_{g,gr}}{V_{unit}}$	Average maximum aggregate size of masonry. Can be taken as $a_{g,av} = 7.0$ mm for concrete block walls with course grout, 3.5 mm for concrete block walls with fine grout and 1.5 mm for brick construction.
$\lambda = \frac{24(s_{nc} + s_{hc})}{a_{g,av} + 16}$	Crack spacing and aggregate size factor.
$\varepsilon_n = \frac{(Vh_e / d_v) + (V) - (0.5P_{axial})}{0.8\rho_{sn} b_w \ell_w E_s}$	Average normal strain in shear critical area of walls subject to single curvature and with $h_e/\ell_w > 1.0$.
$\varepsilon_n = \frac{(Vh_e / d_v) + (V) - (0.5P_{axial})}{2\rho_{sn} b_w \ell_w E_s}$	Average normal strain in shear critical area of walls subject to single curvature and with $h_e/\ell_w \leq 1.0$.
$\varepsilon_n = \frac{(Vh_e / d_v) + (V) - (P_{axial})}{2\rho_{sn} b_w \ell_w E_s}$	Average normal strain in shear critical area of walls subject to double curvature and with $h_e/\ell_w \leq 1.0$. When $h_e/\ell_w \leq 0.45$ a value of zero may be conservatively assumed.
$\theta = \left(\frac{2000J + 4000 - \lambda}{50(18J + 75)}\right)\left(\frac{50}{(1 + 220\varepsilon_n)}\right)$	Average crack inclination angle of wall measured relative to the bed joint.
$\beta = \left(\frac{4000J + 2000 - \lambda}{500(3.5J + 1.5)}\right)\left(\frac{1}{4(1 + 1800\varepsilon_n)}\right)$	Masonry shear strength parameter that accounts for the shear transferred by the compression strut as well as the contribution from aggregate interlock.
$V_f = \phi_m \beta \sqrt{f'_{m(90^o)}} b_w d_v + \phi_s A_{sh} f_{yh} \frac{d_v \tan\theta}{s_h}$	Factored shear force subject to a maximum shear strength of $0.15\phi_m f'_{m(90°)} b_w d_v$. In addition, the contribution of horizontal reinforcement to the overall strength is subject to $d_v \tan\theta \leq h_w$.

Table 5.5 - $V_{Experimental}$ / V_{Theory} for Fully-Grouted Concrete Block Shear Walls and Piers

Shear Provision		**Simplified NSSSE**		**CSA S304.1**		**MSJC**		**NZS 4230**	
Study		**Concrete Block Wall Specimens: $V_{Experimental}$ / V_{Theory} (C.O.V)**							
Sveinsson et al. (1985)	HCBL-13	1.26	**1.16 (6.4%)**	1.08	**1.34 (8.9%)**	0.97	**1.25 (11.5%)**	1.14	**1.54 (14.4%)**
	HCBL-15	1.17		1.23		1.18		1.39	
	HCBL-17	1.05		1.37		1.31		1.55	
	HCBL-18	1.05		1.37		1.31		1.55	
	HCBL-20	1.20		1.43		1.37		1.62	
	HCBL-21	1.13		1.35		1.30		1.53	
	HCBL-23	1.10		1.28		1.12		1.98	
	HCBL-24	1.23		1.48		1.41		1.67	
	HCBL-25	1.17		1.30		1.14		1.34	
	HCBL-26	1.22		1.46		1.40		1.65	
Matsumura (1987)	KW4-1	1.13	**1.07 (5.9%)**	1.52	**1.46 (9.9%)**	1.11	**1.18 (11.7%)**	1.17	**1.24 (14.0%)**
	KW3-1	1.03		1.52		1.06		1.13	
	KW3S-1	1.14		1.67		1.17		1.25	
	KW2-1	1.04		1.56		1.20		1.21	
	WS2	1.06		1.28		0.94		0.85	
	WS4	1.17		1.41		1.09		1.16	
	WS5	1.05		1.40		1.22		1.31	
	WS9	0.98		1.40		1.23		1.31	
	WS10	1.05		1.77		1.55		1.66	
	WS9-2	1.11		1.38		1.17		1.25	
	WSB21	0.95		1.25		1.09		1.17	
	WSB22	1.09		1.49		1.30		1.39	
	WSB3	1.01		1.36		1.19		1.28	
	WSB4	1.13		1.39		1.20		1.29	
Okamoto et al. (1987)	WS1	1.25	**1.18 (20.7%)**	2.52	**1.89 (29.4%)**	1.88	**1.51 (24.1%)**	2.44	**1.69 (30.3%)**
	WS4	1.11		1.38		1.06		1.15	
	WS7	1.57		2.47		1.88		1.96	
	WSN1	1.03		1.48		1.30		1.40	
	WSN2	0.95		1.61		1.41		1.52	
Shing et al. (1991)	3	1.29	**1.30 (7.5%)**	1.37	**1.48 (12.7%)**	1.15	**1.24 (10.5%)**	1.50	**1.38 (14.2%)**
	4	1.21		1.76		1.32		1.54	
	5	1.26		1.56		1.23		1.24	
	7	1.36		1.68		1.31		1.51	
	9	1.46		1.28		1.08		1.23	
	13	1.23		1.25		1.21		1.11	
	14	1.42		1.37		1.13		1.24	
	16	1.21		1.54		1.49		1.66	
Ibrahim & Suter (1999)	1	1.29	**1.22 (5.5%)**	1.05	**1.11 (8.8%)**	0.90	**0.91 (3.5%)**	1.06	**1.10 (9.5%)**
	2	1.21		1.17		0.91		1.29	
	3	1.30		1.09		0.87		1.03	
	4	1.17		1.24		0.96		1.07	
	5	1.15		0.99		0.92		1.06	
Voon and Ingham (2006)	1	1.34	**1.17 (11.9%)**	1.36	**1.35 (10.2%)**	0.96	**0.96 (9.7%)**	1.69	**1.54 (17.7%)**
	2	1.13		1.37		0.94		1.82	
	4	0.99		1.36		0.97		1.60	
	7	1.10		1.37		1.02		1.61	
	8	1.06		1.41		1.03		1.73	
	9	1.18		1.05		0.76		1.24	
	10	1.37		1.50		1.03		1.08	
El-Dakhakhni et al. (2012)	W-1	1.01	**1.11 (10.9%)**	1.21	**1.51 (18.0%)**	0.96	**1.14 (12.7%)**	0.94	**1.13 (16.9%)**
	W-2	0.99		1.61		1.23		1.20	
	W-3	1.13		1.49		1.13		0.98	
	W-4	1.27		1.61		1.24		1.32	
	W-5	1.20		1.21		0.96		0.92	
	W-6	1.03		1.30		1.05		1.00	
	W-7	1.28		2.02		1.37		1.43	
	W-8	1.01		1.63		1.19		1.21	
Average		**1.16**		**1.44**		**1.17**		**1.36**	
C.O.V.		**11.4%**		**19.4%**		**18.4%**		**21.9%**	
95th Percentile		**0.98**		**1.08**		**0.90**		**0.97**	
Maximum		**1.57**		**2.53**		**1.88**		**2.44**	
Minimum		**0.95**		**0.99**		**0.76**		**0.85**	

Table 5.6 - $V_{Experimental}$ / V_{Theory} for Clay Brick Walls and Piers

Shear Provision		**Simplified NSSSE**		**CSA S304.1**		**MSJC**		**NZS 4230**	
Study		**Clay Brick Wall Specimens: $V_{Experimental}$ / V_{Theory} (C.O.V)**							
Sveinsson et al. (1985)	HCBR-19	0.91	**1.02 (17.0%)**	1.01	**1.21 (11.6%)**	0.97	**1.14 (8.2%)**	1.14	**1.34 (8.1%)**
	HCBR-20	0.80		1.05		1.01		1.19	
	HCBR-21	1.11		1.29		1.23		1.46	
	HCBR-22	0.99		1.32		1.26		1.49	
	HCBR-23	0.97		1.11		1.07		1.26	
	HCBR-24	0.91		1.21		1.16		1.36	
	HCBR-25	1.22		1.20		1.15		1.35	
	HCBR-26	0.89		1.17		1.12		1.33	
	HCBR-27	1.07		1.23		1.18		1.39	
	HCBR-28	0.94		1.24		1.19		1.41	
	HCBR-30	1.41		1.53		1.22		1.42	
Okamoto et al. (1987)	WSR1	1.16	**1.50 (20.5%)**	2.53	**2.42 (4.1%)**	1.86	**1.75 (6.4%)**	1.91	**1.64 (14.6%)**
	WSR4	1.76		2.40		1.64		1.54	
	WSR7	1.57		2.33		1.76		1.47	
Matsumura (1988)	WSR2-2	1.38	**1.05 (23.2%)**	1.84	**1.53 (13.5%)**	1.33	**1.23 (7.6%)**	1.18	**1.24 (7.0%)**
	WSR4-2	1.06		1.47		1.12		1.17	
	WSR5-2k	0.95		1.37		1.19		1.27	
	WSR6-2	0.81		1.46		1.27		1.35	
Shing et al. (1991)	21	1.42	**1.38 (5.4%)**	1.34	**1.42 (10.9%)**	1.10	**1.13 (4.2%)**	1.02	**1.03 (1.5%)**
	22	1.35		1.50		1.16		1.04	
Average		**1.07**		**1.31**		**1.16**		**1.28**	
C.O.V.		**19.7%**		**15.5%**		**8.0%**		**11.0%**	
95th Percentile		**0.81**		**1.05**		**1.01**		**1.04**	
Maximum		**1.76**		**2.53**		**1.86**		**1.91**	
Minimum		**0.80**		**1.01**		**0.97**		**1.02**	

5.16 Summary and Conclusions

Masonry has historically suffered from overly conservative shear design expressions that have been developed by empirical curve fitting of a relatively small experimental database. As such, empirical strength reduction factors were needed to ensure conservatism in design. To overcome the reliance on empirical reduction factors and arbitrary limits, a rational expression, derived from first principles, was developed in which constitutive masonry relationships are presented considering the composite and anisotropic nature of masonry. The Normal Strain-adjusted Shear Strength Expression (NSSSE) was subsequently validated using experimental tests on RM panels reported by Khattab (1993). A Simplified NSSSE was then developed and verified with experimental tests on RM walls. As a result, the following conclusions can be made:

The composite behavior of masonry structural walls subject to principal compressive and tensile stresses inclined at an angle θ relative to the bed joint was found to be best represented by the behavior of masonry panels (macro elements), rather than small-scale assemblages (prisms). When the loading angle on masonry assemblages deviates from the uni-axial directions normal to the bed or head joints, significant variability in the strength characteristics will result due to the masonry's inherent anisotropy. With this in mind, a set of constitutive material relationships for grouted concrete block masonry have been proposed which account for the reduction in compressive and tensile strength with changes to θ. In addition, the softening effects of the compressive and tensile strengths of masonry were also derived with respect to the level of lateral tensile strain ε_1. These relationships were needed to solve for equilibrium and compatibility of a masonry macro element.

The theoretically derived equilibrium and compatibility expressions and constitutive material models were verified through an analytical comparison to experimental results of masonry macro elements subject to bi-axial stress at different angles θ and with different amounts of reinforcement ρ_h and ρ_v reported by Khattab (1993) and Drysdale and Khattab (1995). The NSSSE demonstrated the capabilities of capturing the shear deformation history of each panel. However, of greater importance for design purposes, the NSSSE demonstrated strong capabilities of accurately predicting the peak shear resistance of the macro elements. A ratio between the theoretical and experimental peak shear stresses of v_{NSSSE}/v_{test} = 1.03 with a c.o.v. = 10.2% was determined. Based on these results a more simplified NSSSE was derived for direct use in the design or analysis of RM structural walls.

The Simplified NSSSE was verified using the results of 56 tests on RM walls and piers gathered from seven sources. Of the existing design code expressions, the

CSA S304.1 had a $V_{Experimental}/V_{Theory}$ = 1.44 (C.O.V. = 19.4%), the MSJC had a $V_{Experimental}/V_{Theory}$ = 1.17 (C.O.V. = 18.4%) and the NZS 4230:2004 had $V_{Experimental}/V_{Theory}$ = 1.36 (C.O.V. = 21.9%). By contrast, the Simplified NSSSE (with the procedure laid out in Table 5.4) had a ratio of experimental shear strength to the predicted $V_{Experimental}/V_{Theory}$ = 1.16 (C.O.V. = 11.4%) with a maximum value of 1.57 and a minimum of 0.95 indicating that the Simplified NSSSE is sufficiently conservative for direct adoption in design codes.

Overall the Simplified NSSSE provides a sufficiently conservative, more accurate and more precise prediction for the shear strength of RM structural walls and piers compared to current code expressions. The Simplified NSSSE also provides an engineering feel and physical sense of RM walls' characteristics, which would subsequently enhance the designers' confidence in their designs and facilitate better understanding of the factors influencing RM structural wall behavior.

5.17 Notation for Chapter 5

A_g = gross cross-sectional area of the macro element along axis of interest (mm^2);
a_g = maximum aggregate size of concrete (mm);
$a_{g,gr}$ = maximum aggregate size of grout (mm);
$a_{g,mo}$ = maximum aggregate size of mortar (mm);
$a_{g,bl}$ = maximum aggregate size of concrete block (mm);
$a_{g,av}$ = average maximum aggregate size of masonry (mm);
A_{sh} = area of single reinforcing bar along the horizontal axis in structural wall (mm^2);
A_m = gross cross-sectional area of masonry in macro element along axis of interest (mm^2);
A_{sn} = area of single reinforcing bar along the vertical axis in structural wall (mm^2);
b_w = width of masonry unit used in wall construction (mm);
d_v = effective depth of masonry wall resisting shear taken as $0.8\ell_w$ (mm);
E_m = Young's modulus of masonry (MPa);
E_s = Young's modulus of elasticity for steel (MPa);
f_1 = principal tensile stress orientated perpendicular to the formation of the cracks (MPa);
f_2 = principal compressive stress orientated along the compression struts (MPa);
f_{bl} = compressive strength of concrete block (MPa);
f'_c = cylinder strength of concrete (MPa);
$f_{cr(\theta)}$ = cracking strength of masonry based on the angle of loading (MPa);
f_{gr} = compressive strength of grout (MPa);
f_h = average stress of macro element acting along horizontal axis (MPa);

f_m = average stress carried by masonry along axis of interest (MPa);
f_{m1} = principal tension stress carried laterally by masonry strut (MPa);
f_{m2} = principal compression strut carried along compression strut in masonry (MPa);
$f_{m2,max}$ = peak compressive stress of masonry with lateral strains and orientated at angle θ (MPa);
$f'_{m(90°)}$ = compressive strength of masonry prism (MPa);
f_{av} = average compressive strength of individual masonry materials (MPa);
f_{mi} = locally induced normal stress acting along cracks (MPa);
f_{mo} = compressive strength of mortar (MPa);
$f'_{m(\theta)}$ = compressive strength of masonry for different angles of bed joint orientation (MPa);
f_{sh} = average stress in horizontal reinforcement (MPa);
f_{shy} = yield stress of horizontal reinforcement (MPa);
$f_{sh,cr}$ = locally induced stresses in horizontal reinforcement the crosses a crack (MPa);
f_{sn} = average stress in vertical reinforcement (MPa);
$f_{sn,cr}$ = locally induced stresses in vertical reinforcement the crosses a crack (MPa);
f_{sny} = yield stress of vertical reinforcement (MPa);
F_n = average stress of macro element acting along the vertical axis (MPa);
h = horizontal axis aligned with the horizontal (shear) reinforcement within a wall;
h_e = effective height of wall (mm);
h_w = height of wall (mm);
J = homogenized strength factor;
ℓ_w = length of wall (mm);
M = overturning moment in a structural wall (kN·m);
n = vertical axis aligned with the vertical (flexural) reinforcement within a wall;
P,P_{axial} = level of applied axial force in a masonry structural wall (kN);
s_{bj} = crack spacing parameter associated with masonry bed joints (mm);
s_h = spacing between reinforcing bars measured along horizontal axis (mm);
s_{hc} = overall crack space parameter along horizontal axis (mm);
s_{hj} = crack spacing parameter associated with masonry head joints (mm);
s_n = spacing between reinforcing bars measured along vertical axis (mm);
s_{nc} = overall crack space parameter along vertical axis (mm);
s_θ = crack spacing taken as a constant for macro element (mm);
V = level of applied shear force in a masonry structural wall (kN);
V_{bl} = volume of concrete block in a masonry unit (mm^3);
V_{Exp} = experimentally measured shear strength of a RM structural wall

(kN);

V_{gr} = volume of grout in a masonry unit (mm^3);

V_{mo} = volume of mortar in a masonry unit (mm^3);

V_n = total shear resistance of a masonry structural wall (kN);

V_{Theory} = shear strength of a RM structural wall determined with the Simplified NSSSE (kN);

V_{unit} = volume of masonry unit (mm^3);

w = average crack width (mm);

x = distance from equivalent compressive force to neutral axis (mm);

β = masonry shear strength parameter;

γ_{hn} = shear strain of macro element;

ε_h = average strain acting along horizontal axis;

ε_o = compressive strain in masonry corresponding to peak compressive stress;

ε_n = average normal strain;

ε_1 = principal tensile strain of macro element;

ε_2 = principal compression strain of macro element;

θ = angle measured between masonry bed joint and shear cracking (deg);

λ = crack spacing factor;

v_{ci} = shear stress transmitted by aggregate interlock across cracks in concrete (MPa);

$v_{c,max}$ = limit to v_{ci} (MPa);

v_{hn} = average shear stress in macro element (MPa);

v_m = peak shear resistance of a masonry (MPa);

v_{mi} = local shear stress transmitted by aggregate interlocking forces at cracks (MPa);

v_n = peak shear resistance of a masonry structural wall (MPa);

v_{NSSSE} = peak shear stress in macro element determined from NSSSE (MPa);

v_s = peak shear resistance of a reinforcement (MPa);

v_{test} = Experimentally measured peak shear stress in macro element (MPa);

ρ_{sh} = percent area of reinforcement in the horizontal direction (%);

ρ_{sn} = percent area of reinforcement in the vertical direction (%);

χ = factor to account for a reduction in strength when loads are applied parallel to bed joint.

5.18 References for Chapter 5

Anderson, D. L., and Priestley, M. J. N. (1992). "In-plane shear strength of masonry walls." *Proc., 6th Canadian Masonry Symposium*, Saskatoon, Canada, 223–234.

Attkinson, R. H and Hammons, M. I. (1997). "Tension stiffening behavior of reinforced masonry." *J. Struct. Eng.*, 123(5), 597-603.

Bentz, E. C., Vecchio, F. J. and Collins, M. P. (2006). "Simplified modified compression field theory for calculating shear strength of reinforced concrete elements." *ACI Journal*, 103(4), 614-624.

Canadian Standards Association (CSA). (2004a). "Design of masonry structures." *CSA S304.1-04 (R2010)*, CSA, Mississauga, Canada.

Canadian Standards Association (CSA). (2004b). "Design of concrete structures." *CSA A23.3-04 (R2010)*, CSA, Mississauga, Canada.

Canadian Standards Association (CSA). (2004c). "Mortar and grout for unit masonry." *CSA A179-04 (R2010)*, CSA, Mississauga, Canada.

Canadian Standards Association (CSA). (2009). "Concrete materials and methods of concrete construction / Test methods and standard practices for concrete." *CSA A23.1-09*, CSA, Mississauga, Canada.

Collins, M P. and Mitchell, D. (1991). *Prestressed Concrete Structures*, Prentice Hall, Englewood Cliffs, N.J., USA.

Davis, C. L. (2008). "Evaluation of design provisions for in-plane shear in masonry walls." Master of Science in Civil Engineering-Thesis, Washington State University, Washington, USA.

Drysdale, R. G. and Khattab, M. M. (1995). "In-plane behavior of grouted concrete masonry under biaxial tension-compression." *ACI Journal*, 92(6), 1-13.

Drysdale R. G. and Hamid A. A. (2005). *Masonry Structures Behaviour and Design*, Canada Masonry Design Centre, Mississauga, Canada.

El-Dakhakhni, W. W., Drysdale, R. G. and Khattab, M. M. (2006). "Multilaminate macromodel for concrete masonry: formulation and verification." *J. Struct. Eng.*, 132(12), 1984-1996.

El-Dakhankhni, W. W., Banting, B. R. and Miller S. C. (2012). "Seismic performance parameters quantification of shear-critical reinforced concrete masonry squat walls." Accepted for publication, *J. Struct. Eng.*

Fattal, S. G. and Todd, D. R. (1991), "Ultimate strength of masonry shear walls: prediction vs. test results." *NISTIR 4633*, Building and Fire Research Laboratory, Gaithersburg, USA.

Hamid, A. A. and Drysdale, R. G. (1980). "Concrete masonry under combined shear and compression along the mortar joints." *ACI Journal*, 77(5), 314-320.

Ibrahim, K. S., and Suter, G. T. (1999). "Ductility of concrete masonry shear walls subjected to cyclic loading." *Proc., 8th North American Masonry Conference*, Austin, Texas, USA, Paper 3.04-2 on USB Flash Drive.

Khattab, M. M. S. (1993). "In-plane behaviour of grouted concrete masonry under biaxial states of stress." Ph. D. in Civil Engineering-Thesis, McMaster University, Hamilton, Canada.

Liu L., Tang, T. and Zhai X. (2006). "Failure criteria for grouted concrete block masonry under biaxial compression." *Advances in Structural Engineering*, 9(2), 229-239.

Masonry Standards Joint Committee. (MSJC). (2011). "Building Code Requirements for Masonry Structures." *TMS 402/ASCE 5/ACI 530*, The Masonry Society, American Society of Civil Engineers, Boulder, New York/American Concrete Institute, and Detroit, USA.

Matsumura, A. (1987), "Shear strength of reinforced hollow unit masonry walls." *Proceedings of the 4th North America Masonry Conference*, Paper No. 50, Los Angeles, USA, 50-1 - 50-16.

Matsumura, A. (1988a). "Shear strength of reinforced masonry walls." *Proc., 9th World Conf. on Earthquake Engineering*, Vol. 7, Tokyo, 121–126.

Matsumura, A. (1988b). "Effectiveness of shear reinforcement in fully grouted hollow clay masonry walls." *Fourth Meeting of the U.S.-Japan Joint Technical Coordinating Committee on Masonry Research*, San Diego, U.S.A., 1-10.

Okamoto, S., Yamazaki, Y., Kaminosono, T., Teshigawara, M. and Hirashi, H. (1987). "Seismic capacity of reinforced masonry walls and beams." *Proceedings of the 18th Joint Meeting of the U.S.-Japan Cooperative Program in Natural Resource Panel on Wind and Seismic Effects: NBSIR 87-3540*, National Institute of Standards and Technology, Gaithersburg, USA, 307-319.

Priestley, N. M. J., Verma, R. and Xiao, Y. (1994). "Seismic shear strength of Reinforced Concrete Columns." *J. Struct. Eng.*, 120(8), 2310-2329.

Sarhat, S. R., and Sherwood, T. G. (2011). "Shear design of reinforced masonry beams." *Proc., 11th North American Masonry Conference*, Minneapolis, USA, Paper 3.04-2 on USB Flash Drive.

Shing, P. B., Schuller, M., and Hoskere, V. S. (1990). "In-plane resistance of reinforced masonry shear walls." *J. Struct. Eng*., 116 (3)., 619–640.

Shing, P. B., Noland, J. L., Spaech, H., Klamerus, E. and Schuller, M. (1991). "Response of single-storey reinforced masonry shear walls to in-plane lateral loads." *U.S. – Japan Coordinated Program for Masonry Building Research Report No. 3.1(a)-2*, University of Colorado at Boulder, USA.

Standards Association of New Zealand (SANZ). (2004). "Design of reinforced concrete masonry structures." *New Zealand Standards Association* (*NZS) 4230:2004*, CEN, Wellington, New Zealand.

Sveinsson, B. I., McNiven, H. D., and Sucuoglu, H. (1985). "Cyclic loading tests of masonry piers – Volume 4: Additional tests with height to width ratio of 1." *Report No. UCB/EERC-85-15*, Earthquake Engineering Research Center, University of California Berkeley, USA.

Tikalsky, P. J., Atkinson, R. H. and Hammons M. I. (1995). "Compressive strength of reinforced masonry under lateral tension." *J. Struct. Eng.*, 121(2), 283-289.

Vecchio, F. J. and Collins, M. P.(1982) "The response of reinforced concrete to in-plane shear and normal stresses." *Publication No. 82-03*, Department of Civil Engineering, University of Toronto, Canada.

Vecchio, F. J. and Collins, M. P. (1986). "The modified compression-field theory for reinforced concrete elements subjected to shear." *ACI Journal*, 83(2), 219-231.

Voon, K. C. and Ingham, J. M. (2006). "Experimental in-plane shear strength investigation of reinforced concrete masonry walls." *J. Struct. Eng.*, 132(3), 400-408.

Voon, K. C. and Ingham, J. M. (2007). "Design expression for the in-plane shear strength of reinforced concrete masonry." *J. Struct. Eng.*, 133(5), 706-713.

Walraven, J. C. (1981). "Fundamental analysis of aggregate interlock." *Journal of the Structural Division*, 107(11), 2245-2270.

CHAPTER 6: CONCLUSIONS AND RECOMMENDATIONS

6.1 Conclusions

Within this thesis experimental and analytical work regarding a research program covering the seismic behavior of concrete block structural walls possessing confined boundary elements was presented. In Chapter 2, the experimental program was described, whereby a total of 9 half-scale concrete block masonry structural walls were tested under quasi-static reversed cycles of loading. The results from the tested walls were presented in Chapter 3 along with results from two additional walls (Shedid et al. 2010) that fit within the larger test matrix of boundary element walls and were included for comparison purposes. Analysis of the test program was carried-out and presented in Chapter 4 with regard to force-, displacement- and performance-based seismic design parameters. Based on the behavior of the walls a number of design equations were ultimately proposed that may be integrated directly into existing masonry design standards. Furthermore, analysis was also presented in Chapter 5 regarding an improved shear strength expression developed for fully-grouted masonry structural walls. In all, the results from Chapters 4 and 5 were intended to both address concerns raised in Chapter 1 regarding conservatism in masonry seismic design. In this final chapter, a commentary will be provided regarding the relevance of this research program within the context of the existing MSJC and CSA S304.1 masonry design standards. Finally, in the recommendations section of this chapter the results of this research program with regard to confined boundary element walls as well as shear strength of masonry will be distilled and a code-ready set of design rules.

6.1.1 Boundary Element Walls in the CSA S304.1 Design Standards

Within the context of the current CSA S304.1 design standard (CSA 2004a), there is no basis for comparison to prevailing design provisions since none exist regarding masonry walls with boundary elements. However, it was evident from this test program that walls possessing boundary elements can be detailed for reinforcement to carry compressive stresses, and by this effect, also prevent buckling of vertical reinforcement and lateral instability of the compression zone.

Due to the confinement ties, the face shell spalling and vertical cracking which is normally associated with an immediate, and brittle, failure of the masonry, only resulted in a nominal drop in resistance since the inner grout core remained intact and stable. The recorded strength of the walls supports the assumption that tied reinforcement in the compression toe may be counted towards moment calculations. This presents a significant improvement over conventional structural wall design, where reinforcement is typically neglected, and the benefits towards capacity as well as curvature calculations are lost. It was shown, therefore, that the confined boundary element converges more towards RC wall behavior in many ways, including its effective elastic stiffness and ultimate compressive strain. However, it was observed that the tendency for RM structural walls to form horizontal flexural cracks along the mortar joints, would imply different plastic hinging effects than that in RC, where no such inherent planes of weakness exist. Furthermore, a plastic hinge formula was proposed based on the observed relationship between ultimate and yield moments as well as the shear crack angle in regions where large inelastic strains are expected.

In conclusion, the experimentally measured and idealized levels of displacement ductility of all the walls tested illustrated that a new categorization of SFRS for RM structural walls is warranted with a recommended R_d value of 4.0. A set of prescriptive design formulae were proposed in Chapter 4 which were shown to accurately predict wall behavior. In section 6.2.1 of this chapter a set of prescriptive design requirements are proposed based on the results of this study as well as the current design requirements for similar Ductile Concrete Shear Walls appearing the CSA A23.3 (CSA 2004b).

6.1.2. Boundary Element Walls in the MSJC Design Standards

Presently, the masonry standards joint committee (MSJC 2011) design standard, specifies the *special reinforced masonry walls* as a SFRS category with an elastic force reduction factor of R = 5.0. However, there is an additional prescriptive limit on the ratio of the depth of the neutral axis, c, to the wall length, ℓ_w, related to the amplified design displacement, $C_d\delta_{ne}$, as shown by Eq. 6.1 based on the unconfined masonry properties (Wallace and Orakcal, 2002). In cases where Eq. 6.1 is not satisfied due to high seismic displacement demands, a designer can increase the compressive strain of the masonry (ε_{mu}) such that it will satisfy Eq. 6.2 through the detailing of special boundary elements.

$$c \geq \frac{\ell_w}{600\left(C_d\,\delta_{ne}/h_w\right)} \tag{6.1}$$

$$\varepsilon_{mu} = 2\left(\frac{C_d\delta_{ne}}{h_w}\right)\left(\frac{c}{\ell_w}\right) \tag{6.2}$$

The barbell shape of the confined boundary element tested would decrease the depth of neutral axis (c) while also improving compressive strains of the masonry. Thus, such a configuration would be doubly effective towards satisfying curvature demands imposed from Eq. 6.1. However, relying solely on the value of ε_{mu} towards satisfying ductility requirements does not necessarily ensure that under reversed cyclic loads vertical reinforcement would be adequately confined against buckling. A drawback of the current MSJC is a lack of any prescriptive detailing or guidance for the design or detailing of a boundary element. The proposed confined boundary element adopted within this thesis does not require any new construction materials and relies on well-established principles adopted in reinforced concrete unlike other types of confinement schemes. Thus, it would be possible to integrate step-by-step design and detailing requirements in the same vein as done for reinforced concrete shear walls requiring added confinement.

Furthermore, there is a limitation in the MSJC (2011) on the amount of vertical reinforcement which may be detailed within *Special Masonry Shear Walls* such that tension strains cannot exceed four times its yield strain. This is presumably due to potential issues of wall stability that may arise from excessive strains in vertical reinforcement under reversed cycle loading. This condition may be waived when special boundary elements are used, presumably again that sufficient confinement is provided to permit large enough compression strains in the masonry to satisfy curvature demands. However, there is no requirement for a double layer of vertical compression reinforcement or requirement for assurance against buckling of the vertical reinforcement in the boundary element. The fact that the MSJC is silent about boundary element detailing may cause a sense of trepidation and uncertainty for designers who would have to rely on third-party assurance of a particular confinement scheme.

6.1.3 Boundary Element Walls in the Next Generation of Seismic Design Standards

The adoption of displacement-based design principles is prefaced on the assumption that seismic forces and drifts are sufficiently high to warrant an inelastic analysis that necessitates a ductile structural design. It may be that for many low-rise applications in areas of low seismic risk that masonry structures can be feasibly designed to remain elastic. Because masonry walls with confined boundary elements are considered to be highly ductile, their use will most likely be integrated into regions where seismic demands are high and with building heights not currently common for masonry construction. In such instances, it will be much more likely that displacement-based seismic design methods would be applied.

The confined boundary element walls possessed equivalent viscous damping and stiffness degradation properties that could be related to existing expressions derived for conventional RM and RC structural walls. In terms of lateral drift, the proposed design expressions given in Chapter 4 illustrate that through readily accepted analysis techniques and simplifications adopted for RC, accurate predictions of drift can be attained. It was established that this new wall category is well suited to move away from fixed material-based design parameters and broad-based collapse safety design objectives towards specific drifts as design objectives.

With respect to performance-based seismic design objectives, the behavior of the walls illustrated the fallacy with a purely force- or ductility-based design methodology. Whereby, damage was found to be closely related to the maximum level of drift sustained by each wall, as has been observed with other materials as well. Although the walls varied by their properties, high quality fragility curves were generated, implying that the walls behaved very similarly. A method was proposed to estimate crack size openings in flexurally governed walls, which takes advantage of the inherent planes of weakness in the masonry mortar joints. This process was verified through the application of digital image correlation analysis, which shows great promise to be used in future tests with large masonry elements.

6.1.4 Shear Strength of Masonry Walls

As part of the analytical work presented in Chapter 5, a new technique was proposed to estimate the shear strength of fully-grouted masonry walls. The normal strain-adjusted shear strength expression (NSSSE) was an approach similar to the modified compression field theory (MCFT). Equilibrium of a cracked masonry macro-element was used to derive a set of constitutive relationships to describe the shear strength of masonry. A simplified shear strength expression related to the normal strain in structural walls was derived and verified with a database comprised of reinforced concrete block structural walls and piers. Because of the dependence of the NSSSE on the normal strain in calculating the peak shear strength could be directly related to wall curvature. In Chapter 4, the NSSSE was used to estimate shear strength degradation effects in the boundary element walls related to increased levels of displacement ductility. Up to this point much of the work surrounding shear strength of masonry has been derived from empirical data fitting. The NSSSE presents a significant opportunity in masonry design to ensure a theoretical basis in strength calculations as well to keep masonry in step with developments made with concrete structures for which many masonry designers may be more knowledgeable of.

In light of this work, as series of code-ready design steps have been proposed in section 6.2.1 of this chapter. It is of the opinion of the author that, although the NSSSE is only verified for fully-grouted shear walls, the same syntax should be applied to partially-grouted walls that result in the same strength expression presently used. Therefore, it is important that designers are still aware of the β and θ factors; however, the net result for partially-grouted walls would remain unchanged until the time that new data is available. In addition, it is also of the opinion of the author that to facilitate a smooth transition, to what can be judged as a major deviation from previous codes, that for fully-grouted walls a simplified and general method be provided. Whereby, the simplified form results in the same expression as adopted presently as conservative value, but takes minimal computational effort. While the general form will allow a designer to explicitly calculate β and θ with added computational effort, but with an improved prediction of strength.

6.2 Recommendations

In the following sections a series of proposed design code clauses are presented as they relate to the design of boundary element walls and adoption of the NSSSE for shear strength. The presentation of this information represents a simplification of the results presented in the thesis acknowledging the need for a blend of both conservatism and simplicity within a design standard. In addition, given the historical precedent regarding ductile wall and shear strength design in reinforced concrete standards, the current requirements and layout of the CSA A23.3 (CSA 2004b) has served as a template for the proposed code clauses. Finally, a series of recommendations are also prepared with regards to future research needs to fill in areas of the proposed code where masonry specific information is lacking.

6.2.1 Special Ductile Masonry Shear Wall SFRS Category for the CSA S304.1 and Shear Strength Expression

Based on the work presented and the current requirements for *Ductile Reinforced Concrete Walls* in the CSA A23.3 (CSA 2004b), the following prescriptive design requirements are proposed for a *Special Ductile Masonry Shear Wall* category with R_d = 4.0. Provided in the following table are also, when applicable, a brief commentary regarding the applicability of each clause within masonry or a reference to the chapter in the thesis where a more detailed explanation regarding the derivation of an equation can be found. The design standard is presented in three chapters, *Clause X* lays out the requirements for special ductile wall design with an R_d = 2.0. *Clause Y* provides special reinforcement requirements for the confined boundary element which would be included within the reinforcement or column design section of a design standard. Finally, *Clause Z* provides the shear strength expressions for masonry shear walls, including those referenced in *Clause X*.

Code Provision	Commentary
X Special masonry walls (R_d = 4.0)	
X.1 Application	
X.1.1 The requirements specified in Clauses X.1.2 to X.8.5 shall apply to special masonry shear walls serving as parts of the SFRS. Walls with h_w / ℓ_w of 1.5 or less shall be designed for R_d = 2.0.	*Walls tested in this program with aspect ratios as low as 1.5 indicated that ductile plastic hinging can occur. However a value of h_w / ℓ_w of 2.0 may be more practical given the added conservatism within shear strength design requirements.*
X.1.2 A special masonry shear wall with openings shall be designed as a ductile shear wall with a single plastic hinge in accordance with Clauses X.2 to X.8	*The intent of this Clause is to restrict ductile shear walls to walls where plane sections remain essentially plane.*
X.1.3 Walls shall be fully-grouted and constructed in running bond over their entire height and considered as cantilevers under single curvature.	
X.2 General requirements	
X.2.1 Each wall shall be detailed for plastic hinges to occur at all locations over its height, except as specified in Clauses X.2.2 and X.2.3.	
X.2.2 The following shall apply to buildings where the SFRS does not contain structural irregularity types 1, 3, 4, 5, or 6 as defined in Article 4.1.8.6 of the National Building Code of Canada over the building height: (a) the walls shall be detailed for plastic hinges over a height equal to at least 1.5 times the length of the longest wall above the design critical section. In the case of walls designed to the requirements of Clause X.8, the height to be taken shall be at least 1.5 times the length of the longest individual element in the direction under consideration	*The following requirements are in keeping with those imposed on concrete ductile walls with regards to structural irregularities defined by the NBCC 2010. Note that these requirements are with regard to detailing, not demand calculations.*

(b) the flexural and shear reinforcement required for the critical section shall be maintained over the height specified in Item (a); (c) for all elevations above the plastic hinge region, the design overturning moments and shears shall be increased by the ratio of the factored moment resistance to the factored moment, both calculated at the top of the plastic hinge region; and (d) detailing for plastic hinging shall extend below the critical section to the footing unless there is a significant increase in strength and stiffness below the critical section, in which case the detailing shall extend down the distance specified in Item (a) or to the footing, whichever is less.	*This is intended to ensure that footings are adequately detailed to provide the necessary confinement under the increased compression strains.*
X.2.3 For buildings containing structural irregularity types 1 or 3 over their height, the detailing specified in Clauses X.2.2(a) and X.2.2(b) shall be applied at each irregularity and shall continue for the distance specified in Clause X.2.2(a) above and below each irregularity.	
X.3 Dimensional limitations ***X.3.1*** The boundary element thickness within a plastic hinge shall be not less than $\ell_u/10$, except as permitted by Clauses X.3.2 to X.3.4, but shall not be less than $\ell_u/14$.	*This conforms with concrete requirements. Although the applicability of this clause is difficult to quantify in terms of the walls tested, as for safety reasons out-of-plane support was offered at the equivalent of ℓ_u / 7.2 except for Wall 1 which was ℓ_u / 10.3.*
X.3.2 Clause X.3.1 shall be required to apply only to those parts of a wall that under factored vertical and lateral loads are more than halfway from the neutral axis to the compression face of the wall section.	*The web of the wall is absolved from satisfying this requirement assuming it is less than halfway from the neutral axis to the compression face.*

X.3.4 Clause X.3.1 shall not be required to apply to any part of a wall that lies within a distance of $3b_w$ from a continuous line of lateral support provided by a flange or cross wall. The width of the flange providing effective lateral support shall be not less than $\ell_u/5$.	
X.4 Reinforcement ***X.4.1*** Unless otherwise specified, all reinforcement in walls shall be anchored, spliced, or embedded in accordance with the requirements for reinforcement in tension specified in the pertinent clause in the S304.1 and be modified by Clause X.4.2. All lap splices shall have a minimum length of 1.5 ℓ_d.	*Since reinforcement detailing was not a test parameter, the recommended values adopted by concrete shall apply.*
X.4.2 Where Type 2 mechanical splices are used, not more than one half of longitudinal bars in the web or boundary element shall be spliced at any section, and the centre-to-centre distance between splices of adjacent bars shall be not less than $40d_b$, measured along the longitudinal axis of the wall.	*Whereby $40d_b$ of a No. 10 bar reflects a modular spacing of 400 mm or every other cell.*
X.4.3 The reinforcement ratio within the region of concentrated reinforcement located within a boundary element, including regions containing lap splices, shall be not more than 0.04	*This clause is indicative of the current limitation for masonry column design.*
X.5 Distributed web reinforcement ***X.5.1*** Both vertical and horizontal distributed reinforcement shall be provided in such a manner that the reinforcement ratio for this distributed reinforcement is not less than 0.002 in each direction. The reinforcement spacing in each direction shall not exceed 800 mm. Splices shall comply with Clause X.4.1 or X.4.2. Vertical distributed reinforcement shall be tied as specified in Clause Y.3. Ties may be omitted if (a) the area of vertical steel is less than $0.005A_g$; and (b) the maximum bar size is 20M or smaller.	*A spacing of 450 mm is reflective of the current requirements of the CSA A23.3. The equivalent spacing of the walls tested was as high as 800 mm in full-scale in the plastic hinge.* *The requirements for a double layer of reinforcement in the web of a wall defined as requiring ties, may be waived for lightly reinforced walls.*

X.5.2 In regions of plastic hinging, the spacing of distributed reinforcement in each direction shall not exceed 400 mm, and if the area of vertical distributed reinforcement is greater than $0.005A_g$ or the maximum bar size is greater than 15M, the vertical distributed reinforcement shall be tied as specified in Clause X.6.8.	*The spacing in the plastic hinge region is restricted in the CSA A23.3, however, web spacing of 800 mm equivalent was tested, a conservative restriction of 400 mm is given.* *Therefore, a double layer of vertical tied reinforcement may be omitted in the plastic hinge for:* *<u>20 cm units</u> (10M@200mm, 15M@400mm);* *<u>25 cm units</u> (10M@200mm, 15M@200mm, 15M@400mm);* *<u>30cm units</u> (15M@200mm)*
X.5.3 At least two curtains of reinforcement shall be used if, in regions of plastic hinging, the in-plane factored shear force assigned to the wall exceeds the basic shear strength of masonry of $0.16\phi_m\sqrt{f'_m}b_w d_v$ where b_w is taken as the thickness of the web of the wall.	*Basic masonry shear strength is given.*
X.5.4 Horizontal reinforcement shall be provided by reinforcing bars, be continuous over the length of the web of the wall, and shall be contained at each end of the wall within the boundary element as specified in Clause X.6.	
X.5.5 In regions of plastic hinging, horizontal reinforcement shall be anchored within the boundary element to develop $1.25f_y$.	*This may be achieved through a standard hook around vertical reinforcement or, given a large enough unit in the boundary element, a straight bar.*

X.6 Boundary element reinforcement ***X.6.1*** Vertical reinforcement in a boundary element shall be provided at each end of the wall. Each boundary element shall be detailed to possess a minimum of four bars placed in at least two layers. ***X.6.2*** The boundary element reinforcement shall be proportioned to resist that portion of factored load effects, including earthquake, not resisted by distributed vertical reinforcement in the web of the wall. ***X.6.3*** The minimum concentrated reinforcement within a boundary element shall be not less than $0.001 b_w \ell_w$ at each end of the wall. ***X.6.4*** The minimum area of concentrated reinforcement within a boundary element in regions of plastic hinging shall be at least $0.0015\ b_w \ell_w$ at each end of the wall. ***X.6.5*** The vertical reinforcement shall consist of straight bars. ***X.6.6*** In regions of plastic hinging, not more than 50% of the reinforcement at each end of a wall shall be spliced at the same location. In such walls, a total of at least one-half of the height of each storey shall be completely clear of lap splices in the concentrated reinforcement. ***X.6.7*** The concentrated reinforcement shall be tied at least as specified in Clause Y, and the ties shall be detailed as hoops. In regions of plastic hinging, the boundary element reinforcement shall be tied with buckling prevention ties as specified in Clause X.6.8.	*This corresponds to a wall with a standard Pilaster (390 mm × 390 mm) with 6-10M bars and a maximum wall length of 2.1 m (20cm web units) and is conducive with current CSA A23.3. The minimum ratio tested was 0.00167 for Wall 11.*

X.6.8 Buckling prevention ties shall comply with Clause Y.3.4 or Y.3.5 and be detailed as hoops. The tie spacing shall not exceed the smallest of (a) six longitudinal bar diameters; (b) 24 tie diameters; (c) one-half of the least dimension of the member; or (d) the tie spacing required by Clause X.7, if applicable.	*Therefore, tie spacing for vertical bars in boundary element in plastic hinge:* *10M = 68mm,* *15M = 96mm,* *20M = 117mm,* *25M = 151mm,* *30M = 179mm, this limits use to a pilaster unit or some other open/ recessed webbed units with knock-outs etc., standard units with uninterrupted webs will not work in plastic hinge region.*
X.7 Ductility of boundary element walls	
X.7.1 To ensure ductility in the hinge region, the inelastic displacement capacity of the wall, Δ_{ic}, shall be greater than the inelastic displacement demand, Δ_{id}.	*Rather than rotations, drifts have been adopted for design as they are felt to have a more significant physical meaning.*
X.7.2 The inelastic rotational demand on a wall, Δ_{id}, may be taken as: $\Delta_{id} = \left(\Delta_f R_o R_d - \Delta_f \gamma_w\right) \geq 0.004$ Where $\Delta_f R_o R_d$ = the design drift $\Delta_f \gamma_w$ = the elastic portion of the drift ℓ_w = the length of the longest wall in the direction considered 0.004 is the minimum drift demand	*Displacement demands should be calculated using the reduced stiffness from Eq. 4.9 in Chapter 4. In addition, the calculation of a displacement rather than rotation negates the need to assume a plastic hinge length for demand calculations, since this value can be determined explicitly from the elastic displacement.*
X.7.3 The inelastic drift capacity of a wall, Δ_{ic} , may be taken as $\Delta_{ic} = \left(\phi_u - \frac{2.10\varepsilon_y}{\ell_w}\right)\left(\frac{\ell_p}{h_w}\right)\left(h_w - \frac{\ell_p}{2}\right) \leq 0.025$	*This expression was derived from Chapter 4 Eqs. 4.15 – 4.20.*

Where ε_y = the yield strain of vertical reinforcement ℓ_p = the length of plastic hinge defined in Cl. X.7.3.1 ϕ_u = the inelastic curvature capacity of the wall defined in Cl. X.7.3.2	
X.7.3.1 The plastic hinge length may be taken as $\ell_p = 0.25h_w + 0.5\ell_w\sqrt{\left(\frac{A_{sv} f_y / s_v}{A_{sh} f_y / s_h}\right)}$ But not greater than the minimum of a) 1.5 times the length of the longest wall *b)* h_w	*This expression was derived in Chapter 4 and appears in Eq. 4.14.*
X.7.3.2 The inelastic curvature capacity of the wall may be taken as $\phi_u = \frac{\varepsilon_{mu}}{c}$ Where the maximum strain of the masonry in the boundary element, ε_{mu}, can be taken as 0.003 unless the boundary element is detailed as a confined boundary element where ε_{mu} shall be determined in Cl. Y.1 but shall not be taken greater than 0.008 and c shall be determined by plane section analysis. If the boundary element is to be detailed as a confined boundary element than it should extend over a distance not less than c (ε_{mu} – 0.003) / ε_{mu}.	*Even without any additional benefit from confinement detailing, it can be conservatively assumed that the masonry will reach its normal compression strain of 0.003 rather than the value of 0.0025 currently adopted by the CSA S304.1 for moderately ductile walls.*
X.7.3.3 In lieu of the calculations given in Clauses X.7.3 and X.7.3, ductility requirements will be deemed satisfied if: $c/l_w \le \frac{\varepsilon_{mu}}{\frac{4A_r}{(2A_r - 1)}\left(\frac{\Delta_f R_d R_o}{h_w}\right)\left(1 - \gamma_w / R_d R_o\right) + 2\varepsilon_y}$ where $A_r = h_w/\ell_w$	*This expression can be arrived at by re-arranging the above expressions and solving for $\ell_p = \ell_w/2$ to solve for the wall capacity and $\ell_p = \ell_w$ to solve for the demand.*

X.8 Shear strength of special masonry shear walls

This is identical to the approach taken by the CSA A23.3.

X.8.1

Walls shall have a factored shear resistance greater than the shear due to the effects of factored loads. The shear due to the effects of factored loads shall account for the magnification of the shear due to the inelastic effects of higher modes. In addition, the factored shear resistance shall not be less than the smaller of

(a) the shear corresponding to the development of the probable moment capacity of the wall system at its plastic hinge locations; or

(b) the shear resulting from design load combinations that include earthquake, with load effects calculated using $R_d R_o$ equal to 1.3.

X.8.2

The shear design of ductile walls shall meet the requirements specified in *Clause Z* and X.8.3 to X.8.5.

X.8.3

The effective shear depth, d_v, of a wall need not be taken as less than $0.8\ell_w$.

X.8.4

All construction joints in walls between the web of a wall and the boundary elements shall meet the requirements specified in Clause Y.4.

X.8.5

For regions of plastic hinging, the following additional requirements shall apply:

(a) The factored shear demand on the wall shall not exceed $0.06\ \phi_m f'_m b_w d_v$ unless it is shown that the inelastic drift demand on the wall, Δ_{id}, is less than 0.015. When Δ_{id} = 0.005, the factored shear demand shall not exceed $0.09\ \phi_m f'_m b_w d_v$. For inelastic rotational demands between these limits, linear interpolation may be used.

This is indicative of similar requirements made in the CSA A23.3, but have been scaled down to reflect the lower peak shear resistance

(b) The value of β specified in *Clause Z* shall be taken as zero unless it is shown that the inelastic drift demand on the wall, Δ_{id}, is less than 0.015. When Δ_{id} = 0.005, the value of shall not be taken greater than 0.16. For inelastic rotational demands between these limits, linear interpolation may be used. (c) The value of θ in *Clause Z* shall be taken as 45° unless the axial compression (P_f) acting on the wall is greater than $0.1f'_mA_g$. When (P_f) = $0.2f'_mA_g$, the value of θ shall not be taken more than 55°. For axial compressions between these limits, linear interpolation may be used.	*of masonry ($0.15f'_m$) relative to concrete ($0.25f'_m$).* *This is reflective of a similar clause in the A23.3, but with the basic value of β reflective of masonry taken as 0.16.* *Limits established from NSSSE and described in Cl. Z.*
Y Boundary element reinforcement requirements **Y.1 General** Boundary element reinforcement shall comply with Clauses Y.2 to Y.5. **Y.2 Spirals for boundary elements** ***A.2.1*** Spiral reinforcement for boundary elements shall be permitted for use but may not be less than the value given by: $\rho_s = 0.45\left(\frac{A_g}{A_c} - 1\right)\frac{f'_m}{f_y}$ where A_g = the gross area of the boundary element and, with respect to construction and spacers, shall comply with CSA A23.1. ***Y.2.2*** Spiral reinforcement shall have a minimum diameter of 6 mm. ***Y.2.3*** The pitch or distance between turns of the spirals shall not exceed 1/6 of the core diameter.	*Shedid et al. (2010b) indicated that spiral reinforcement could be used.*

Y.2.4 The clear spacing between successive turns of a spiral shall not be less than 25 mm or greater than 75 mm.	
Y.3 Ties for compression members ***Y.3.1*** In boundary elements, all non-prestressed longitudinal bars shall be enclosed by ties having a diameter of at least 30% of that of the largest longitudinal bar. Deformed wire or welded wire fabric of equivalent area may be used.	*Therefore, for standard bar sizes, the following tie diameters would apply:* *10M = 3.4mm,* *15M = 4.8mm,* *20M = 5.9mm,* *25M = 7.6mm,* *30M = 9.0 mm*
Y.3.2 Tie spacing shall not exceed the smallest of (a) 16 times the diameter of the smallest longitudinal bar; (b) 48 tie diameters; (c) the least dimension of the compression member.	*Requirements for ties for typical bars* *10M = 181mm,* *15M = 256mm,* *20M = 312mm,* *25M = 403mm,* *30M = 478mm*
Y.3.3 Ties shall be located not more than one-half of a tie spacing above the slab or footing and shall be spaced to not more than one-half of a tie spacing below the lowest reinforcement in the slab or drop panel above.	
Y.3.4 Ties shall be arranged so that every corner and alternate longitudinal bar shall have lateral support provided by the corner of a tie having an included angle of not more than 135°, and no bar shall be farther than 150 mm clear on either side from such a laterally supported bar.	
Y.3.5 Where the bars are located around the periphery of a circle, a complete circular tie may be used, provided that the ends of the ties are lap welded or bent at least 135° around a longitudinal bar or otherwise anchored within the core of the boundary element.	*For a standard 390 mm × 390 mm pilaster 3 bars could be placed on each side and it would be satisfied with a*

Y.4 Boundary element to web of wall connection

Y.4.1 General

When a running bond cannot be created between the boundary element and the web of the wall a crack shall be assumed to occur between the boundary element and the web of the wall along the shear plane and relative displacement shall be considered to be resisted by cohesion and friction maintained by the shear friction reinforcement crossing the crack. The factored shear stress resistance of the plane shall be computed from

$$v_r = \phi_m \left(c_p + \mu\sigma \right)$$

where the expression $\phi_m(c_p + \mu\sigma)$ shall not exceed $0.15\phi_m f'_m$.

Y.4.2 Values of c and μ

For bonded boundary elements with continuous grout that flows between the web of the wall into the boundary element, the following values shall be taken for c_p and μ:

(a) the area of continuous grout can be considered as part of a monolithic pour such that
c_p = 1.00 MPa
μ = 1.40

(b) the area of mortar bond only
c_p = 0 MPa
μ = 1.00

Where σ is normally taken as the factored tensile force at yield of the horizontal reinforcement that crosses the interface shear plane, and has been detailed to develop yield strength on both sides of the shear plane.

Y.5 Boundary element strain calculation

Y.5.1 General

Ties in boundary elements may be used to increase the compressive strain of the masonry towards estimating the ultimate curvature for the cross-section of a wall for drift capacity calculations. Such calculations shall follow the procedure laid out in Cl. Y.5.2

Y.5.2

The maximum compressive strain of the confined boundary element, ε_{mu}, can be determined as the following

square tie.

$\varepsilon_{mu} = \frac{A_s A_c f_y}{15 k_n f'_m s_s h_c} - \frac{1}{300}$ Where A_s = the area of reinforcement of the stirrup along either axis A_c = confined area measured as the outside-to-outside dimension of the ties f_y = the yield strength the of the ties not to be taken as more than 500MPa s_s = the spacing of the ties h_c = the dimension of the confined core k_n = a factor accounting for the number of bars in contact with the stirrup, *n*, determined as *n/(n-2)*	*This is based on the successful adaption of the reinforced concrete column equation as a conservative estimate for compressive strain in a masonry boundary element as derived in Eq. 2.2.*

Z Design for shear in walls

Z.1 Required shear strength

Members shall be designed such that $Vr \geq Vf$

Z.2 Factored shear resistance

The factored shear resistance shall be determined by

$$V_r = V_m + V_s$$

However, V_r shall not exceed

$$V_{r,\max} = 0.15 \phi_m f'_m b_w d_v \gamma_g$$

Z.3 Determination of V_m

The factored shear resistance of masonry shall be determined from

$$V_m = \phi_m \beta \sqrt{f'_m} b_w d_v \gamma_g$$

Where β is determined as specified in Clause Z.5

Z.4 Determination of V_s

The factored shear resistance of horizontal reinforcement shall be determined from

$$V_s = \frac{\phi_s A_v f_y d_v \tan\theta}{s_h}$$

Where θ is determined as specified in Clause Z.5 and the value of $d_v \tan\theta$ shall be taken as less than or equal to h_w

This is added in since it is possible to have crack angles that deviate from 45°.

Z.5 Determination of β and θ for partially-grouted masonry

Z.5.1 General

The values of β and θ may be determined in accordance with Clauses Z.5.2 to Z.5.3 where θ is measured as the angle between principal shear crack and the bed joint of a wall.

Since there was no evaluation of partially-grouted walls within Chapter 5, the NSSSE cannot be applied. However, for consistency, the existing S304.1 shear strength expression has been presented here, adopting the same syntax used by NSSSE, however the results will be no different than the current S304.1 expression.

Z.5.2 Value of θ for partially-grouted masonry

For partially-grouted members the value of θ shall be taken as 30°

Z.5.3 Value of β for partially-grouted masonry

The value of β shall be determined as follows

$$\beta = 0.16\left(2 - \frac{M_f}{V_f d_v}\right) + \frac{0.25 P_d}{\sqrt{f'_m}\, b_w d_v}$$

Where

$$\frac{M_f}{V_f d_v}$$

= a value that shall not be more than 1 or less than 0.25 for the concurrent factored moment, M_f, and factored shear, V_f, at the section under consideration

Z.6 Determination of β and θ for fully-grouted masonry

Z.6.1 General

The values of β and θ may be determined in accordance with the simplified method described in Clause Z.6.2 and Z.6.3 or by the general method described in Clause Z.6.4 to Z.6.7.

The designer has the option to use a simplified method that does not deviate from the previous code version, but is put into the syntax of the NSSSE.

Z.6.2 Simplified method to determine β

The value of β shall be determined as follows

$$\beta = 0.16\left(2 - \frac{M_f}{V_f d_v}\right) + \frac{0.25 P_d}{\sqrt{f'_m}\, b_w d_v}$$

Where

$$\frac{M_f}{V_f d_v}$$

= a value that shall not be more than 1 or less than 0.25 for the concurrent factored moment, M_f, and factored shear, V_f, at the section under consideration

Z.6.3 Simplified method to determine θ

The value of θ may be taken as 45°

Z.6.4 General method to determine β

The value of β shall be determined as follows

$$\beta = \left(\frac{8000 - \lambda}{3375}\right)\left(\frac{1}{4(1 + 1800\varepsilon_n)}\right)$$

Solved assuming J = 1.5 from Eq. 5.40a as a conservative simplification.

where
λ = as determined by Clause Z.6.6
ε_n = the normal strain parameter determined in Z.6.7

Z.6.5 General method to determine θ

The value of θ shall be determined as follows

$\theta = \left(\frac{7000-\lambda}{5100}\right)\left(\frac{50}{(1+220\varepsilon_n)}\right)$ where λ = as determined by Clause Z.6.6 ε_n = the normal strain parameter determined in Z.6.7	*Solved assuming J = 1.5 from Eq. 5.40b as a conservative simplification.*
Z.6.6 Determination of the factor λ $\lambda = \frac{24(s_v + s_h)}{a_g + 16}$ where a_g = Average maximum aggregate size of masonry can be taken as 7.0 mm for concrete block walls with course grout and 3.5 mm for concrete block walls with fine grout. s_v = Spacing of vertical reinforcement in the web of a wall. s_h = Spacing of horizontal reinforcement.	*Spacing parameters have been conservatively simplified.*
Z.6.7 Determination of the normal strain ε_n In lieu of a more comprehensive analysis the normal strain for the critical cross-section for a wall will be taken at its base and will be determined as the following walls subject to single curvature and with $h_w/\ell_w > 1.0$ $\varepsilon_n = \frac{(V_f h_w / d_v) + (V_f) - (0.5P_d)}{0.8\rho b_w \ell_w E_s}$ walls subject to single curvature and with $h_w/\ell_w \leq 1.0$ $\varepsilon_n = \frac{(V_f h_w / d_v) + (V_f) - (0.5P_d)}{2\rho b_w \ell_w E_s}$	*This statement is based on the observation that there would be a nominal variation in normal strain over the bottom courses of a cracked wall and moments will be greatest at a wall's base.*

walls subject to double curvature $\varepsilon_n = \frac{(V_f h_w / 2d_v) + (V_f) - (P_d)}{2\rho b_w \ell_w E_s}$ where ε_n shall not be taken greater than 0.002 nor less than 0	*For double curvature the effective height would be h_w /2*

6.2.3 Future Research

There is an immediate need for future work to quantify the effects of different boundary element detailing on wall performance. This would have to entail material, assemblage and structural wall testing such that a more comprehensive set of prescriptive dealing details can be provided. The results presented in this dissertation can be interpreted as a minimum level of detailing that would be required to gain benefits from boundary elements. However, it does not mean that there are no greater gains to be made through testing different arrangements of vertical reinforcement and lateral stirrups as well through the development of new specialized boundary element units that could be standardized for construction application.

The use of boundary elements with tied reinforcement offers advantages with respect to how walls are constructed and detailed. For instance, using pre fashioned cages that could be dropped in to pilaster units at the ends of walls would save significantly over having to place reinforcement as walls are constructed. Therefore, in addition to detailing of the boundary element reinforcement, there is a need to investigate the effects of connections within the confined region, as lap splices with vertical reinforcement or starter bars as well as the requirements for horizontal reinforcement, including whether there is a need for 180° hooks, or if this can be relaxed as done with RC.

Within this context, the masonry boundary elements would act essentially as permanent formwork. Whereas the construction of RC structural walls with large boundary elements can be cost prohibitive because of the construction and assembly of formwork. It would be useful to conduct an economic analysis comparing the two construction methods to judge the commercialization and future development of this wall type, since these are key factors with its real world adoption. Within this context there needs be consideration of partially grouted walls, walls with openings as well as exploring the potential for coupled

wall systems. Finally, there is great potential for future testing at the reduced-scale walls, to allow the testing of more complex wall configurations as well as full RM buildings constructed with walls containing boundary elements.

6.3 Notation for Chapter 6

A_c = confined area of boundary element measured as outside-to-outside dimension of confinement hoops (mm^2);
A_g = gross cross-sectional area of wall (mm^2);
a_g = average maximum aggregate size of masonry (mm);
A_s = area of reinforcement in boundary element stirrup (mm^2);
A_{sh} = area of single flexural reinforcing bar at spacing s_v (mm^2);
A_{sv} = area of single shear reinforcing bar at a spacing s_h (mm^2);
b_w = width of the web of a shear wall (mm);
c = depth of neutral axis (mm);
c_p = cohesion stress (MPa);
d_b = diameter of rebar (mm);
d_v = effective depth of masonry wall resisting shear, can be taken as $0.8\ell_w$ (mm);
E_s = Young's modulus of elasticity for steel (MPa);
f'_m = compressive strength of masonry (MPa);
f_y = yield stress of reinforcement (MPa);
h_c = dimension of the confined core (mm);
h_w = height of wall (mm);
k_n = factor to number of bars in contact with confinement tie;
ℓ_d = development length of rebar (mm);
ℓ_p = plastic hinge length of wall (mm);
ℓ_w = length of wall (mm);
ℓ_u = unsupported height of a wall (mm);
M_f = overturning moment in a wall (N·mm);
n = number of bars in a boundary element in contact with tie;
P_d = dead load on wall for shear calculations taken as 0.9 of the dead load (kN);
P_f = level of factored applied axial force in a masonry structural wall (kN);
R_d = ductility-based seismic force reduction factor of the NBCC;
R_o = overstregnth seismic force reduction factor of the NBCC;
s_h = spacing between shear reinforcing bars measured along horizontal axis (mm);
s_s = spacing of confinement ties (mm);
s_v = spacing between flexural reinforcing bars measured along vertical axis (mm);
V_f = factored shear force (N);
V_m = shear resistance of the masonry within a wall (N);
V_r = shear resistance of a wall (N);
V_s = shear strength of reinforcement (N);

β = masonry shear strength parameter;
γ_w = wall overstregnth factor taken an ratio of nominal strength to factored moment, need not be taken less than 1.3;
Δ_f = drift of a wall due to factored loads;
Δ_{ic} = inelastic displacement capacity of a wall given as a drift;
Δ_{id} = inelastic displacement demand of a wall given as a drift;
γ_g = factor to account for partial grouting defined by the CSA S304.1;
ε_{mu} = ultimate compressive strain in masonry;
ε_y = yield strain of vertical reinforcement;
ε_n = average normal strain;
θ = angle measured between masonry bed joint and shear cracking (deg);
λ = crack spacing factor;
μ = coefficient of friction;
v_r = shear stress transmitted by aggregate interlock across cracks (MPa);
ρ = percent area of vertical reinforcement (%);
ρ_s = percent area of spiral reinforcement (%);
ϕ_m = material reduction factor for masonry taken as 0.6;
ϕ_u = curvature of wall at ultimate strength (rad/mm);

6.4 References for Chapter 6

Canadian Standards Association (CSA). (2004a). "Design of masonry structures." *CSA S304.1-04 (R2010)*, CSA, Mississauga, Canada.

Canadian Standards Association (CSA). (2004b). "Design of concrete structures." *CSA A23.3-04 (R2010)*, CSA, Mississauga, Canada.

Masonry Standards Joint Committee. (MSJC). (2008). "Building Code Requirements for Masonry Structures." *TMS 402/ASCE 5/ACI 530*, The Masonry Society, American Society of Civil Engineers, Boulder, New York/American Concrete Institute, and Detroit, USA.

Shedid, M. T., El-Dakhakhni, W. W. and Drysdale, R. G. (2010). "Alternative strategies to enhance the seismic performance of reinforced concrete-block shear wall systems." *J. Struct. Eng.*, 136(6), 676-689.

Wallace, J.W. and Orakcal, K., (2002). "ACI 318-99 Provisions for Seismic Design of Structural Walls," *ACI Structural Journal*, 99(4), 498-508